

Novel Solid Electrolytes Derived From Polymer Syntheses

by

Xinyu Zhang

A dissertation submitted in partial fulfillment
of the requirements for the degree of
Doctor of Philosophy
(Materials Science and Engineering)
in the University of Michigan
2021

Doctoral Committee:

Professor Richard M. Laine, Chair
Professor John Heron
Professor Stephen Maldonado
Professor Wenhao Sun

Xinyu Zhang

xinyumz@umich.edu

ORCID iD: 0000-0003-2971-9185

© Xinyu Zhang 2021

Dedication

To my parents and my friends who supported me and made everything possible.

In the memory of Prof. Dr. Andreas Hintennach.

Acknowledgements

First, I would like to express my appreciation to my advisor, Professor Richard M. Laine, for his mentorship. I would not be where I am without his guidance, support, patience and encouragement over the years. I am also grateful for the support of Professor John Heron, Professor Wenhao Sun, and Professor Stephen Maldonado for serving on my committee.

I would also like to thank my colleagues in the Laine group, including Dr. Eleni Temeche, Mengjie Yu, Jun Guan, Taylor Brandt, Philyong Kim, and Dr. Eongyu Yi. I also want to thank visiting scholars and undergraduate student researchers for their assistance and contribution, especially Tiffany Liu, Xiaopo Chen, Zejun Sun, Christina Said, Dr. Jonathan Rubio Arias, Monika Jansohn and Dr. Mitra Khiabani.

I want to express my special thanks to my parents, family and friends. In particular, I must thank my friend Andrew Alexander for his contribution of the MALDI calculation computer program that made it possible for polymer precursor structural analyses, as well as his support and partnership along this journey.

I would like to thank Dr. Eleni Temeche a second time for not only her important contribution on electrochemical characterization of the polymer precursors, but also her great friendship.

Finally, I would like to acknowledge the financial support from Department of Energy, National Science Foundation, and Mercedes-Benz Research & Development North America. I especially thank Mr. Tobias Glossmann and Prof. Dr. Andreas Hintennach for their support, encouragement and collaboration.

Table of Contents

Dedication	ii
Acknowledgements.....	iii
List of Tables	vii
List of Schemes.....	x
List of Figures.....	xi
List of Appendices	xx
Abstract	xxi
Chapter 1 Introduction.....	1
1.1 Research background and motivation.....	1
1.2 Polymer electrolytes.....	2
1.2.1 Polymer matrices.....	4
1.2.2 Lithium salts.....	6
1.3 Inorganic solid electrolytes.....	9
1.3.1 Garnet-type electrolytes	11
1.3.2 Perovskite-type electrolytes	12
1.3.3 NASICON-type electrolytes	13
1.3.4 LISICON-type electrolytes	13
1.3.5 LiPON-type electrolytes.....	15
1.3.6 Sulfide-type electrolytes.....	16
1.4 Overview of subsequent chapters	17
References	20
Chapter 2 Experimental	31
2.1 Introduction.....	31

2.2	Materials	31
2.3	Synthetic methods.....	32
2.3.1	Oxysilylation of diepoxides	32
2.3.2	Syntheses of LiPON-like polymer precursors.....	33
2.3.3	Syntheses of Li_xSiON ($x = 2, 4, 6$) precursors	34
2.4	Analytical methods	37
	References	41
Chapter 3	An Approach to Epoxy Resins, Oxysilylation of Epoxides.....	42
3.1	Introduction.....	42
3.1.1	Epoxy resin syntheses	42
3.1.2	Organic-inorganic hybrid materials	45
3.2	Experimental section.....	48
3.3	Results and Discussion	49
3.3.1	Oxysilylation of diepoxides with TMDS	49
3.3.2	Oxysilylation reaction of diepoxides with OHS	59
3.3.3	Oxysilylations of diepoxides with a mixture of TMDS and OHS	67
3.3.4	Oxysilylation of diepoxides with $\text{D}_4\text{H}/\text{D}_5\text{H}$	69
3.4	Conclusions.....	73
	References	74
Chapter 4	Design, Synthesis, Characterization and Electrochemical performance of Polymer Precursors to Li_xPON and Li_xSiPON Glasses	79
4.1	Introduction.....	79
4.2	Experimental section.....	82
4.3	Results and discussion	84
4.3.1	Polymer precursor syntheses and characterization.....	84
4.3.2	Li^+ conductivity measurements	104
4.3.3	Electrochemical performance of polymer precursor electrolytes	106
4.3.4	LiPON-like polymer precursor solid solutions with PEO.....	110
4.4	Conclusions.....	115
	References	118
Chapter 5	Li_xSiON ($x = 2, 4, 6$), A Novel Solid Electrolyte System Derived from Agricultural Waste.....	124

5.1	Introduction.....	124
5.2	Experimental section.....	128
5.3	Results and discussion	129
5.3.1	Characterization of Li_xSiON precursors	130
5.3.2	Ionic conductivity measurements.....	149
5.3.3	Electrochemical characterization of Celgard/ Li_xSiON electrolytes.....	152
5.3.4	$\text{Li}_4\text{Ti}_5\text{O}_{12}$ composite anodes with addition of LiAlO_2 and Li_6SiON	156
5.4	Conclusions.....	159
	References	161
Chapter 6	Conclusions and Future Work	167
6.1	Summaries.....	167
6.2	Future work.....	169
6.2.1	Li_xSiON polymer precursor solid solutions with PEO.....	170
6.2.2	Polymer precursor coated solid-state electrolyte thin films	171
6.2.3	Silica dissolution with ethylene glycol.....	176
	References	180
Appendices	182

List of Tables

Table 1.1. Common polymer matrices for PEs and their properties.	5
Table 1.2. Properties of reported polymeric single-ion conductors.	7
Table 1.3. Conductivities (σ) of selected inorganic solid electrolytes.	10
Table 2.1. Oxysilylations of diepoxides in solvent catalyzed by $B(C_6F_5)_3$	32
Table 2.2. P, N source and the stoichiometry of the first step of polymer precursor syntheses. ...	33
Table 2.3. Lithiation of polymer precursors.	34
Table 2.4. Syntheses of Li_xSiON precursors.	37
Table 3.1. GPC data of oxysilylations of diepoxides with TMDS.	50
Table 3.2. 1H NMR data for diepoxide oxysilylations with TMDS.	54
Table 3.3. GPC data for diepoxide oxysilylations with TMDS <i>vs.</i> solvent volumes after 1 d.	55
Table 3.4. Molecular weights of oxysilylations of diepoxides with TMDS, with different amounts of catalyst and solvent.	57
Table 3.5. Selected TGA-DTA of oxysilylation of diepoxides with OHS.	65
Table 3.6. Average percent mass gain in solvent impregnation studies.	66
Table 3.7. BET SSA analysis of oxysilylation of diepoxides with OHS.	66
Table 3.8. Molecular weights of oxysilylations of diepoxides with TMDS and OHS.	67
Table 3.9. Molecular weights of oxysilylations of diepoxides with D_4H	69
Table 3.10. Molecular weights of oxysilylations of diepoxides with D_5H	69
Table 4.1. MWs and estimated compositions of polymer precursors.	89
Table 4.2. Reported FTIR of LiPON glasses.	89

Table 4.3. ^7Li NMR studies on various compounds in solution from the literature.....	94
Table 4.4. ^7Li NMR and atomic ratios based on XPS analyses for polymer precursors (RT/vacuum dried).....	94
Table 4.5. XPS analyses of Li_xPON , Li_2SiPHN and Li_xSiPON pellets.....	100
Table 4.6. Total conductivities (σ_{RT}) of polymer precursor pellets heated to 200-400 °C/2 h/ N_2	106
Table 4.7. Calculated atomic compositions from XPS analyses and total conductivities (σ_{RT}) of PE composite films.	111
Table 5.1. Ionic conductivities (σ) and activation energies (E_a) for $\text{Li}_{3+x}\text{PO}_{4-x}\text{N}_x$, $\text{Li}_{3+x}\text{VO}_{4-x}\text{N}_x$, $\text{Li}_{2+y}\text{ZnSiO}_{4-y}\text{N}_y$ and $\text{Li}_{2+y}\text{MgSiO}_{4-y}\text{N}_y$ solid solutions. ⁴³	126
Table 5.2. Properties of Li_xSiON precursors derived from MALDI.....	134
Table 5.3. Average atomic percentage (At.%) of Li_xSiON precursors dried at different temperatures in comparison with SP (60 °C/12 h/vacuum), analyzed by CasaXPS.	143
Table 5.4. XPS analyses (by CasaXPS) of the Li_4SiON precursor treated at different temperatures.	147
Table 5.5. Densities (g/cm^3) of Li_xSiON precursors treated under different conditions.	149
Table 5.6. Total conductivities (σ_{RT}) of Li_xSiON pellets heated to 100-400 °C/2 h/ N_2	151
Table 5.7. Comparison of ionic conductivities (σ) of Li_4SiO_4 and LiSiON systems with different synthesis/processing methods in the literature.....	152
Table 5.8. Comparison of t_{Li^+} calculated using <i>eq (5.3)</i> and <i>eq (5.4)</i>	153
Table 5.9. Comparison of discharge capacities of LTO-composite anode materials at 5 C.	159
Table 6.1. Selected properties of 60PEO/ Li_xSiON PE films.	171
Table 6.2. Total ambient conductivities (σ_{RT}) of LiPON-like precursor coated SE films after heating to selected temperatures.	174
Table A.1. GPC data for oxysilylation of DEB with OHS.	182
Table A.2. Possible compositions of Li_xPON precursors based on Figures A.3-A.4	185

Table A.3. Possible compositions of Li ₂ SiPHN precursor based on Figures A.5-A.6.	186
Table A.4. Possible compositions of Li _x SiPON precursors based on Figures A.7-A.8.	189
Table A.5. Electronegativity of selected elements.	191
Table A.6. Atomic ratios based on EDX analyses for Li _x PON, Li ₂ SiPHN and Li _x SiPON after heating to various temperatures for 2 h.	193
Table A.7. Possible compositions of Li _x SiON precursors based on MALDI.†	197
Table A.8. Average atomic percentage (At.%) of Li _x SiON pellets based on EDX analyses.	203
Table A.9. Diffusivities and potential gap for pristine and composite LTO electrodes.	205
Table D.1. Comparison of ZTA ceramics in literature and this work.	214
Table D.2. Starting materials of <i>t</i> -ZrO ₂ (0-50 mol.%) doped δ-Al ₂ O ₃ suspension.	219
Table D.3. Suspension of coating material: 10 % ZrO ₂ doped δ-Al ₂ O ₃	221
Table D.4. Selected properties of (ZrO ₂) _x (Al ₂ O ₃) _{1-x} (x = 0, 15, 30, 50 mol.%) NPs.	225
Table D.5. Compositions of ZTA films.	229
Table D.6. Lateral shrinkage of ZTA films (A-D per Table D.5) sintered at 1400-1500 °C/5 h/N ₂ /H ₂	233
Table D.7. AGSs and shrinkages of ZTA films (composition D, size ≈ 1×1 cm ² × 200 μm). ...	235
Table D.8. Selected properties of ~200 μm ZTA films (composition D) sintered at 1500 °C/5 h/N ₂ /H ₂ with different sintering ramp rates.	238
Table D.9. Selected properties of ~200 μm ZTA films (composition D) sintered at different binder burnout conditions with BN insulation.	244

List of Schemes

Scheme 1.1. Oxysilylation of OHS with diepoxide.	6
Scheme 1.2. Example structures of polymeric lithium salts.	8
Scheme 1.3. Example structures of Li_xPON , Li_xSiPON and Li_xSiON oligomer/polymer electrolytes.	9
Scheme 3.1. General pathway for amine curing of epoxides with 2:1 N:epoxy ratios.	43
Scheme 3.2. $\text{B}(\text{C}_6\text{F}_5)_3$ catalyzed oxysilylation of epoxides gives two products.	43
Scheme 3.3. $\text{B}(\text{C}_6\text{F}_5)_3$ catalyzed oxysilylations of diepoxides with OHS.	47
Scheme 3.4. $\text{B}(\text{C}_6\text{F}_5)_3$ catalyzed oxysilylations of diepoxides with D_4H and D_5H	48
Scheme 3.5. Crosslinking and cyclomer models from diepoxide oxysilylation with D_4H and D_5H	71
Scheme 4.1. Synthesis of Li_xPON ($x = \text{Li}/\text{P}$) precursors.	85
Scheme 4.2. Synthesis of Li_xSiPON ($x = \text{Li}/\text{P}$) precursors.	85
Scheme 4.3. Synthesis of Li_xSiPHN ($x = \text{Li}/\text{P}$) precursors.	85
Scheme 4.4. Synthesis of Li_xSiPON precursors with $(\text{Me}_3\text{Si})_2\text{NH}/\text{OPCl}_3 = 1.8$	87
Scheme 6.1. Coating procedure of LiPON-like polymer precursors on SE substrates.	173
Scheme D.1. Liquid feed flame spray pyrolysis (LF-FSP) for nanopowder production.	218
Scheme D.2. Schematics of sample preparation and testing procedure of SEPB test.	224

List of Figures

Figure 1.1. Ion transport in SPEs.	3
Figure 1.2. Structures of example inorganic solid electrolytes.....	11
Figure 2.1. Optical images of typical syntheses of Li_xSiON precursors.....	36
Figure 2.2. Optical images of representative dried Li_xSiON precursor powders (top) and hydraulically pressed pellets (bottom, 5 ksi/20 sec with a 13 mm diameter die).	37
Figure 3.1. Cubic cages. (a) Q_8 ($\text{Q} = \text{SiO}_4$) $\text{R} = \text{H}$, vinyl, epoxy, 3-hydroxypropyl, aminopropyl, glycidylepoxy, ethylcyclohexylepoxy, methacrylate, <i>etc.</i> (b) R_8T_8 ($\text{T} = \text{carbon-SiO}_{1.5}$) $\text{R} = \text{alkyl}$, alkene, acetylene, acrylate, $\text{R}'\text{X}$ ($\text{X} = \text{halogen}$, $-\text{CN}$, amine, epoxy, ester, <i>etc.</i> $\text{R}' = \text{R}$ same or mixed).	45
Figure 3.2. Diepoxide structures: (a) 1,3-diepoxbutane (DEB). (b) 1,7-Diepoxyoctane (DEO). (c) Bisphenol A diglycidyl ether (DGEBA). (d) 3,4-epoxycyclohexylmethyl-3',4'-epoxycyclohexane carboxylate (ECHX).....	47
Figure 3.3. GPC of oxysilylations of diepoxides with TMDS. (a) 1:1 DEB:TMDS, (b)1:1 DEO:TMDS, (c) 1:1 DGEBA:TMDS, (d) 1:1 ECHX:TMDS.....	51
Figure 3.4. FTIRs of oxysilylations of diepoxides with TMDS.	52
Figure 3.5. $^1\text{HNMR}$ models (top) and record (bottom) of 1:1 DEB:TMDS.....	53
Figure 3.6. $^1\text{HNMR}$ models (top) and record (bottom) of 1:1 DEO:TMDS.....	53
Figure 3.7. $^1\text{HNMR}$ models (top) and record (bottom) of 1:1 DGEBA:TMDS.	54
Figure 3.8. Optical images of solventless oxysilylation products.....	56
Figure 3.9. FTIRs of diepoxide oxysilylation with TMDS, 0.5 mg $\text{B}(\text{C}_6\text{F}_5)_3$, in 2.5 mL DCM + 2.5 mL hexane.....	58

Figure 3.10. FTIRs of (a) 1:1 DEB:TMDS, (b) 1:1 DEO:TMDS, (c) 1:1 DGEBA:TMDS, (d) 1:1 ECHX:TMDS before and after boiling in water for 5 h.	59
Figure 3.11. Optical images of as-formed 1:1 DEO:OHS and 1:1 DGEBA:OHS gels, and 1:1 ECHX:OHS solid (precipitate).	60
Figure 3.12. Optical images of dried (100 °C/vacuum/24 h) 1:1 DEO:OHS and 1:1 DGEBA:OHS gels, and 1:1 ECHX:OHS solid.	60
Figure 3.13. Optical images of a cast 1:1 DEO:OHS film on a PTFE substrate, 5 d of reaction in 5 mL DCM + 5 mL hexane.	61
Figure 3.14. GPC (a) and FTIR (b) of oxysilylation of DEB with OHS.	62
Figure 3.15. FTIRs of (a) 1:1 DEO:OHS, (b) 1:1 DGEBA:OHS, (c) 1:1 ECHX:OHS before and after boiling in water for 5 h in comparison to OHS.	63
Figure 3.16. TGA/DTA/air/10°C/min of 1:1 DEB:OHS after drying (left) and estimated structure of repeating unit of 1:1 DEB:OHS (right).	64
Figure 3.17. TGA/DTA/air/10°C/min of 1:1 DEO:OHS after drying (left) and estimated structure of repeating unit of 1:1 DEO:OHS (right).	64
Figure 3.18. TGA/DTA/air/10°C/min of 1:1 DGEBA:OHS after drying (left) and estimated structure of repeating unit of 1:1 DGEBA:OHS (right).	65
Figure 3.19. TGA/DTA/air/10°C/min of 1:1 ECHX:OHS after drying (left) and estimated structure of repeating unit of 1:1 ECHX:OHS (right).	65
Figure 3.20. FTIRs of diepoxide oxysilylation with TMDS + 5 mol.% OHS, 0.5 mg B(C ₆ F ₅) ₃ . ..	68
Figure 3.21. FTIRs of diepoxide oxysilylation with D ₄ H (a) and D ₅ H (b), 0.5 mg B(C ₆ F ₅) ₃ in 5 mL DCM + 5 mL hexane.	71
Figure 3.22. FTIRs of (a) 1:1 DEB:D ₅ H, (b) 1:1 DEO:D ₅ H, (c) 1:1 DGEBA:D ₅ H, (d) 1:1 ECHX:D ₅ H before and after boiling in water for 5 h.	72
Figure 4.1. FTIR spectra of Li ₃ PON (a), Li ₆ PON (b), Li ₂ SiPHN (c), Li ₃ SiPON (d), and Li ₆ SiPON (e) precursors at different temperatures.	90

Figure 4.2. TGA-DTA (800 °C/10 °C min ⁻¹ /N ₂) of Li ₃ PON, Li ₆ PON, Li ₂ SiPHN, Li ₃ SiPON and Li ₆ SiPON precursors.....	91
Figure 4.3a. ⁷ Li NMR of Li ₃ PON, Li ₆ PON, Li ₂ SiPHN, Li ₃ SiPON and Li ₆ SiPON precursors (RT/vacuum dried, dissolved in CDCl ₃). b. Exemplary structures of Li _x PON, Li _x SiPHN and Li _x SiPON precursors with Li ⁺ highlighted.	93
Figure 4.4. ¹³ C NMR (a) and ²⁹ Si NMR (b) of Li ₂ SiPHN, Li ₃ SiPON and Li ₆ SiPON precursors (RT/vacuum dried, dissolved in CDCl ₃) in comparison with (Me ₃ Si) ₂ NH.	96
Figure 4.5. ¹ H NMR of Li ₂ SiPHN, Li ₃ SiPON and Li ₆ SiPON precursors (RT/vacuum dried, dissolved in CDCl ₃) in comparison with (Me ₃ Si) ₂ NH.....	97
Figure 4.6. XRD plots of Li ₃ PON (a), Li ₆ PON (b), Li ₂ SiPHN (c), Li ₃ SiPON (d), and Li ₆ SiPON (e) heated to 100-600 °C/2 h/N ₂	99
Figure 4.7. SEM fracture surface images of Li _x PON, Li ₂ SiPHN and Li _x SiPON pellets heated between 100-400 °C/2 h/N ₂	103
Figure 4.8. Nyquist plots of polymer precursor pellets heated to 200-400 °C/2 h/N ₂	105
Figure 4.9a. Ionic conductivity vs. N/P ratio of SS/Celgard + polymer precursor/SS cells, b. t_{Li^+} and c. electrical conductivities of Li/Celgard + polymer precursor/Li cells.	108
Figure 4.10. Specific capacity (a) and coulombic efficiency (b) vs. cycle number plots of SPAN/Celgard + Li ₆ SiPON/Li at 0.5 C.....	109
Figure 4.11a. Thermal properties of PEs and PEO films and b. correlation between the N/P ratio (black), crystallinity percentage (red), and ionic conductivity at RT of PEs (blue).	113
Figure 4.12a. t_{Li^+} of PE films in Li/60PEO/PEs/Li cell configuration and example precursor structures. b. Galvanostatic cycling of Li/60PEO/Li ₆ PON/Li at ±1.5-7.5 mA at RT.	114
Figure 4.13. Specific capacity (a) and coulombic efficiency (b) vs. cycle number of SPAN/60PEO/Li ₆ SiPON/Li at selected C-rates.	115
Figure 5.1. FTIRs of a. Li _x SiON precursors (60 °C/1 h/vacuum) and SP (60 °C/12 h/vacuum), b. Li ₆ SiON dried at RT, 60 and 100 °C/1 h/vacuum.	130

Figure 5.2. Positive-ion MALDIs of blank vs. Li_xSiON precursors, a. Li_2SiON , b. Li_4SiON and c. Li_6SiON , and possible compositions of selected peaks. S = SP, A = $-\text{NH}_2$, L = Li^+	133
Figure 5.3. ^1H NMRs of Li_xSiON precursors (60 °C/24 h/vacuum) and SP.	135
Figure 5.4. ^{13}C NMRs of Li_xSiON precursors (60 °C/24 h/vacuum) and SP.	136
Figure 5.5. ^7Li NMRs of Li_xSiON precursors (RT/1 h/vacuum).	137
Figure 5.6. TGA-DTAs (800 °C/10 °C $\text{min}^{-1}/\text{N}_2$) of a. Li_2SiON , b. Li_4SiON and c. Li_6SiON precursors dried at 60 °C/1 h/vacuum.....	138
Figure 5.7. XRDs of a. Li_xSiON precursors (60 °C/1 h/vacuum) and SP (60 °C/12 h/vacuum), b. Li_6SiON dried at RT, 60 and 100 °C/1 h/vacuum.	139
Figure 5.8. XRDs of a. Li_2SiON , b. Li_4SiON , c. Li_6SiON pellets heated to 100-400 °C/2 h/ N_2	141
Figure 5.9. Wide-scan survey XPS spectra of Li_2SiON (a), Li_4SiON (b) and Li_6SiON (c) precursors dried at RT, 60 and 100 °C/1 h/vacuum respectively.	142
Figure 5.10. N 1s core-level XPS spectra of Li_xSiON precursors (60 °C/1 h/vacuum). b. Si 2p XPS core-level spectra of Li_xSiON precursors (60 °C/1 h/vacuum) compared to SP (60 °C/12 h/vacuum).	145
Figure 5.11a. FTIRs of Li_xSiON pellets heated to 800 °C/1 h/ N_2 . b. XRDs of Li_4SiON (800 °C/1 h/ N_2) pellet and powder compared to Li_4SiO_4 (monoclinic). c. Wide-scan survey XPS spectra of Li_4SiON treated at RT/1 h/vacuum and 800 °C/1 h/ N_2 . d. C 1s core-level spectra of Li_4SiON treated at RT/1 h/vacuum and 800 °C/1 h/ N_2	146
Figure 5.12. SEM fracture surface images of Li_xSiON pellets heated to 100-400 °C/2 h/ N_2 . ..	148
Figure 5.13. Nyquist plots of Li_xSiON pellets heated to 100-400 °C/2 h/ N_2	150
Figure 5.14a. Nyquist plots of SS/Celgard + Li_xSiON /SS symmetric cells and b. Li/Si ratio vs. ionic conductivity at ambient.....	153
Figure 5.15a. CV plot of Li/Celgard + Li_6SiON /SS at sweep rate of 1 mV/sec and b. galvanostatic cycling of Li/Celgard + Li_6SiON /Li symmetric cell at ambient.....	155

Figure 5.16. Cycle number vs. specific capacity and coulombic efficiency of SPAN/Celgard + Li ₆ SiON/Li half-cell cycled between 1-3 V at ambient.....	156
Figure 5.17. Preparation of LTO-composite anodes.....	157
Figure 5.18. Comparison of discharge capacities of the various electrodes cycled between 0.01 and 2.5 V at selected C-rates.....	159
Figure 6.1. Optical images of 60PEO/Li ₆ SiON (a) and SEM fracture surface images of 60PEO/Li _x SiON PE films (b) heated to 65 °C/24 h/vacuum.....	171
Figure 6.2. SEM fracture surface images of LiAlO ₂ + LiPON-like precursor films heated to 400°, 500° and 600 °C/2 h/N ₂	173
Figure 6.3. SEM fracture surface images of Li ₃ SiPON precursor bonding interface between LTO and LiAlO ₂ thin films (sample heated to 400 °C/2 h/N ₂).	175
Figure 6.4. Optical images of a. Li _x SiO (x = 0.2 and 0.4) dried products and pellets, and b. Li _x SiO-5TEA (x = 0.2 and 0.4) dried products and pellets.	177
Figure 6.5. Optical images of Li _{0.6} SiO powders and pellets from the suspension mixture and soluble portion.	178
Figure 6.6. Representative Nyquist plots (a) and summarized conductivities (b) of Li _x SiO (x = 0.2, 0.4) and Li _{0.6} SiO pellets (100 °C/5 ksi/5min) from the soluble part and suspension mixture.....	179
Figure A.1. Representative FTIRs of OHS (bottom) and precipitated cubes in diepoxide oxysilylation with TMDS + (5-20 mol.%) OHS.....	182
Figure A.2. GPC of unlithiated PON, SiPHN and SiPON precursors.	183
Figure A.3. Negative-ion mode MALDI of Li ₃ PON (left) and Li ₆ PON (right) precursors.....	184
Figure A.4. Possible Li _x PON monomer structures.	184
Figure A.5. Negative-ion mode MALDI of the Li ₂ SiPHN precursor.	185
Figure A.6. Possible monomer structures of Li ₂ SiPHN precursor.	186
Figure A.7. Negative-ion mode MALDI of Li ₃ SiPON (left) and Li ₆ SiPON (right) precursors.	187
Figure A.8. Possible Li _x SiPON monomer structures.	188

Figure A.9. FTIR spectra of unlithiated PON, SiPHN and SiPON precursors.....	190
Figure A.10. ^{13}C NMR of a. $(\text{Me}_3\text{Si})_2\text{O}$ and b. Me_3SiCl from Chemical Book database. Solvent: CDCl_3	190
Figure A.11. ^1H NMR models of a. Me_3SiNH_2 , b. $(\text{Me}_3\text{Si})_2\text{O}$, and c. Me_3SiCl by ChemDraw.	191
Figure A.12. Wide-scan survey XPS spectra (600 to 0 eV) of Li_3PON (a), Li_6PON (b), Li_2SiPHN (c), Li_3SiPON (d), and Li_6SiPON (e) pellets (RT/vacuum dried).....	192
Figure A.14. Optical image of PEO (60 wt.%) /polymer precursor films.	193
Figure A.15a. XPS Spectra (600 to 0 eV) of PEs and the PEO film, and b. Nyquist plots of PEs at ambient.....	194
Figure A.16. DSC thermograms of pristine PEO and PE films after the 3rd cycle.	194
Figure A.17. FTIRs of Li_6SiON (dried at $60\text{ }^\circ\text{C}/1\text{ h/vacuum}$) and LiNH_2	195
Figure A.18. Negative-ion mode MALDIs of blank vs Li_xSiON precursors, a. Li_2SiON , b. Li_4SiON and c. Li_6SiON	196
Figure A.19. ^1H NMRs of Li_xSiON precursors (RT/1 h/vacuum), THF and SP.	198
Figure A.20. ^{13}C NMRs of Li_xSiON precursors (RT/1 h/vacuum), THF and SP.	199
Figure A.21. ^7Li NMRs of Li_xSiON precursors ($60\text{ }^\circ\text{C}/24\text{ h/vacuum}$).	199
Figure A.22. ^{29}Si NMRs of Li_xSiON precursors dried at a. RT/1 h/vacuum and b. $60\text{ }^\circ\text{C}/24\text{ h/vacuum}$	200
Figure A.23. TGA-DTA ($600\text{ }^\circ\text{C}/10\text{ }^\circ\text{C min}^{-1}/\text{N}_2$) of SP ($60\text{ }^\circ\text{C}/12\text{ h/vacuum}$).	200
Figure A.24. Wide-scan survey XPS spectra of Li_xSiON precursors dried at RT/1 h/vacuum compared to SP ($60\text{ }^\circ\text{C}/12\text{ h/vacuum}$).	201
Figure A.25. EDX map of Li_2SiON pellets heated to $100\text{-}400\text{ }^\circ\text{C}/2\text{ h/ N}_2$	201
Figure A.26. EDX map of Li_4SiON pellets heated to $100\text{-}400\text{ }^\circ\text{C}/2\text{ h/ N}_2$	202
Figure A.27. EDX map of Li_6SiON pellets heated to $100\text{-}400\text{ }^\circ\text{C}/2\text{ h/ N}_2$	202

Figure A.28. CV plots of a. Li/Celgard + Li ₂ SiON/SS and b. Li/Celgard + Li ₄ SiON/SS at sweep rate of 1 mV/sec.....	203
Figure A.29. Galvanostatic cycling of a. Li/Celgard + Li ₂ SiON/Li and b. Li/Celgard + Li ₄ SiON/Li at ambient.....	204
Figure A.30. SEM images of LTO and LTO-composite powders.....	204
Figure A.31. Long-term cycling stability of LTO-5LiAlO ₂ -10Li ₆ SiON/Li half-cell at 5 C.	205
Figure A.32. CV plots of the LTO-pristine, LTO-LiAlO ₂ , and LTO-Li ₆ SiON (a) and LTO-LiAlO ₂ -Li ₆ SiON (b) half-cells.....	205
Figure A.33. SEM fracture surface images of LATSP + LiPON-like precursor films heated to 400°, 500° and 600 °C/2 h/N ₂	206
Figure A.34. Example optical image of a Li _x SiO-5TEA pellet.	206
Figure C.1. Optical images of a. dried 1:1 DEO:OHS + LiClO ₄ film and b. after sputter coating.	212
Figure D.1. Typical sintering schedules, a. in O ₂ , b. in N ₂ /H ₂	220
Figure D.2. Coating setup of Si ₃ N ₄ films.....	221
Figure D.3. SEMs of a. as-produced LF-FSP Al ₂ O ₃ and b. 50 mol.% ZrO ₂ doped Al ₂ O ₃ nanoparticles.	225
Figure D.4. XRDs of (ZrO ₂) _x (Al ₂ O ₃) _{1-x} (x = 0, 15, 30, 50 mol.%) NPs.	226
Figure D.5. SEM fracture surfaces of sintered (ZrO ₂) _x (Al ₂ O ₃) _{1-x} (x = 0, 15, 30, 50 mol.%) thin films.	227
Figure D.6. AGSs vs ZrO ₂ content b. sintered film thicknesses for (ZrO ₂) _x (Al ₂ O ₃) _{1-x} (x = 0, 15, 30, 50 mol.%).....	227
Figure D.7. SEM fractures surfaces of (ZrO ₂) _x (Al ₂ O ₃) _{1-x} films sintered at 1400 °C/5 h/N ₂ /H ₂ (a, b, c) and O ₂ (d, e, f), where x = 15 (a, d), 30 (b, e), and 50 mol.% ZrO ₂ (c, f).....	228
Figure D.8. SEM fracture surfaces of ZTA films (A-D per Table D.5) sintered at 1300-1500 °C/5 h/O ₂ . The red arrow suggests transgranular fracture.	230
Figure D.9. XRDs of ZTA films (A-D per Table D.5) sintered at 1300-1500 °C/5 h/O ₂	231

Figure D.10. SEM fracture surfaces of ZTA films (A-D per Table D.5) sintered at 1400-1500 °C/5 h/N ₂ /H ₂ . Red arrows suggest transgranular fracture.	232
Figure D.11. XRDs of ZTA films (A-D per Table D.5) sintered at 1400-1500 °C/5 h/N ₂ /H ₂ . ..	233
Figure D.12. SEM fracture surfaces of ZTA films (composition D , size ≈ 1×1 cm ² × 200 μm) sintered at 1500 °C/5 h/O ₂ (a, c) and 1500 °C/5 h/ N ₂ /H ₂ (b, d). Initial thickness ≈ 200 μm before sintering.....	235
Figure D.13. XRDs of ZTA films (composition D , size ≈ 1×1 cm ² × 200 μm) sintered at 1500 °C/5 h/O ₂ (bottom) and 1500 °C/5 h/N ₂ /H ₂ (top).....	236
Figure D.14. Optical images of ~200 μm ZTA films (composition D) sintered at 1500 °C/5 h/N ₂ /H ₂ with different sintering ramp rates.	237
Figure D.15. SEM fracture surfaces of ~200 μm ZTA films (composition D) sintered (1500 °C/5 h/N ₂ /H ₂) at 5 °C/min (a, d), 2.5 °C/min (b, e) and 1 °C/min (c, f). Green film thicknesses were 220-250 μm before sintering.....	238
Figure D.16. XRDs of ~200 μm ZTA films (composition D) sintered at 1500 °C/5 h/N ₂ /H ₂ with different sintering ramp rates.....	239
Figure D.17. Sintering schedule of ~200 μm ZTA films (composition D) with different binder burnout temperatures of 600, 800 and 1100 °C in air, with BN insulation.	239
Figure D.18. Optical images of ~200 μm ZTA films (composition D) sintered at 1500 °C/5 h/N ₂ /H ₂ , 2.5 °C/min with different binder burnout temperatures and BN insulation.	240
Figure D.19. SEM fracture surfaces of ~200 μm ZTA films (composition D , sintered at 1500 °C/5 h/N ₂ /H ₂ , 2.5 °C/min) debinded at 600 °C/1 h/air (a, d), 800 °C/1 h/air (b, e), and 1100 °C/1 h/air (c, f) with BN insulation.	241
Figure D.20. XRDs of ~200 μm ZTA films (composition D) sintered at 1500 °C/5 h/N ₂ /H ₂ , 2.5 °C/min with different binder burnout temperatures and BN insulation.	241
Figure D.21. TGA (1000 °C/air) of 10 mol.% ZrO ₂ doped Al ₂ O ₃ (composition D) green films.	242
Figure D.22. Sintering schedule of 200 μm ZTA films with slow binder burnout ramp rates and BN insulation.	242

Figure D.23. Optical images of ~200 μm ZTA films (composition **D**) before and after binder burnout and sintering. Thicknesses and lateral lengths are given on the films and on the right, respectively.243

Figure D.24. SEM fracture surfaces of ~200 μm ZTA film (composition **D**) sintered with 3-step binder burnout procedure per Figure **D.22**.244

Figure D.25. Fracture toughness (K_{IC}) of standard Al_2O_3 films and ~200 μm ZTA films (composition **D**) sintered with 3-step binder burnout procedure per Figure **D.22**, experiment performed by Rogers Germany GmbH.245

Figure D.26. Representative examples (a) and dye test (b) of Si_3N_4 films coated with ZTA (composition **D**) after sintering at 1500 °C/5 h/ N_2/H_2246

Figure D.27. SEM fracture surface (a) and surface (b) of Si_3N_4 films coated with ZTA (composition **D**) sintered at 1500 °C/5 h/ N_2/H_2 . c. SEM surface of an uncoated Si_3N_4 film.246

Figure D.28. EDSs of a Si_3N_4 film coated with ZTA (composition **D**) sintered at 1500 °C/5 h/ N_2/H_2247

Figure D.29. XRDs of Si_3N_4 films coated with ZTA (composition **D**) sintered at 1500 °C/5 h/ N_2/H_2247

Figure D.30. Optical images of a. uncoated and b. coated Si_3N_4 films and SEM surfaces of c. uncoated and d. coated Si_3N_4 films with ZTA (composition **D**) after heating at 1500 °C/1 h/ O_2248

List of Appendices

Appendix A. Supplemental Data	182
Appendix B. MALDI-Calculation.....	207
Appendix C. Incorporation of LiClO ₄ to 1:1 DEO:OHS	211
Appendix D. <i>t</i> -ZrO ₂ Toughened Al ₂ O ₃ Free-standing Films and as Oxidation Mitigating Thin Films on Silicon Nitride via Colloidal Processing of Flame Made Nanopowders	213

Abstract

Lithium-ion batteries (LIBs) have become the most important electrochemical storage system owing to their high energy densities (~250 Wh/kg), providing an escape from consumption of fossil fuels. However, current LIBs with flammable organic liquid electrolytes suffer from poor electrochemical and thermal stabilities that can lead to severe thermal runaway accidents. All-solid-state batteries (ASSBs) are regarded as a fundamental solution to address the safety issue by applying solid-state electrolytes (SSEs). Therefore, we explore novel polymeric SSE materials and develop new synthesis methods with low-cost, scalable and environmentally friendly features.

We first explore nanocomposites by oxysilylation of $[\text{HSiMe}_2\text{O}(\text{SiO})_{1.5}]_8$ (OHS) crosslinked via ring-opening of epoxy groups. The linkages containing ether oxygens may facilitate Li^+ transport, while the 3-D ordered organic-inorganic hybrid structure offers mechanical stability. We describe oxysilylations of different diepoxides with TMDS $[\text{O}(\text{SiMe}_2\text{H})_2]$, OHS, D₄H and D₅H $[(\text{CH}_3\text{SiHO})_{4,5}]$ catalyzed by $\text{B}(\text{C}_6\text{F}_5)_3$ at ambient. Although we were able to cast flexible transparent films, they failed to offer ionic conductivity with LiClO_4 impregnation due to its rigid structure. Nevertheless, a novel synthesis of self-reinforced epoxy resin nanocomposites is established.

We then investigate polymer precursor electrolytes based on lithium phosphorous oxynitride (LiPON) glasses. LiPON glasses form lithium dendrite impenetrable interfaces at electrodes offering the potential to replace liquid electrolytes. Unfortunately, to date such materials are introduced only via gas phase deposition. We demonstrate the design and synthesis of easily scaled, low-temperature, solution processable inorganic polymers containing LiPON/LiSiPON elements.

OPCl₃ and (Cl₂P=N)₃ provide starting points for elaboration using NaNH₂ or (Me₃Si)₂NH producing OP(NH₂)_{3-x}(NH)_x, OP(NH₂)_{3-x}(NHSiMe₃)_x and (P=N)₃(NHSiMe₃)_{6-x}(NH)_x. It is followed by lithiation with selected amounts of LiNH₂ providing varying degrees of lithiation. Produced oligomers/polymers show higher N/P ratios (1-3) than traditional LiPON glasses (≤ 0.9) correlating with enhanced ionic conductivities. Li₂SiPHN offers the highest ambient conductivity of 2.7×10^{-4} S/cm after treating at 400 °C/2 h/N₂. These LiPON-like precursor solutions can coat Celgard separators and dried (90 °C/12 h/vac) prior to cell assembly. A nearly all-solid-state Li-S battery assembled using celgard/Li₆SiPON exhibits a reversible capacity of 750 mAh/g_{sulfur} and excellent cycle performance at 0.25 and 0.5 C rate over 120 cycles at ambient. They also form solid solutions with PEO (60 wt.%) forming composite SSE films for ASSBs offering discharge capacities of ~1000 mAh/g_{sulfur} (at 0.25-1 C) retaining coulombic efficiency of ~100 % over 100 cycles.

We also studied another set of Li_xSiON (Li/Si = x = 2, 4, 6) polymer precursors derived from rice hull ash (RHA), an agricultural waste, providing a green route towards ASSBs. Silica, ~90 wt. % in RHA, can be catalytically dissolved (20-40 wt.%) in hexylene glycol and distilled directly as spiroxiloxane [(C₆H₁₄O₂)₂Si, SP] at 200 °C. SP can be lithiated using LiNH₂ to produce Li_xSiON oligomers/polymers, and the Li content is easily controlled by LiNH₂ amounts correlating with Li⁺ conductivity. Li₆SiON exhibits the highest ambient conductivity of ~10⁻⁵ S/cm after treating at 200 °C/2 h/N₂. Similar to LiPON-like precursors, Li_xSiON coated Celgard enable nearly ASSB assembly delivering a reversible capacity of ~725 mAh/g at 0.5 C over 50 cycles.

Overall, the research objectives for this dissertation are to develop novel polymeric electrolytes through polymer syntheses based on LiPON and LISICON type SSEs and establish new synthesis chemistries, moving towards the goal of ASSBs assembly through low-cost, scalable and environmentally friendly fabrication methods that can be commercialized.

Chapter 1 Introduction

1.1 Research background and motivation

Replacing traditional combustion-based energy sources, i.e., fossil fuels, with clean and reliable energy supply is one of the most important research goals for the 21st century. Electrochemical energy storage/conversion systems, including lithium-ion batteries (LIBs), electrochemical capacitors (ECs), and fuel cells (FCs), have thus become subjects of great interest.¹⁻⁴ LIBs were first commercialized in the early 90s and were immediately accepted with increasing interest due to their high energy density (reaching 350 Wh/kg in 2020)⁵, good performance and absence of a memory effect as seen with nickel-cadmium (Ni-Cd) or nickel-hydride (Ni-MH) batteries.^{4,6,7} LIBs are now used widely in applications ranging from microbatteries for integrated circuits and medical devices, to larger scale batteries for portable electronics including smart phones and laptops, and are instrumental in the commercialization of electric vehicles.^{6,8}

Conventional LIBs rely on flammable organic liquid electrolytes due to their high ionic conductivity and excellent wetting of electrode surfaces. However, they often suffer from inadequate electrochemical and thermal stabilities giving rise to inherent safety risks and restrained operating temperatures.⁷⁻¹⁰ Non-flammable, solid-state electrolytes (SSEs or SEs) offer an escape from such problems offering potential for wider operating temperatures, higher energy-densities, and simplification in the cell design.¹¹⁻¹⁴ In addition, SSEs with high structural integrity may prevent lithium dendrite growth, making it possible to use Li metal as the anode (theoretical capacity 3860 mAh/g).^{15,16}

From a practical standpoint, solid electrolytes for ASSBs should possess offer high ionic conductivity ($>10^{-4}$ S/cm), negligible electrical conductivity ($<10^{-8}$ S/cm), wide electrochemical windows (≥ 5 V vs. Li^+/Li), appreciable Li^+ transference numbers (close to 1), high critical current densities (≥ 1 mA/cm²), good mechanical and dimensional stabilities for cell assembly, chemical stability with electrodes, and thermal stability during extensive cycling.^{17,18}

There are two general classes of SSEs for LIBs: polymer and inorganic solid electrolytes. The following sections of this introduction give detailed background on polymer and inorganic solid electrolytes respectively, and development of new methods and materials in an effort to improve the current electrolyte properties and synthesis approaches.

1.2 Polymer electrolytes

Polymer electrolytes are characterized by low density, low elastic moduli and high ductility, offering shape versatility, flexible and light weight features, and therefore reduced fabrication costs. However, they often suffer from low ambient ionic conductivity, insufficient electrochemical stability and poor flame resistance.^{11,12,18,19}

There are two major groups of PEs, solid polymer electrolytes (SPEs) and gel polymer electrolytes (GPEs). A SPE typically consists of a polymer matrix impregnated with lithium salts, and a GPE typically consists of SPE (polymer-salt system) with liquid plasticizer or solvent. Generally, SPEs provide features including safety, easy fabrication, low cost, high energy density, good electrochemical stability, and excellent compatibility with lithium salts. However, they also exhibit poor ambient ionic conductivities of 10^{-8} - 10^{-4} S/cm.¹⁸⁻²¹ In contrast, the conductivities of GPEs can reach 10^{-3} S/cm, but poor mechanical strength and poor interfacial properties often arise due to the incorporation of a liquid phase.^{18,22,23} To improve ionic conductivities for SPEs, or improve mechanical properties and mitigate electrolyte/electrode compatibility issues and safety hazards

for GPEs, ceramic fillers are often incorporated, and such electrolyte systems are called composite polymer electrolytes (CPEs).^{24,25}

Ion transport in PEs is typically achieved by breaking/forming electrostatic interaction between alkali-metal cations (M^+) with ether oxygen atoms along the polymer backbone, through either intrachain or interchain hopping (Figure 1.1).^{19,26} Polyethers (e.g., PEO) with strong electron-donor character are known for their ability to complex M^+ .¹⁹ Ionic conduction is generally attributed to the amorphous polymer phase and the presence of free volume above the glass transition temperature (T_g). M^+ transport is facilitated by segmental motion of polymer chains along with M^+ intra/inter-segmental hopping.²⁶

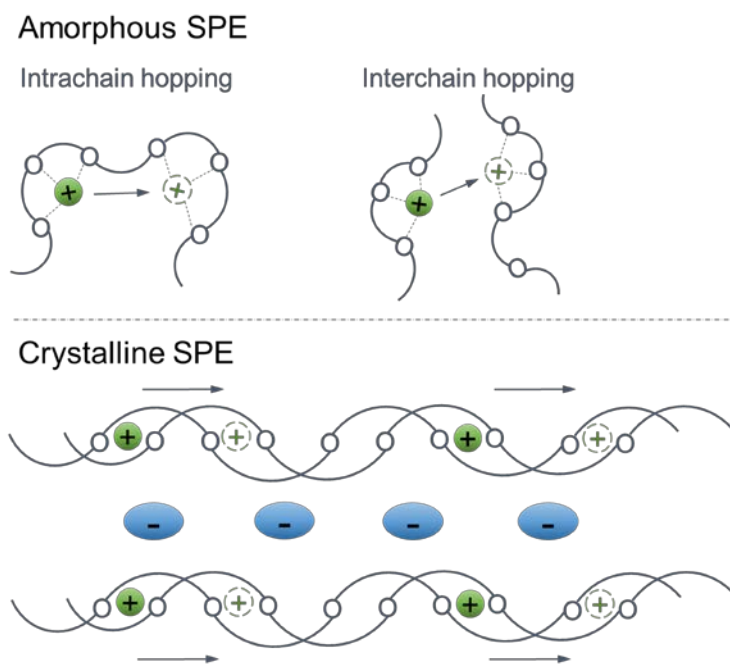


Figure 1.1. Ion transport in SPEs.

In some cases, ionic conductivity is also reported in the crystalline domains of the polymer electrolyte.²⁷ In the crystalline domains, polymer chains fold into cylindrical tunnels that permit M^+ diffusion via ion hopping, while the anions are separated from the cations located outside these tunnels.^{26,28} Nevertheless, ion transport is typically constrained in crystalline domains, and it is

widely accepted that reducing crystallinity is key to increasing ionic conductivity in polymer electrolytes.²⁶

1.2.1 Polymer matrices

PEO is the most studied polymer matrix for PEs owing to its flexible ethylene oxide segments and ether oxygen atoms with lone electron pairs that readily interact with Li⁺ ions, facilitating Li⁺ transport. It also has advantages such as low toxicity, easy fabrication and low cost.^{18,19,21} Since first reported by Fenton *et al.*²⁹ in 1973, poly(ethylene oxide) (PEO) based PEs have been studied extensively, in which a lithium salt is dissolved in the PEO matrix by coordination between the Li⁺ ions and the ether oxygen in the polymer chains.^{18,19} However, PEO is a semi-crystalline polymer with $T_g \approx -65$ °C and at room temperature (RT), the amorphous phase with limited interchain mobility aids ion transportation.

Typically, PEO based electrolytes show poor ionic conductivities of 10^{-8} - 10^{-4} S/cm at ambient, and only show good conductivity (up to 10^{-3} S/cm) above the melting point (~ 65 °C), in which case the PEO electrolyte becomes a gel electrolyte rather than a SSE.^{18,19} The PEO gel can gradually diffuse across the porous solid electrolyte interphase (SEI) layer and can lead to a continuous loss of lithium from the cathode. Therefore, suppression of PEO crystallinity is essential for PEO-based electrolytes. In addition, PEO electrolytes generally show low ionic transference numbers (t_{Li^+}) of 0.2-0.5, which can result in concentration overpotential, promoting uneven Li plating and dendrite formation.^{12,18,19,30}

To solve these issues, various strategies have been explored including optimization of the lithium salt structure,³¹⁻³³ the addition of plasticizer³⁴⁻³⁶ and/or nanofiller,^{12,24,36-38} polymer blends,³⁹⁻⁴¹ and designing copolymers with PEO blocks/oligomers including linear,⁴²⁻⁴⁴ grafted,⁴⁵⁻⁴⁷ and crosslinked structures.^{38,48-50}

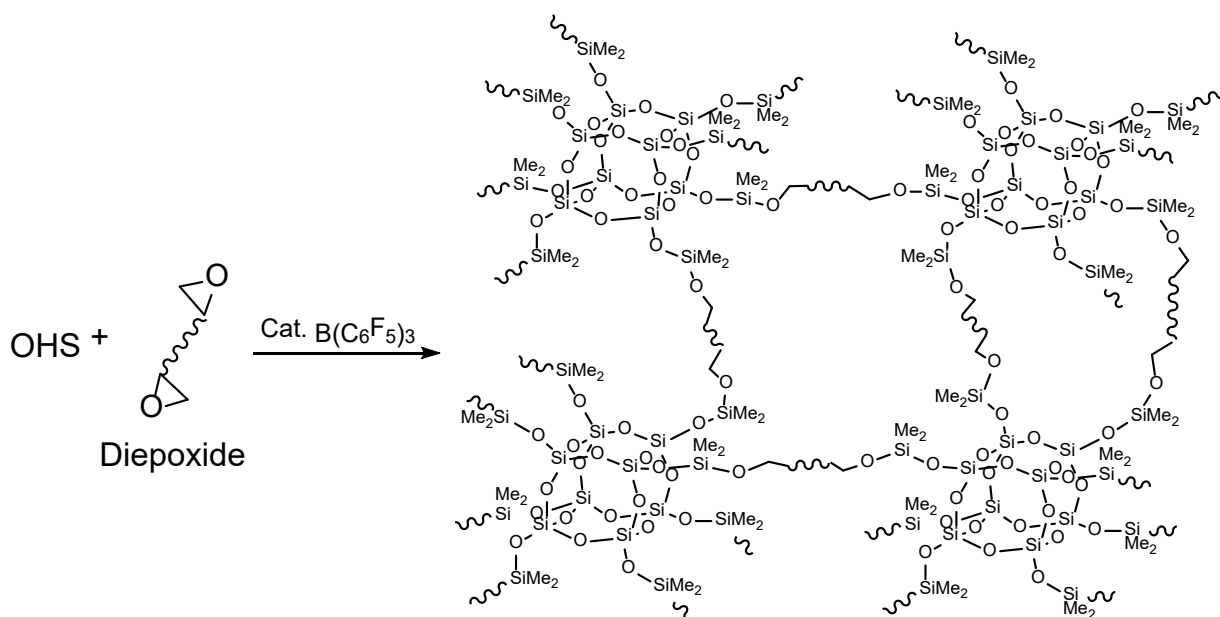
In addition to PEO, many other polymer matrices have been studied as summarized in Table 1.1. For SPEs, polymer matrices with a low T_g ($<RT$) are typically employed, including poly(propylene oxide) (PPO),^{51–53} poly[bis(methoxy-ethoxy-ethoxy)phosphazene] (MEEP),^{54,55} polysiloxane (PSi),^{56–58} polycarbonates (PCs),^{59–61} etc. (Table 1.1), which are amorphous at RT. For GPEs, polymers with good mechanical strength and capability to accommodate liquid electrolyte are needed, such as polyvinyl chloride (PVC),^{62,63} polyacrylonitrile (PAN),^{64–66} poly(methyl methacrylate) (PMMA),^{67,68} polyvinylidene fluoride (PVDF),^{69–71} poly(vinylidene fluoride-co-hexafluoropropylene) (PVDF-HFP),^{72–74} etc. (Table 1.1).

Table 1.1. Common polymer matrices for PEs and their properties.

Polymer matrix	Molecular structure	T_g (°C)	T_m (°C)*	Applied PE system
PEO		-65	65	SPE/GPE
PPO		-60	-	SPE
MEEP		-54	-	SPE
PSi		<-60	-	SPE
PC	Contains:	<0	-	SPE
PVC		80	220	GPE
PAN		125	300	GPE
PMMA		105	-	GPE
PVDF		-40	170	GPE
PVDF-HFP		-90	140	GPE

*No melting temperature for amorphous polymers.

In this dissertation, organic/inorganic hybrid nanocomposite silsesquioxane cage [HMe₂SiO-SiO_{1.5}]₈ (OHS) crosslinked by EO containing oligomers were investigated. The initial goal was to develop materials with three-dimensional (3D) networked structures through oxysilylation that offer excellent structural and chemical stabilities, good mechanical properties and ionic conductivities, Scheme 1.1. Although the resulting products failed to facilitate ionic transport, by investigating various reactions between different diepoxides and Si-H containing compounds under different reaction conditions, a novel and simple approach to self-reinforced epoxy resin nanocomposites was established, as discussed in Chapter 3.



Scheme 1.1. Oxysilylation of OHS with diepoxide.

1.2.2 Lithium salts

The most important requirement for lithium salts is good solubility in the polymer matrix. Generally, the bulkier the anion, the higher the ionic conductivity, as larger anions more easily dissociate in the polymer matrix leaving free Li⁺ ions to interact with polar groups along the polymer backbone, facilitating ionic transport.^{18,19,75} Therefore, Li salts with delocalized anion and

low basicity are preferred. Commonly used lithium salts include LiClO_4 ,^{76,77} LiPF_6 ,^{78,79} LiAsF_6 ,^{80,81} LiBF_4 ,^{82,83} LiCF_3SO_3 (LiTf),^{84,85} $\text{LiN}(\text{SO}_2\text{F})_2$ (LiFSI),^{86,87} $\text{LiN}(\text{CF}_3\text{SO}_2)_2$ (LiTFSI),^{88,89} $\text{LiN}(\text{SO}_2\text{C}_2\text{F}_5)_2$ (LiBETI),^{90,91} etc.

It is known that the addition of a Li salt reduces PEO crystallinity and significantly reduces T_g resulting in enhanced mobility of EO segments and ionic conductivity.^{19,75,92} Another major drawback for polymer-salt systems is that as cations bind to the polymer matrix, anions can move faster which increases ionic conductivity, resulting in lower t_{Li^+} . The migration of anions to the anode induces serious concentration polarization, which can lead to a substantial decay in conductivity. Therefore, such PEs are also called bi-ionic conductors. To minimize polarization, a common method is to develop single-ion conducting PEs by anchoring anions to the polymer backbone.^{18,19}

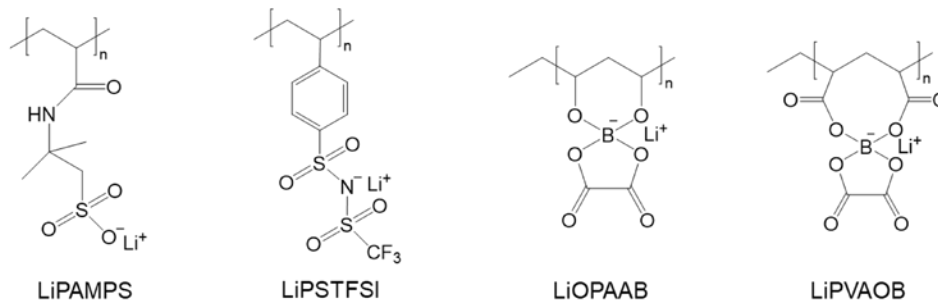
Recent efforts have targeted the synthesis of polymeric lithium salts as single-ion conductors. In general, there are three types of polymeric Li salts: homopolymers, copolymers and organic-inorganic hybrid polymers.¹⁸ Reported properties of example single-ion conductors and their structures are given in Table 1.2 and Scheme 1.2, respectively.

Table 1.2. Properties of reported polymeric single-ion conductors.

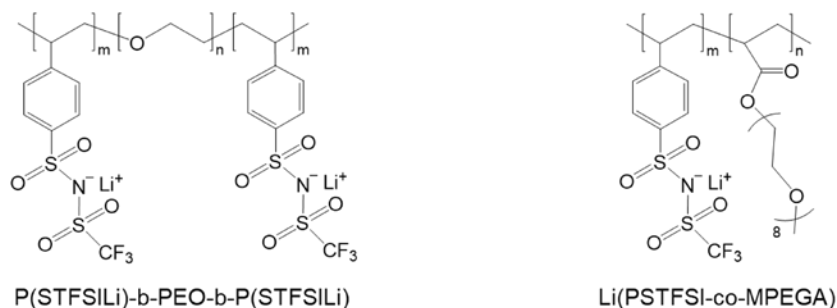
Polymeric lithium salt ^a	σ (S/cm)	t_{Li^+}	Stability window (V vs. Li^+/Li)	Reference
LiPAMPS^b	2.1×10^{-5} (20 °C)	-	4.4	93
LiPSTFSI^c	$\sim 10^{-6}$ (RT)	~ 1	-	31
LiOPAAB^d	2.3×10^{-6} (RT)	-	7	94
LiPVAOB^e	6.1×10^{-6} (RT)	-	7	100
$\text{P}(\text{STFSILi})\text{-b-PEO-b-P}(\text{STFSILi})$	1.3×10^{-5} (60 °C)	~ 1	5	95
$\text{Li}(\text{PSTFSI-co-MPEGA})$	7.6×10^{-6} (25 °C)	> 0.9	-	96
Polysiloxane type	$\sim 10^{-6}$ (RT)	~ 1	-	57,97,101
Organic aluminate type	$10^{-6}\text{-}10^{-5}$ (RT)	0.95	5	98,102
Organoborate type	$\sim 10^{-6}$ (50 °C)	~ 0.8	-	99,103

^aStructures of Li salts listed are given in Scheme 1.2. ^b LiPAMPS : lithium poly(2-acrylamido-2-methylpropanesulfonic acid). ^c LiPSTFSI : lithium poly(4-styrenesulfonyl(trifluoromethylsulfonyl)imide). ^d LiOPAAB : lithium oxalate polyacrylic acid borate. ^e LiPVAOB : lithium polyvinyl alcohol oxalate borate.

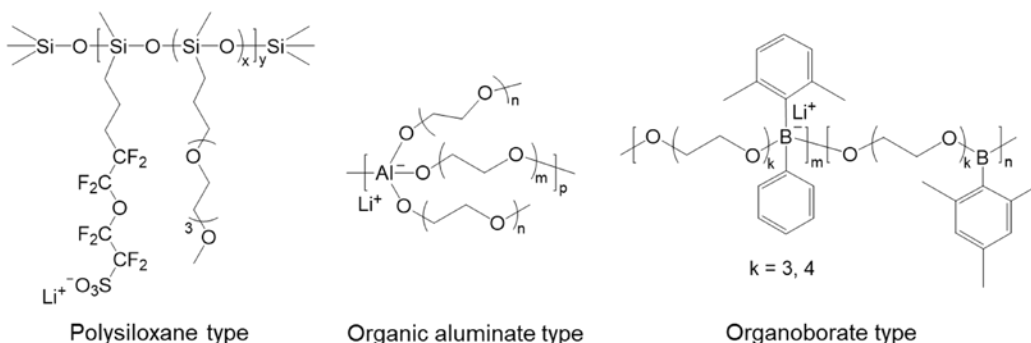
(1) Homopolymer Li salts



(2) Copolymer Li salts



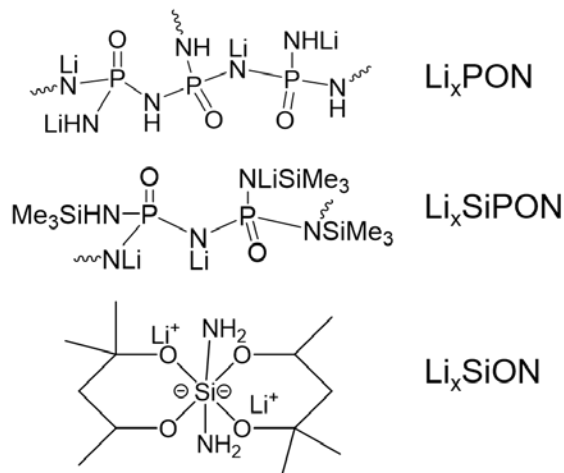
(3) Organic-inorganic hybrid polymeric Li salts



Scheme 1.2. Example structures of polymeric lithium salts.^{18,31,93-99}

In studies reported here, we synthesized Li_xPON, Li_xSiPON and Li_xSiON polymeric electrolytes (Scheme 1.3) based on lithium superionic conductor (LISICON) type inorganic solid electrolytes, which are introduced in the following section. When impregnated in/on Celgard separators, these polymer/oligomer electrolytes show conductivities approaching 10⁻⁵ S/cm at RT and with t_{Li^+} of 0.7-1. When mixed with PEO (60 wt.%), these polymer electrolytes act as polymeric

Li salts forming SPEs with high ambient conductivities up to $\sim 3 \times 10^{-3}$ S/cm and t_{Li^+} up to 0.8. Detailed design, synthesis and characterization are discussed in Chapters 4 and 5.



Scheme 1.3. Example structures of Li_xPON, Li_xSiPON and Li_xSiON oligomer/polymer electrolytes.

1.3 Inorganic solid electrolytes

Inorganic solid electrolytes (ISEs), typically ceramics, provide greater electrochemical stability window and t_{Li^+} , enhanced thermal and chemical stabilities, and diminished flammability compared to PEs.¹⁷ They are also suitable for rigid battery designs, namely thin-film-based devices, due to their high elastic moduli.^{11,12} However, due to low fracture toughness and ductility, ceramic electrolytes often show poor interfacial contact with electrodes and fail to meet requirements for fabricating thin and flexible films in practical applications.^{11,15,30,104} In addition, fabrication costs for ISEs are typically high, e.g. solid-state reactions, high temperature sintering and gas phase deposition, limiting bulk production for commercialization.

Ion transport in ceramic ISEs is dominantly facilitated by defects within the crystalline lattice, including interstices and vacancies (e.g., Schottky and Frenkel defects), providing pathways for fast ion movement.^{17,26} Lattice distortion near grain/phase boundaries and interfaces allow mobile

carriers to redistribute according to potential differences, which may provide additional interfacial charge-transport pathways. Additionally, impurity inclusion and/or solid solution induced structural distortions can also create free space assisting ion transport.²⁶ In general, to achieve fast Li⁺ conduction in ISEs, Li⁺ should be able to fit through bottlenecks in the conduction channel(s), available sites for Li⁺ should be interconnected allowing continuous diffusion pathways, interactions between Li⁺ and the framework should be weak, and concentrations of vacancy and interstitial sites should be optimized to minimize migration energy.¹⁷

Common types of ISEs include garnet, perovskite, sodium super ion conductor (NASICON) and LISICON crystalline electrolytes and glassy electrolytes such as lithium phosphorus oxynitride (LiPON). Ionic conductivities and structures of representative ISEs are summarized in Table 1.3 and Figure 1.2, respectively.

Table 1.3. Conductivities (σ) of selected inorganic solid electrolytes.

Electrolyte	Prototype	Composition	σ (S/cm)	Reference	
Garnet	Li ₇ La ₃ Zr ₂ O ₁₂	Li ₇ La ₃ Zr ₂ O ₁₂	3×10^{-4} (25 °C)	105	
		Li _{6.75} La ₃ (Zr _{1.75} Nb _{0.25})O ₁₂	8×10^{-4} (25 °C)	106	
		Li _{6.25} Ga _{0.25} La ₃ Zr ₂ O ₁₂	1.5×10^{-3} (25 °C)	107,108	
Perovskite	Li _{3x} La _{2/3-x} TiO ₃	Li _{0.34} La _{0.51} TiO _{2.94}	2×10^{-5} (RT)	109	
		Li _{3/8} Sr _{7/16} Ta _{3/4} Zr _{1/4} O ₃	2.7×10^{-4} (27 °C)	110	
		Li _{3/8} Sr _{7/16} Ta _{3/4} Hf _{1/4} O ₃	3.8×10^{-4} (25 °C)	111	
NASICON	LiTi ₂ (PO ₄) ₃	Li _{1.3} Al _{0.3} Ti _{1.7} (PO ₄) ₃	7×10^{-4} (25 °C)	112	
		2[Li _{1.4} Ti ₂ Si _{0.4} P _{2.6} O ₁₂]-AlPO ₄	1.5×10^{-3} (RT)	113	
		Li _{1.7} Al _{0.3} Ti _{1.7} Si _{0.4} P _{2.6} O ₁₂	2.4×10^{-3} (RT)	114	
	LiGe ₂ (PO ₄) ₃	Li _{1.5} Al _{0.5} Ge _{1.5} (PO ₄) ₃	4×10^{-4} (RT)	115	
		Li _{1.5} Al _{0.4} Cr _{0.1} Ge _{1.5} (PO ₄) ₃	6.7×10^{-3} (26 °C)	116	
LISICON	γ -Li ₃ PO ₄	Li ₁₄ Zn(GeO ₄) ₄	1.3×10^{-6} (33 °C)	117,118	
		Li _{4-x} Si _{1-x} P _x O ₄ (x = 0.5, 0.6)	$\sim 10^{-6}$ (RT)	119	
		Li _{10.42} Ge _{1.5} P _{1.5} Cl _{0.08} O _{11.92}	3.7×10^{-5} (27 °C)	120	
		Li ₄ Al _{1/3} Si _{1/6} Ge _{1/6} P _{1/3} O ₄	9×10^{-4} (RT)	121	
LiPON glass	defective γ -Li ₃ PO ₄	Li ₃ PO ₄ (deposition target)	$2-3 \times 10^{-6}$ (RT)	122–124	
Sulfide glass/glass-ceramic	Li ₂ S-P ₂ S ₅	70Li ₂ S-30P ₂ S ₅	10^{-2} - 10^{-3} (RT)	125,126	
		80Li ₂ S-20P ₂ S ₅	9×10^{-4} (RT)	127	
Thio-LISICON	Li ₁₀ GeP ₂ S ₁₂	Li ₄ GeS ₄	Li _{3.25} Ge _{0.25} P _{0.75} S ₄	2.2×10^{-3} (25 °C)	128
			Li ₁₀ GeP ₂ S ₁₂	1.2×10^{-2} (RT)	129
			Li _{9.54} Si _{1.74} P _{1.44} S _{11.7} Cl _{0.3}	2.5×10^{-2} (RT)	130

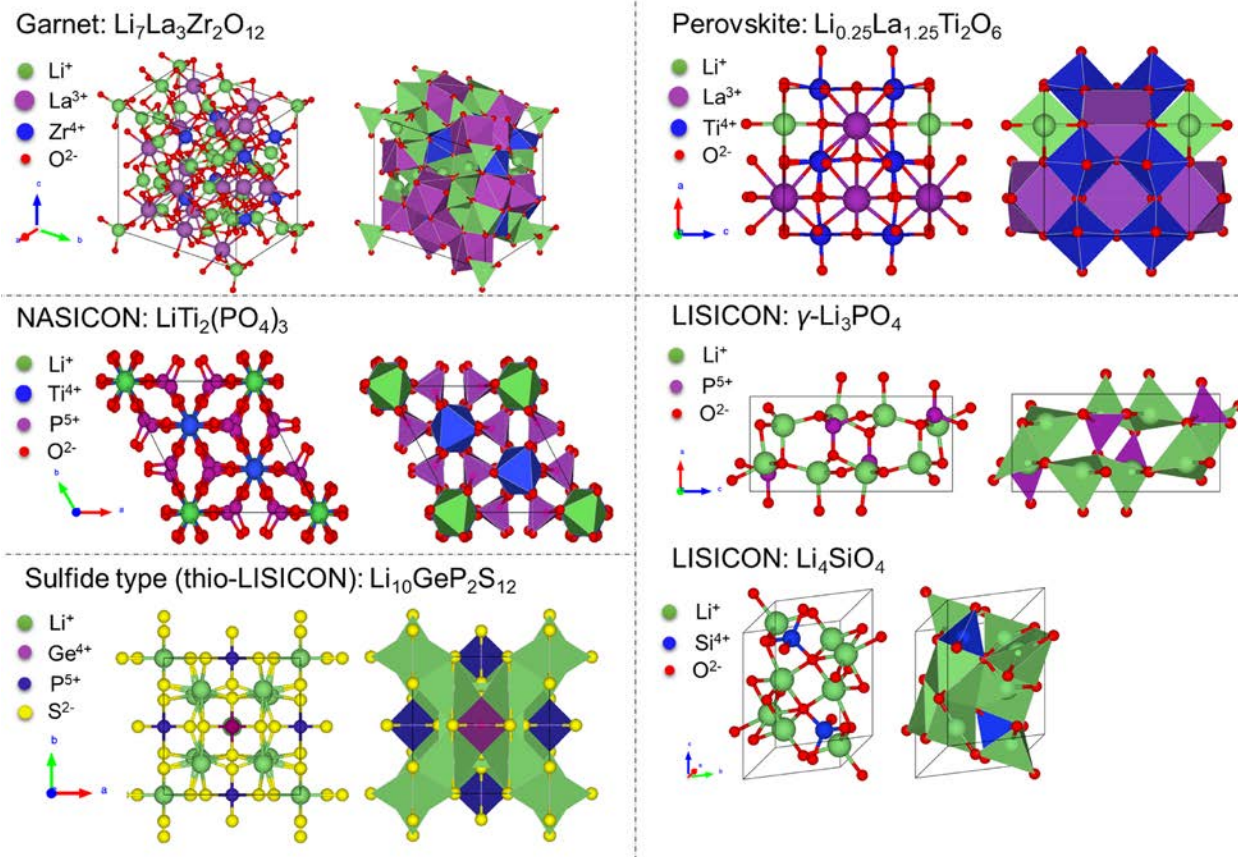


Figure 1.2. Structures of example inorganic solid electrolytes.

1.3.1 Garnet-type electrolytes

Garnet-type materials have the general formula $A_3B_2Si_3O_{12}$, where the A and B cations have eightfold and sixfold coordination, respectively.¹⁴ Since first discovered in 1969 for $[Li_3M_2Ln_3O_{12}$ (M = W or Te)],¹³¹ a series of garnet-type materials has been developed. The representative systems are $Li_5La_3M_2O_{12}$ (M = Nb or Ta), $Li_6Ala_2M_2O_{12}$ (A = Ca, Sr or Ba; M = Nb or Ta), $Li_{5.5}La_3M_{1.75}B_{0.25}O_{12}$ (M = Nb or Ta; B = In or Zr), and the cubic systems $Li_7La_3Zr_2O_{12}$ (LLZO) and $Li_{7.06}M_3Y_{0.06}Zr_{1.94}O_{12}$ (M = La, Nb or Ta).^{105,132–135} A high ionic conductivity of 1.5×10^{-3} S/cm was achieved at RT for Ga doped LLZO, $Li_{6.25}Ga_{0.25}La_3Zr_2O_{12}$.^{107,108} However, they are generally not stable in contact with moisture or CO_2 in ambient atmosphere, and it is important to improve LLZO stability through material modifications.¹³⁶ In addition, dense

cubic LLZO films ($\geq 94\%$ dense, $<40\ \mu\text{m}$ thick) are typically sintered at $1100\text{-}1250\ \text{°C}$ for $10\text{-}40\ \text{h}$.^{105,137} To shorten the sintering time, energy and equipment intensive processes are used, such as hot-pressing, and field assisted or spark plasma sintering, which can reduce sintering temperature and time to $1000\text{-}1100\ \text{°C}/\leq 1\ \text{h}$.¹³⁸⁻¹⁴⁰ Previously we reported processing Al^{3+} or Ga^{3+} doped, dense and flexible LLZO thin films ($<30\ \mu\text{m}$) by pressureless sintering at $\sim 1100\ \text{°C}/\leq 1\ \text{h}$ from flame made nanopowders (NPs).^{107,141}

1.3.2 Perovskite-type electrolytes

The representative perovskite SE is (ABO_3) -type $\text{Li}_{3x}\text{La}_{2/3-x}\text{TiO}_3$ (LLTO, $0 < x < 0.16$) exhibits a bulk Li^+ conductivity exceeding $10^{-3}\ \text{S/cm}$ at RT, and total conductivity of $\sim 2 \times 10^{-5}\ \text{S/cm}$.^{14,109,142} The high bulk conductivity derives from the crystal structure of tetragonal $\text{Li}_{3x}\text{La}_{(2/3-x)}\square_{(1/3-2x)}\text{TiO}_3$ ($\square = \text{vacancy}$) with a large concentration of A-site vacancies that allow Li^+ motion by vacancy diffusion and through a square planar bottleneck formed by four O^{2-} between two neighboring A sites.^{136,142} However, LLTO is not stable at voltages below about $1.8\ \text{V vs. Li/Li}^+$, making it incompatible with low potential anode materials, including Li metal which can lead to reduction of Ti^{4+} .^{14,143} A different perovskite-type SE $\text{LiSr}_{1.65}\text{Zr}_{1.3}\text{Ta}_{1.7}\text{O}_9$ was found to be stable in contact with Li as Zr^{4+} and Ta^{5+} oxidation states are stable against reduction. However, its ionic conductivity is as low as $1.3 \times 10^{-5}\ \text{S/cm}$ at $30\ \text{°C}$.¹⁴⁴ Further studies on $\text{Li}_{3/8}\text{Sr}_{7/16}\text{Ta}_{3/4}\text{Zr}_{1/4}\text{O}_3$ (LSTZ) and $\text{Li}_{3/8}\text{Sr}_{7/16}\text{Ta}_{3/4}\text{Hf}_{1/4}\text{O}_3$ (LSTH) show improved ionic conductivities of $2\text{-}4 \times 10^{-4}\ \text{S/cm}$ at $25\ \text{°C}$.^{110,111} Although LSTZ/LSTH is promising for applications in ASSBs, they are typically sintered at $\sim 1300\ \text{°C}$, which is incompatible with electrode materials for battery construction using co-sintering methods.^{136,142}

1.3.3 NASICON-type electrolytes

First studied in the 1960s, $\text{Na}_{1+x}\text{Zr}_2\text{Si}_x\text{P}_{3-x}\text{O}_{12}$ -like compounds gave rise to the term ‘NASICON’.^{14,145} These materials generally have an $\text{AB}_2(\text{PO}_4)_3$ formula with the A site occupied by Li, Na or K. The B site is usually occupied by Ge, Zr or Ti.^{14,146} The structure can be described as a covalent skeleton $[\text{B}_2\text{P}_3\text{O}_{12}]^-$ consisting of BO_6 octahedra and PO_4 tetrahedra, which form 3D interconnected channels and two types of interstitial positions (M' and M'') where conductor cations A^+ are distributed. A^+ can move from one site to another through bottlenecks, the size of which depends on the nature of the skeleton ions and the carrier concentrations in both sites (M' and M'').^{142,147}

In particular, the $\text{LiTi}_2(\text{PO}_4)_3$ system has been widely investigated. The ionic conductivity of $\text{LiZr}_2(\text{PO}_4)_3$ is very low ($\sim 10^{-8}$ S/cm),^{148,149} but can be improved by substitution to form $\text{Li}_{1+x}\text{M}_x\text{Ti}_{2-x}(\text{PO}_4)_3$ ($\text{M} = \text{Al}, \text{Cr}, \text{Ga}, \text{Fe}, \text{Sc}, \text{In}, \text{Lu}, \text{Y}$ or La), with Al substitution, $\text{Li}_{1+x}\text{Al}_x\text{Ti}_{2-x}(\text{PO}_4)_3$ (LATP), having been demonstrated to be the most effective (bulk $\sigma = 3 \times 10^{-3}$ S/cm at RT).¹⁵⁰⁻¹⁵³ The $\text{Li}_{1+x}\text{Al}_x\text{Ge}_{2-x}(\text{PO}_4)_3$ (LAGP) system has also been widely investigated because of its relatively wide electrochemical stability window (up to 7 V vs. Li/Li^+) and high ionic conductivity $> 10^{-4}$ S/cm.^{151,154,155} NASICON-type materials are considered suitable SEs for high-voltage solid electrolyte batteries. However, one of the LAGP precursor, GeO_2 , is expensive and can significantly increase the cost of LAGP based ASSBs. Therefore, it is necessary to develop cost effective new NASICON electrolytes.¹³⁶

1.3.4 LISICON-type electrolytes

Typical LISICON-type compounds crystallize into structures similar to $\gamma\text{-Li}_3\text{PO}_4$ with an orthorhombic unit cell and $Pnma$ space group, where all cations are tetrahedrally coordinated.^{17,156} The Li^+ ions located in LiO_4 tetrahedra diffuse between these tetrahedra and interstitial

sites located in the PO₄ network.¹⁵⁷ A LISICON-type SE, Li₁₄Zn(GeO₄)₄, was first reported in 1978 showing ionic conductivities of 1.25×10^{-1} S/cm at 300 °C and 1.3×10^{-6} S/cm at 33 °C.^{117,118} It was proposed that Li⁺ can diffuse freely between interstitial sites in the [Li₁₁Zn(GeO₄)₃]³⁻ network. Bottlenecks between interstitial sites are large enough for Li⁺ transport, and each O²⁻ is bonded to four network cations (Li⁺, Zn²⁺, Ge⁴⁺) and bonds weakly to mobile Li⁺, which is similar to the γ -Li₃PO₄ structure.^{136,158}

Aliovalent substitution of P⁵⁺ by Si⁴⁺ or Ge⁴⁺ in γ -Li₃PO₄ can create compositions such as Li_{3+x}(P_{1-x}Si_x)O₄,^{117,119,159} which gives rise to fast Li⁺ conduction and the LISICON-type SE family. The excess Li⁺ created by such substitution occupies interstitial sites, as it cannot be accommodated in tetrahedral sites, making the adjacent Li-Li⁺ distances unusually short and resulting in a high conductivity of 3×10^{-6} S/cm.¹⁷

By partially substituting O²⁻ with Cl⁻ forming compositions of Li_{10.42}Si_{1.5}P_{1.5}Cl_{0.08}O_{11.92} and Li_{10.42}Ge_{1.5}P_{1.5}Cl_{0.08}O_{11.92}, ionic conductivities increase to 1.0 and 3.7×10^{-5} S/cm at 27 °C, respectively, and the electrochemical stability with Li metal is up to 9 V vs. Li/Li⁺.¹²⁰ As Cl⁻ is larger than O²⁻ while having a lower electronegativity, lattice constants and bottleneck sizes increase for Li⁺ diffusion and weaker bonding forms between Li⁺ and Cl⁻ compared to Li⁺ and O²⁻, resulting in increased ionic conductivities.^{120,136}

Molecular dynamics (MD) simulation of Li_{4±x}Si_{1-x}X_xO₄ (X = P, Al, or Ge) reveals temperature-dependent (from low to high) Li⁺ diffusion mechanisms: local oscillation, isolated hopping, and superionic motion.¹²¹ Substitution of Si in Li₄SiO₄ by P, Al or Ge can induce mixed polyanion effects, lowering transition temperatures for diffusion mechanisms and therefore increasing ionic conductivities. Li₄Al_{1/3}Si_{1/6}Ge_{1/6}P_{1/3}O₄ was predicted to have an ionic conductivity of 9×10^{-4} S/cm at RT, much higher than that of Li₄SiO₄ ($\sim 2 \times 10^{-7}$ S/cm).^{121,136}

Overall, LISICON-type of SEs have good chemical and electrochemical stability, but low ionic conductivities compared with other oxide solid electrolytes.¹³⁶

1.3.5 LiPON-type electrolytes

Different from the above ISEs, LiPON is a type of amorphous Li^+ SE. In principle, LiPON can be considered a Li^+ defective $\gamma\text{-Li}_3\text{PO}_4$ with O partially substituted by N, with an example composition of $\text{Li}_{2.88}\text{PO}_{3.73}\text{N}_{0.14}$.^{142,160,161} LiPON was first synthesized at the Oak Ridge National Laboratory by radio frequency magnetron sputtering (RFMS) Li_3PO_4 target in N_2 plasma, which showed an ionic conductivity of 2×10^{-6} S/cm at RT and was found to be stable to Li metal from 0 to 5 V.¹²² In thin-film form, LiPON is an important SE for all-solid Li ion microbatteries.^{124,142}

In general, the ionic conductivity of LiPON thin films increases significantly while the activation energy (E_a) for Li diffusion decreases with the atom percentage (at.%) of N incorporated in the structure.¹⁶⁰ Bates *et al.*^{123,124} showed that ionic conductivity increased more than 45 \times at 25 $^\circ\text{C}$ when increasing the N content from 0 at.% ($\sigma = 7 \times 10^{-8}$ S/cm) to 6 at.% ($\sigma = 3.3 \times 10^{-6}$ S/cm). It was proposed that N bridged among P atoms with double (N_d) or triple (N_t) coordination, and these crosslinked structures might increase the Li^+ mobility by providing interconnected pathways.^{122,123}

However, another argument was made by Wang *et al.*¹⁶² that most N would form PO_3N as apical N (N_a) and the rest would be N_d . By applying MD simulations, Lacivita *et al.*¹⁶⁰ and Li *et al.*¹⁶¹ both found N_d bridges and apical N_a configurations in LiPON structures with no triple N_t bridges between P atoms found. The overall conductivity is correlated with the amount of disorder and therefore amorphous LiPON exhibits higher conductivities than crystalline $\gamma\text{-Li}_3\text{PO}_4$, and N_d bridging increases the connectivity which enables amorphous LiPON to act as a single-ion conductor.^{160,161}

LiPON thin films are typically processed by gas phase deposition methods, such as RF magnetron sputtering,^{122–124} ion beam assisted deposition (IBAD),^{163,164} metalorganic-chemical vapor deposition (MOCVD),¹⁶⁵ etc. Low deposition rates (typically <100 nm/min) and specialized apparatus required for gas phase depositions drive up the fabrication cost for large, homogeneous composition targets at commodity scales. In addition, although LiPON glasses are promising for thin-film ASSBs, they are not appropriate for bulk ASSBs due to low ionic conductivities of 10^{-6} - 10^{-5} S/cm at RT.¹³⁶

As discussed in Chapters 4 and 5, we explored polymer synthesis methods of preparing LiPON-like and Li_xSiON (based on N-doped LISICON-type SE) precursors that exhibit ambient conductivities of $\sim 10^{-5}$ S/cm, providing a novel, low cost, low temperature and scalable approach towards SSEs. Especially for Li_xSiON precursors which are derived from agricultural waste, rice hull ash, a green synthesis method is established.

1.3.6 Sulfide-type electrolytes

Research into sulfide-type SEs started in 1986 with the $\text{Li}_2\text{S-SiS}_2$ system,^{166,167} with the highest reported conductivity of 7×10^{-4} S/cm achieved by doping the $\text{Li}_2\text{S-SiS}_2$ system with $\gamma\text{-Li}_3\text{PO}_4$.¹⁶⁸ In 2001, a class of thio-LISICON crystalline material was found in the $\text{Li}_2\text{S-P}_2\text{S}_5$ system.¹²⁸ Generally, substituting O^{2-} by S^{2-} in LISICON-type electrolytes gives rise to the thio-LISICON family.¹⁷ As interactions between S^{2-} and Li^+ are weaker than those between O^{2-} and Li^+ , the sulfide-type SEs exhibit higher Li^+ mobility and ionic conductivities than the oxide-type counterparts.^{136,169} There are generally three types of sulfide SEs: glasses, glass-ceramics and ceramics, which all show ionic conductivities comparable to organic liquid electrolytes. Glass/glass-ceramic $\text{Li}_2\text{S-P}_2\text{S}_5$ and ceramic thio-LISICON $\text{Li}_{4-x}\text{Ge}_{1-x}\text{P}_x\text{S}_4$ ($0 < x < 1$) are the most promising SEs, see examples in Table 1.3.¹³⁶

The $\text{Li}_{10}\text{MP}_2\text{S}_{12}$ ($\text{M} = \text{Si}, \text{Ge}, \text{or Sn}$)^{129,170,171} and $\text{Li}_{11}\text{Si}_2\text{PS}_{12}$ ¹⁷² families show the highest Li^+ conductivities, above 10^{-2} S/cm at RT. The $\text{Li}_{10}\text{GeP}_2\text{S}_{12}$ (LGPS) structure consists of $(\text{Ge}_{0.5}\text{P}_{0.5})\text{S}_4$, PS_4 and LiS_4 tetrahedra and LiS_6 octahedra. $(\text{Ge}_{0.5}\text{P}_{0.5})\text{S}_4$ tetrahedra and LiS_6 octahedra connect to one another forming one-dimensional (1D) chains along c-axis, and these chains are connected by PS_4 tetrahedra. It was found that thermal vibrations of Li^+ inside the LiS_4 tetrahedra (16h and 8f sites) are highly anisotropic, and the Li^+ are displaced toward interstitial sites between two 16h sites and between 16h and 8f sites forming 1D conduction pathways.^{17,136,173,174} As a result, $\text{Li}_{10}\text{GeP}_2\text{S}_{12}$ shows a high bulk ionic conductivity of $>10^{-2}$ S/cm at RT and is stable with Li up to 5 V vs. Li/Li^+ .^{17,136}

Overall, sulfide-type SEs have the highest ionic conductivities of the order of 10^{-2} S/cm at RT. However, they are not stable in ambient atmosphere reacting with moisture to form H_2S gas. Therefore, they must be used in a controlled atmosphere for bulk batteries and not for thin-film applications due to immature deposition technologies for sulfide electrolytes.^{14,136} Additionally, compatibility issues between electrode materials and sulfide SEs make it difficult to achieve stable cycling performance.^{175,176} The strong reducing capability of Li metal towards almost all sulfide SEs makes the use of Li metal as the anode directly against sulfide electrolyte extremely challenging.^{177,178} Moreover, the uneven Li deposition leads to dendrite formation, which can penetrate through the soft electrolyte resulting in catastrophic failure.^{175,179}

1.4 Overview of subsequent chapters

The following chapters are organized as follows.

Chapter 2 describes synthetic and experimental techniques used in this dissertation. Synthesis procedures include oxysilylation of diepoxides with various Si-H sources, LiPON-like polymer

precursor syntheses, and Li_xSiON precursor syntheses. Analytical methods include Fourier-transform infrared spectroscopy (FTIR), matrix-assisted laser desorption/ionization-time of flight (MALDI-ToF), thermogravimetric analysis (TGA) and differential thermal analysis (DTA), multi-nuclear magnetic resonance spectroscopy (NMR), X-ray diffraction (XRD), X-ray photoelectron spectroscopy (XPS), scanning electron microscopy (SEM) and energy-dispersive X-ray spectroscopy (EDX) and electrochemical impedance spectroscopy (EIS).

Chapter 3 describes several basic aspects of oxysilylation of diepoxides with TMDS ($\text{HMe}_2\text{SiOSiMe}_2\text{H}$, tetramethyldisiloxane), OHS [$\text{HSiMe}_2\text{OSiO}_{1.5}$]₈, D₄H [$(\text{CH}_3\text{SiHO})_4$, tetramethylcyclotetrasiloxane] and D₅H [$(\text{CH}_3\text{SiHO})_5$, pentamethylcyclopentasiloxane] in mixtures of dichloromethane and hexane, or as simple mixtures catalyzed by $\text{B}(\text{C}_6\text{F}_5)_3$ at ambient, which offers a method of synthesizing self-reinforced epoxy resin nanocomposites that avoids the use of polyamines.

Chapter 4 presents the design and synthesis of easily scaled, low-temperature, low-cost, solution processable inorganic polymers containing LiPON/LiSiPON elements, providing a novel method of fabricating LiPON emulating SEs. OPCl_3 and hexachlorphosphazene [$\text{Cl}_2\text{P}=\text{N}$]₃ provide starting points for elaboration using MNH_2 ($\text{M} = \text{Li}/\text{Na}$) or $(\text{Me}_3\text{Si})_2\text{NH}$ followed by reaction with controlled amounts of LiNH_2 to produce oligomers/polymers with MWs $\approx 1\text{-}2$ kDa. Detailed characterization and electrochemical performance tests are discussed.

Chapter 5 presents a set of Li_xSiON ($x = 2, 4, 6$) polymer precursors to a novel SSE system were synthesized starting from rice hull ash (RHA), an agricultural waste, providing a green route towards all solid-state batteries (ASSBs). Silica, ~ 90 wt. % in RHA, can be catalytically (alkali base) dissolved (20-40 wt %) in hexylene glycol (HG) and distilled directly from the reaction mixture as the spiroxiloxane [$(\text{C}_6\text{H}_{14}\text{O}_2)_2\text{Si}$, SP] at 200 °C. SP can be lithiated using controlled

amounts of LiNH_2 to produce Li_xSiON oligomers/polymers with MWs up to ~ 1.5 kDa as characterized by FTIR, MALDI-ToF, multinuclear NMR, TGA-DTA, XRD, XPS, SEM and EDX, followed by electrochemical performance tests.

Finally, Chapter 6 gives an overall summary and conclusions of this work followed by a discussion of future work.

References

1. Changzhou, Y.; Haobin, W.; Yi, X.; Xiongwen, L. Mixed Transition-Metal Oxides: Design, Synthesis, and Energy-Related Applications. *Angew. Chem. Int. Ed.* **2014**, *53* (6), 1488–1504.
2. Peterson, S. B.; Michalek, J. J. Cost-Effectiveness of Plug-in Hybrid Electric Vehicle Battery Capacity and Charging Infrastructure Investment for Reducing US Gasoline Consumption. *Energy Policy* **2013**, *52*, 429–438.
3. Gaines, L. L.; Dunn, J. B. Lithium-Ion Battery Environmental Impacts. In *Lithium-Ion Batteries*; Pistoia, G., Ed.; Elsevier: Amsterdam, 2014; pp 483–508.
4. Dehghani-Sani, A. R.; Tharumalingam, E.; Dusseault, M. B.; Fraser, R. Study of Energy Storage Systems and Environmental Challenges of Batteries. *Renew. Sustain. Energy Rev.* **2019**, *104*, 192–208.
5. Battery500: Progress Update <https://www.energy.gov/eere/articles/battery500-progress-update> (accessed Dec 8, 2020).
6. *Lithium-Ion Batteries*; Yoshio, M., Brodd, R. J., Kozawa, A., Eds.; Springer New York: New York, NY, 2009.
7. Tarascon, J. M.; Armand, M. Issues and Challenges Facing Rechargeable Lithium Batteries. *Nature* **2001**, *414* (6861), 359–367.
8. Wang, Y.; Liu, B.; Li, Q.; Cartmell, S.; Ferrara, S.; Deng, Z. D.; Xiao, J. Lithium and Lithium Ion Batteries for Applications in Microelectronic Devices: A Review. *J. Power Sources* **2015**, *286*, 330–345.
9. Scrosati, B.; Hassoun, J.; Sun, Y. K. Lithium-Ion Batteries. A Look into the Future. *Energy Environ. Sci.* **2011**, *4* (9), 3287–3295.
10. Xu, K. Nonaqueous Liquid Electrolytes for Lithium-Based Rechargeable Batteries. *Chem. Rev.* **2004**, *104* (10), 4303–4418.
11. Jiang, T.; He, P.; Wang, G.; Shen, Y.; Nan, C. W.; Fan, L. Z. Solvent-Free Synthesis of Thin, Flexible, Nonflammable Garnet-Based Composite Solid Electrolyte for All-Solid-State Lithium Batteries. *Adv. Energy Mater.* **2020**, *10* (12), 1903376.
12. Fergus, J. W. Ceramic and Polymeric Solid Electrolytes for Lithium-Ion Batteries. *J. Power Sources* **2010**, *195* (15), 4554–4569.
13. Cheng, X. B.; Zhang, R.; Zhao, C. Z.; Wei, F.; Zhang, J. G.; Zhang, Q. A Review of Solid Electrolyte Interphases on Lithium Metal Anode. *Adv. Sci.* **2016**, *3* (3), 1500213.
14. Manthiram, A.; Yu, X.; Wang, S. Lithium Battery Chemistries Enabled by Solid-State Electrolytes. *Nat. Rev. Mater.* **2017**, *2* (4), 1–16.
15. Chen, R. J.; Zhang, Y. B.; Liu, T.; Xu, B. Q.; Lin, Y. H.; Nan, C. W.; Shen, Y. Addressing the Interface Issues in All-Solid-State Bulk-Type Lithium Ion Battery via an All-Composite Approach. *ACS Appl. Mater. Interfaces* **2017**, *9* (11), 9654–9661.
16. Xu, W.; Wang, J.; Ding, F.; Chen, X.; Nasybulin, E.; Zhang, Y.; Zhang, J. G. Lithium Metal Anodes for Rechargeable Batteries. *Energy Environ. Sci.* **2014**, *7* (2), 513–537.
17. Bachman, J. C.; Muy, S.; Grimaud, A.; Chang, H. H.; Pour, N.; Lux, S. F.; Paschos, O.; Maglia, F.; Lupart, S.; Lamp, P.; Giordano, L.; Shao-Horn, Y. Inorganic Solid-State Electrolytes for Lithium Batteries: Mechanisms and Properties Governing Ion Conduction. *Chem. Rev.* **2016**, *116* (1), 140–162.
18. Long, L.; Wang, S.; Xiao, M.; Meng, Y. Polymer Electrolytes for Lithium Polymer Batteries. *J. Mater. Chem. A* **2016**, *4* (26), 10038–10069.

19. Xue, Z.; He, D.; Xie, X. Poly(Ethylene Oxide)-Based Electrolytes for Lithium-Ion Batteries. *J. Mater. Chem. A* **2015**, *3* (38), 19218–19253.
20. Agrawal, R. C.; Pandey, G. P. Solid Polymer Electrolytes: Materials Designing and All-Solid-State Battery Applications: An Overview. *J. Phys. Appl. Phys.* **2008**, *41* (22), 223001.
21. Yue, L.; Ma, J.; Zhang, J.; Zhao, J.; Dong, S.; Liu, Z.; Cui, G.; Chen, L. All Solid-State Polymer Electrolytes for High-Performance Lithium Ion Batteries. *Energy Storage Mater.* **2016**, *5*, 139–164.
22. Stephan, A. M. *Review on Gel Polymer Electrolytes for Lithium Batteries*; 2006.
23. Li, W.; Pang, Y.; Liu, J.; Liu, G.; Wang, Y.; Xia, Y. A PEO-Based Gel Polymer Electrolyte for Lithium Ion Batteries. *RSC Adv.* **2017**, *7* (38), 23494–23501.
24. Yu, X.; Manthiram, A. A Review of Composite Polymer-Ceramic Electrolytes for Lithium Batteries. *Energy Storage Mater.* **2021**, *34*, 282–300.
25. Manuel Stephan, A.; Nahm, K. S. Review on Composite Polymer Electrolytes for Lithium Batteries. *Polymer* **2006**, *47*, 5952–5964.
26. Zhao, Q.; Stalin, S.; Zhao, C.-Z.; Archer, L. A. Designing Solid-State Electrolytes for Safe, Energy-Dense Batteries. *Nat. Rev. Mater.* **2020**, *5* (3), 229–252.
27. Gadjourova, Z.; Andreev, Y. G.; Tunstall, D. P.; Bruce, P. G. Ionic Conductivity in Crystalline Polymer Electrolytes. *Nature* **2001**, *412*, 520–523.
28. Staunton, E.; Andreev, Y. G.; Bruce, P. G. Structure and Conductivity of the Crystalline Polymer Electrolyte β -PEO₆:LiAsF₆. *J. Am. Chem. Soc.* **2005**, *127* (35), 12176–12177.
29. Fenton, D. E. Complexes of Alkali Metal Ions with Poly(Ethylene Oxide). *Polymer* **1973**, *14* (11), 589.
30. Zhou, W.; Wang, S.; Li, Y.; Xin, S.; Manthiram, A.; Goodenough, J. B. Plating a Dendrite-Free Lithium Anode with a Polymer/Ceramic/Polymer Sandwich Electrolyte. *J. Am. Chem. Soc.* **2016**, *138* (30), 9385–9388.
31. Meziane, R.; Bonnet, J. P.; Courty, M.; Djellab, K.; Armand, M. Single-Ion Polymer Electrolytes Based on a Delocalized Polyanion for Lithium Batteries. *Electrochimica Acta* **2011**, *57*, 14–19.
32. Wu, X. L.; Xin, S.; Seo, H. H.; Kim, J.; Guo, Y. G.; Lee, J. S. Enhanced Li⁺ Conductivity in PEO–LiBOB Polymer Electrolytes by Using Succinonitrile as a Plasticizer. *Solid State Ion.* **2011**, *186* (1), 1–6.
33. Egashira, M.; Scrosati, B.; Armand, M.; Béranger, S.; Michot, C. Lithium Dicyanotriazolate as a Lithium Salt for Poly(Ethylene Oxide) Based Polymer Electrolytes. *Electrochem. Solid-State Lett.* **2003**, *6* (4), A71–A73.
34. Nicotera, I.; Ranieri, G. A.; Terenzi, M.; Chadwick, A. V.; Webster, M. I. A Study of Stability of Plasticized PEO Electrolytes. *Solid State Ion.* **2002**, *146* (1), 143–150.
35. Kumar, Y.; Hashmi, S. A.; Pandey, G. P. Lithium Ion Transport and Ion–Polymer Interaction in PEO Based Polymer Electrolyte Plasticized with Ionic Liquid. *Solid State Ion.* **2011**, *201* (1), 73–80.
36. Vignarooban, K.; Dissanayake, M. A. K. L.; Albinsson, I.; Mellander, B.-E. Effect of TiO₂ Nano-Filler and EC Plasticizer on Electrical and Thermal Properties of Poly(Ethylene Oxide) (PEO) Based Solid Polymer Electrolytes. *Solid State Ion.* **2014**, *266*, 25–28.
37. Wang, W.; Yi, E.; Fici, A. J.; Laine, R. M.; Kieffer, J. Lithium Ion Conducting Poly(Ethylene Oxide)-Based Solid Electrolytes Containing Active or Passive Ceramic Nanoparticles. *J. Phys. Chem. C* **2017**, *121* (5), 2563–2573.

38. Shim, J.; Kim, D. G.; Kim, H. J.; Lee, J. H.; Lee, J. C. Polymer Composite Electrolytes Having Core–Shell Silica Fillers with Anion-Trapping Boron Moiety in the Shell Layer for All-Solid-State Lithium-Ion Batteries. *ACS Appl. Mater. Interfaces* **2015**, *7* (14), 7690–7701.
39. Wen, Z.; Itoh, T.; Ichikawa, Y.; Kubo, M.; Yamamoto, O. Blend-Based Polymer Electrolytes of Poly(Ethylene Oxide) and Hyperbranched Poly[Bis(Triethylene Glycol)Benzoate] with Terminal Acetyl Groups. *Solid State Ion.* **2000**, *134* (3), 281–289.
40. Park, C. H.; Sun, Y.-K.; Kim, D.-W. Blended Polymer Electrolytes Based on Poly(Lithium 4-Styrene Sulfonate) for the Rechargeable Lithium Polymer Batteries. *Electrochimica Acta* **2004**, *50* (2), 375–378.
41. Brandell, D.; Kasemägi, H.; Tamm, T.; Aabloo, A. Molecular Dynamics Modeling the Li-PolystyreneTFSI/PEO Blend. *Solid State Ion.* **2014**, *262*, 769–773.
42. Singh, M.; Odusanya, O.; Wilmes, G. M.; Eitouni, H. B.; Gomez, E. D.; Patel, A. J.; Chen, V. L.; Park, M. J.; Fragouli, P.; Iatrou, H.; Hadjichristidis, N.; Cookson, D.; Balsara, N. P. Effect of Molecular Weight on the Mechanical and Electrical Properties of Block Copolymer Electrolytes. *Macromolecules* **2007**, *40* (13), 4578–4585.
43. Young, W. S.; Albert, J. N. L.; Schantz, A. B.; Epps, T. H. Mixed-Salt Effects on the Ionic Conductivity of Lithium-Doped PEO-Containing Block Copolymers. *Macromolecules* **2011**, *44* (20), 8116–8123.
44. Young, N. P.; Devaux, D.; Khurana, R.; Coates, G. W.; Balsara, N. P. Investigating Polypropylene-Poly(Ethylene Oxide)-Polypropylene Triblock Copolymers as Solid Polymer Electrolytes for Lithium Batteries. *Solid State Ion.* **2014**, *263*, 87–94.
45. Hu, Q.; Osswald, S.; Daniel, R.; Zhu, Y.; Wesel, S.; Ortiz, L.; Sadoway, D. R. Graft Copolymer-Based Lithium-Ion Battery for High-Temperature Operation. *J. Power Sources* **2011**, *196* (13), 5604–5610.
46. Sun, J.; Stone, G. M.; Balsara, N. P.; Zuckermann, R. N. Structure–Conductivity Relationship for Peptoid-Based PEO–Mimetic Polymer Electrolytes. *Macromolecules* **2012**, *45* (12), 5151–5156.
47. Sun, J.; Liao, X.; Minor, A. M.; Balsara, N. P.; Zuckermann, R. N. Morphology-Conductivity Relationship in Crystalline and Amorphous Sequence-Defined Peptoid Block Copolymer Electrolytes. *J. Am. Chem. Soc.* **2014**, *136* (42), 14990–14997.
48. Walker, C. N.; Versek, C.; Touminen, M.; Tew, G. N. Tunable Networks from Thiolene Chemistry for Lithium Ion Conduction. *ACS Macro Lett.* **2012**, *1* (6), 737–741.
49. Khurana, R.; Schaefer, J. L.; Archer, L. A.; Coates, G. W. Suppression of Lithium Dendrite Growth Using Cross-Linked Polyethylene/Poly(Ethylene Oxide) Electrolytes: A New Approach for Practical Lithium-Metal Polymer Batteries. *J. Am. Chem. Soc.* **2014**, *136* (20), 7395–7402.
50. Shim, J.; Kim, D. G.; Joong Kim, H.; Hong Lee, J.; Baik, J. H.; Lee, J. C. Novel Composite Polymer Electrolytes Containing Poly(Ethylene Glycol)-Grafted Graphene Oxide for All-Solid-State Lithium-Ion Battery Applications. *J. Mater. Chem. A* **2014**, *2* (34), 13873–13883.
51. Andersson, D.; Carlsson, P.; Engberg, D.; Torell, L. M.; Börjesson, L.; McGreevy, R. L.; Howells, W. S. Modelling of Segmental Dynamics in Polymer Electrolyte PPO-LiClO₄, by Surface Fitting of Quasi-Elastic Neutron Scattering Data. *Phys. B Condens. Matter* **1999**, *266* (1), 126–130.
52. Tominaga, Y.; Mizumo, T.; Ohno, H. Ionic Conductivity of PPO-Sulfonamide Salt Hybrids and Their Network Polymers. *Polym. Adv. Technol.* **2000**, *11*, 524–528.

53. Kono, M.; Hayashi, E.; Watanabe, M. Network Polymer Electrolytes with Free Chain Ends as Internal Plasticizer. *J. Electrochem. Soc.* **1998**, *145* (5), 1521–1527.
54. Paulsdorf, J.; Burjanadze, M.; Hagelschur, K.; Wiemhöfer, H.-D. Ionic Conductivity in Polyphosphazene Polymer Electrolytes Prepared by the Living Cationic Polymerization. *Solid State Ion.* **2004**, *169* (1), 25–33.
55. Luther, T. A.; Stewart, F. F.; Budzien, J. L.; LaViolette, R. A.; Bauer, W. F.; Harrup, M. K.; Allen, C. W.; Elayan, A. On the Mechanism of Ion Transport through Polyphosphazene Solid Polymer Electrolytes: NMR, IR, and Raman Spectroscopic Studies and Computational Analysis of ¹⁵N-Labeled Polyphosphazenes. *J. Phys. Chem. B* **2003**, *107* (14), 3168–3176.
56. Kang, Y.; Lee, J.; Suh, D. H.; Lee, C. A New Polysiloxane Based Cross-Linker for Solid Polymer Electrolyte. *J. Power Sources* **2005**, *146* (1), 391–396.
57. Snyder, J. F.; Ratner, M. A.; Shriver, D. F. Ion Conductivity of Comb Polysiloxane Polyelectrolytes Containing Oligoether and Perfluoroether Sidechains. *J. Electrochem. Soc.* **2003**, *150* (8), A1090–A1094.
58. Karatas, Y.; Banhatti, R. D.; Kaskhedikar, N.; Burjanadze, M.; Funke, K.; Wiemhöfer, H.-D. Synthesis and Modeling of Polysiloxane-Based Salt-in-Polymer Electrolytes with Various Additives. *J. Phys. Chem. B* **2009**, *113* (47), 15473–15484.
59. Sun, B.; Mindemark, J.; Edström, K.; Brandell, D. Polycarbonate-Based Solid Polymer Electrolytes for Li-Ion Batteries. *Solid State Ion.* **2014**, *262* (1), 738–742.
60. Zhang, J.; Yang, J.; Dong, T.; Zhang, M.; Chai, J.; Dong, S.; Wu, T.; Zhou, X.; Cui, G. Aliphatic Polycarbonate-Based Solid-State Polymer Electrolytes for Advanced Lithium Batteries: Advances and Perspective. *Small* **2018**, *14* (36), 1800821.
61. Bao, J.; Shi, G.; Tao, C.; Wang, C.; Zhu, C.; Cheng, L.; Qian, G.; Chen, C. Polycarbonate-Based Polyurethane as a Polymer Electrolyte Matrix for All-Solid-State Lithium Batteries. *J. Power Sources* **2018**, *389*, 84–92.
62. Vickraman, P.; Ramamurthy, S. A Study on the Blending Effect of PVDF in the Ionic Transport Mechanism of Plasticized PVC-LiBF₄ Polymer Electrolyte. *Mater. Lett.* **2006**, *60* (28), 3431–3436.
63. Rajendran, S.; Babu, R.; Sivakumar, P. Optimization of PVC-PAN-Based Polymer Electrolytes. *J. Appl. Polym. Sci.* **2009**, *113* (3), 1651–1656.
64. Choi, S. W.; Kim, J. R.; Jo, S. M.; Lee, W. S.; Kim, Y. R. Electrochemical and Spectroscopic Properties of Electrospun PAN-Based Fibrous Polymer Electrolytes. *J. Electrochem. Soc.* **2005**, *152* (5), A989–A995.
65. Min, H. S.; Ko, J. M.; Kim, D. W. Preparation and Characterization of Porous Polyacrylonitrile Membranes for Lithium-Ion Polymer Batteries. *J. Power Sources* **2003**, *119*, 469–472.
66. Carol, P.; Ramakrishnan, P.; John, B.; Cheruvally, G. Preparation and Characterization of Electrospun Poly(Acrylonitrile) Fibrous Membrane Based Gel Polymer Electrolytes for Lithium-Ion Batteries. *J. Power Sources* **2011**, *196* (23), 10156–10162.
67. Meneghetti, P.; Qutubuddin, S.; Webber, A. Synthesis of Polymer Gel Electrolyte with High Molecular Weight Poly(Methyl Methacrylate)-Clay Nanocomposite. *Electrochimica Acta* **2004**, *49* (27), 4923–4931.
68. Ramesh, S.; Ang, G. P. Impedance and FTIR Studies on Plasticized PMMA-LiN(CF₃SO₂)₂ Nanocomposite Polymer Electrolytes. *Ionics* **2010**, *16* (5), 465–473.
69. Choi, S. W.; Jo, S. M.; Lee, W. S.; Kim, Y. R. An Electrospun Poly(Vinylidene Fluoride) Nanofibrous Membrane and Its Battery Applications. *Adv. Mater.* **2003**, *15* (23), 2027–2032.

70. Kim, J. R.; Choi, S. W.; Jo, S. M.; Lee, W. S.; Kim, B. C. Electrospun PVdF-Based Fibrous Polymer Electrolytes for Lithium Ion Polymer Batteries. *Electrochimica Acta* **2004**, *50* (1), 69–75.
71. Zhang, M. Y.; Li, M. X.; Chang, Z.; Wang, Y. F.; Gao, J.; Zhu, Y. S.; Wu, Y. P.; Huang, W. A Sandwich PVDF/HEC/PVDF Gel Polymer Electrolyte for Lithium Ion Battery. *Electrochimica Acta* **2017**, *245*, 752–759.
72. Liu, W.; Zhang, X. K.; Wu, F.; Xiang, Y. A Study on PVDF-HFP Gel Polymer Electrolyte for Lithium-Ion Batteries. *IOP Conf. Ser. Mater. Sci. Eng.* **2017**, *213*, 012036.
73. Jie, J.; Liu, Y.; Cong, L.; Zhang, B.; Lu, W.; Zhang, X.; Liu, J.; Xie, H.; Sun, L. High-Performance PVDF-HFP Based Gel Polymer Electrolyte with a Safe Solvent in Li Metal Polymer Battery. *J. Energy Chem.* **2020**, *49*, 80–88.
74. Chen, G.; Zhang, F.; Zhou, Z.; Li, J.; Tang, Y. A Flexible Dual-Ion Battery Based on PVDF-HFP-Modified Gel Polymer Electrolyte with Excellent Cycling Performance and Superior Rate Capability. *Adv. Energy Mater.* **2018**, *8* (25), 1801219.
75. Henderson, W. A. Crystallization Kinetics of Glyme–LiX and PEO–LiX Polymer Electrolytes. *Macromolecules* **2007**, *40* (14), 4963–4971.
76. Fullerton-Shirey, S. K.; Maranas, J. K. Effect of LiClO₄ on the Structure and Mobility of PEO-Based Solid Polymer Electrolytes. *Macromolecules* **2009**, *42* (6), 2142–2156.
77. Karmakar, A.; Ghosh, A. Dielectric Permittivity and Electric Modulus of Polyethylene Oxide (PEO)–LiClO₄ Composite Electrolytes. *Curr. Appl. Phys.* **2012**, *12* (2), 539–543.
78. Ibrahim, S.; Yassin, M. M.; Ahmad, R.; Johan, M. R. Effects of Various LiPF₆ Salt Concentrations on PEO-Based Solid Polymer Electrolytes. *Ionics* **2011**, *17* (5), 399–405.
79. Angulakshmi, N.; Nahm, K. S.; Nair, J. R.; Gerbaldi, C.; Bongiovanni, R.; Penazzi, N.; Stephan, A. M. Cycling Profile of MgAl₂O₄-Incorporated Composite Electrolytes Composed of PEO and LiPF₆ for Lithium Polymer Batteries. *Electrochimica Acta* **2013**, *90*, 179–185.
80. MacGlashan, G. S.; Andreev, Y. G.; Bruce, P. G. Structure of the Polymer Electrolyte Poly(Ethylene Oxide)₆:LiAsF₆. *Nature* **1999**, *398* (6730), 792–794.
81. Martin-Litas, I.; Andreev, Y. G.; Bruce, P. G. Ab Initio Structure Solution of the Polymer Electrolyte Poly(Ethylene Oxide)₃:LiAsF₆. *Chem. Mater.* **2002**, *14* (5), 2166–2170.
82. Andreev, Y. G.; Seneviratne, V.; Khan, M.; Henderson, W. A.; Frech, R. E.; Bruce, P. G. Crystal Structures of Poly(Ethylene Oxide)₃:LiBF₄ and (Diglyme)_n:LiBF₄ (n = 1,2). *Chem. Mater.* **2005**, *17* (4), 767–772.
83. Kalita, M.; Bukat, M.; Ciosek, M.; Siekierski, M.; Chung, S. H.; Rodríguez, T.; Greenbaum, S. G.; Kovarsky, R.; Golodnitsky, D.; Peled, E.; Zane, D.; Scrosati, B.; Wiczorek, W. Effect of Calixpyrrole in PEO–LiBF₄ Polymer Electrolytes. *Electrochimica Acta* **2005**, *50* (19), 3942–3948.
84. Zardalidis, G.; Ioannou, E.; Pispas, S.; Floudas, G. Relating Structure, Viscoelasticity, and Local Mobility to Conductivity in PEO/LiTf Electrolytes. *Macromolecules* **2013**, *46* (7), 2705–2714.
85. Karan, N. K.; Pradhan, D. K.; Thomas, R.; Natesan, B.; Katiyar, R. S. Solid Polymer Electrolytes Based on Polyethylene Oxide and Lithium Trifluoro- Methane Sulfonate (PEO–LiCF₃SO₃): Ionic Conductivity and Dielectric Relaxation. *Solid State Ion.* **2008**, *179* (19), 689–696.
86. Seki, S.; Takei, K.; Miyashiro, H.; Watanabe, M. Physicochemical and Electrochemical Properties of Glyme–LiN(SO₂F)₂ Complex for Safe Lithium-Ion Secondary Battery Electrolyte. *J. Electrochem. Soc.* **2011**, *158* (6), A769–A774.

87. Zhang, H.; Liu, C.; Zheng, L.; Xu, F.; Feng, W.; Li, H.; Huang, X.; Armand, M.; Nie, J.; Zhou, Z. Lithium Bis(Fluorosulfonyl)Imide/Poly(Ethylene Oxide) Polymer Electrolyte. *Electrochimica Acta* **2014**, *133*, 529–538.
88. Bernhard, R.; Latini, A.; Panero, S.; Scrosati, B.; Hassoun, J. Poly(Ethylenglycol)Dimethylether–Lithium Bis(Trifluoromethanesulfonyl)Imide, PEG500DME–LiTFSI, as High Viscosity Electrolyte for Lithium Ion Batteries. *J. Power Sources* **2013**, *226*, 329–333.
89. Borodin, O.; Smith, G. D. Mechanism of Ion Transport in Amorphous Poly(Ethylene Oxide)/LiTFSI from Molecular Dynamics Simulations. *Macromolecules* **2006**, *39* (4), 1620–1629.
90. Appetecchi, G. B.; Shin, J. H.; Alessandrini, F.; Passerini, S. 0.6 Ah Li/V₂O₅ Battery Prototypes Based on Solvent-Free PEO–LiN(SO₂CF₂CF₃)₂ Polymer Electrolytes. *J. Power Sources* **2005**, *143* (1), 236–242.
91. Shin, J. H.; Alessandrini, F.; Passerini, S. Comparison of Solvent-Cast and Hot-Pressed P(EO)₂₀LiN(SO₂CF₂CF₃)₂ Polymer Electrolytes Containing Nanosized SiO₂. *J. Electrochem. Soc.* **2004**, *152* (2), A283–A288.
92. Robitaille, C. D.; Fauteux, D. Phase Diagrams and Conductivity Characterization of Some PEO - LiX Electrolytes. *J. Electrochem. Soc.* **1986**, *133* (2), 315–325.
93. Cui, W. W.; Tang, D. Y. Electrospun Poly(Lithium 2-Acrylamido-2-Methylpropanesulfonic Acid) Fiber-Based Polymer Electrolytes for Lithium-Ion Batteries. *J. Appl. Polym. Sci.* **2012**, *126* (2), 510–518.
94. Zhu, Y. S.; Gao, X. W.; Wang, X. J.; Hou, Y. Y.; Liu, L. L.; Wu, Y. P. A Single-Ion Polymer Electrolyte Based on Boronate for Lithium Ion Batteries. *Electrochem. Commun.* **2012**, *22*, 29–32.
95. Bouchet, R.; Maria, S.; Meziane, R.; Aboulaich, A.; Lienafa, L.; Bonnet, J.-P.; Phan, T. N. T.; Bertin, D.; Gigmes, D.; Devaux, D.; Denoyel, R.; Armand, M. Single-Ion BAB Triblock Copolymers as Highly Efficient Electrolytes for Lithium-Metal Batteries. *Nat. Mater.* **2013**, *12* (5), 452–457.
96. Feng, S.; Shi, D.; Liu, F.; Zheng, L.; Nie, J.; Feng, W.; Huang, X.; Armand, M.; Zhou, Z. Single Lithium-Ion Conducting Polymer Electrolytes Based on Poly[(4-Styrenesulfonyl)(Trifluoromethanesulfonyl)Imide] Anions. *Electrochimica Acta* **2013**, *93*, 254–263.
97. Snyder, J. F.; Hutchison, J. C.; Ratner, M. A.; Shriver, D. F. Synthesis of Comb Polysiloxane Polyelectrolytes Containing Oligoether and Perfluoroether Side Chains. *Chem. Mater.* **2003**, *15* (22), 4223–4230.
98. Onishi, K.; Matsumoto, M.; Nakacho, Y.; Shigehara, K. Synthesis of Aluminate Polymer Complexes as Single-Ionic Solid Electrolytes. *Chem. Mater.* **1996**, *8* (2), 469–472.
99. Matsumi, N.; Sugai, K.; Ohno, H. Ion Conductive Characteristics of Alkylborane Type and Boric Ester Type Polymer Electrolytes Derived from Mesitylborane. *Macromolecules* **2003**, *36* (7), 2321–2326.
100. Zhu, Y. S.; Wang, X. J.; Hou, Y. Y.; Gao, X. W.; Liu, L. L.; Wu, Y. P.; Shimizu, M. A New Single-Ion Polymer Electrolyte Based on Polyvinyl Alcohol for Lithium Ion Batteries. *Electrochimica Acta* **2013**, *87*, 113–118.
101. Siska, D. P.; Shriver, D. F. Li⁺ Conductivity of Polysiloxane–Trifluoromethylsulfonamide Polyelectrolytes. *Chem. Mater.* **2001**, *13* (12), 4698–4700.
102. Aoki, T.; Konno, A.; Fujinami, T. Li-Ion Conductivity of Aluminate and Borate Complex Polymers Containing Fluoroalkane Dicarboxylate. *J. Electrochem. Soc.* **2004**, *151* (6), A887–A890.

103. Matsumi, N.; Sugai, K.; Ohno, H. Selective Ion Transport in Organoboron Polymer Electrolytes Bearing a Mesitylboron Unit. *Macromolecules* **2002**, *35* (15), 5731–5733.
104. Chen, L.; Li, Y.; Li, S. P.; Fan, L. Z.; Nan, C. W.; Goodenough, J. B. PEO/Garnet Composite Electrolytes for Solid-State Lithium Batteries: From “Ceramic-in-Polymer” to “Polymer-in-Ceramic.” *Nano Energy* **2018**, *46*, 176–184.
105. Murugan, R.; Thangadurai, V.; Weppner, W. Fast Lithium Ion Conduction in Garnet-Type $\text{Li}_7\text{La}_3\text{Zr}_2\text{O}_{12}$. *Angew. Chem. Int. Ed.* **2007**, *46* (41), 7778–7781.
106. Ohta, S.; Kobayashi, T.; Asaoka, T. High Lithium Ionic Conductivity in the Garnet-Type Oxide $\text{Li}_{7-x}\text{La}_3(\text{Zr}_{2-x}, \text{Nb}_x)\text{O}_{12}$ ($X=0-2$). *J. Power Sources* **2011**, *196* (6), 3342–3345.
107. Yi, E.; Wang, W.; Kieffer, J.; Laine, R. M. Key Parameters Governing the Densification of Cubic- $\text{Li}_7\text{La}_3\text{Zr}_2\text{O}_{12}$ Li^+ conductors. *J. Power Sources* **2017**, *352*, 156–164.
108. Wu, J. F.; Chen, E. Y.; Yu, Y.; Liu, L.; Wu, Y.; Pang, W. K.; Peterson, V. K.; Guo, X. Gallium-Doped $\text{Li}_7\text{La}_3\text{Zr}_2\text{O}_{12}$ Garnet-Type Electrolytes with High Lithium-Ion Conductivity. *ACS Appl. Mater. Interfaces* **2017**, *9* (2), 1542–1552.
109. Inaguma, Y.; Liqun, C.; Itoh, M.; Nakamura, T.; Uchida, T.; Ikuta, H.; Wakihara, M. High Ionic Conductivity in Lithium Lanthanum Titanate. *Solid State Commun.* **1993**, *86* (10), 689–693.
110. Inada, R.; Kimura, K.; Kusakabe, K.; Tojo, T.; Sakurai, Y. Synthesis and Lithium-Ion Conductivity for Perovskite-Type $\text{Li}_{3/8}\text{Sr}_{7/16}\text{Ta}_{3/4}\text{Zr}_{1/4}\text{O}_3$ Solid Electrolyte by Powder-Bed Sintering. *Solid State Ion.* **2014**, *261*, 95–99.
111. Huang, B.; Xu, B.; Li, Y.; Zhou, W.; You, Y.; Zhong, S.; Wang, C.-A.; Goodenough, J. B. Li-Ion Conduction and Stability of Perovskite $\text{Li}_{3/8}\text{Sr}_{7/16}\text{Hf}_{1/4}\text{Ta}_{3/4}\text{O}_3$. *ACS Appl. Mater. Interfaces* **2016**, *8* (23), 14552–14557.
112. Aono, H.; Imanaka, N.; Adachi, G. High Li^+ Conducting Ceramics. *Acc. Chem. Res.* **1994**, *27* (9), 265–270.
113. Fu, J. Fast Li^+ Ion Conduction in $\text{Li}_2\text{O}-\text{Al}_2\text{O}_3-\text{TiO}_2-\text{SiO}_2-\text{P}_2\text{O}_5$ Glass-Ceramics. *J. Am. Ceram. Soc.* **1997**, *80* (7), 1901–1903.
114. Yi, E.; Wang, W.; Mohanty, S.; Kieffer, J.; Tamaki, R.; Laine, R. M. Materials That Can Replace Liquid Electrolytes in Li Batteries: Superionic Conductivities in $\text{Li}_{1.7}\text{Al}_{0.3}\text{Ti}_{1.7}\text{Si}_{0.4}\text{P}_{2.6}\text{O}_{12}$. Processing Combustion Synthesized Nanopowders to Free Standing Thin Films. *J. Power Sources* **2014**, *269* (10), 577–588.
115. Fu, J. Fast Li^+ Ion Conducting Glass-Ceramics in the System $\text{Li}_2\text{O}-\text{Al}_2\text{O}_3-\text{GeO}_2-\text{P}_2\text{O}_5$. *Solid State Ion.* **1997**, *104* (3), 191–194.
116. Illbeigi, M.; Fazlali, A.; Kazazi, M.; Mohammadi, A. H. Effect of Simultaneous Addition of Aluminum and Chromium on the Lithium Ionic Conductivity of $\text{LiGe}_2(\text{PO}_4)_3$ NASICON-Type Glass–Ceramics. *Solid State Ion.* **2016**, *289*, 180–187.
117. Hong, H. Y.P. Crystal Structure and Ionic Conductivity of $\text{Li}_{14}\text{Zn}(\text{GeO}_4)_4$ and Other New Li^+ Superionic Conductors. *Mater. Res. Bull.* **1978**, *13* (2), 117–124.
118. Mazumdar, D.; Bose, D. N.; Mukherjee, M. L. Transport and Dielectric Properties of Lisicon. *Solid State Ion.* **1984**, *14* (2), 143–147.
119. Hu, Y.W.; Raistrick, I. D.; Huggins, R. A. Ionic Conductivity of Lithium Orthosilicate—Lithium Phosphate Solid Solutions. *J. Electrochem. Soc.* **1977**, *124* (8), 1240–12442.
120. Song, S.; Lu, J.; Zheng, F.; Duong, H. M.; Lu, L. A Facile Strategy to Achieve High Conduction and Excellent Chemical Stability of Lithium Solid Electrolytes. *RSC Adv.* **2014**, *5* (9), 6588–6594.

121. Deng, Y.; Eames, C.; Fleutot, B.; David, R.; Chotard, J.-N.; Suard, E.; Masquelier, C.; Islam, M. S. Enhancing the Lithium Ion Conductivity in Lithium Superionic Conductor (LISICON) Solid Electrolytes through a Mixed Polyanion Effect. *ACS Appl. Mater. Interfaces* **2017**, *9* (8), 7050–7058.
122. Bates, J. B.; Dudney, N. J.; Gruzalski, G. R.; Zuhr, R. A.; Choudhury, A.; Luck, C. F.; Robertson, J. D. Electrical Properties of Amorphous Lithium Electrolyte Thin Films. *Solid State Ion.* **1992**, *53*, 647–654.
123. Bates, J. B.; Dudney, N. J.; Gruzalski, G. R.; Zuhr, R. A.; Choudhury, A.; Luck, C. F.; Robertson, J. D. Fabrication and Characterization of Amorphous Lithium Electrolyte Thin Films and Rechargeable Thin-Film Batteries. *J. Power Sources* **1993**, *43–44*, 103–110.
124. Yu, X.; Bates, J. B.; Jellison, G. E.; Hart, F. X. A Stable Thin-Film Lithium Electrolyte: Lithium Phosphorus Oxynitride. *J. Electrochem. Soc.* **1997**, *144*, 524–532.
125. Mizuno, F.; Hayashi, A.; Tadanaga, K.; Tatsumisago, M. New, Highly Ion-Conductive Crystals Precipitated from $\text{Li}_2\text{S}-\text{P}_2\text{S}_5$ Glasses. *Adv. Mater.* **2005**, *17* (7), 918–921.
126. Seino, Y.; Ota, T.; Takada, K.; Hayashi, A.; Tatsumisago, M. A Sulphide Lithium Super Ion Conductor Is Superior to Liquid Ion Conductors for Use in Rechargeable Batteries. *Energy Environ. Sci.* **2014**, *7* (2), 627–631.
127. Hayashi, A.; Hama, S.; Morimoto, H.; Tatsumisago, M.; Minami, T. High Lithium Ion Conductivity of Glass–Ceramics Derived from Mechanically Milled Glassy Powders. *Chem. Lett.* **2001**, *30* (9), 872–873.
128. Kanno, R.; Murayama, M. Lithium Ionic Conductor Thio-LISICON: The $\text{Li}_2\text{S}-\text{GeS}_2-\text{P}_2\text{S}_5$ System. *J. Electrochem. Soc.* **2001**, *148* (7), A742–A746.
129. Kamaya, N.; Homma, K.; Yamakawa, Y.; Hirayama, M.; Kanno, R.; Yonemura, M.; Kamiyama, T.; Kato, Y.; Hama, S.; Kawamoto, K.; Mitsui, A. A Lithium Superionic Conductor. *Nat. Mater.* **2011**, *10* (9), 682–686.
130. Kato, Y.; Hori, S.; Saito, T.; Suzuki, K.; Hirayama, M.; Mitsui, A.; Yonemura, M.; Iba, H.; Kanno, R. High-Power All-Solid-State Batteries Using Sulfide Superionic Conductors. *Nat. Energy* **2016**, *1* (4), 1–7.
131. Kasper, H. M. A New Series of Rare Earth Garnets $\text{Ln}^{3+}_3\text{M}_2\text{Li}^{+}_3\text{O}_{12}$ (M=Te, W). *Inorg. Chem.* **1969**, *8* (4), 1000–1002.
132. Thangadurai, V.; Kaack, H.; Weppner, W. J. F. Novel Fast Lithium Ion Conduction in Garnet-Type $\text{Li}_5\text{La}_3\text{M}_2\text{O}_{12}$ (M = Nb, Ta). *J. Am. Ceram. Soc.* **2003**, *86* (3), 437–440.
133. Geiger, C. A.; Alekseev, E.; Lazic, B.; Fisch, M.; Armbruster, T.; Langner, R.; Fechtelkord, M.; Kim, N.; Pettke, T.; Weppner, W. Crystal Chemistry and Stability of “ $\text{Li}_7\text{La}_3\text{Zr}_2\text{O}_{12}$ ” Garnet: A Fast Lithium-Ion Conductor. *Inorg. Chem.* **2011**, *50* (3), 1089–1097.
134. Murugan, R.; Ramakumar, S.; Janani, N. High Conductive Yttrium Doped $\text{Li}_7\text{La}_3\text{Zr}_2\text{O}_{12}$ Cubic Lithium Garnet. *Electrochem. Commun.* **2011**, *13* (12), 1373–1375.
135. Allen, J. L.; Wolfenstine, J.; Rangasamy, E.; Sakamoto, J. Effect of Substitution (Ta, Al, Ga) on the Conductivity of $\text{Li}_7\text{La}_3\text{Zr}_2\text{O}_{12}$. *J. Power Sources* **2012**, *206*, 315–319.
136. Zheng, F.; Kotobuki, M.; Song, S.; Lai, M. O.; Lu, L. Review on Solid Electrolytes for All-Solid-State Lithium-Ion Batteries. *J. Power Sources* **2018**, *389*, 198–213.
137. Imagawa, H.; Ohta, S.; Kihira, Y.; Asaoka, T. Garnet-Type $\text{Li}_{6.75}\text{La}_3\text{Zr}_{1.75}\text{Nb}_{0.25}\text{O}_{12}$ Synthesized by Coprecipitation Method and Its Lithium Ion Conductivity. *Solid State Ion.* **2014**, *262*, 609–612.
138. Zhang, Y.; Chen, F.; Tu, R.; Shen, Q.; Zhang, L. Field Assisted Sintering of Dense Al-Substituted Cubic Phase $\text{Li}_7\text{La}_3\text{Zr}_2\text{O}_{12}$ Solid Electrolytes. *J. Power Sources* **2014**, *268*, 960–964.

139. Kim, Y.; Jo, H.; Allen, J. L.; Choe, H.; Wolfenstine, J.; Sakamoto, J. The Effect of Relative Density on the Mechanical Properties of Hot-Pressed Cubic $\text{Li}_7\text{La}_3\text{Zr}_2\text{O}_{12}$. *J. Am. Ceram. Soc.* **2016**, *99* (4), 1367–1374.
140. Baek, S. W.; Lee, J. M.; Kim, T. Y.; Song, M. S.; Park, Y. Garnet Related Lithium Ion Conductor Processed by Spark Plasma Sintering for All Solid State Batteries. *J. Power Sources* **2014**, *249*, 197–206.
141. Yi, E.; Wang, W.; Kieffer, J.; Laine, R. M. Flame Made Nanoparticles Permit Processing of Dense, Flexible, Li^+ Conducting Ceramic Electrolyte Thin Films of Cubic- $\text{Li}_7\text{La}_3\text{Zr}_2\text{O}_{12}$ (c-LLZO). *J. Mater. Chem. A* **2016**, *4* (33), 12947–12954.
142. Knauth, P. Inorganic Solid Li Ion Conductors: An Overview. *Solid State Ion.* **2009**, *180* (14), 911–916.
143. Chen, C. H.; Amine, K. Ionic Conductivity, Lithium Insertion and Extraction of Lanthanum Lithium Titanate. *Solid State Ion.* **2001**, *144* (1), 51–57.
144. Thangadurai, V.; Shukla, A. K.; Gopalakrishnan, J. $\text{LiSr}_{1.65}\text{B}_{0.35}\text{B}'_{1.7}\text{O}_9$ (B = Ti, Zr; B' = Nb, Ta): New Lithium Ion Conductors Based on the Perovskite Structure. *Chem. Mater.* **1999**, *11* (3), 835–839.
145. Goodenough, J. B.; Hong, H. Y.-P.; Kafalas, J. A. Fast Na^+ -Ion Transport in Skeleton Structures. *Mater. Res. Bull.* **1976**, *11* (2), 203–220.
146. Thangadurai, V.; Weppner, W. Recent Progress in Solid Oxide and Lithium Ion Conducting Electrolytes Research. *Ionics* **2006**, *12* (1), 81–92.
147. Cretin, M.; Fabry, P. Comparative Study of Lithium Ion Conductors in the System $\text{Li}_{1+x}\text{Al}_x\text{A}_{2-x}\text{IV}(\text{PO}_4)_3$ with $\text{A}^{\text{IV}}=\text{Ti}$ or Ge and $0 \leq x \leq 0.7$ for Use as Li^+ Sensitive Membranes. *J. Eur. Ceram. Soc.* **1999**, *19* (16), 2931–2940.
148. Catti, M.; Comotti, A.; Di Blas, S. High-Temperature Lithium Mobility in $\alpha\text{-LiZr}_2(\text{PO}_4)_3$ NASICON by Neutron Diffraction. *Chem. Mater.* **2003**, *15* (8), 1628–1632.
149. Hanghofer, I.; Gadermaier, B.; Wilkening, A.; Rettenwander, D.; Wilkening, H. M. R. Lithium Ion Dynamics in $\text{LiZr}_2(\text{PO}_4)_3$ and $\text{Li}_{1.4}\text{Ca}_{0.2}\text{Zr}_{1.8}(\text{PO}_4)_3$. *Dalton Trans.* **2019**, *48* (25), 9376–9387.
150. Morimoto, H.; Awano, H.; Terashima, J.; Shindo, Y.; Nakanishi, S.; Ito, N.; Ishikawa, K.; Tobishima, S. Preparation of Lithium Ion Conducting Solid Electrolyte of NASICON-Type $\text{Li}_{1+x}\text{Al}_x\text{Ti}_{2-x}(\text{PO}_4)_3$ ($x = 0.3$) Obtained by Using the Mechanochemical Method and Its Application as Surface Modification Materials of LiCoO_2 Cathode for Lithium Cell. *J. Power Sources* **2013**, *240*, 636–643.
151. Xu, X.; Wen, Z.; Wu, X.; Yang, X.; Gu, Z. Lithium Ion-Conducting Glass–Ceramics of $\text{Li}_{1.5}\text{Al}_{0.5}\text{Ge}_{1.5}(\text{PO}_4)_3\text{-XLi}_2\text{O}$ ($X=0.0\text{--}0.20$) with Good Electrical and Electrochemical Properties. *J. Am. Ceram. Soc.* **2007**, *90* (9), 2802–2806.
152. Xu, X.; Wen, Z.; Yang, X.; Chen, L. Dense Nanostructured Solid Electrolyte with High Li-Ion Conductivity by Spark Plasma Sintering Technique. *Mater. Res. Bull.* **2008**, *43* (8), 2334–2341.
153. Aono, H.; Sugimoto, E.; Sadaoka, Y.; Imanaka, N.; Adachi, G. Ionic Conductivity of the Lithium Titanium Phosphate ($\text{Li}_{1+x}\text{M}_x\text{Ti}_{2-x}(\text{PO}_4)_3$, M = Al, Sc, Y, and La) Systems. *J. Electrochem. Soc.* **1989**, *136* (2), 590.
154. Feng, J. K.; Lu, L.; Lai, M. O. Lithium Storage Capability of Lithium Ion Conductor $\text{Li}_{1.5}\text{Al}_{0.5}\text{Ge}_{1.5}(\text{PO}_4)_3$. *J. Alloys Compd.* **2010**, *501* (2), 255–258.
155. Fu, J. Fast Li^+ Ion Conducting Glass-Ceramics in the System $\text{Li}_2\text{O}\text{-Al}_2\text{O}_3\text{-GeO}_2\text{-P}_2\text{O}_5$. *Solid State Ion.* **1997**, *104* (3), 191–194.

156. West, A. R. Crystal Chemistry of Some Tetrahedral Oxides. *Z. Für Krist.* **1975**, *141* (5–6), 422–436.
157. Du, Y. A.; Holzwarth, N. A. W. Mechanisms of Li⁺ Diffusion in Crystalline γ - and β -Li₃PO₄ Electrolytes from First Principles. *Phys. Rev. B* **2007**, *76* (17), 174302.
158. Du, Y. A.; Holzwarth, N. a. W. Li Ion Diffusion Mechanisms in the Crystalline Electrolyte γ -Li₃PO₄. *J. Electrochem. Soc.* **2007**, *154* (11), A999–A1004.
159. Shannon, R. D.; Taylor, B. E.; English, A. D.; Berzins, T. New Li Solid Electrolytes. *Electrochimica Acta* **1977**, *22*, 783–796.
160. Lacivita, V.; Artrith, N.; Ceder, G. Structural and Compositional Factors That Control the Li-Ion Conductivity in LiPON Electrolytes. *Chem. Mater.* **2018**, *30* (20), 7077–7090.
161. Li, J.; Lai, W. Structure and Ionic Conduction Study on Li₃PO₄ and LiPON (Lithium Phosphorous Oxynitride) with the Density-Functional Tight-Binding (DFTB) Method. *Solid State Ion.* **2020**, *351*, 115329.
162. Wang, B.; Chakoumakos, B. C.; Sales, B. C.; Kwak, B. S.; Bates, J. B. Synthesis, Crystal Structure, and Ionic Conductivity of a Polycrystalline Lithium Phosphorus Oxynitride with the γ -Li₃PO₄ Structure. *J. Solid State Chem.* **1995**, *115* (2), 313–323.
163. Li, G.; Li, M.; Dong, L.; Li, X.; Li, D. Low Energy Ion Beam Assisted Deposition of Controllable Solid State Electrolyte LiPON with Increased Mechanical Properties and Ionic Conductivity. *Int. J. Hydrog. Energy* **2014**, *39* (30), 17466–17472.
164. Vereda, F.; Goldner, R. B.; Haas, T. E.; Zerigian, P. Rapidly Grown IBAD LiPON Films with High Li-Ion Conductivity and Electrochemical Stability. *Electrochem. Solid-State Lett.* **2002**, *5*, 239–241.
165. Fujibayashi, T.; Kubota, Y.; Iwabuchi, K.; Yoshii, N. Highly Conformal and High-Ionic Conductivity Thin-Film Electrolyte for 3D-Structured Micro Batteries: Characterization of LiPON Film Deposited by MOCVD Method. *AIP Adv.* **2017**, *7* (8), 085110.
166. Kennedy, J. H.; Sahami, S.; Shea, S. W.; Zhang, Z. Preparation and Conductivity Measurements of SiS₂-Li₂S Glasses Doped with LiBr and LiCl. *Solid State Ion.* **1986**, *18–19*, 368–371.
167. Kennedy, J. H.; Yang, Y. A Highly Conductive Li⁺-Glass System: (1-x)(0.4 SiS₂-0.6 Li₂S)-xLiI. *J. Electrochem. Soc.* **1986**, *133*, 2437–2438.
168. Ahn, B. T.; Huggins, R. A. Phase Behavior and Conductivity of Li₂SiS₃ Composition. *Solid State Ion.* **1991**, *46* (3–4), 237–242.
169. Tatsumisago, M.; Hayashi, A. Sulfide Glass-Ceramic Electrolytes for All-Solid-State Lithium and Sodium Batteries. *Int. J. Appl. Glass Sci.* **2014**, *5* (3), 226–235.
170. Bron, P.; Johansson, S.; Zick, K.; Schmedt auf der Günne, J.; Dehnen, S.; Roling, B. Li₁₀SnP₂S₁₂: An Affordable Lithium Superionic Conductor. *J. Am. Chem. Soc.* **2013**, *135* (42), 15694–15697.
171. Whiteley, J. M.; Woo, J. H.; Hu, E.; Nam, K. W.; Lee, S. H. Empowering the Lithium Metal Battery through a Silicon-Based Superionic Conductor. *J. Electrochem. Soc.* **2014**, *161* (12), A1812–A1817.
172. Kuhn, A.; Gerbig, O.; Zhu, C.; Falkenberg, F.; Maier, J.; V. Lotsch, B. A New Ultrafast Superionic Li-Conductor: Ion Dynamics in Li₁₁Si₂PS₁₂ and Comparison with Other Tetragonal LGPS-Type Electrolytes. *Phys. Chem. Chem. Phys.* **2014**, *16* (28), 14669–14674.
173. Hu, C. H.; Wang, Z. Q.; Sun, Z. Y.; Ouyang, C. Y. Insights into Structural Stability and Li Superionic Conductivity of Li₁₀GeP₂S₁₂ from First-Principles Calculations. *Chem. Phys. Lett.* **2014**, *591*, 16–20.

174. Kuhn, A.; Köhler, J.; V. Lotsch, B. Single-Crystal X-Ray Structure Analysis of the Superionic Conductor $\text{Li}_{10}\text{GeP}_2\text{S}_{12}$. *Phys. Chem. Chem. Phys.* **2013**, *15* (28), 11620–11622.
175. Zhao, F.; Liang, J.; Yu, C.; Sun, Q.; Li, X.; Adair, K.; Wang, C.; Zhao, Y.; Zhang, S.; Li, W.; Deng, S.; Li, R.; Huang, Y.; Huang, H.; Zhang, L.; Zhao, S.; Lu, S.; Sun, X. A Versatile Sn-Substituted Argyrodite Sulfide Electrolyte for All-Solid-State Li Metal Batteries. *Adv. Energy Mater.* **2020**, *10* (9), 1903422.
176. Lau, J.; DeBlock, R. H.; Butts, D. M.; Ashby, D. S.; Choi, C. S.; Dunn, B. S. Sulfide Solid Electrolytes for Lithium Battery Applications. *Adv. Energy Mater.* **2018**, *8* (27), 1800933.
177. Albertus, P.; Babinec, S.; Litzelman, S.; Newman, A. Status and Challenges in Enabling the Lithium Metal Electrode for High-Energy and Low-Cost Rechargeable Batteries. *Nat. Energy* **2018**, *3* (1), 16–21.
178. Fan, L.; Wei, S.; Li, S.; Li, Q.; Lu, Y. Recent Progress of the Solid-State Electrolytes for High-Energy Metal-Based Batteries. *Adv. Energy Mater.* **2018**, *8* (11), 1702657.
179. Cheng, X. B.; Zhang, R.; Zhao, C. Z.; Zhang, Q. Toward Safe Lithium Metal Anode in Rechargeable Batteries: A Review. *Chem. Rev.* **2017**, *117* (15), 10403–10473.

Chapter 2 Experimental

2.1 Introduction

This chapter summarizes synthesis and experimental methods, and characterization tools used in this dissertation. Detailed descriptions can be found in each chapter.

2.2 Materials

All chemicals and solvents were obtained from commercial suppliers, their detailed information is as follows. Octakis(dimethylsiloxyl)octasilsesquioxane [(HSiOSiO_{1.5})₈, OHS] was supplied by Mayaterials Inc. Tetramethyldisiloxane (HMe₂SiOSiMe₂H, TMDS) was purchased from Gelest Inc. Tetra- and penta- methylcyclotetrasiloxane [(CH₃SiHO)_{4,5}, D₄H/D₅H], phosphorus oxychloride (OPCl₃) and hexamethyldisilazane [HMDS, (Me₃Si)₂NH] were obtained from Alfa Aesar. Diepoxybutane (DEB), diepoxyoctane (DEO), bisphenol A diglycidyl ether (DGEBA) and 3,4-epoxycyclohexylmethyl-3',4'-epoxycyclohexane carboxylate (ECHX) were purchased from Sigma-Aldrich. Hexane and dichloromethane (DCM) were purchased from Fisher Scientific. Sodium amide (NaNH₂), lithium amide (LiNH₂) and 2-Methyl-2,4-pentanediol (hexylene glycol, HG) were obtained from Acros Organics. Hexachlorophosphazene (Cl₆N₃P₃) was purchased from abcr GmbH.

Rice hull ash (RHA) was provided by Wadham Energy LP (Williams, CA); it was milled in dilute hydrochloric acid (HCl) to remove impurities prior to use.^{1,2} HCl and tetrahydrofuran (THF) were purchased from Sigma-Aldrich. THF was distilled over sodium benzophenone ketyl prior to use. All other chemicals were used as received.

2.3 Synthetic methods

2.3.1 Oxysilylation of diepoxides

All oxysilylations were performed with Si-H 1:1 molar equivalent with epoxy group. Detailed experimental conditions are provided in Table 2.1.

Oxysilylation of diepoxides in solvent

To a 25 mL round bottom flask equipped with a magnetic stirrer, diepoxide and Si-H reactant (see Table 2.1) were dissolved in a mixture of DCM and hexane, three different solvent volumes were chosen: 5 mL DCM + 5 mL hexane, 2.5 mL DCM + 2.5 mL hexane, and 1 mL DCM + 1 mL hexane. The solution was stirred at RT for 5 min, then the prepared solution of 1 mg/mL B(C₆F₅)₃ (0.1-3 mg, 0.2-6 μmol) in DCM was added using a syringe. The solution was then kept stirring magnetically for 1 week (w). The final products were dried in a vacuum oven at 60 °C/24 h/vacuum.

Table 2.1. Oxysilylations of diepoxides in solvent catalyzed by B(C₆F₅)₃.

Reaction	Si-H reactant (Si-H = 11.3 mmol)	Diepoxide (epoxy = 11.3 mmol)
Diepoxide + TMDS	TMDS (1 mL, 5.7 mmol)	Diepoxide (5.7 mmol): DEB (0.49 g) DEO (0.80 g) DEGBA (1.92 g) ECHX (1.43 g)
Diepoxide + OHS	OHS (1.4 g, 1.4 mmol)	
Diepoxide + TMDS + 5 mol.% OHS	TMDS (0.95 mL, 5.4 mmol) OHS (0.07 g, 0.07 mmol)	
Diepoxide + TMDS + 10 mol.% OHS	TMDS (0.9 mL, 5.1 mmol) OHS (0.14 g, 0.14 mmol)	
Diepoxide + TMDS + 20 mol.% OHS	TMDS (0.8 mL, 4.6 mmol) OHS (0.29 g, 0.28 mmol)	
Diepoxide + D ₄ H	D ₄ H (0.7 mL, 2.8 mmol)	
Diepoxide + D ₅ H	D ₅ H (0.7 mL, 2.3 mmol)	

Oxysilylation of diepoxides without solvent

In a 25 mL round bottom flask equipped with a magnetic stirrer, the mixture of diepoxide (5.7 mmol, except DGEBA) and TMDS (1 mL, 5.7 mmol) was stirred at RT for 5 min, then prepared solution of 1 mg/mL B(C₆F₅)₃ (0.1-3 mg, 0.2-6 μmol) in DCM was added using a syringe.

For DGEBA, it was first melted in an oil bath at 50 °C in a 25 mL round bottom flask. TMDS was added after removing the oil bath and the mixture was stirred at RT for 5 min, then B(C₆F₅)₃ (0.1-3 mg, 0.2-6 μmol, 1 mg/mL in DCM) was added following the same procedure as described above.

All solventless reaction products were dried in a vacuum oven at 60 °C/24 h/vacuum.

2.3.2 Syntheses of LiPON-like polymer precursors

LiPON-like polymer precursors, Li_xPON, Li_xSiPON (x = 3, 6) and Li₂SiPHN, are synthesized in two steps. The first step is to substitute the -Cl in the phosphorus source (OPCl₃ or Cl₆N₃P₃) with -NH₂ (from NaNH₂) or -NHSiMe₃ [from (Me₃Si)₂NH] producing byproduct NaCl or Me₃SiCl (Table 2.2). It is followed by lithiation from the lithium source LiNH₂.

Table 2.2. P, N source and the stoichiometry of the first step of polymer precursor syntheses.

Polymer precursor (unlithiated)	P source	N source	Byproduct	Stoichiometry
PON	OPCl ₃	NaNH ₂	NaCl	Na/Cl = 1.1
SiPON	OPCl ₃	(Me ₃ Si) ₂ NH	Me ₃ SiCl	Me ₃ Si/Cl = 1.2
SiPHN	Cl ₆ N ₃ P ₃	(Me ₃ Si) ₂ NH	Me ₃ SiCl	NH/Cl = 1.1

Typical synthesis procedures. In a dried 200 mL round bottom Schlenk flask, NaNH₂ (7.0 g, 0.179 mol) or (Me₃Si)₂NH (20.1 mL, 96.6 mmol) was first added to 80 mL of distilled THF, then OPCl₃ (5.0 mL, 53.6 mmol) or Cl₆N₃P₃ (5.2 g, 14.9 mmol) was added. All was done in an ice bath under N₂. The ice bath was removed after 1 d of reaction and the reaction mixture was kept running at RT/N₂/1 w. Centrifugation was followed to separate the soluble and insoluble parts of the reaction mixture. The supernatant was collected into another dried 200 mL round bottom Schlenk flask.

Thereafter, LiNH₂ (see Table 2.3) was added to the supernatant under N₂ in an ice bath. The reaction mixture stayed cloudy due to low solubility of LiNH₂. After 1 d of reaction, the ice bath was removed and changed to an oil bath for heating. The reaction was kept running at 40 °C/N₂

for 1 w. Centrifugation was followed to separate the soluble and insoluble parts in the reaction mixture. The supernatant was collected into another dried 200 mL round bottom Schlenk flask.

To obtain the yield, a small sample (3 mL) was taken from the centrifuged supernatant and vacuum dried at 60 °C on a Schlenk line and the mass of the product was measured. The total volume of the supernatant was measured by a graduated pipette.

Table 2.3 lists the LiNH₂ used in the lithiation, and the properties of final products.

Table 2.3. Lithiation of polymer precursors.

Polymer precursor	LiNH ₂ /-NH ^a	Appearance ^b	Typical yield ^c , %
Li ₃ PON	1	Light-yellow suspension	50-70
Li ₆ PON	2	Light-yellow suspension	50-70
Li ₂ SiPHN	1	Orange solution	80-90
Li ₃ SiPON	1	Yellow solution	≥90
Li ₆ SiPON	2	Orange solution	≥90

^aThe molar ratio of LiNH₂ to the -NH in the unlithiated precursors. ^bThe appearance of the centrifuged precursor supernatants. ^cThe obtained yield divided by the theoretical yield.

2.3.3 Syntheses of Li_xSiON (x = 2, 4, 6) precursors

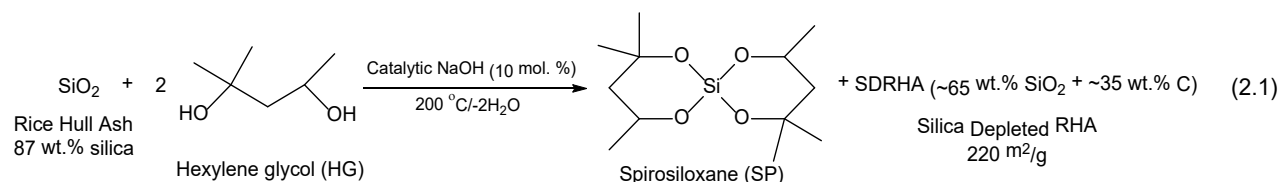
Rice hull ash (RHA) impurity removal

RHA (200 g) was milled mechanically for 48 h in a 2 L bottle with 200 g of milling media (yttria-stabilized zirconia, $\Phi = 3$ mm) and 2 L of HCl solution (3.7 wt.% HCl). Thereafter, the acid milled RHA was recovered by suction filtration through a Buchner funnel. The recovered RHA was then washed with 500 mL deionized water.

Thereafter, the acid milled RHA and 1 L of deionized water were introduced to a 2 L flask equipped with a stir bar and a reflux condenser. The mixture was boiled for 24 h before separation by filtration through a Buchner funnel. The boiling and filtration processes were repeated. After the second filtration, the filtered water was confirmed neutral by pH test. The treated RHA was dried at 60 °C/vacuum/overnight.

Synthesis of spiroxiloxane (SP)

Silica from RHA can react with hexylene glycol (HG) using catalytic base forming SP at 200 °C,^{3,4} which distills directly out of the reaction mixture per equation (2.1).

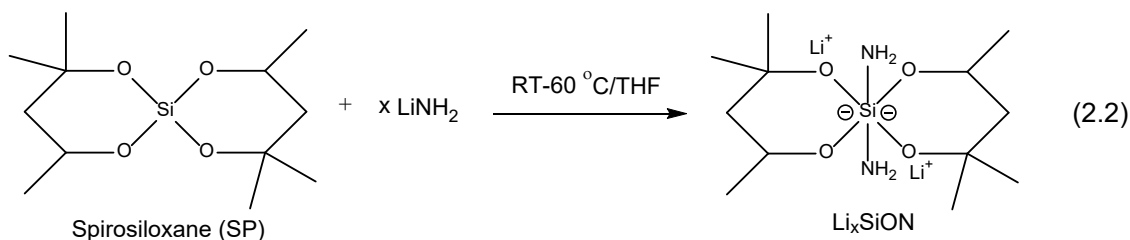


Typical SP synthesis: to a dry 500 mL round-bottom flask were added 300 mL HG (excess amount) and NaOH (3.0 g, 75 mmol). The solution was heated to 200 °C/3 h with stirring to remove water, then dried RHA (~50 g, ~90 wt.% silica content) was added. After 100 mL HG distills off, another 100 mL HG was added until 500 mL HG reacted and/or distilled out as a mixture of SP, H₂O and HG during silica depolymerization.

The distilled mixture of SP, H₂O and HG (500 mL) was then washed with hexane (500 mL) and water (3 × 250 mL) as HG is soluble in water while SP is not. Then the hexane layer (containing SP) was dried over magnesium sulfate and collected. In the final step, the hexane was removed on a rotary evaporator to yield 37 g of the SP product (~70 % yield). The SP product can be further purified by redistillation. The product was dried at 60 °C/12 h/vacuum.

Li_xSiON precursor syntheses

Li_xSiON precursors are synthesized by reacting SP with LiNH₂ (mole ratio of LiNH₂/SP = x), as suggested in equation (2.2). In theory, one SP molecule can be envisioned to offer two coordination sites for LiNH₂ (Li₂SiON).⁵ But as suggested in Chapter 5, excess LiNH₂ can react with SP forming Li₄SiON and Li₆SiON precursors, likely by partial displacement of one or more Si-O bonds, or by interaction of Li⁺ with O from SP forming clusters.



Example of Li₆SiON synthesis: in a 200 mL round bottom Schlenk flask equipped with a reflux condenser, SP (3.9 g, 15.0 mmol) and LiNH₂ (2.2 g, 95.8 mmol) were added to ~80 mL distilled THF under N₂. The reaction was kept running at 60 °C/2 w/N₂. Initially, the reaction was a cloudy white mixture that turns darker over time. After running at 60 °C/2 w, the reaction mixture became a brown solution (Figure 2.1).

To obtain the yield, the reaction mixture was allowed to settle for 1 h, a small sample (5 mL) was taken from the top of the mixture to a 25 mL Schlenk flask, and vacuum dried at 60 °C/1 h. The product was a 0.37 g orange solid indicating a total yield for the solution of ~6 g; slightly lower than the mass sum of the starting materials (6.1 g) suggesting the product is almost fully soluble and stable in THF. Table 2.4 records the LiNH₂ quantities used for different precursors.

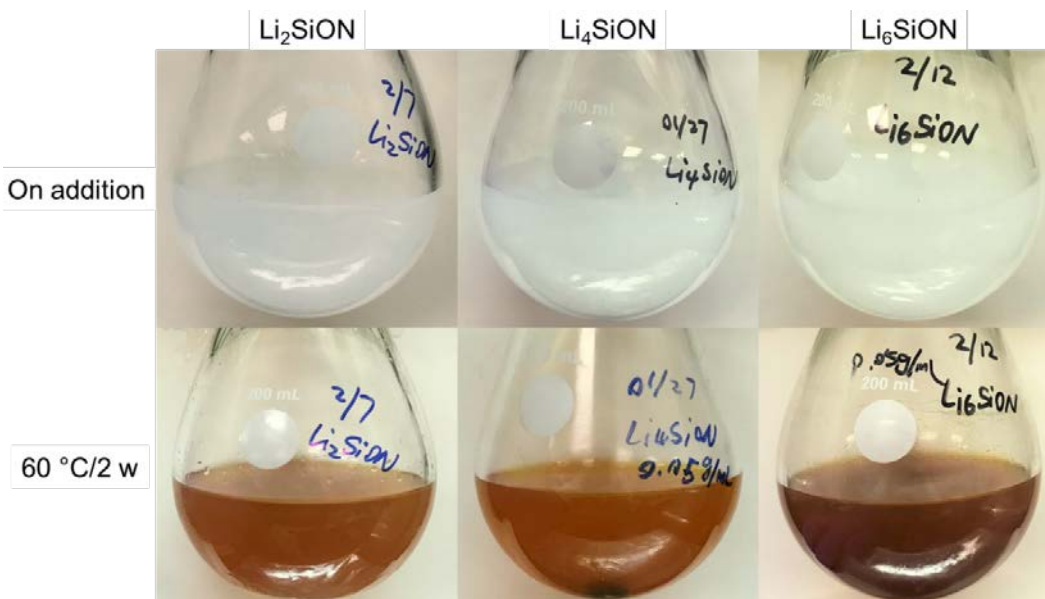


Figure 2.1. Optical images of typical syntheses of Li_xSiON precursors.

Table 2.4. Syntheses of Li_xSiON precursors.

Precursor	$\text{LiNH}_2/\text{SP}^a$	Appearance ^b
Li_2SiON	2.1-2.2	Orange/light-brown solution
Li_4SiON	4.2-4.4	Orange/light-brown solution
Li_6SiON	6.4-6.6	Brown solution

^aTypically, a 5-10 mol.% excess LiNH_2 is added. ^bThe appearances of precursor THF solutions (Figure 2.1).

Dried Li_xSiON products (60 °C/1 h/vacuum) can be hydraulically pelletized at 5 ksi/20 sec with a 13 mm diameter die, Figure 2.2.

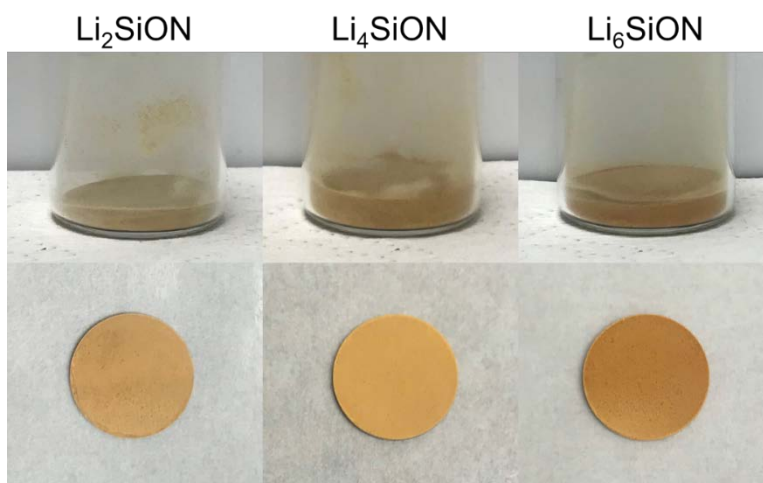


Figure 2.2. Optical images of representative dried Li_xSiON precursor powders (top) and hydraulically pressed pellets (bottom, 5 ksi/20 sec with a 13 mm diameter die).

2.4 Analytical methods

The following procedures were used as a standard set of characterization methods for materials synthesized in this dissertation.

Gel permeation chromatography (GPC) analyses were run on a Waters 440 system equipped with Waters Styragel columns (7.8 × 300, HT 0.5, 2, 3, 4) with RI detection using an Optilab DSP interferometric refractometer and THF as the solvent. The system was calibrated using polystyrene standards. Analyses were performed using Empower 3 Chromatography Data Software (Waters, Corp.).

Fourier-transform infrared spectroscopy (FTIR) was run on a Nicolet 6700 Series FTIR spectrometer (Thermo Fisher Scientific, Inc.). Samples (1 wt.%) were mixed with KBr powder (400 mg, Alfa Aesar); the mixtures were ground rigorously with an alumina mortar pestle, and the dilute samples were packed in a metal sample holder to be analyzed. Prior to data acquisition in the range of 4000-400 cm^{-1} , the sample chamber (rubber sealed) was purged with N_2 for 10-20 min.

Matrix-assisted laser desorption/ionization-time of flight (MALDI-ToF) was done on a Bruker AutoFlex Speed MALDI-TOF, both negative- and positive-ion reflectron modes were used. Trihydroxyanthracene was used as the matrix. Samples were prepared by mixing solutions of the matrix (10 mg/mL in THF) and polymer precursor solution (1 mg/mL in THF), 1:1 volumetric ratio, and blotting the mixture on the target plate (MSP 96 polished steel BC, Bruker). For positive-ion mode, a AgNO_3 solution (1 mg/mL in THF) is added (AgNO_3 :matrix = 1:5 vol.) as the ion source. The calculation of polymer precursor structures based on MALDI was done by a Python program *MALDI-Calculation*, see Appendix B for details and <https://github.com/haveamission/MALDI-Calculation> for the newest version and instructions.

Thermogravimetric analysis (TGA) and differential thermal analysis (DTA) were performed on an SDT Q600 series simultaneous TGA/DTA (TA instrument, Inc.). Samples (10-20 mg) were hand-pressed in a 3-mm dual-action die and placed in alumina pans; the experiments ramped to 800-1000 $^\circ\text{C}$ at 10 $^\circ\text{C}/\text{min}$ under constant N_2 flow (60 mL/min).

Nuclear magnetic resonance spectroscopy (NMR). All NMR spectra were collected from dried samples dissolved in CDCl_3 (0.1 g/mL) and recorded on a Varian vnmrs 500 MHz spectrometer. ^7Li NMR spectra were collected using a spectral width of 39 kHz, a relaxation delay of 0.1 s, 32 k data points, a pulse width of 250. An aqueous solution of LiCl (9.7 M) was used as the reference ($\delta = 0$ ppm). ^1H NMR spectra were collected using a spectral width of 6 kHz, a relaxation delay of

0.5 s, 30 k data points, a pulse width of 38°, and CHCl₃ (7.26 ppm) as the internal reference. ¹³C NMR spectra were collected using a spectral width of 30 kHz, a relaxation delay of 0.1 s, 32 k data points, a pulse width of 250, and CHCl₃ (77.16 ppm) as the internal reference. ²⁹Si NMR spectra were collected using a spectral width of 20 kHz, a relaxation delay of 2.0 s, 16 k data points, a pulse width of 2.5. Tetramethylsilane (TMS, δ = 0 ppm) was used as the reference for ¹H, ¹³C and ²⁹Si NMR spectra.

X-ray diffraction (XRD) was performed on dried precursor powders (60 °C/1 h/vacuum) using a Rigaku MiniFlex 600 XRD and Rigaku Smartlab XRD spectrometers (Rigaku Denki., LTD., Tokyo, Japan). Cu Kα (λ = 1.54 Å) radiation operates at a working voltage of 40 kV and currents of 15 and 44 mA. Scans were continuous from 10 to 80° 2θ using a scan rate of 5° min⁻¹ in 0.01 increments. The presence of crystallographic phases was determined by using Jade 2010 (Version 1.1.5 from Materials Data, Inc.), Rigaku PDXL II (version 2.8.4.0) and Expo2014 (version 1.20.03).

X-ray photoelectron spectroscopy (XPS) experiments were carried out on a Kratos Axis Ultra XPS system at RT below 10⁻⁷ Torr using monochromatic Al source (14 kV and 8 mA). The binding energies of all the elements were calibrated relative to Au 4f_{7/2} at 84 eV. All data were analyzed by CASAXPS software using linear type background.

Scanning electron microscopy (SEM) and energy-dispersive X-ray spectroscopy (EDX). JSM-IT300HR In Touch Scope SEM (JEOL USA, Inc.) was used to analyze the microstructures and elemental compositions of polymer precursor pellets (pelletized hydraulically at 5 ksi/20 sec, Φ = 13 mm).

Electrochemical impedance spectroscopy (EIS). AC impedance data were collected with a broadband dielectric spectrometer (Biologics) in a frequency range of 7 MHz to 1 Hz. “EIS spectrum analyser” software was used for extracting total resistance. Concentric Au/Pd electrodes (3 mm in diameter) were deposited using an SPI sputter coater on both surfaces of polymer precursor pellets using a deposition mask. An equivalent circuit consisting of $(R_{total}Q_{total})(Q_{electrode})$ was used to measure the ionic resistivity. R and Q denote resistance and constant phase element, respectively. The total conductivity (σ_t) was calculated using the equation $\sigma_t = t/(A \times R)$, where t is the thickness of the polymer precursor pellet (0.2-0.3 mm), A is the active area of the polymer precursor, and R is the total resistivity obtained from the Nyquist plots.

References

1. Temeche, E.; Yu, M.; Laine, R. M. Silica Depleted Rice Hull Ash (SDRHA), an Agricultural Waste, as a High-Performance Hybrid Lithium-Ion Capacitor. *Green Chem.* **2020**, *22* (14), 4656–4668.
2. Marchal, J. C.; Krug, D. J.; McDonnell, P.; Sun, K.; Laine, R. M. A Low Cost, Low Energy Route to Solar Grade Silicon from Rice Hull Ash (RHA), a Sustainable Source. *Green Chem.* **2015**, *17* (7), 3931–3940.
3. Laine, R. M.; Furgal, J. C.; Doan, P.; Pan, D.; Popova, V.; Zhang, X. Avoiding Carbothermal Reduction: Distillation of Alkoxysilanes from Biogenic, Green, and Sustainable Sources. *Angew. Chem. - Int. Ed.* **2016**, *55* (3), 1065–1069.
4. Furgal, J. C.; Laine, R. M. Nucleophilic Attack of R-Lithium at Tetrahedral Silicon in Alkoxysilanes. An Alternate Mechanism. *Bull. Chem. Soc. Jpn.* **2016**, *89* (6), 705–725.
5. Hoppe, M. L.; Laine, R. M.; Kampf, J.; Gordon, M. S.; Burggraf, L. W. Ba[Si(OCH₂CH₂O)₃], a Hexaalkoxysilicate Synthesized from SiO₂. *Angew. Chem. Int. Ed. Engl.* **1993**, *32* (2), 287–289.

Chapter 3 An Approach to Epoxy Resins, Oxysilylation of Epoxides

Published: Zhang, X.; Yu, M.; Laine, R. M. *Macromolecules* **2020**, *53* (6), 2249–2263.

3.1 Introduction

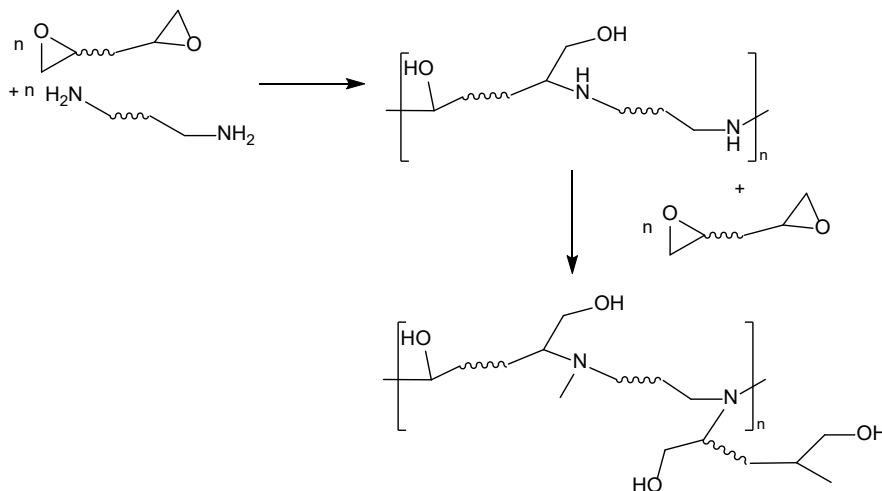
3.1.1 Epoxy resin syntheses

Epoxy resins are ubiquitous in our society finding applications ranging from fiber-reinforced composites for aircraft components, to paints, to dental restoratives, to flip-chip underfill, to bonding glues for household use.^{1–7} The typical epoxy resin is a two-component mixture where one component contains two or more epoxy groups and a hardener that is most often a diamine. In some instances, accelerating catalysts can be added to promote curing at low temperatures. Several mechanistic pathways to curing are typically recognized as suggested in Scheme 3.1.

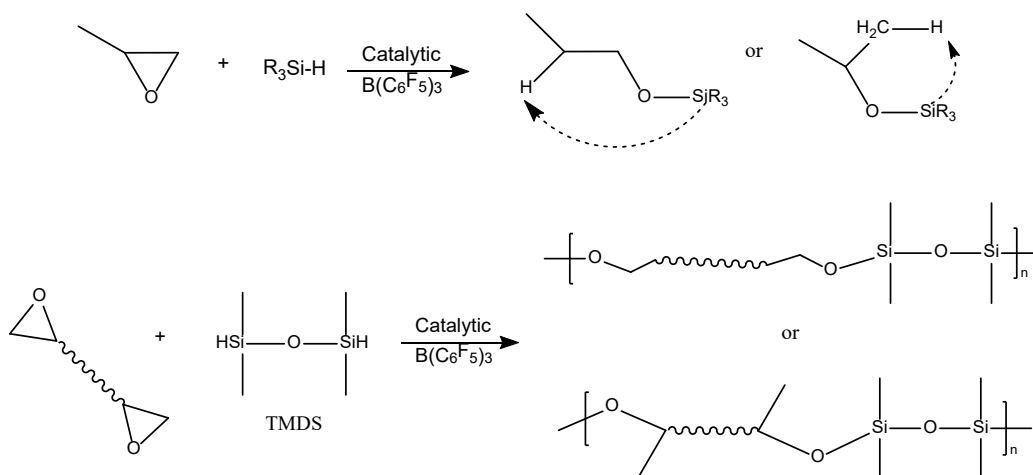
Many properties rely on the chemical structure of the epoxy, the hardener used, and the ratio of one to the other though this is typically 2:1. One of the more troubling issues with epoxy resins is their susceptibility to moisture uptake leading to mass and volume changes coincident with changes in multiple physical properties.^{8–12} One solution is to employ protective coatings; e.g. topcoats for aircraft primer layers.^{13–15} Alternately one should avoid applications that support humid environments. There are books and multiple reviews covering many of these aspects and a review here is not pertinent to the current work.^{1–3,5–7,16}

Here, we present an alternate conceptual approach to what might be termed epoxy resins. Our approach also employs two components and a catalyst. One component is a traditional diepoxide. However, the “hardener” consists of compounds containing two or more Si-H groups, and the

reaction is affected using catalytic amounts of $B(C_6F_5)_3$ [tris(pentafluorophenyl)borane]. The curing reaction adds Si-H across one epoxide C-O bond to form new Si-O and C-H bonds coincident with ring-opening.¹⁷⁻²⁰ We term this reaction oxysilylation, as suggested in Scheme 3.2.

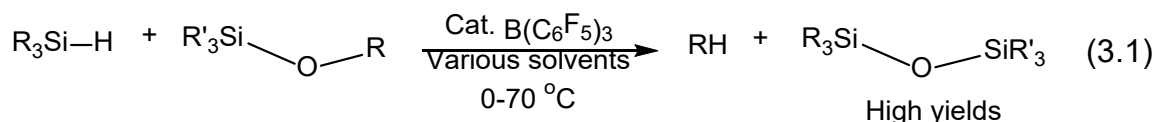


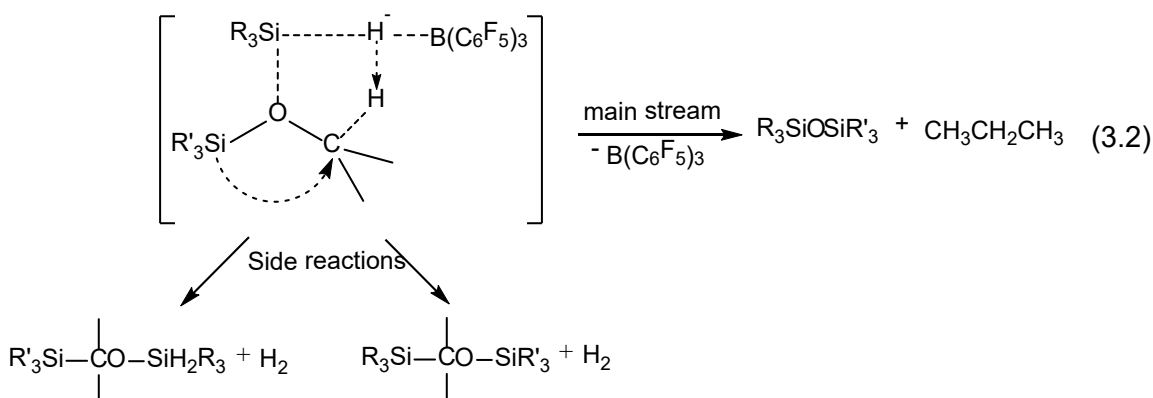
Scheme 3.1. General pathway for amine curing of epoxides with 2:1 N:epoxy ratios.



Scheme 3.2. $B(C_6F_5)_3$ catalyzed oxysilylation of epoxides gives two products.

The basic concept arises from research reported originally from the Piers-Rubinsztajn groups as illustrated in reactions (3.1) and (3.2).²¹⁻²⁶





Crivello *et al.* studied the ring-opening photopolymerization of epoxides from Si-H containing monomers.²⁷⁻³² Such syntheses require a two-step manner where noble metal complex-catalyzed monomers formed prior to photoinitiated cationic polymerization, whereas the proposed approach reacts epoxy and Si-H groups directly. Another advantage is the low concentration required for $\text{B}(\text{C}_6\text{F}_5)_3$ as a catalyst in comparison with polyamines.

Our first efforts in this area were prompted by work of the Brook group.^{18,33-36} The work reported here extends from simple attempts to promote the polymerization of diepoxides using both TMDS ($\text{HMe}_2\text{SiOSiMe}_2\text{H}$, tetramethyldisiloxane) and/or $[\text{HMe}_2\text{SiOSiO}_{1.5}]_8$ (OHS) to form either linear (Scheme 3.2) or highly crosslinked polymers. Initial efforts focused on exploring using solvents to produce processable polymers, but it became evident that the reactions are akin to those for forming epoxy resins and moved to solvent-free curing. As in traditional epoxy resin chemistry, the structures of both components will control eventual properties; however, one advantage to the current systems is that the products are typically hydrophobic and even resist hydrolysis in boiling water for up to 5 h.

The goal of the work reported here is simply to demonstrate the potential utility of oxysilylation of epoxides as a route to new epoxy resins but not to completely detail all the possible properties as this will be a goal for future studies.

3.1.2 Organic-inorganic hybrid materials

Organic-inorganic hybrid materials typically show considerable enhancement in a variety of physical properties such as processability, toughness, thermal and oxidative stability, especially when the component sizes approach nanometer scales.^{37,38} Silsesquioxanes $[(\text{RSiO}_{1.5})_{8,10,12}]$ and the corresponding Q cages $[(\text{RSiMe}_2\text{OSiO}_{1.5})_8]$ can be regarded as molecular level organic-inorganic hybrid materials. Such cages possess a rigid cubic structure where the central inorganic core (Si_8O_{12} , 0.5 nm) is functionalized with appended organic moieties (R or RSiMe_2O , 1-2 nm depending on the structure) at each corner (Figure 3.1). The rigid silica core provides excellent thermal and chemical stability. In addition, these cubic cages offer entrée to a variety of highly symmetrical and star-shaped 3-D structures. Thus, they have received considerable attention as building blocks for constructing many types of hybrid molecules and materials.³⁹⁻⁶²

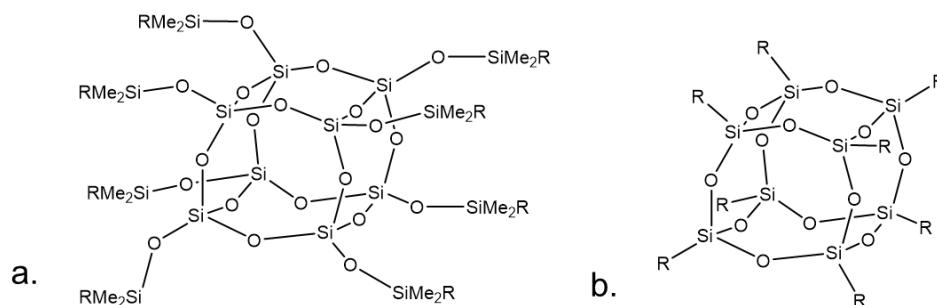


Figure 3.1. Cubic cages. (a) Q_8 ($\text{Q} = \text{SiO}_4$) $\text{R} = \text{H}$, vinyl, epoxy, 3-hydroxypropyl, aminopropyl, glycidylepoxy, ethylcyclohexylepoxy, methacrylate, *etc.* (b) R_8T_8 ($\text{T} = \text{carbon-SiO}_{1.5}$) $\text{R} = \text{alkyl}$, alkene, acetylene, acrylate, $\text{R}'\text{X}$ ($\text{X} = \text{halogen}$, $-\text{CN}$, amine, epoxy, ester, *etc.* $\text{R}' = \text{R}$ same or mixed).³⁷⁻⁴⁰

Epoxy resins have been developed extensively and are now widely used commercially as thermosets with excellent engineering properties including useful thermal, mechanical, and electrical properties. They are used in diverse applications as noted above including as adhesives, coatings, and composite matrices.⁶³⁻⁶⁵ Previous work in our group explored the reactions of epoxy group terminated octakis(glycidyl dimethylsiloxy)octasilsesquioxane $[(\text{glycidylMe}_2\text{SiOSiO}_{1.5})_8]$ (OG)

and octa(dimethylsiloxyethylcyclohexyl epoxide) Q cages linked using an aromatic amine curing agent to form tethers and cross-linked, three-dimensional (3-D) nanocomposites.^{40,65-68} The effects of the tether length, rigidity, and structure on physicochemical properties were assessed to establish structure-processing-property relationships. These studies demonstrated that epoxy resin nanocomposites can be very well-defined in terms of chemical bonding/structural periodicity and can be completely discontinuous at nanometer length scales. The tether structures combined with variations in stoichiometric control of crosslinking chemistries and processing conditions strongly affect thermomechanical properties.⁶⁶⁻⁶⁸

Here, we explore a new approach to 2-D and 3-D nanostructured hybrid epoxy resins using oxysilylation of diepoxides with both the difunctional siloxane TMDS and octafunctional cubic silsesquioxane OHS. In typical oxysilylation, a Si-H bond reacts with an R-O-Si linkage to form siloxane (Si-O-Si) linkages and RH in the presence of catalytic amounts of $B(C_6F_5)_3$. The suggested mechanism is shown as reaction (3.2).^{21,22}

In earlier work,⁶⁹ we reported that oxysilylation of OHS with ethoxysilanes in hexane rapidly (minutes) forms irreversible microporous 3-D networks with surface areas $>700 \text{ m}^2/\text{g}$ and average pore sizes of $\sim 0.6 \text{ nm}$.

In this work, we report a new route to linear polymers via the oxysilylation of diepoxides using TMDS per Scheme 3.2. $B(C_6F_5)_3$ catalyzed oxysilylation opens the epoxy ring to form new Si-O and C-H bonds. As shown in Scheme 3.2, two possible products can form. Thus, our first efforts to create new families of epoxy resins begin with studies of the reaction of TMDS with: 1,3-diepoxbutane (DEB), 1,7-diepoxyoctane (DEO), bisphenol A diglycidyl ether (DGEBA), and 3,4-epoxycyclohexylmethyl-3',4'-epoxycyclohexane carboxylate (ECHX) respectively (Figure 3.2).

Optimization of the reaction conditions for these studies allowed further efforts wherein we sought to generate 3-D ordered networks by reacting OHS with diepoxides per Scheme 3.3.

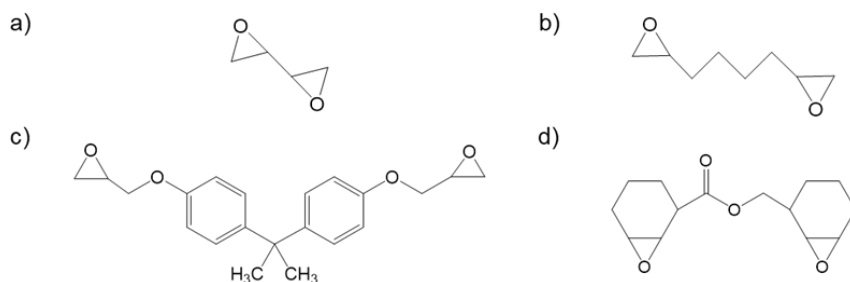
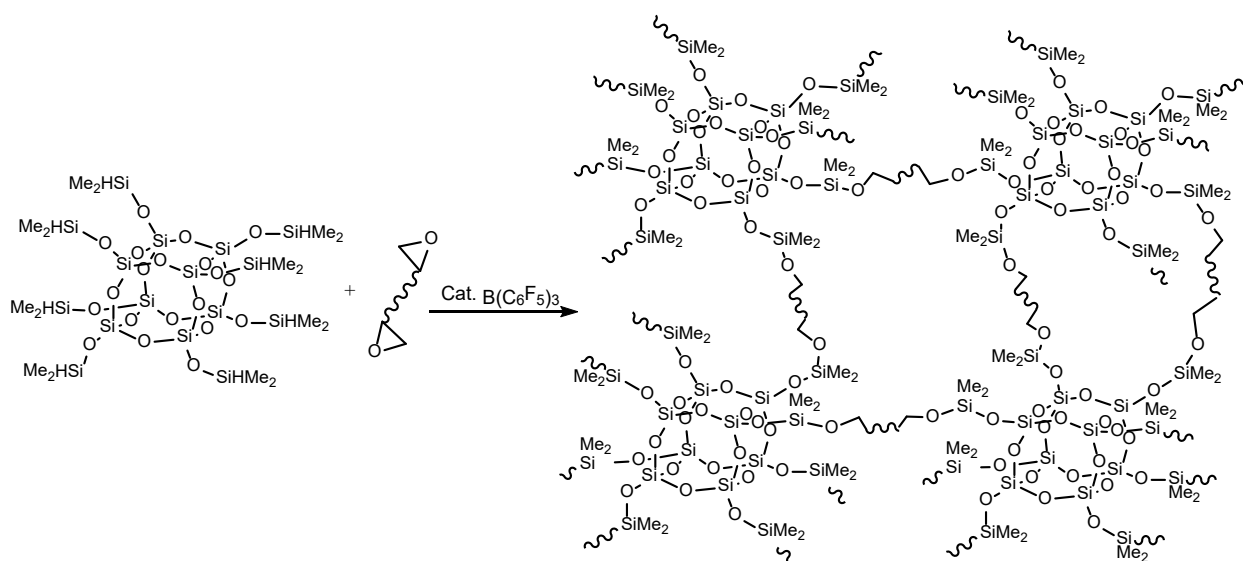
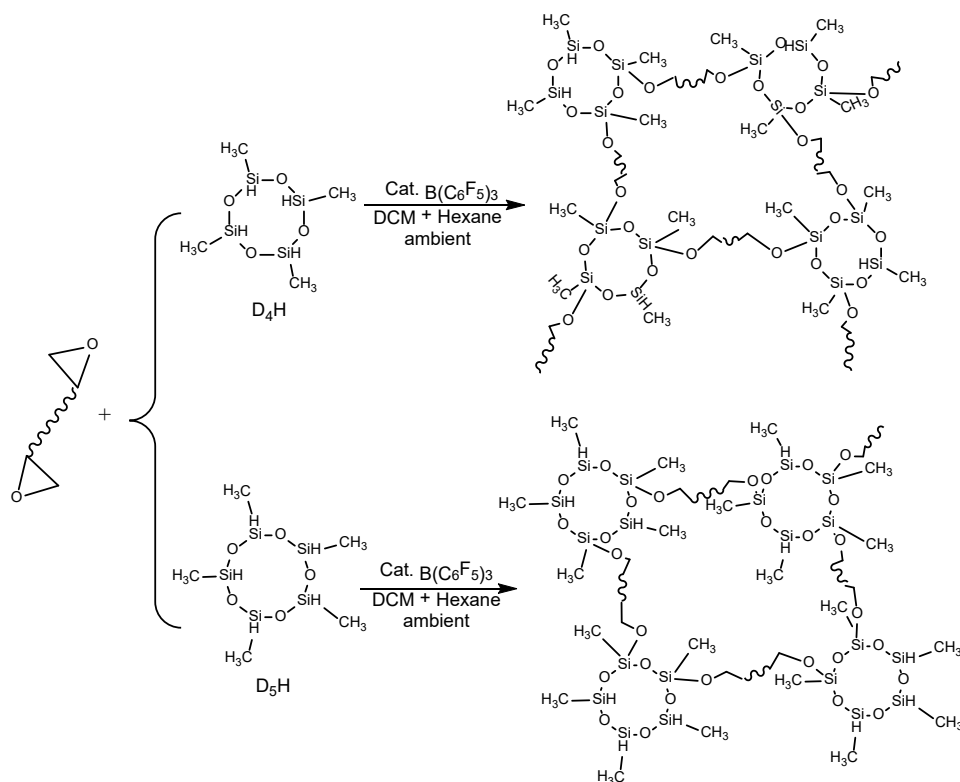


Figure 3.2. Diepoxide structures: (a) 1,3-diepoxybutane (DEB). (b) 1,7-Diepoxyoctane (DEO). (c) Bisphenol A diglycidyl ether (DGEBA). (d) 3,4-epoxycyclohexylmethyl-3',4'-epoxycyclohexane carboxylate (ECHX).



Scheme 3.3. $B(C_6F_5)_3$ catalyzed oxysilylations of diepoxides with OHS.

However, it is found that these reactions typically gel before completion of the reaction, leaving unreacted Si-H function groups in the system. Therefore, alternate studies with D₄H [(CH₃SiHO)₄, tetramethylcyclotetrasiloxane] and D₅H [(CH₃SiHO)₅, pentamethylcyclopentasiloxane] as the Si-H source with the ability to introduce crosslinking were also explored by systematically varying conditions, per Scheme 3.4.



Scheme 3.4. $B(C_6F_5)_3$ catalyzed oxysilylations of diepoxides with D_4H and D_5H .

Our initial goal was to prove that the oxysilylation of epoxy with Si-H groups occurred as anticipated with diepoxides and TMDS to give linear polymer chains per the Scheme 3.2 mechanism. The influences of the amount of solvent and catalyst are also investigated. As shown in Schemes 3.3 and 3.4, oxysilylation also works on reacting different diepoxides with OHS and D_4H/D_5H providing access to polymers with MW's up to ~30 kDa or gel-like materials as found before.⁶⁹

3.2 Experimental section

Solvent impregnation studies. Dried gels (50-200 mg) were placed in clean vials and covered with 20 mL of different solvent for 24 h. The mixture was then gravity filtered, and the gels were patted dry with a Kimwipe[®] and air-dried for 5 min before weighing. Solvent mass retention was

calculated from the difference between wet and dry mass using the following formula:

$$\frac{mass_{wet} - mass_{dry}}{mass_{dry}} \times 100\% = mass\ gain.$$

Water stability studies. Deionized water (20-30 mL) was added into clean 50-mL round-bottom flasks topped with a reflux condenser. They were heated to 100 °C to allow the water to boil. Gels/solids (300-500 mg) were then placed into the boiling water for 5 h. FTIR spectra on gels were obtained before and after the boiling experiment for comparison.

Specific surface area (SSA) and porosity analyses based on Brunauer-Emmett-Teller (BET) were carried out using an ASAP 2020 sorption analyzer (Micromeritics Inc., Norcross, GA). Samples (1-2 g) were ground into fine powders using and degassed at 150 °C/8 h. Each analysis was done at -196 °C (77 K) with N₂. The SSAs were determined by the BET multipoint method using ten data points at relative pressures (p/p_0) of 0.05-0.30. The micropore size distribution was determined by the Horvath-Kawazoe method. Data points were collected with low-pressure incremental dose mode at $0 < p/p_0 \leq 0.1$. Mesopore size distributions were calculated using the BJH method from data points collected at $0 < p/p_0 \leq 0.1$.

Synthetic methods and other characterization procedures are given in Chapter 2.

3.3 Results and Discussion

3.3.1 Oxysilylation of diepoxides with TMDS

In general, oxysilylation of diepoxides with TMDS takes place rapidly and violently. Within seconds to minutes of catalyst addition, bubbling is observed. Oxysilylation of ECHX with TMDS gives a gel immediately after bubbling ceases. In this instance, a mixture of 5 mL dichloromethane (DCM) and 5 mL hexane was used as solvent with a catalytic amount (3 mg, 6 μmol) of B(C₆F₅)₃, which will be relevant in later discussions.

GPC studies (Table 3.1 and Figure 3.3) show that TMDS oxysilylations of DEB and DEO produce polymers with MWs of ~1 and 5 kDa just minutes after addition of the catalyst at RT. Thereafter the polymers remain stable. For 1:1 DGEBA:TMDS, MWs decrease over time, likely due to a second type of oxysilylation reaction that breaks initially formed Si-O-CH₂ bonds forming new Si-O-Si or reacts with C-O bonds in DGEBA forming another Si-O-CH₂. For 1:1 ECHX:TMDS, a polymer with an Mw ≈ 20 kDa forms before gelation.

Table 3.1. GPC data of oxysilylations of diepoxides with TMDS.

Polymer	Reaction time	Mn (kDa)	Mw (kDa)	PDI
1:1 DEB:TMDS	1 min	0.6	1.2	2.1
	1 d	0.7	1.3	2.0
	2 d	0.6	1.3	2.1
1:1 DEO:TMDS	5 min	2.5	5.1	2.0
	1 d	2.4	4.9	2.0
	2 d	2.3	4.6	2.0
1:1 DGEBA:TMDS	1 min	9.4	20	2.1
	1 d	6.8	13	1.9
	2 d	6.2	12	1.9
1:1 ECHX:TMDS	1 min*	12	23	1.9

*GPC MWs obtained before gelation.

The epoxide group steric environment tracks with the found MWs: DEB < DEO < DGEBA < ECHX. Surprisingly, the more encumbered the epoxide group, the higher the MW of the resulting polymer. It is possible that cyclomers form with unencumbered epoxy groups, while with more encumbered epoxies, the polymers are more rigid and hence less likely to cyclize favoring the formation of linear polymers resulting in longer chains with higher MWs. These reactions are similar to condensation polymerization reactions which is in agreement with the found PDIs close to 2.

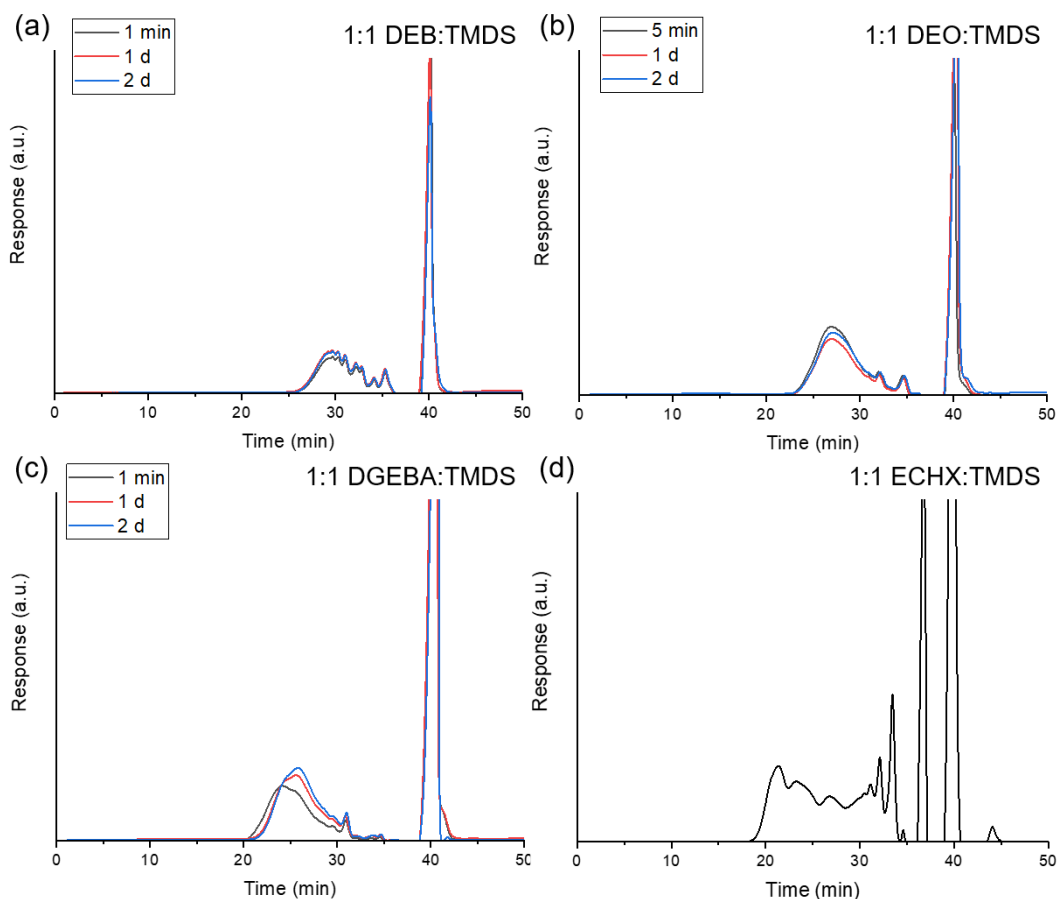


Figure 3.3. GPC of oxysilylations of diepoxides with TMDS. (a) 1:1 DEB:TMDS, (b) 1:1 DEO:TMDS, (c) 1:1 DGEBA:TMDS, (d) 1:1 ECHX:TMDS.

Figure 3.4 shows FTIR spectra of products from oxysilylations of diepoxides with TMDS. A ν Si-H band at 2134 cm^{-1} and a ν Si-O band at 1074 cm^{-1} are seen in TMDS, whereas no ν Si-H band is observed in any of the products, and new ν Si-O bands appear typically at $1050\text{-}1100\text{ cm}^{-1}$. The complete absence of a ν Si-H band and the appearance of new ν Si-O bands suggest that reactions go to completion.

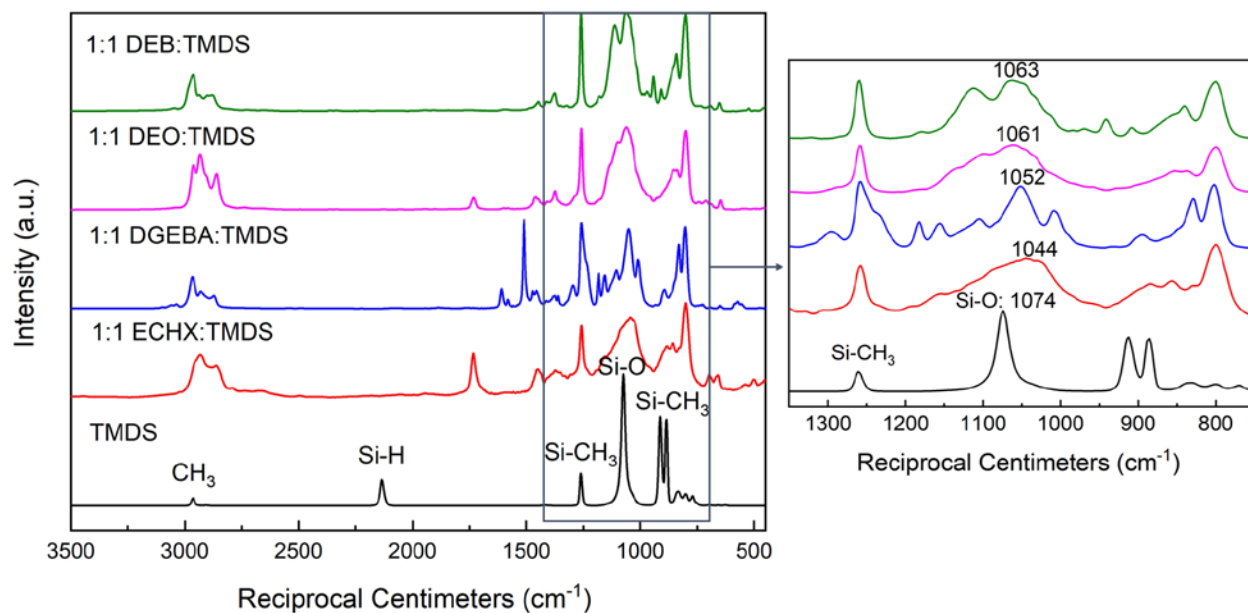


Figure 3.4. FTIRs of oxysilylations of diepoxides with TMDS.

Figures 3.5-3.7 show recorded ^1H NMRs for each reaction and suggested models from ChemDraw, and Table 3.2 details ^1H NMR analyses of oxysilylation of diepoxides (DEB, DEO, and DGEBA) with TMDS. For each reaction, two different structures are possible depending on the epoxy ring-opening mechanism (Scheme 3.2 and Figures 3.5-3.7), the main difference is whether there is a resulting $-\text{CH}_2$ or $-\text{CH}_3$ group formed. Integration shows that the number of protons for $-\text{CH}_2$ and $-\text{CH}_3$ is between the two suggested models (Figures 3.5-3.7), but all the results show that protons from $-\text{CH}_3$ are more than those from $-\text{CH}_2$ with a typical ratio of 4:1, suggesting the dominate ring-opening mechanism follows the second structure per Scheme 3.2.

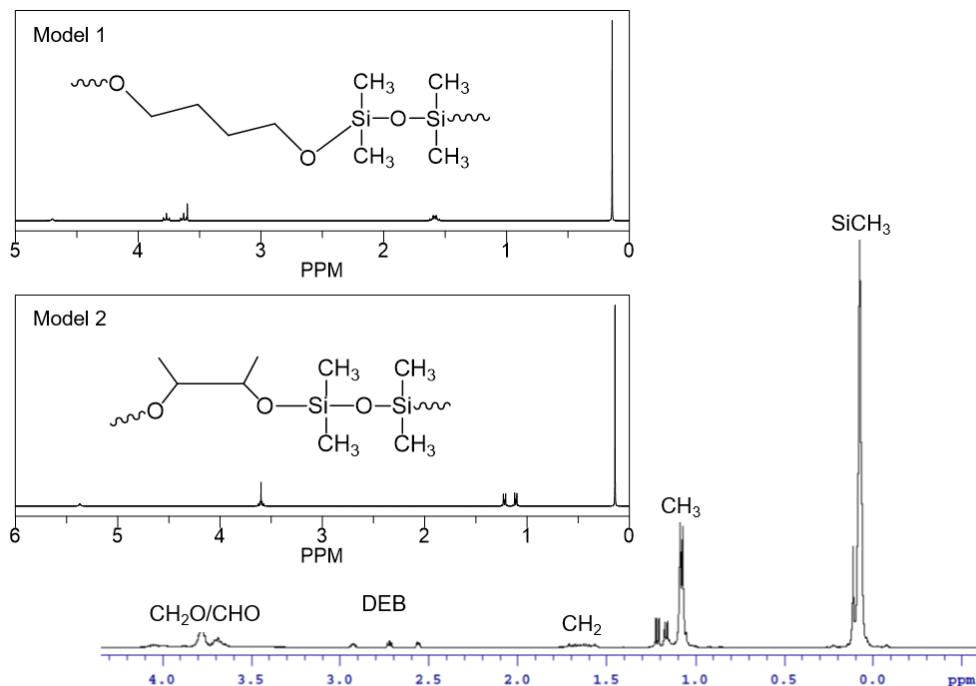


Figure 3.5. ^1H NMR models (top) and record (bottom) of 1:1 DEB:TMS.

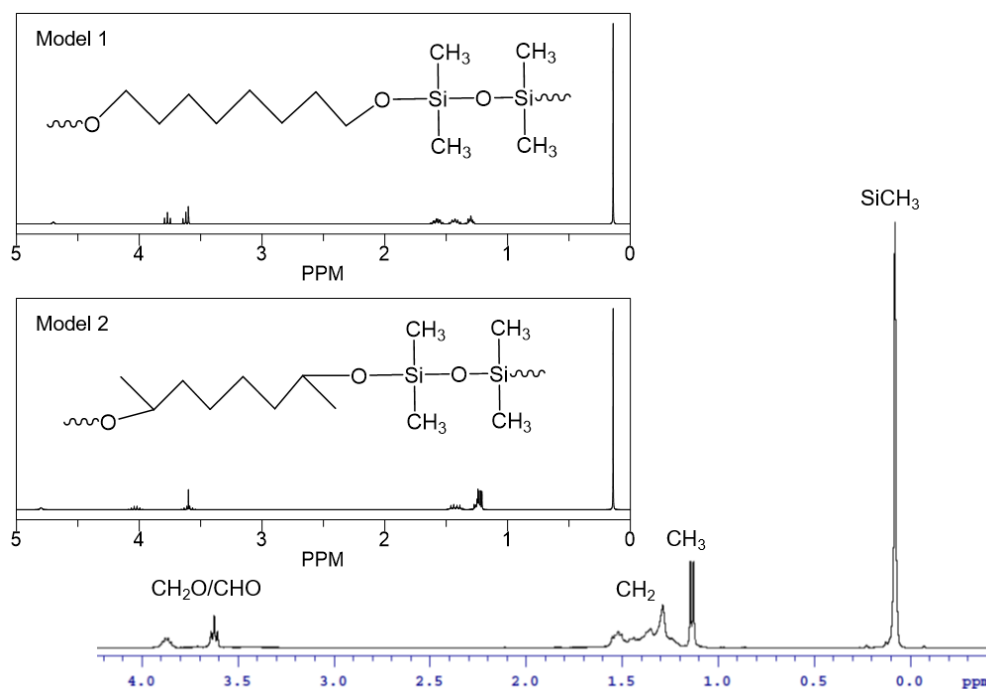


Figure 3.6. ^1H NMR models (top) and record (bottom) of 1:1 DEO:TMS.

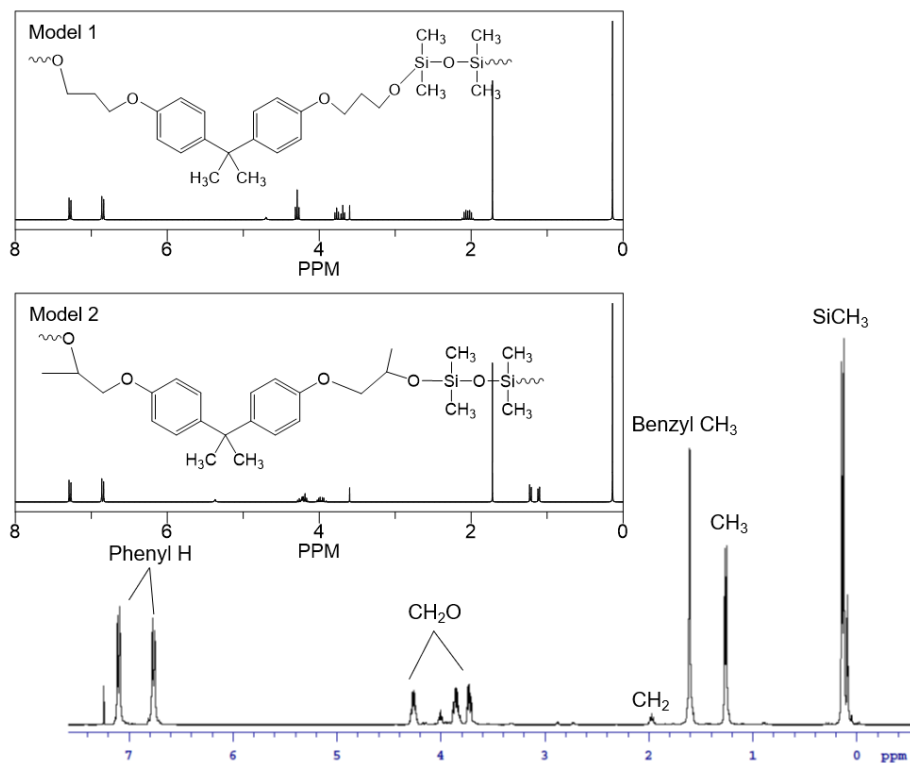


Figure 3.7. ^1H NMR models (top) and record (bottom) of 1:1 DGEBA:TMDS.

Table 3.2. ^1H NMR data for diepoxy oxysilylations with TMDS.

Diepoxy	Model 1			Model 2			Found			
	Proton type	δ	No. of H^+	Proton type	δ	No. of H^+	Proton type	δ	Int.	*No. of H^+
DEB	Si- CH_3	0.1	12	Si- CH_3	0.1	12	Si- CH_3	0.1	57.6	12
	CH_3	-	-	CH_3	1.2	6	CH_3	1.1	25.1	5.2
	CH_2	1.6	4	CH_2	-	-	CH_2	1.6	2.7	0.6
	CH_2O	3.8	4	CHO	3.6	2	$\text{CHO}/\text{CH}_2\text{O}$	3.8	11.4	2.4
DEO	Si- CH_3	0.1	12	Si- CH_3	0.1	12	Si- CH_3	0.1	41.1	12
	CH_3	-	-	CH_3	1.2	6	CH_3	1.1	12.1	3.5
	CH_2	1.3-1.6	12	CH_2	1.2-1.4	8	CH_2	1.3-1.5	36.2	10.6
	CH_2O	3.8	4	CHO	3.6	2	$\text{CHO}/\text{CH}_2\text{O}$	3.8	10.0	2.9
DGEBA	Si- CH_3	0.1	12	Si- CH_3	0.1	12	Si- CH_3	0.1	30.9	12
	Benzyl CH_3	1.7	6	Benzyl CH_3	1.7	6	Benzyl CH_3	1.6	16.4	6.4
	CH_3	-	-	CH_3	1.2	6	CH_3	1.3	13.1	5.1
	CH_2	2.1	4	CH_2	-	-	CH_2	2.0	1.1	0.4
	CH_2O	3.8, 4.3	8	$\text{CHO}/\text{CH}_2\text{O}$	4.0-4.3	6	$\text{CHO}/\text{CH}_2\text{O}$	3.7-4.3	16.4	6.4
	Ph-H	6.9, 7.3	8	Ph-H	6.9, 7.3	8	Ph-H	6.8, 7.1	20.8	8.1

*Number of protons using Si- CH_3 as reference.

When the solvent volume is halved from 5 mL DCM + 5 mL hexane (listed as 5 mL for convenience) to 2.5 mL DCM + 2.5 mL hexane (listed as 2.5 mL) provided everything else remains the same, MWs and reaction rate increase as might be expected, Table 3.3.

If reduced solvent volumes increase MWs, it is reasonable to assume that solventless reactions will lead to even higher MWs. This then would be the equivalent of epoxy resins. Therefore, solventless reactions were carried out using 1:1 DEB:TMDS, 1:1 DEO:TMDS, and 1:1 ECHX:TMDS systems provided all the reactants involved are liquid at RT. Because all the reactions with solvent were violent with heating and bubbling, the amount of catalyst was reduced from 3 to 1 mg. However, smoke was generated from all the reactions and gels formed immediately after addition of the catalyst. This implies that these systems could be used as epoxy resin analogs if catalyst activity was reduced. This suggests efforts should be directed to develop less active catalysts to aid in better designing epoxy resin analogue systems.

Table 3.3. GPC data for diepoxide oxysilylations with TMDS vs. solvent volumes after 1 d.

Epoxy	Solvent volume (mL)	Mn (kDa)	Mw (kDa)	PDI	Reaction time
DEB	5	0.7	1.3	2.0	< 20 s
	2.5	1.7	3.5	2.1	< 10 s
DEO	5	2.4	4.9	2.0	3-5 min
	2.5	2.7	5.7	2.1	2-3 min
DGEBA	5	6.8	13	1.9	10-30 s
	2.5*	15	30	2.0	< 10 s
ECHX	5*	12	23	1.9	3-5 min
	2.5*	-	-	-	1-2 min

*These reactions fully or partially gel, GPC MWs obtained before gelation or for soluble portion.

Thus, the amount of catalyst was further reduced to 0.25 mg eliminating the violent phenomenon as reaction rates were reduced significantly, 1:1 DEB:TMDS and 1:1 DEO:TMDS gelled overnight, and 1:1 ECHX:TMDS gelled in ~1 h. Images of the products of solventless oxysilylations are shown in Figure 3.8.

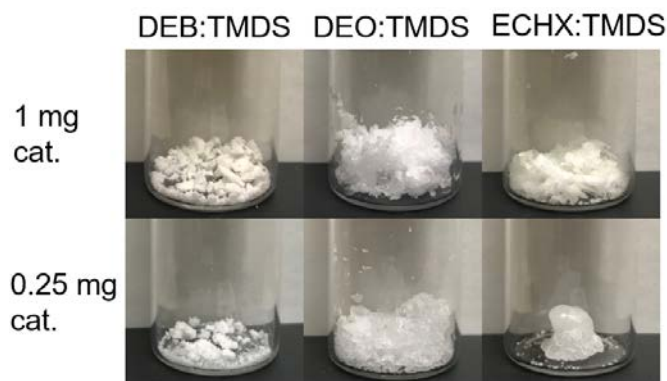


Figure 3.8. Optical images of solventless oxysilylation products.

DGEBA, on the other hand, is a solid at RT (melting point $T_m = 40\text{ }^\circ\text{C}$). If it were to be reacted in a solventless reaction at RT, only the surface will participate resulting in incomplete reaction. Therefore, 1:1 DGEBA:TMDS solventless reactions were warmed to $50\text{ }^\circ\text{C}$. Based on the violent reaction phenomena observed in other oxysilylation systems, a reduced amount of catalyst (0.25 mg) was used but smoke was still generated on the addition of $\text{B}(\text{C}_6\text{F}_5)_3$ resulting in a gel. Thereafter, the catalyst amount was reduced to 0.1 mg; however, smoke was generated again. The increased temperature is the problem here despite low amounts of catalyst used. Again, one solution would be to find a less active catalyst as noted just above.

The halved solvent and solventless reactions reveal influences of solvent volume and catalyst concentration on reaction rates and product MWs. To further investigate their relationships, oxysilylations with varying amounts of catalyst and solvent were carried out, the MWs of the resulting products are summarized in Table 3.4. Overall, MWs increase with decreasing solvent volumes and increasing catalyst amounts. With 1 mL DCM + 1 mL hexane (listed as 1 mL), most of the oxysilylations gels due to resulting high MWs and insufficient solvent volumes. Additionally, the MWs of products track with the MWs of the diepoxides, that is more encumbered epoxides give higher MWs polymer, in good agreement of the Table 3.1 results.

More interestingly for 1:1 ECHX:TMDS, when the catalyst amount is reduced to 0.1 mg, the products in different solvent volumes stay in solution; with 0.5 mg of catalyst, precipitates form over time for reactions in 1 and 2.5 mL of solvent; when the catalyst is ≥ 1.0 mg, gels form. This unique observation, especially the formation of precipitates, suggests a structural difference between epoxy resins via oxysilylation with ECHX compared to the other systems, see below.

Table 3.4. Molecular weights of oxysilylations of diepoxides with TMDS, with different amounts of catalyst and solvent.

Epoxy	Cat. (mg) ^a	Solvent volume		
		1 mL	2.5 mL	5 mL
DEB	0.25	1.0 kDa	0.6 kDa	0.5 kDa
	0.5	(Gel)	0.6 kDa	0.7 kDa
	1.0	(Gel)	10 kDa	1.7 kDa
DEO	0.1	1.0 kDa	0.9 kDa	1.0 kDa
	0.5	(Gel)	3.4 kDa	1.8 kDa
	0.75	(Gel)	20 kDa	9.0 kDa
DGEBA	0.05	(Gel)	3.2 kDa	0.8 kDa
	0.1	(Gel)	(Gel)	18 kDa
	0.5	(Gel)	(Gel)	20 kDa
ECHX	0.25	6.0 kDa	3.0 kDa	2.0 kDa
	0.5	(PPT) ^b	(PPT)	30 kDa
	1.0	(Gel)	(Gel)	31 kDa

^aCat. = catalyst. ^bPPT = precipitate.

Nevertheless, most oxysilylations listed in Table 3.4 are quite exothermic. More specifically, all oxysilylations of 1:1 DEB:TMDS, 1:1 DEO:TMDS with ≥ 0.5 mg catalyst, and 1:1 DGEBA:TMDS with ≥ 0.1 mg catalyst cause solvent to boil within 10 min, again speaking to the need for a different less reactive catalyst.

Representative FTIRs of the oxysilylations of diepoxides with TMDS with 0.5 mg of catalyst in 2.5 mL DCM + 2.5 mL hexane are shown in Figure 3.9. All spectra reveal residual ν Si-H at ~ 2100 cm^{-1} indicative of incomplete reactions, as also seen in Table 3.4, but differing from Figure 3.4, where no ν Si-H is observed with 3 mg of catalyst. Note that all FTIR studies shown in this

work are run 3-5 d after reaction and constant MWs were observed by GPC. Clearly the extent of reaction relies on catalyst concentration but at the expense of a highly exothermic process.

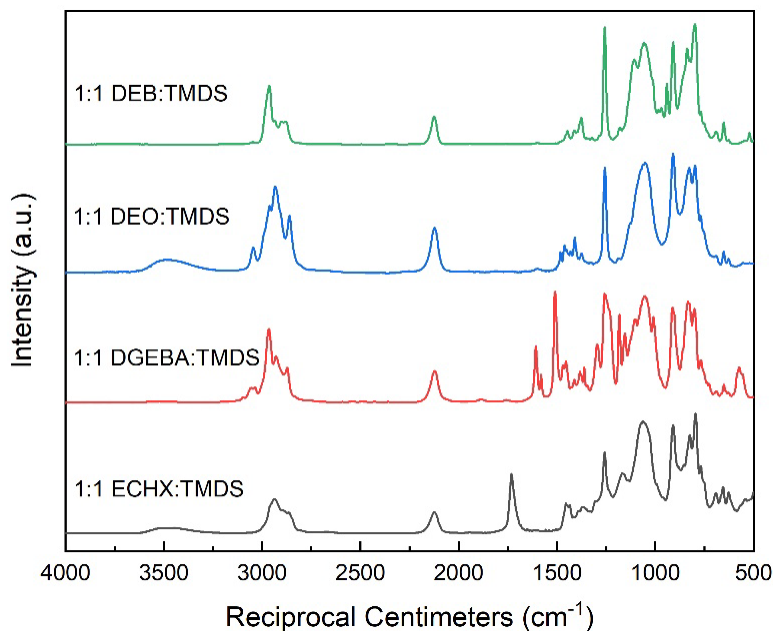


Figure 3.9. FTIRs of diepoxide oxysilylation with TMDS, 0.5 mg $B(C_6F_5)_3$, in 2.5 mL DCM + 2.5 mL hexane.

Water stability studies were conducted on gels/solids formed in 1 mL solvent per Table 3.4. All gels/solids remain stable after boiling in water for 5 h, no obvious decomposition or degradation observed. Figure 3.10 shows representative FTIRs of solids before and after boiling in water for 5 h.

A decreased intensity of ν Si-H ($\sim 2100\text{ cm}^{-1}$) is shown after boiling. It's likely that any unreacted TMDS was distilled off in boiling water. Otherwise, all IRs show very little difference in FTIR before and after. A small ν O-H band at $\approx 3400\text{ cm}^{-1}$ is observed for 1:1 DEO:TMDS and 1:1 ECHX:TMDS, which suggests some water uptake as well as hydrolysis forming Si-OH groups. Overall, reasonably good water stability is surprising as Si-O bonds are normally water sensitive.⁷⁰⁻⁷³

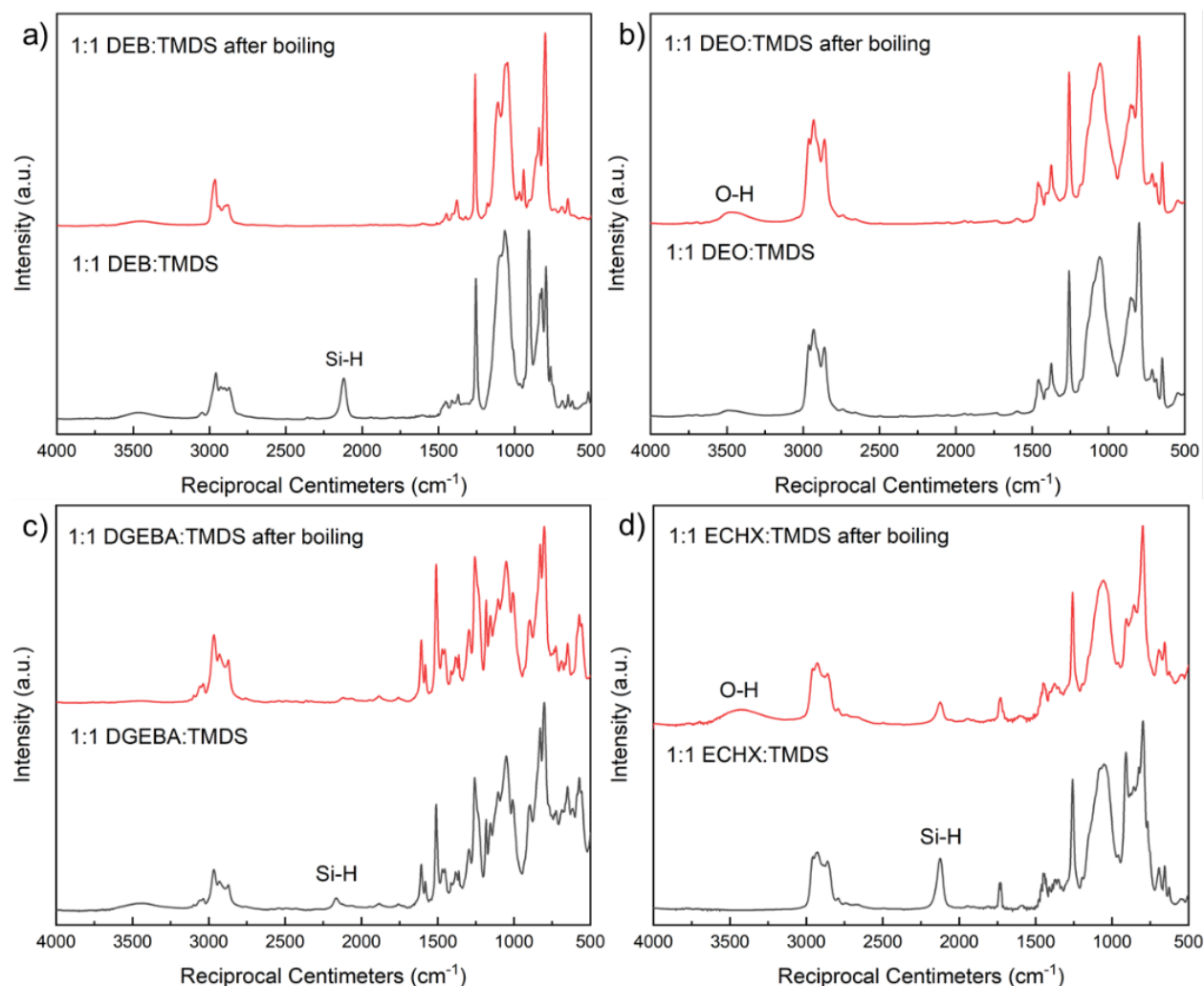


Figure 3.10. FTIRs of (a) 1:1 DEB:TMDS, (b) 1:1 DEO:TMDS, (c) 1:1 DGEBA:TMDS, (d) 1:1 ECHX:TMDS before and after boiling in water for 5 h.

3.3.2 Oxysilylation reaction of diepoxides with OHS

In principle, this reaction should generate 3-D ordered structures, gels. All the reactions do result in gels/solids with the exception of 1:1 DEB:OHS. Optical images of as-formed and dried gels/solids are shown in Figures 3.11 and 3.12 respectively. All reactions in this section were catalyzed by 3 mg of $\text{B}(\text{C}_6\text{F}_5)_3$.

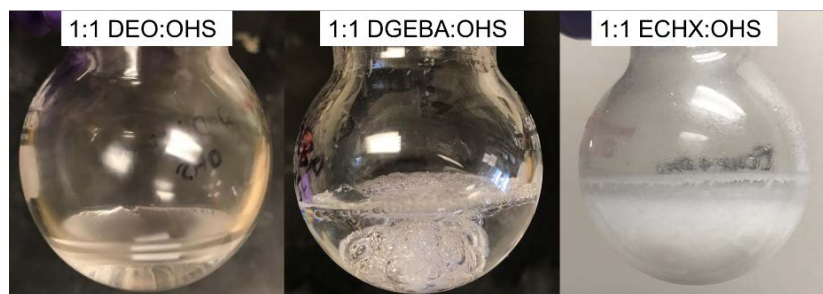


Figure 3.11. Optical images of as-formed 1:1 DEO:OHS and 1:1 DGEBA:OHS gels, and 1:1 ECHX:OHS solid (precipitate).

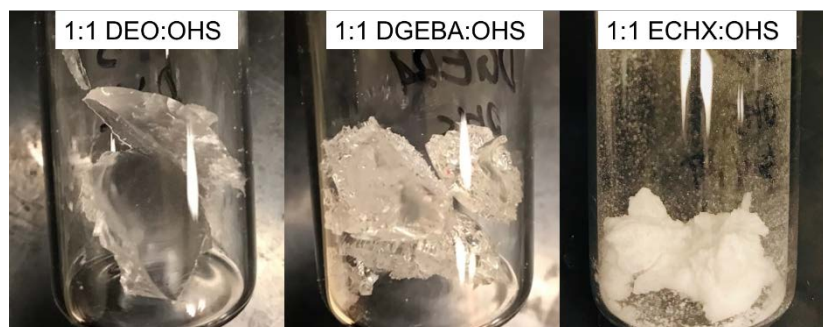


Figure 3.12. Optical images of dried (100 °C/vacuum/24 h) 1:1 DEO:OHS and 1:1 DGEBA:OHS gels, and 1:1 ECHX:OHS solid.

For the 1:1 DEO:OHS system, gels form only after 10-12 d of reaction, the slow gelation rate makes it possible to cast films, Figure 3.13. The cast 1:1 DEO:OHS films are transparent, flexible, and hydrolytically stable, which makes it a potential candidate for thin film processing applications. As discussed in Appendix C, in an attempt to cast polymer electrolyte films using 1:1 DEO:OHS incorporated with LiClO_4 , a translucent, flat, and brittle 1:1 DEO:OHS + LiClO_4 film formed. However, the film failed to show ionic conductivity owing to its highly crosslinked rigid structure that inhibits Li^+ mobility.

In contrast, 1:1 DGEBA:OHS gives rigid gels exothermically in 20-30 min preventing film processing. The 1:1 ECHX:OHS system forms solids/precipitates in 1-2 d, similar to precipitates that form in some of the 1:1 ECHX:TMDS oxysilylations.

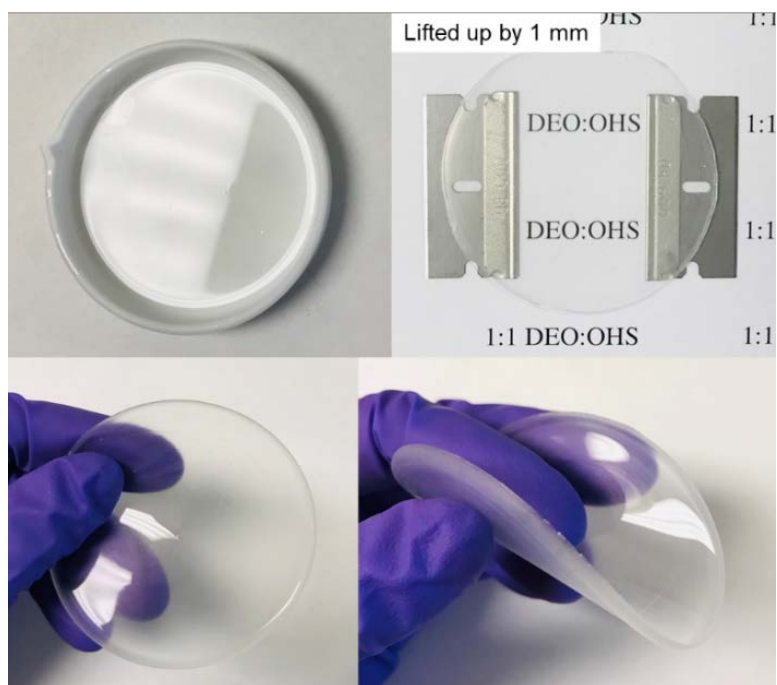


Figure 3.13. Optical images of a cast 1:1 DEO:OHS film on a PTFE substrate, 5 d of reaction in 5 mL DCM + 5 mL hexane.

DEB is the simplest diepoxide and never forms a polymer with high enough MW to gel, it is possible that cyclomers form as the main product. One can envision using it as a comonomer for reactions to control various properties.

Table A.1 and Figure 3.14a show GPC traces for oxysilylation of DEB with OHS. No significant changes occur over time in the product MW and PDI. The reaction exotherms (boils) 10-30 min after addition of $B(C_6F_5)_3$, this process lasts ≈ 1 min. GPC data suggest that further reaction stops following heat generation.

Figure 3.14b shows the FTIR of oxysilylation of DEB with OHS vs. OHS. Residual $\nu Si-H$ is seen indicating that the reaction stops before completion. A new $\nu Si-O$ band appears at 1110 cm^{-1} with retention of the original cage $\nu Si-O$ band at 1100 cm^{-1} .

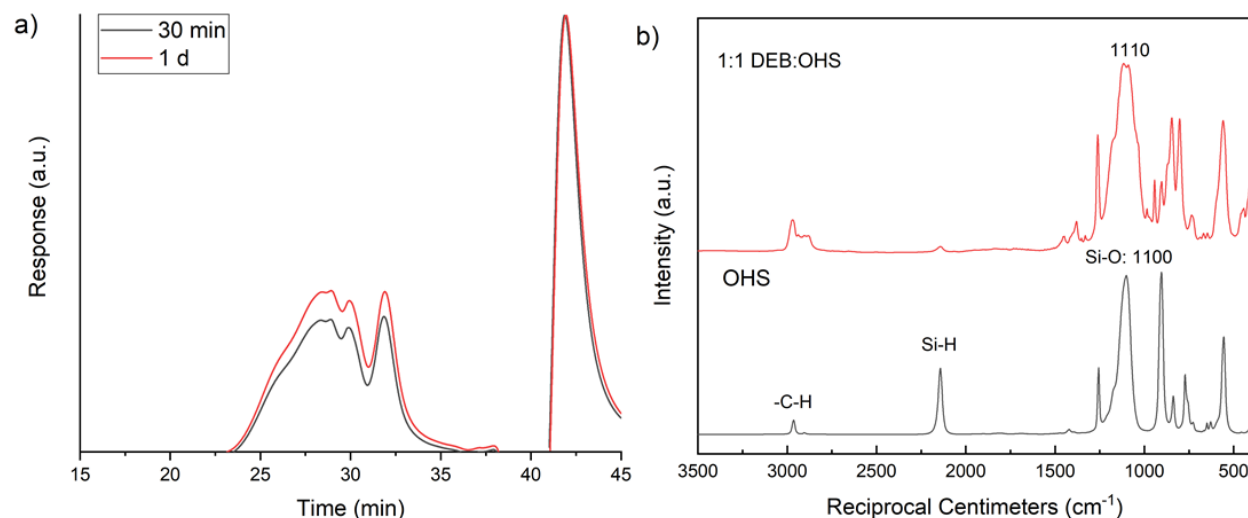


Figure 3.14. GPC (a) and FTIR (b) of oxysilylation of DEB with OHS.

Water stability, TGA-DTA, and solvent impregnation studies were conducted on the gels/solids formed from diepoxide oxysilylation with OHS. All diepoxide:OHS gels/solids remain stable after boiling in water for 5 h; no decomposition or degradation is observed. Figure 3.15 compares the FTIR of each gel before and after boiling in water for 5 h. All show very little difference in FTIR before and after, only 1:1 DEO:OHS shows a very small ν O-H band at $\approx 3400\text{ cm}^{-1}$ suggesting some water uptake and/or hydrolysis forming Si-OH groups. Overall, diepoxide:OHS gels/solids exhibit good water stability.

The presence of ν Si-H in all of the gels indicates the reaction is incomplete. The high viscosity of the resulting gels prevents completion. This may allow future modification to introduce new functionality.

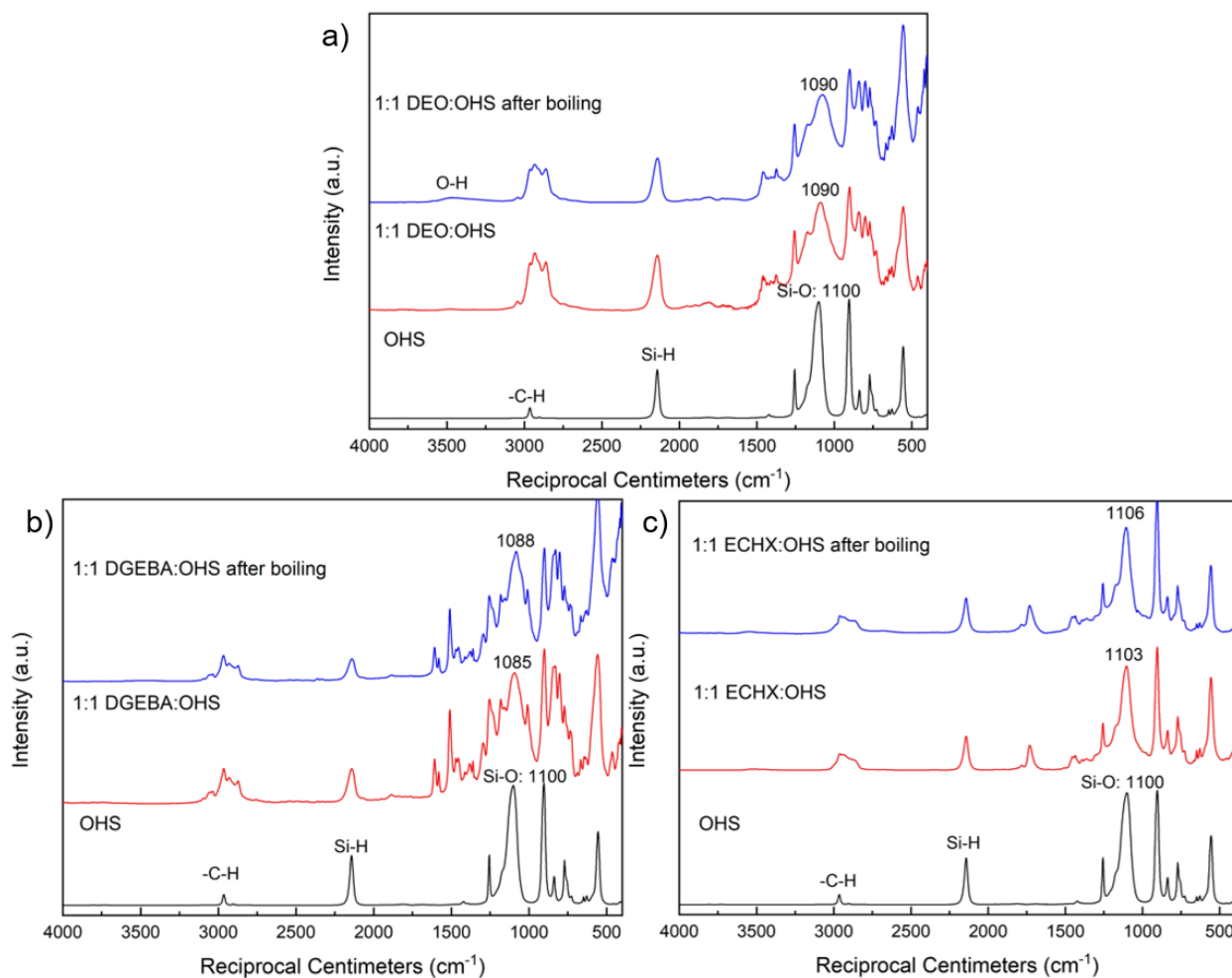


Figure 3.15. FTIRs of (a) 1:1 DEO:OHS, (b) 1:1 DGEBA:OHS, (c) 1:1 ECHX:OHS before and after boiling in water for 5 h in comparison to OHS.

TGA (1000 °C/air) and the estimated structures for the dried oxysilylation products are shown in Figures 3.16-3.19. Table 3.5 summarizes ceramic yields (CY) and decomposition temperatures (T_d), showing reasonable agreement with theory, where the theoretical CYs were calculated from the estimated structures. All the gels decompose ~ 200 °C associated with an exotherm likely oxidation of residual Si-H groups. The 1:1 DGEBA:OHS system offers higher decomposition temperatures ($T_d \approx 300$ °C) likely because of the phenyl component.

The 1:1 ECHX:OHS system shows two main mass losses: 200-270 °C, and 400-440 °C. The first mass loss may be associated with oxidation of residual Si-H groups. The second mass loss is

similar to other systems involves oxidation of carbon species ($\geq 350\text{ }^{\circ}\text{C}$). The slow mass loss from 440° to $600\text{ }^{\circ}\text{C}$ is typical for hybrid materials that decompose with partitioning of the products into gaseous fragments and char, the char then slowly oxidizes at higher temperatures in air. Unlike the other resins, the CY of 1:1 ECHX:OHS is $\sim 10\%$ lower than calculated, likely due to the steric environment of epoxide groups in ECHX that impedes oxysilylation with Si-H groups, leaving a large amount of unreacted Si-H groups or OHS, which can sublime, resulting in lower CY.

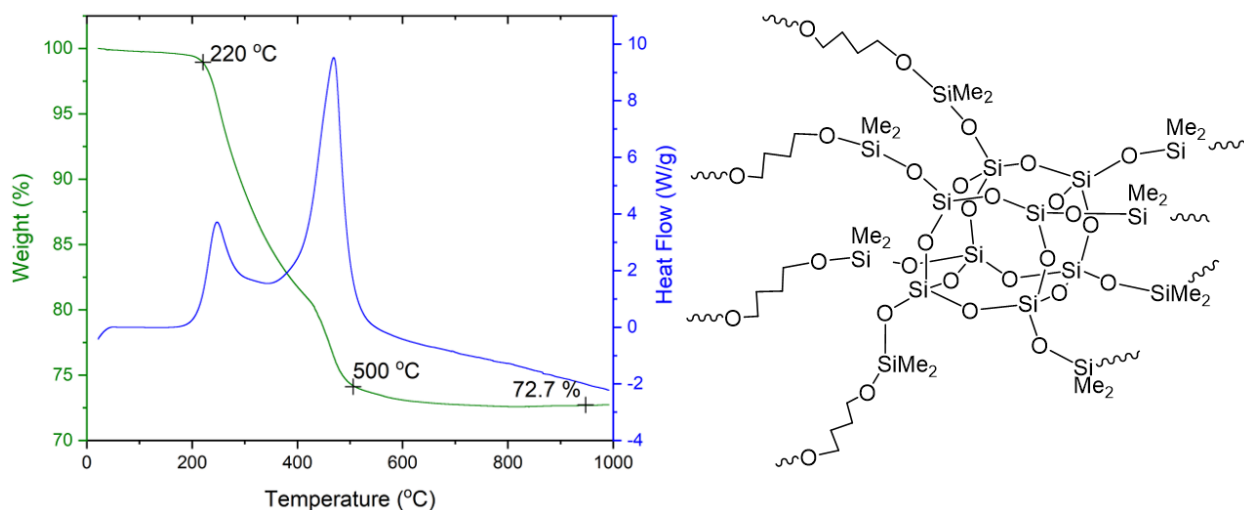


Figure 3.16. TGA/DTA/air/ $10^{\circ}\text{C}/\text{min}$ of 1:1 DEB:OHS after drying (left) and estimated structure of repeating unit of 1:1 DEB:OHS (right).

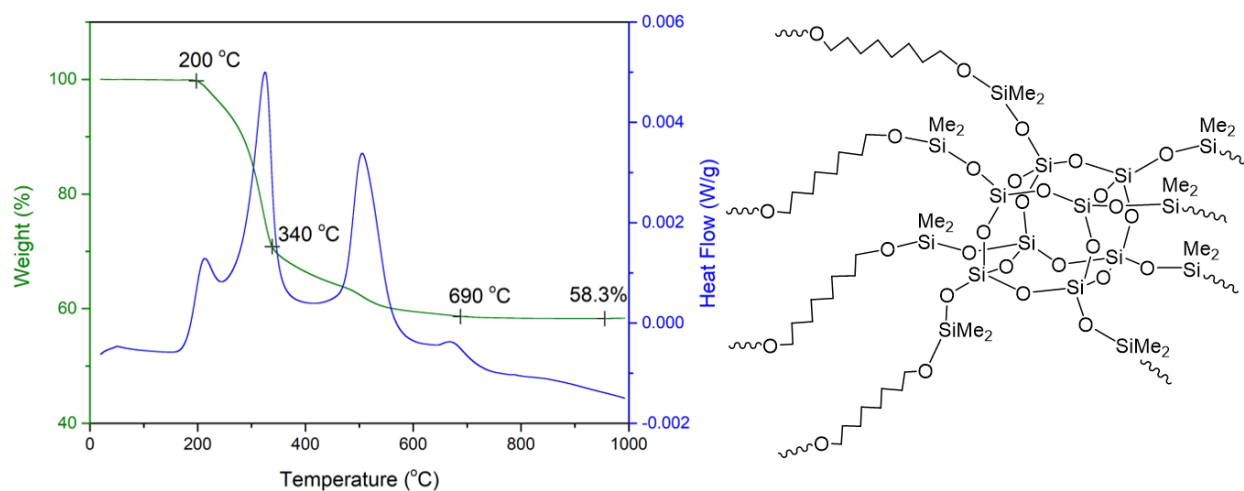


Figure 3.17. TGA/DTA/air/ $10^{\circ}\text{C}/\text{min}$ of 1:1 DEO:OHS after drying (left) and estimated structure of repeating unit of 1:1 DEO:OHS (right).

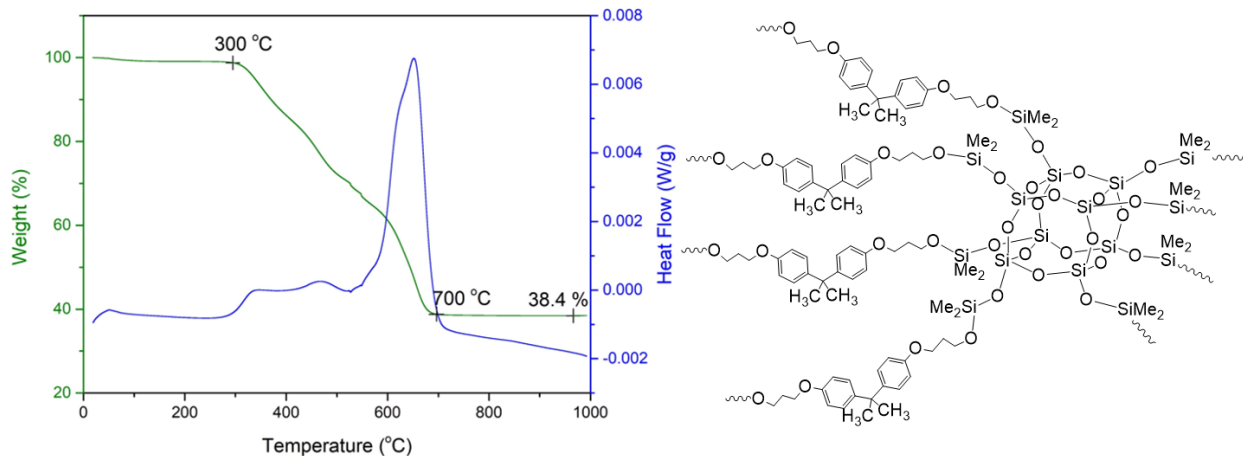


Figure 3.18. TGA/DTA/air/10°C/min of 1:1 DGEBA:OHS after drying (left) and estimated structure of repeating unit of 1:1 DGEBA:OHS (right).

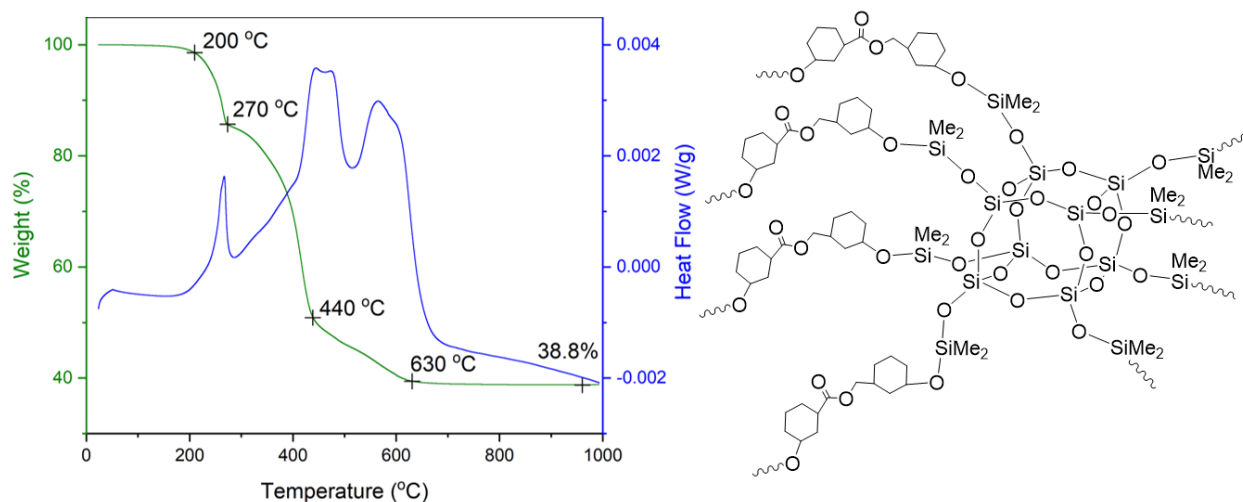


Figure 3.19. TGA/DTA/air/10°C/min of 1:1 ECHX:OHS after drying (left) and estimated structure of repeating unit of 1:1 ECHX:OHS (right).

Table 3.5. Selected TGA-DTA of oxysilylation of diepoxides with OHS.

Epoxy resin	CY (wt %, found)	CY (wt %, theory)	T _d (°C)
1:1 DEB:OHS	73	71	220
1:1 DEO:OHS	58	61	200
1:1 DGEBA:OHS	38	40	300
1:1 ECHX:OHS	39	47	200, 270

Gels produced with OHS can be considered to be modified silica with octahedral units bridged by linear linkers (Scheme 3.3). Simple water boiling tests reveal almost no water uptake as well

as excellent stability suggesting hydrophobic properties. On the other hand, the gels offer some affinity for solvents as seen in Table 3.6. Mass gains for 1:1 DEO:OHS and 1:1 DGEBA:OHS gels vary 20-80 %, but 1:1 ECHX:OHS shows a much lower solvent uptake. This may suggest high stiffness of the 1:1 ECHX:OHS solid, owing to the two cyclohexyl rings in the ECHX structure.^{74,75}

It is worth mentioning that most of oxysilylations of ECHX form precipitates, despite different Si-H sources (TMDS, OHS, D₄H, and D₅H), which could be a result of high MWs as well as high stiffness as condensation proceeds.

One surprising result comes from Brunauer-Emmett-Teller (BET) specific surface area (SSA) analyses conducted on all the dried OHS derived resins, Table 3.7. The 1:1 ECHX:OHS offers a SSA of 35 m²/g and small pore size of 3 nm compared to all the other epoxy resins. Given the rigid nature of ECHX one can suggest that this porosity arises from an inability of the gel nanostructure to collapse.

Table 3.6. Average percent mass gain in solvent impregnation studies.

Solvent [Snyder's Polarity Index]	1:1 DEO:OHS	1:1 DGEBA:OHS	1:1 ECHX:OHS
Acetonitrile [5.8]	18%	24%	21%
Tetrahydrofuran [4.0]	25%	21%	4%
Dichloromethane [3.1]	65%	50%	11%
Toluene [2.4]	63%	81%	14%
Hexane [0.0]	62%	25%	3%

Table 3.7. BET SSA analysis of oxysilylation of diepoxides with OHS.

Epoxy resin	Surface Area, m ² /g	Pore Size, nm
1:1 DEB:OHS	0.4	26
1:1 DEO:OHS	0.6	23
1:1 DGEBA:OHS	0.3	25
1:1 ECHX:OHS	35	3

Taken *in toto*, the above data show materials ranging from flexible and transparent to brittle, quite porous and hydrophobic. One can conclude that our premise that these materials may offer

alternative epoxy resins is valid, but much more work needs to be done.

3.3.3 Oxysilylations of diepoxides with a mixture of TMDS and OHS

Given that oxysilylation of diepoxides with TMDS gives linear polymers, while with OHS, highly crosslinked 3-D gels result; it is reasonable to assume that adding OHS provides crosslinking allowing properties tailoring.

Thus, a series of oxysilylations were run replacing 5-20 mol.% of Si-H from TMDS with OHS in various amounts of solvent. Table 3.8 compares the MWs of selected reactions with TMDS and OHS at 0, 5, and 10 mol.%. No significant increase in MW arises as the amount of OHS increases. In fact, crystalline OHS cubes precipitate out (Figure A.1) especially with 10-20 mol.% OHS and/or in low solvent volumes (1 and 2.5 mL). On adding OHS >10 mol.%, no obvious changes in MWs are seen, therefore the results are omitted here.

Table 3.8. Molecular weights of oxysilylations of diepoxides with TMDS and OHS.

Epoxy	Solvent (mL)	Cat. (mg)	OHS		
			0 %	5 %	10 %
DEB	1	0.25	1.0 kDa	1.3 kDa	1.3kDa
		0.5	(Gel)	(Gel)	18 kDa
DEO	1	0.1	1.0 kDa	1.3 kDa	1.4 kDa
		0.5	(Gel)	(Gel)	(Gel)
DGEBA	5	0.1	18 kDa	1.7 kDa	1.7 kDa
		0.25	18 kDa	12 kDa	(Gel)
		0.5	20 kDa	14 kDa	(Gel)
ECHX	5	0.25	2.0 kDa	3.0 kDa	(Gel)
		0.5	30 kDa	30 kDa	(Gel)

In contrast, oxysilylation of DGEBA shows an interesting trend: the MW decreases when 5 mol.% OHS compared to without OHS, but it increases when the amount of OHS is increased to 10 mol.%. It is possible that the epoxy groups in DGEBA react with Si-H in TMDS preferably and the presence of a small amount of OHS impedes the reaction between DGEBA and TMDS, and further reaction between DGEBA and OHS is hindered due to the rigidity of their structures. When

the amount of OHS is increased, the abundance of OHS promotes the competing reaction with DGEBA resulting in a gel.

For oxysilylations of DEB and DEO, reactions in higher solvent volumes (2.5 and 5 mL) give lower MWs (see Table 3.4) with the same trend as with 1 mL solvent in Table 3.8 and are thus omitted here. For oxysilylation of DGEBA and ECHX, reactions in lower solvent volumes (1 and 2.5 mL) give gels, therefore only the reactions with 5 mL solvent are listed.

Figure 3.20 shows representative FTIRs of oxysilylations of diepoxides with TMDS and 5 mol.% of OHS with 0.5 mg of catalyst. All spectra show a small ν Si-H at $\sim 2100\text{ cm}^{-1}$, except for the oxysilylation of DGEBA where almost no ν Si-H is seen. This suggests that the reactions are close to completion. Compared to the 1:1 epoxide:TMDS systems with the same amount of catalyst (Figure 3.9), the intensity of ν Si-H reduces when 5 mol.% of TMDS is replaced with OHS. Based on the observation of pure OHS precipitates, it's likely that OHS is not fully reacted, hence the observed ν Si-H band, but the reaction between the epoxides and TMDS is close to completion.

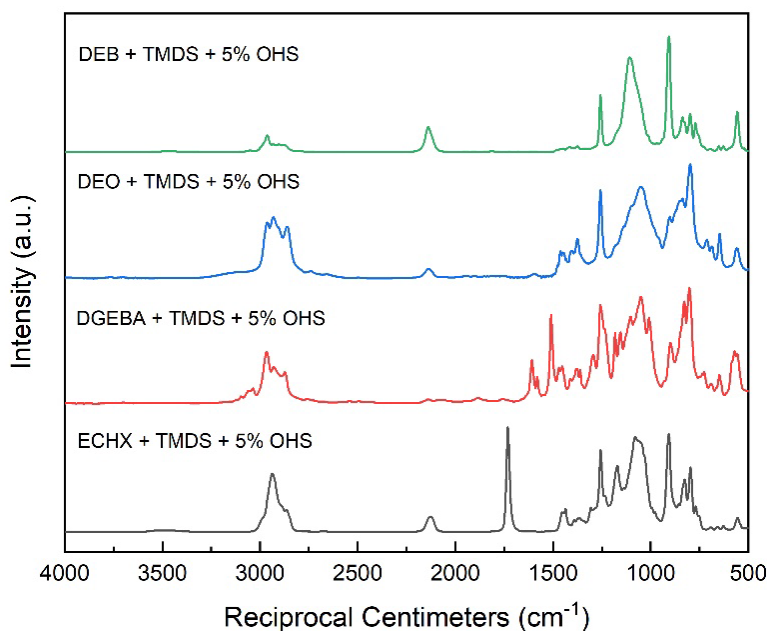


Figure 3.20. FTIRs of diepoxide oxysilylation with TMDS + 5 mol.% OHS, 0.5 mg $\text{B}(\text{C}_6\text{F}_5)_3$.

3.3.4 Oxysilylation of diepoxides with D₄H/D₅H

Mixing OHS with TMDS shows little improvement in MWs, prompting exploration of alternate Si-H sources D₄H/D₅H. The cyclic nature of D₄H/D₅H offers a 2-D opportunity to imbue crosslinking.

Tables 3.9 and 3.10 summarize the MWs of diepoxide oxysilylation with D₄H and D₅H, respectively. Compared to TMDS (Table 3.4), most oxysilylations with D₄H show decreased MWs per Table 3.9. Oxysilylations with D₅H on the other hand, show large increases in MWs compared with Table 3.4, with the exception of 1:1 DEO:D₅H (Table 3.10). Precipitates form in 1:1 DEB:D₄H in 1 mL of solvent simply as a result of the small solvent volume, at higher volumes, no precipitates form.

Table 3.9. Molecular weights of oxysilylations of diepoxides with D₄H.

Epoxy	Cat. (mg)	Solvent (mL)		
		1	2.5	5
DEB	0.5	(PPT)	3.0 kDa	1.7 kDa
	1.0	(PPT)	3.5 kDa	1.9 kDa
DEO	0.5	1.8 kDa	1.3 kDa	0.7 kDa
	1.0	1.9 kDa	1.2 kDa	0.8 kDa
DGEBA	0.5	32 kDa	2.0 kDa	1.0 kDa
	1.0	(Gel)	9.0 kDa	1.3 kDa
ECHX	0.5	(PPT)	(PPT)	(PPT)
	1.0	(PPT)	(PPT)	(PPT)

Table 3.10. Molecular weights of oxysilylations of diepoxides with D₅H.

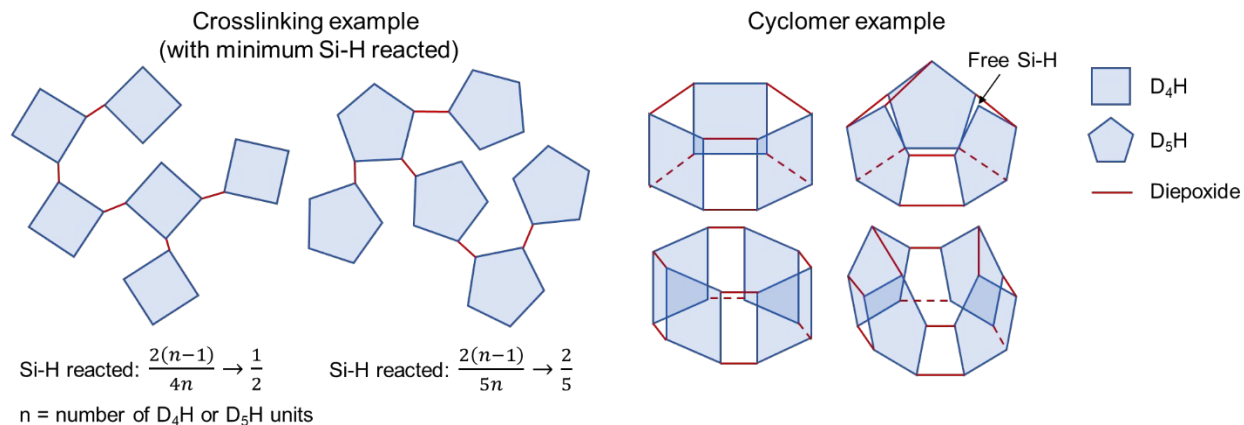
Epoxy	Cat. (mg)	Solvent (mL)		
		1	2.5	5
DEB	0.5	(Gel)	(Gel)	39 kDa
	1.0	(Gel)	(Gel)	38 kDa
DEO	0.5	13 kDa	1.3 kDa	0.8 kDa
	1.0	(Gel)	1.4 kDa	1.4 kDa
DGEBA	0.5	(Gel)	(Gel)	38 kDa
	1.0	(Gel)	(Gel)	38 kDa
ECHX	0.5	(PPT)	(PPT)	(PPT)
	1.0	(PPT)	(PPT)	(PPT)

The clear difference in MWs from oxysilylations with D₄H vs. D₅H seems quite surprising because they vary by just one additional Si-H group. Scheme 3.5 depicts two idealized scenarios: (a) crosslinking with one bridge between every two monomers, and (b) cyclomer formed. Nevertheless, the actual structure is likely a mixture of the two and/or irregular partial cyclomers.

Statistically, half of the Si-H groups in D₄H need to react to connect all D₄H molecules by diepoxides, while only 40 % of Si-H groups in D₅H are needed (Scheme 3.5 left). Additionally, D₅H (300.6 g/mol) has a higher MW than D₄H (240.4 g/mol); as a result, with the same number of Si-H groups reacted, diepoxide oxysilylation with D₅H will have a higher MW than D₄H, about 1.5 times higher to be exact.

However, the difference between the resulting MWs of oxysilylation with D₄H and D₅H shown in Tables 3.9 and 3.10 is much higher, reaching almost 20× in some cases. Another explanation may be that oxysilylation with D₄H gives bridging cyclomers and no extra free Si-H is available to form polymers, hence low MWs. But for D₅H, the additional free Si-H can bridge cyclomeric intermediates promoting chain growth as suggested by Scheme 3.5 right. Furthermore, the pentagon-like structure of D₅H requires linkers with different lengths for cyclomers to form, which may make it difficult when only one diepoxide species available.

On the other hand, both oxysilylations of DEO with D₄H and D₅H show lower MWs than the other diepoxides. One distinctive feature of DEO is that its four-carbon chain between the two epoxy groups gives it higher flexibility compared to the other diepoxides, such flexibility enables cyclomers with D₅H to form, resulting in lower MWs.



Scheme 3.5. Crosslinking and cyclomer models from diepoxide oxysilylation with D₄H and D₅H.

Figure 3.21 compares the FTIRs of oxysilylations of diepoxides with D₄H and D₅H. All the oxysilylations show $\nu\text{Si-H}$ at $\sim 2100\text{ cm}^{-1}$, suggesting the reactions are incomplete. On the other hand, oxysilylations with D₅H shows a higher intensity $\nu\text{Si-H}$ band ($\sim 2100\text{ cm}^{-1}$) compared to D₄H. This indicates that epoxy groups react with Si-H groups in D₄H more easily than D₅H given the same conditions, likely due to the slight structural differences between D₄H and D₅H.

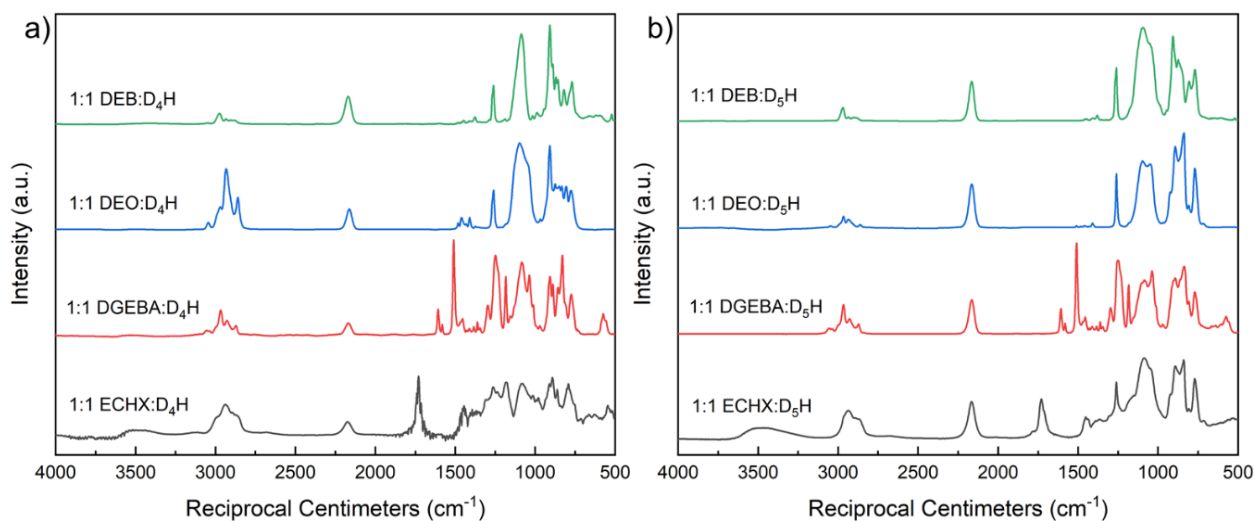


Figure 3.21. FTIRs of diepoxide oxysilylation with D₄H (a) and D₅H (b), 0.5 mg B(C₆F₅)₃ in 5 mL DCM + 5 mL hexane.

Water stability was also assessed for 1:1 diepoxide:D₅H gels/solids formed in 1 mL solvent per Table 3.10. Again, all gels/solids remain stable after boiling in water for 5 h, no obvious decomposition or degradation occurs. Figure 3.22 shows representative FTIRs of solids before and after boiling in water for 5 h.

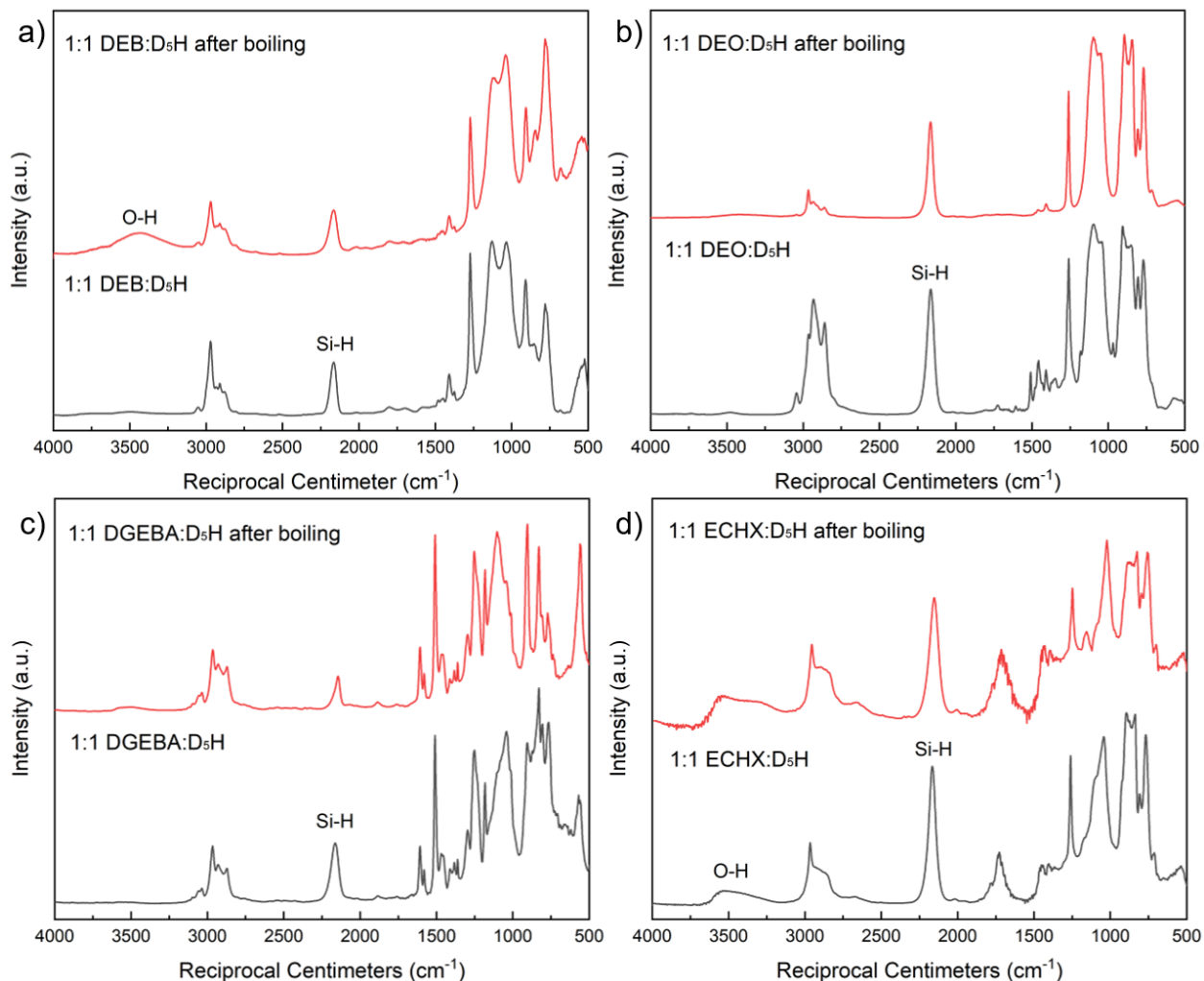


Figure 3.22. FTIRs of (a) 1:1 DEB:D₅H, (b) 1:1 DEO:D₅H, (c) 1:1 DGEBA:D₅H, (d) 1:1 ECHX:D₅H before and after boiling in water for 5 h.

The decreased intensity of ν Si-H ($\sim 2100\text{ cm}^{-1}$) may be a result of the loss of unreacted D₅H in boiling water. Otherwise, all IRs show little difference in FTIR before and after, some solids show a small ν O-H band at $\approx 3400\text{ cm}^{-1}$ suggesting water uptake and/or hydrolysis forming Si-OH

groups after boiling. For the 1:1 ECHX:D₅H system, an νO-H band is exhibited before boiling (see Figure 3.21 also), it's possible that not only the epoxy groups in ECHX reacted with Si-H, the C=O group may also participate in the reaction resulting in O-H bonds. In general, these gels/solids show reasonably good water stability.

3.4 Conclusions

We have demonstrated a new oxysilylation reaction of Si-H bonds with epoxides that provides additional utility to this recently discovered reaction. Studies of the reaction of diepoxides with TMDS give linear polymers with good to excellent MWs. These reactions are quite rapid and may be useful in the development of novel self-curing systems. With low solvent volume (1 mL), diepoxide oxysilylations with TMDS give gels/solids that are stable in boiling water up to 5 h suggesting good water stability.

Highly ordered networks can be made through oxysilylation of diepoxides with a cubic symmetry Q-cage (OHS). Due to high crosslink density, gels/solids form from reactions of diepoxides with OHS and show good water stability, solvent affinities, and solvent uptake. The 1:1 DEO:OHS system in particular, can be cast as transparent and flexible thin films. In contrast, the 1:1 ECHX:OHS system gives brittle solids with lower solvent affinity and much higher SSAs compared to other gels, which may be a result of the stiffness of the ECHX structure.

The addition of OHS to oxysilylations of diepoxides with TMDS shows little improvement in MWs. For the alternative Si-H sources D₄H/D₅H; D₅H shows superior MWs compared to D₄H or a mixture of TMDS and OHS.

References

1. Clayton A. May. *Epoxy Resins: Chemistry and Technology, Second Edition*; 1988; Vol. 53.
2. Sprenger, S. Epoxy Resin Composites with Surface-Modified Silicon Dioxide Nanoparticles: A Review. *J. Appl. Polym. Sci.* **2013**, *130* (3), 1421–1428.
3. Jin, F. L.; Li, X.; Park, S. J. Synthesis and Application of Epoxy Resins: A Review. *J. Ind. Eng. Chem.* **2015**, *29*, 1–11.
4. Weil, E. D.; Levchik, S. A Review of Current Flame Retardant Systems for Epoxy Resins. *J. Fire Sci.* **2004**, *22* (1), 25–40.
5. Hodgkin, J. H.; Simon, G. P.; Varley, R. J. Thermoplastic Toughening of Epoxy Resins: A Critical Review. *Polym. Adv. Technol.* **1998**, *9* (1), 3–10.
6. Hughes, J. D. H. The Carbon Fibre/Epoxy Interface-A Review. *Compos. Sci. Technol.* **1991**, *41* (1), 13–45.
7. Ratna, D. Modification of Epoxy Resins for Improvement of Adhesion: A Critical Review. *J. Adhes. Sci. Technol.* **2003**, *17* (12), 1655–1668.
8. Abdelkader, A. F.; White, J. R. Water Absorption in Epoxy Resins: The Effects of the Cross-linking Agent and Curing Temperature. *J. Appl. Polym. Sci.* **2005**, *98* (6), 2544–2549.
9. Dodiuk, H.; Goodman, S. H. Epoxy Resins. In *Handbook of Thermoset Plastics*; 2013; pp 193–268.
10. Ramezanzadeh, B.; Attar, M. M. Studying the Corrosion Resistance and Hydrolytic Degradation of an Epoxy Coating Containing ZnO Nanoparticles. *Mater. Chem. Phys.* **2011**, *130* (3), 1208–1219.
11. Soles, C. L.; Yee, A. F. A Discussion of the Molecular Mechanisms of Moisture Transport in Epoxy Resins. *J. Polym. Sci. Part B Polym. Phys.* **2000**, *38* (5), 792–802.
12. Soles, C. L.; Chang, F. T.; Gidley, D. W.; Yee, A. F. Contributions of the Nanovoid Structure to the Kinetics of Moisture Transport in Epoxy Resins. *J. Polym. Sci. Part B Polym. Phys.* **2000**, *38* (5), 776–791.
13. Du, Y. J.; Damron, M.; Tang, G.; Zheng, H.; Chu, C. J.; Osborne, J. H. Inorganic/Organic Hybrid Coatings for Aircraft Aluminum Alloy Substrates. *Prog. Org. Coat.* **2001**, *41*, 226–232.
14. Kaysser, W. Surface Modifications in Aerospace Applications. *Surf. Eng.* **2001**, *17*, 305–312.
15. Voevodin, N. N.; Balbyshev, V. N.; Donley, M. S. Investigation of Corrosion Protection Performance of Sol-Gel Coatings on AA2024-T3. *Prog. Org. Coat.* **2005**, *52*, 28–33.
16. Mezzenga, R.; Boogh, L.; Månson, J. A. E. A Review of Dendritic Hyperbranched Polymer as Modifiers in Epoxy Composites. *Compos. Sci. Technol.* **2001**, *61* (5), 787–795.
17. Brook, M. A.; Grande, J. B.; Ganachaud, F. New Synthetic Strategies for Structured Silicones Using B(C₆F₅)₃. In *Silicon Polymers*; 2011; pp 161–183.
18. Grande, J. B.; Thompson, D. B.; Gonzaga, F.; Brook, M. A. Testing the Functional Tolerance of the Piers-Rubinsztajn Reaction: A New Strategy for Functional Silicones. *Chem. Commun.* **2010**, *46*, 4988–4990.
19. Pouget, E.; Garcia, E. H.; Ganachaud, F. Direct Synthesis of PVA-g-PDMS in Microsuspension. *Macromol. Rapid Commun.* **2008**, *29* (5), 425–430.
20. Xue, L.; Kawakami, Y. Precise Synthesis of Poly(Silphenylenesiloxane)s with Epoxy Side Functioned Groups by Tris(Pentafluorophenyl)Borane as a Catalyst. *Polym. J.* **2007**, *39* (4), 379–388.

21. Rubinsztajn, S.; Cella, J. A. A New Polycondensation Process for the Preparation of Polysiloxane Copolymers. *Macromolecules* **2005**, *38*, 1061–1063.
22. Chojnowski, J.; Rubinsztajn, S.; Cella, J. A.; Fortuniak, W.; Cypriak, M.; Kurjata, J.; Kaźmierski, K. Mechanism of the B(C₆F₅)₃-Catalyzed Reaction of Silyl Hydrides with Alkoxysilanes. Kinetic and Spectroscopic Studies. *Organometallics* **2005**, *24*, 6077–6084.
23. Chojnowski, J.; Fortuniak, W.; Kurjata, J.; Rubinsztajn, S.; Cella, J. A. Oligomerization of Hydrosiloxanes in the Presence of Tris(Pentafluorophenyl)Borane. *Macromolecules* **2006**, *39*, 3802–3807.
24. Kurjata, J.; Fortuniak, W.; Rubinsztajn, S.; Chojnowski, J. B(C₆F₅)₃ Catalyzed Dehydrocarbon Polycondensation of PhSiH₃ with (MeO)₄Si as Model Polyfunctional Comonomers in New Route to Hydrophobic Silicone TQ Resins. *Eur. Polym. J.* **2009**, *45*, 3372–3379.
25. Cella, J.; Rubinsztajn, S. Preparation of Polyaryloxysilanes and Polyaryloxysiloxanes by B(C₆F₅)₃ Catalyzed Polyetherification of Dihydrosilanes and Bis-Phenols. *Macromolecules* **2008**, *41*, 6965–6971.
26. Rubin, M.; Schwier, T.; Gevorgyan, V. Highly Efficient B(C₆F₅)₃-Catalyzed Hydrosilylation of Olefins. *J. Org. Chem.* **2002**, *67*, 1936–1940.
27. Crivello, J. V.; Lee, J. L. The Synthesis, Characterization, and Photoinitiated Cationic Polymerization of Silicon-containing Epoxy Resins. *J. Polym. Sci. Part Polym. Chem.* **1990**, *28* (3), 479–503.
28. Crivello, J. V.; Bi, D. Regioselective Hydrosilations. II. The Synthesis of Silicon–Hydrogen Functional Compounds. *J. Polym. Sci. Part Polym. Chem.* **1993**, *31* (11), 2729–2737.
29. Crivello, J. V.; Bi, D. Regioselective Hydrosilations. III. The Synthesis and Polymerization of Ambifunctional Silicon-containing Epoxy Monomers. *J. Polym. Sci. Part Polym. Chem.* **1993**, *31* (12), 3109–3119.
30. Crivello, J. V.; Bi, D. Regioselective Hydrosilations. IV. The Synthesis and Polymerization of Monomers Containing Epoxy and Alkoxysilane Groups. *J. Polym. Sci. Part Polym. Chem.* **1993**, *31* (12), 3121–3132.
31. Crivello, J. V.; Fan, M. Regioselective Rhodium-containing Catalysts for Ring-opening Polymerizations and Hydrosilylations. *J. Polym. Sci. Part Polym. Chem.* **1992**, *30* (1), 1–11.
32. Jang, M.; Crivello, J. V. Synthesis and Cationic Photopolymerization of Epoxy-Functional Siloxane Monomers and Oligomers. *J. Polym. Sci. Part Polym. Chem.* **2003**, *41* (19), 3056–3073.
33. Kamino, B. A.; Mills, B.; Reali, C.; Gretton, M. J.; Brook, M. A.; Bender, T. P. Liquid Triarylamines: The Scope and Limitations of Piers-Rubinsztajn Conditions for Obtaining Triarylamine-Siloxane Hybrid Materials. *J. Org. Chem.* **2012**, *77*, 1663–1674.
34. Gretton, M. J.; Kamino, B. A.; Brook, M. A.; Bender, T. P. The Use of Piers-Rubinsztajn Conditions for the Placement of Triarylamines Pendant to Silicone Polymers. *Macromolecules* **2012**, *45*, 723–728.
35. Grande, J. B.; Fawcett, A. S.; McLaughlin, A. J.; Gonzaga, F.; Bender, T. P.; Brook, M. A. Anhydrous Formation of Foamed Silicone Elastomers Using the Piers-Rubinsztajn Reaction. *Polymer* **2012**, *53*, 3135–3142.
36. Laengert, S. E.; Schneider, A. F.; Lovinger, E.; Chen, Y.; Brook, M. A. Sequential Functionalization of a Natural Crosslinker Leads to Designer Silicone Networks. *Chem. - Asian J.* **2017**, *12*, 1208–1212.

37. Gnanasekaran, D.; Madhavpan, K.; Reddy, R. S. R. Developments of Polyhedral Oligomeric Silsesquioxanes (POSS), POSS Nanocomposites and Their Applications: A Review. *J. Sci. Ind. Res.* **2009**, *68*, 437–464.
38. Li, G.; Wang, L.; Ni, H.; Pittman, C. U. Polyhedral Oligomeric Silsesquioxane (POSS) Polymers and Copolymers: A Review. *J. Inorg. Organomet. Polym.* **2001**, *11*, 123–154.
39. Tanaka, K.; Chujo, Y. Advanced Functional Materials Based on Polyhedral Oligomeric Silsesquioxane (POSS). *J. Mater. Chem.* **2012**, *22*, 1733–1746.
40. Laine, R. M. Nanobuilding Blocks Based on the $[\text{OSiO}_{1.5}]_x$ ($x = 6, 8, 10$) Octasilsesquioxanes. *J. Mater. Chem.* **2005**, *15*, 3725–3744.
41. Hanssen, R. W. J. M.; Van Santen, R. A.; Abbenhuis, H. C. L. The Dynamic Status Quo of Polyhedral Silsesquioxane Coordination Chemistry. *Eur. J. Inorg. Chem.* **2004**, *4*, 675–683.
42. Baney, R. H.; Itoh, M.; Sakakibara, A.; Suzuki, T. Silsesquioxanes. *Chem. Rev.* **1995**, *95*, 1409–1430.
43. Zhang, Z.; Horsch, M. A.; Lamm, M. H.; Glotzer, S. C. Tethered Nano Building Blocks: Toward a Conceptual Framework for Nanoparticle Self-Assembly. *Nano Lett.* **2003**, *3*, 1341–1346.
44. Sulaiman, S.; Bhaskar, A.; Zhang, J.; Guda, R.; Goodson, T.; Laine, R. M. Molecules with Perfect Cubic Symmetry as Nanobuilding Blocks for 3-D Assemblies. Elaboration of Octavinylsilsesquioxane. Unusual Luminescence Shifts May Indicate Extended Conjugation Involving the Silsesquioxane Core. *Chem. Mater.* **2008**, *20*, 5563–5573.
45. Liu, H.; Kondo, S. I.; Takeda, N.; Unno, M. Synthesis of Octacarboxy Spherosilicate. *J. Am. Chem. Soc.* **2008**, *130*, 10074–10075.
46. Mitsuishi, M.; Zhao, F.; Kim, Y.; Watanabe, A.; Miyashita, T. Preparation of Ultrathin Silsesquioxane Nanofilms via Polymer Langmuir - Blodgett Films. *Chem. Mater.* **2008**, *20*, 4310–4316.
47. Hosaka, N.; Torikai, N.; Otsuka, H.; Takahara, A. Structure and Dewetting Behavior of Polyhedral Oligomeric Silsesquioxane-Filled Polystyrene Thin Films. *Langmuir* **2007**, *23*, 902–907.
48. Takamura, N.; Gunji, T.; Hatano, H.; Abe, Y. Preparation and Properties of Polysilsesquioxanes: Polysilsesquioxanes and Flexible Thin Films by Acid-catalyzed Controlled Hydrolytic Polycondensation of Methyl- and Vinyltrimethoxysilane. *J. Polym. Sci. Part Polym. Chem.* **1999**, *37*, 1017–1026.
49. Zhang, C.; Babonneau, F.; Bonhomme, C.; Laine, R. M.; Soles, C. L.; Hristov, H. A.; Yee, A. F. Highly Porous Polyhedral Silsesquioxane Polymers. Synthesis and Characterization. *J. Am. Chem. Soc.* **1998**, *120*, 8380–8391.
50. Feher, F. J.; Wyndham, K. D.; Scialdone, M. A.; Hamuro, Y. Octafunctionalized Polyhedral Oligosilsesquioxanes as Scaffolds: Synthesis of Peptidyl Silsesquioxanes. *Chem. Commun.* **1998**, *14*, 1469–1470.
51. Phillips, S. H.; Haddad, T. S.; Tomczak, S. J. Developments in Nanoscience: Polyhedral Oligomeric Silsesquioxane (POSS)-Polymers. *Curr. Opin. Solid State Mater. Sci.* **2004**, *8*, 21–29.
52. Schwab, J. J.; Lichtenhan, J. D. Polyhedral Oligomeric Silsesquioxane (POSS)-Based Polymers. *Appl. Organomet. Chem.* **1998**, *12*, 707–713.
53. Wu, S.; Hayakawa, T.; Kakimoto, M. A.; Oikawa, H. Synthesis and Characterization of Organosoluble Aromatic Polyimides Containing POSS in Main Chain Derived from Double-Decker-Shaped Silsesquioxane. *Macromolecules* **2007**, *40*, 5698–5705.

54. Lin, H. C.; Kuo, S. W.; Huang, C. F.; Chang, F. C. Thermal and Surface Properties of Phenolic Nanocomposites Containing Octaphenol Polyhedral Oligomeric Silsesquioxane. *Macromol. Rapid Commun.* **2006**, *27*, 537–541.
55. Laine, R. M.; Zhang, C.; Sellinger, A.; Viculis, L. Polyfunctional Cubic Silsesquioxanes as Building Blocks for Organic/Inorganic Hybrids. *Appl. Organomet. Chem.* **1998**, *12*, 715–723.
56. Ghanbari, H.; Cousins, B. G.; Seifalian, A. M. A Nanocage for Nanomedicine: Polyhedral Oligomeric Silsesquioxane (POSS). *Macromol. Rapid Commun.* **2011**, *32*, 1032–1046.
57. Lo, M. Y.; Ueno, K.; Tanabe, H.; Sellinger, A. Silsesquioxane-Based Nanocomposite Dendrimers with Photo-Luminescent and Charge Transport Properties. *Chem. Rec.* **2006**, *6*, 157–168.
58. Mee, Y. Lo; Zhen, C.; Lauters, M.; Jabbour, G. E.; Sellinger, A. Organic-Inorganic Hybrids Based on Pyrene Functionalized Octavinylsilsesquioxane Cores for Application in OLEDs. *J. Am. Chem. Soc.* **2007**, *129*, 5808–5809.
59. Roll, M. F.; Asuncion, M. Z.; Kampf, J.; Laine, R. M. Para-Octaiodophenylsilsesquioxane, [p-IC₆H₄SiO_{1.5}]₈, a Nearly Perfect Nano-Building Block. *ACS Nano* **2008**, *2*, 320–326.
60. Ervithayasuporn, V.; Wang, X.; Kawakami, Y. Synthesis and Characterization of Highly Pure Azido-Functionalized Polyhedral Oligomeric Silsesquioxanes (POSS). *Chem. Commun.* **2009**, *34*, 5130–5132.
61. Fabritz, S.; Heyl, D.; Bagutski, V.; Empting, M.; Rikowski, E.; Frauendorf, H.; Balog, I.; Fessner, W. D.; Schneider, J. J.; Avrutina, O.; Kolmar, H. Towards Click Bioconjugations on Cube-Octameric Silsesquioxane Scaffolds. *Org. Biomol. Chem.* **2010**, *8*, 2212–2218.
62. Roll, M. F.; Kampf, J. W.; Laine, R. M. Crystalline Hybrid Polyphenylene Macromolecules from Octaalkynylsilsesquioxanes, Crystal Structures, and a Potential Route to 3-D Graphenes. *Macromolecules* **2011**, *44*, 3425–3435.
63. Mya, K. Y.; He, C.; Huang, J.; Xiao, Y.; Dai, J.; Siow, Y. P. Preparation and Thermomechanical Properties of Epoxy Resins Modified by Octafunctional Cubic Silsesquioxane Epoxides. *J. Polym. Sci. Part Polym. Chem.* **2004**, *42*, 3490–3503.
64. Lu, T.; Chen, T.; Liang, G. Synthesis, Thermal Properties, and Flame Retardance of the Epoxy-Silsesquioxane Hybrid Resins. *Polym. Eng. Sci.* **2007**, *47*, 225–234.
65. Choi, J.; Harcup, J.; Yee, A. F.; Zhu, Q.; Laine, R. M. Organic/Inorganic Hybrid Composites from Cubic Silsesquioxanes. *J. Am. Chem. Soc.* **2001**, *123*, 11420–11430.
66. Laine, R. M.; Choi, J.; Lee, I. Organic-Inorganic Nanocomposites with Completely Defined Interfacial Interactions. *Adv. Mater.* **2001**, *13*, 800–803.
67. Choi, J.; Yee, A. F.; Laine, R. M. Organic/Inorganic Hybrid Composites from Cubic Silsesquioxanes. Epoxy Resins of Octa(Dimethylsiloxyethylcyclohexylepoxide) Silsesquioxane. *Macromolecules* **2003**, *36*, 5666–5682.
68. Choi, J.; Yee, A. F.; Laine, R. M. Toughening of Cubic Silsesquioxane Epoxy Nanocomposites Using Core-Shell Rubber Particles: A Three-Component Hybrid System. *Macromolecules* **2004**, *37*, 3267–3276.
69. Pan, D.; Yi, E.; Doan, P. H.; Furgal, J. C.; Schwartz, M.; Clark, S.; Goodson, T.; Laine, R. M. Microporous Inorganic/Organic Hybrids via Oxysilylation of a Cubic Symmetry Nanobuilding Block [(HMe₂SiOSiO_{1.5})₈] with R_xSi(OEt)_{4-x}. *J. Ceram. Soc. Jpn.* **2015**, *123*, 756–763.
70. Liao, M.; Schneider, A. F.; Laengert, S. E.; Gale, C. B.; Chen, Y.; Brook, M. A. Living Synthesis of Silicone Polymers Controlled by Humidity. *Eur. Polym. J.* **2018**, *107*, 287–293.
71. Heggie, M.; Jones, R. Density Functional Analysis of the Hydrolysis of Si-O Bonds in Disiloxane Application to Hydrolytic Weakening in Quartz. *Philos. Mag. Lett.* **1987**, *55*, 47–51.

72. Pelmenschikov, A.; Strandh, H.; Pettersson, L. G. M.; Leszczynski, J. Lattice Resistance to Hydrolysis of Si-O-Si Bonds of Silicate Minerals: Ab Initio Calculations of a Single Water Attack onto the (001) and (111) β -Cristobalite Surfaces. *J. Phys. Chem. B* **2000**, *104*, 5779–5783.
73. Kouno, T.; Ogata, S.; Shimada, T.; Tamura, T.; Kobayashi, R. Enhanced Si-O Bond Breaking in Silica Glass by Water Dimer: A Hybrid Quantum-Classical Simulation Study. *J. Phys. Soc. Jpn.* **2016**, *85*, 054601.
74. Thorat, S. D.; Phillips, P. J.; Semenov, V.; Gakh, A. Physical Properties of Aliphatic Polycarbonates Made from CO₂ and Epoxides. *J. Appl. Polym. Sci.* **2003**, *89* (5), 1163–1176.
75. Hokajo, T.; Terao, K.; Nakamura, Y.; Norisuye, T. Solution Properties of Polymacromonomers Consisting of Polystyrene V. Effect of Side Chain Length on Chain Stiffness. *Polym. J.* **2001**, *33*, 481–485.

Chapter 4 Design, Synthesis, Characterization and Electrochemical performance of Polymer Precursors to Li_xPON and Li_xSiPON Glasses

Published: Zhang, X.; Temeche, E.; Laine, R. M. *Macromolecules* **2020**, *53* (7), 2702–2712.

4.1 Introduction

Micro-electronic devices play an increasingly important role in our lives. A main component of these devices is the power source/energy storage unit-battery. Currently, rechargeable lithium ion batteries are widely employed for their high energy densities and long cycle lives. Classical Li^+ batteries use liquid electrolytes that consist of inorganic salts dissolved in organic solvents which often restricts their size, design, and have inherent safety risks that together restrain operating temperature windows.^{1,2} In contrast, solid-state electrolytes offer considerable design potential especially for miniaturization and/or scaling, improved safety and a wider operating temperature window.^{2–5}

However, most solid electrolytes suffer from low ionic conductivities, a limited stability window, or from irreversible reduction [e.g. $\text{LASi}(\text{Ge})\text{TP}$ materials]^{6–11} on cycling or lithium dendrite growth along grain boundaries (e.g. LLZO materials)^{11–16} leading to short circuiting. Fortunately, amorphous lithium phosphorus oxynitrides (Li_xPON) has been found to offer protection against both processes.^{9,16–19}

LiPON is one of the most commonly employed solid-state electrolytes owing to its broad electrochemical stability window (0–5 V vs. Li^+/Li),^{20,21} high critical current density (>10 mA/cm^2),^{22–25} and negligible electronic conductivity (10^{-13} S/cm).^{1,26,27} However, due to its limited

ionic conductivity (10^{-8} - 10^{-6} S/cm),^{1,20,21,26,28,29} its application is restricted to thin-film batteries with limited energy densities and capacities.^{2,25,30,31}

Recently, silicon-containing LiPON (or LiSiPON) has attracted attention due to its increased ionic conductivity induced by silicon doping. Lee *et al.*^{32,33} report that LiSiPON films can reach 10^{-5} S/cm at RT and increasing Si/P ratios reduces the activation energy (E_a) for ionic transport. Su *et al.*³⁴ reported depositing LiSiPON thin films (~ 1 μm) by radio frequency magnetron sputtering (RFMS) with ionic conductivities at ambient $\approx 10^{-5}$ S/cm and an E_a of 0.41 eV at Si/P = 1. Famprakis *et al.*³⁵ reported LiSiPON thin films with ionic conductivity of 2.06×10^{-5} S/cm ($E_a = 0.45$ eV) at RT by sputtering $\text{Li}_{3+x}\text{Si}_x\text{P}_{1-x}\text{O}_4$ under N_2 .

LiPON-like thin films are typically processed by gas phase methods, such as RFMS,^{20,32-34,36} pulse laser deposition,³⁷ ion beam assisted deposition,³⁸ plasma-assisted direct vapor deposition,³⁹ plasma-enhanced metalloorganic chemical vapor deposition,⁴⁰ atomic layer deposition,⁴¹ etc. The main limitations of gas phase deposition are low deposition rates (typically < 100 nm/min),³⁶⁻³⁹ the need for specialized apparatus, fabrication of large, homogeneous composition targets and likely costly economics at commodity scales. Thus, there are considerable economic and performance mandates driving the search for easier processing routes to the same materials especially for the practical processing of ASSBs. The use of chemical precursor routes to the same materials seems to offer considerable potential to solve these issues.

The concept of designing ceramic materials “atom by atom” using molecular precursors had its origins in work published by Chantrell and Popper *et al.*⁴² and Aylett *et al.*⁴³ in the mid 1960’s, but became main stream with a review by Wynne and Rice from the Office of Naval Research,⁴⁴ and coincidental efforts by Ulrich *et al.* from the Air Force Office of Scientific Research through the “Better Ceramics Through Chemistry” symposia in the 80’s.^{45,46}

This field has progressed considerably since that time and there is now sufficient literature to allow development of design principles for generating precursors with multiple desirable properties including: control of final elemental compositions, high ceramic yields from initial components while engendering processability and minimizing unwanted off gassing of supporting moieties used to enhance processability.⁴⁷⁻⁵⁰ Based on these design principles, we have explored the development of LiPON and LiSiPON-like, and Li_xSiPHN precursors and demonstrated their efficacy as ion conducting polymers in Li-S half-cells.⁵¹ These materials seem to offer properties superior to gas phase deposited LiPON materials.

Our designed approach uses easily available starting materials, either OPCl_3 or $[\text{Cl}_2\text{P}=\text{N}]_3$. The logic behind the synthetic designs and approaches are detailed in the following sections. The resulting precursors are typically oligomers or low MW polymers derived from lithiation of $\text{OP}(\text{NH}_2)_{3-x}(\text{NH})_x$ [from $\text{OP}(\text{NH})_3$], $\text{OP}(\text{NH}_2)_{3-x}(\text{NHSiMe}_3)_x$ and $[\text{P}=\text{N}]_3(\text{NHSiMe}_3)_{6-x}(\text{NH})_x$, respectively. Selected amounts of LiNH_2 provide varying degrees of lithiation and Li^+ conducting properties commensurate with Li^+ content. After heating the dried precursor pellets to various temperatures between 200-400 °C/2 h, they exhibit conductivities up to 2.7×10^{-4} S/cm at RT.

The current report presents in-depth characterization of the above-mentioned precursors providing detailed analyses of various structural components, and Li^+ environments. A diverse set of analytical methods were used including GPC, TGA, MALDI, NMR and XPS. Furthermore, FTIR, XRD and EIS characterization was conducted on all precursors following heating to 100-600 °C), as phase and compositional changes are anticipated to influence materials' processing methods and conductivities, and shed light on potential applications for such materials as polymer and/or ceramic electrolytes.

To further study electrochemical properties, these LiPON emulating polymer precursors were coated with Celgard separators fabricating polymer electrolytes and used as stable interface between Li metals for symmetrical cells, and Li and a sulfur-based cathode (SPAN) for half cells.^{51,52} Polymer electrolytes impregnated in/on Celgard exhibit Li⁺ conductivities up to $\sim 1 \times 10^{-5}$ S/cm at RT and are thermally stable to ~ 150 °C. The SPAN/Celgard + Li₆SiPON/Li half-cell exhibits an initial capacity of 2000 mAh/g_{sulfur} and excellent cycle performance at 0.25 and 0.5 C rate over 120 cycles at RT.

We also explored the possibility of using the polymer precursors as active fillers in PEO matrix forming SPE films. The PEO solid-solution films exhibit enhanced ionic conductivities of $\sim 0.1-2 \times 10^{-3}$ S/cm at ambient and low E_a (0.2-0.5 eV) for cation transport. In addition, galvanostatic cycling of the SPAN/PES/Li battery shows discharge capacities of 1000 mAh/g_{sulfur} at 0.25C and 800 mAh/g_{sulfur} at 1C with high (~ 100 %) coulombic efficiency over extensive cycles.

4.2 Experimental section

Electrochemical impedance spectroscopy (EIS). Li₃PON, Li₆PON, Li₂SiPHN, Li₃SiPON, and Li₆SiPON precursors were heated to 100 °C/vacuum/24 h. The dried polymer precursors (3 g) powder were compacted into a pellet using a $\Phi = 13$ mm die at 5 ksi/RT. The resulting pellets were heated between alumina plates to 200-400 °C/2 h at 1 °C/min under 120 mL/min N₂ flow. Concentric Au/Pd electrodes ($\Phi = 3$ mm) were deposited using a SPI sputter coater on both surface of the pellets using a deposition mask. For Celgard/polymer precursor electrolytes, precursor THF solutions (0.05 g/mL in THF, 20 μ L) were coated on Celgard separators (18 mm \times 25 μ m) and assembled between stainless steel (SS) disks ($\Phi = 8$ mm) forming symmetrical cells.

An equivalent circuit consisting of ($R_{\text{total}}Q_{\text{total}}$)($Q_{\text{electrode}}$) was used. R and Q denote resistance and constant phase element, respectively. The total conductivity (σ_t) was calculated using the equation $\sigma_t = t/(A \times R)$, where t is the thickness of the polymer precursor pellet or coated Celgard PE, A is the active area and R is the total resistivity obtained from the Nyquist plots.

Lithium transference number (t_{Li^+}) was determined following the procedure and equation suggested by Evans *et al.*⁵³ Symmetrical cells (Li/polymer coated Celgard electrolytes/Li) were monitored under chronoamperometry until a steady-state current was reached. The initial (I_0) and steady-state (I_{ss}) currents in addition to the initial (Z_0) and steady-state (Z_{ss}) resistances were obtained from the chronoamperometry and EIS measurements. t_{Li^+} was calculated using the equation $t_{\text{Li}^+} = I_{ss}(DV - Z_0 \times I_0)/I_0(DV - Z_{ss} \times I_{ss})$.

Electronic conductivities of the polymer electrolytes were determined by DC measurements of the current under potential polarization using Bio-Logic SP 300 potentiostat with low current functions (current resolution < 1nA). The potential was ramped in the ranges of ± 0.03 V with a step of 10 mV and was held at each step for up to 1 h. The stabilized current at each step was used to determine the electronic conductivity. The electronic conductivity is deduced from the stabilized current (I_{ss}) using the relation: $\sigma_e = (t \times I_{ss})/(A \times U)$, where t is the thickness of the Celgard (25 μm), A is the area of the Li electrode (radius = 8 mm), and U is the applied voltage.

Galvanostatic cycling tests were conducted using SP-300 potetntiostats/galvanostat (Bio-Logic Science Instruments, Knoxville, TN). Detailed cell fabrication procedures and cycling conditions are reported elsewhere.^{51,54}

Differential scanning calorimetry (DSC) measurements of PEO based polymer electrolyte films were performed from RT to 100 °C at a heating rate of 3 °C/min for three cycles. Thermal

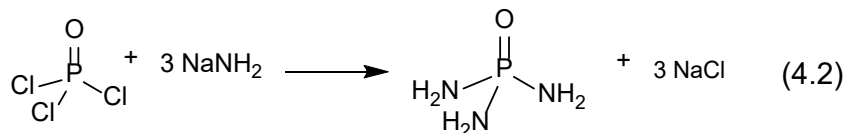
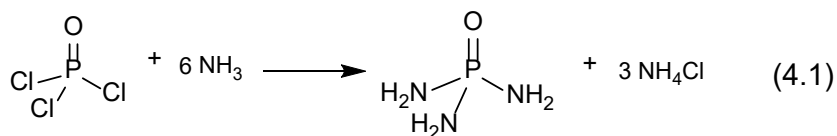
properties were determined during the third scan of DSC measurements, while the first scan serves to erase the thermal history of which the samples had been subjected to.

Detailed synthetic methods, processing techniques, and other characterization procedures are given above in Chapter 2.

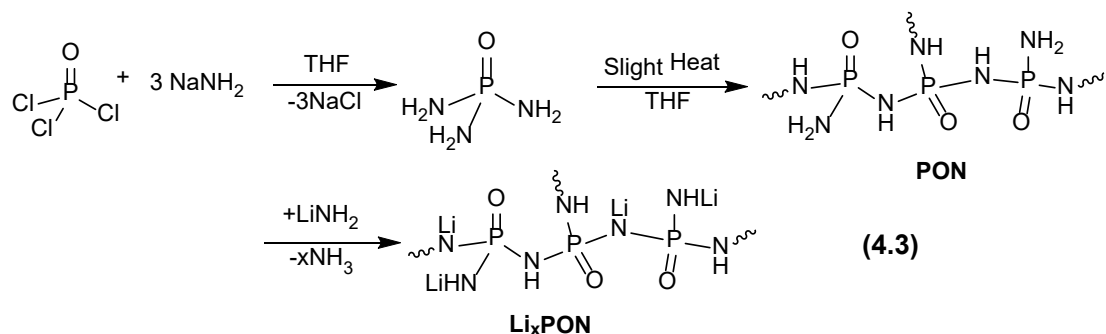
4.3 Results and discussion

4.3.1 Polymer precursor syntheses and characterization

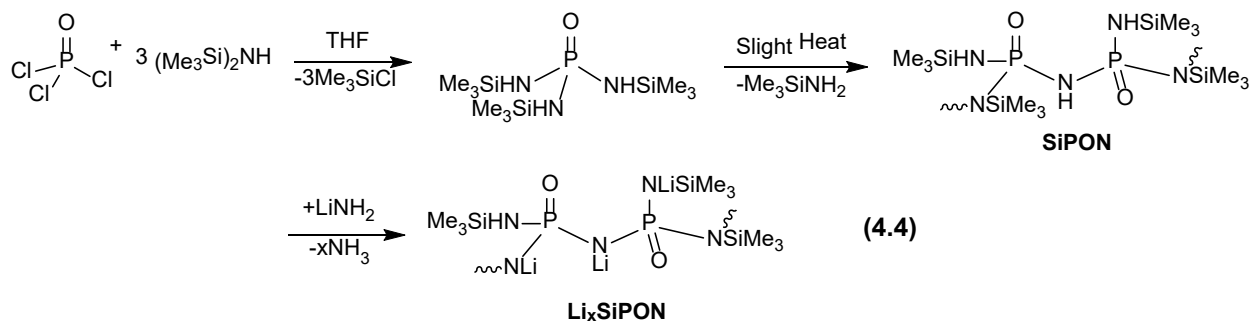
The syntheses of LiPON-like oligomer/polymer precursors start with phosphoramidate, $OP(NH_2)_3$. The simplest synthetic approach to $OP(NH_2)_3$ is via ammonolysis, reaction (4.1). However, it is difficult to remove byproduct NH_4Cl which can interfere with purification depending on the solvent.⁴⁶⁻⁴⁹ The alternative is to use $NaNH_2$ per reaction (4.2). The higher solubility of $LiCl$ vs. $NaCl$ in polar solvents can prevent simple precipitation, therefore $NaNH_2$ is preferable to $LiNH_2$.



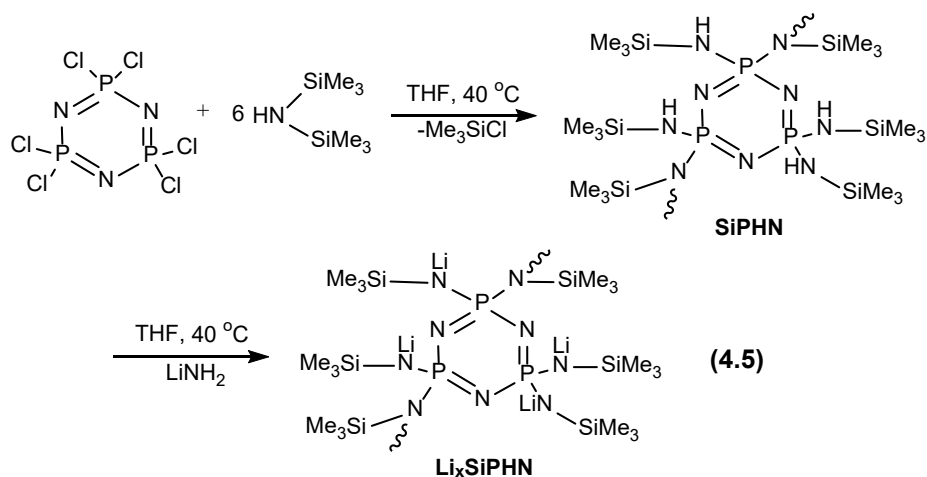
Designs of LiPON-like oligomer/polymer precursor syntheses are presented in Schemes 4.1-4.3. For both $Li_x\text{PON}$ and $Li_x\text{SiPON}$ precursors, the syntheses start by reacting $OPCl_3$ with $NaNH_2$ or $(\text{Me}_3\text{Si})_2\text{NH}$ respectively [reaction sequences (4.3) and (4.4)]. On gently heating ($40^\circ\text{C}/1$ week) or reacting at RT for 1-2 weeks, the product forms oligomeric/polymeric PON (SiPON) precursor. The byproduct $NaCl$ in the $Li_x\text{PON}$ system precipitates and is removed simply by filtration. The byproduct Me_3SiCl (b.p. = 57°C) is removed by vacuum evaporation at 40°C .



Scheme 4.1. Synthesis of Li_xPON ($x = \text{Li/P}$) precursors.



Scheme 4.2. Synthesis of Li_xSiPON ($x = \text{Li/P}$) precursors.



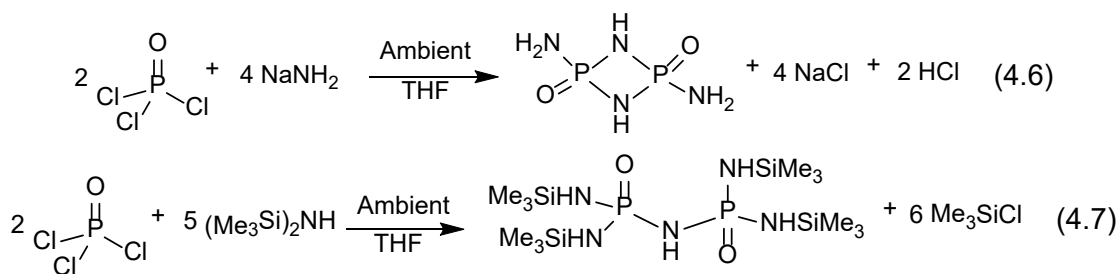
Scheme 4.3. Synthesis of Li_xSiPHN ($x = \text{Li/P}$) precursors.

For Li_xSiPHN precursors, the first step is amination via silyl exchange between the phosphazene cyclomer $[\text{Cl}_2\text{P}=\text{N}]_3$ and $(\text{Me}_3\text{Si})_2\text{NH}$ obtaining SiPHN [synthesis sequence (4.5)] coincident with volatile byproduct Me_3SiCl .

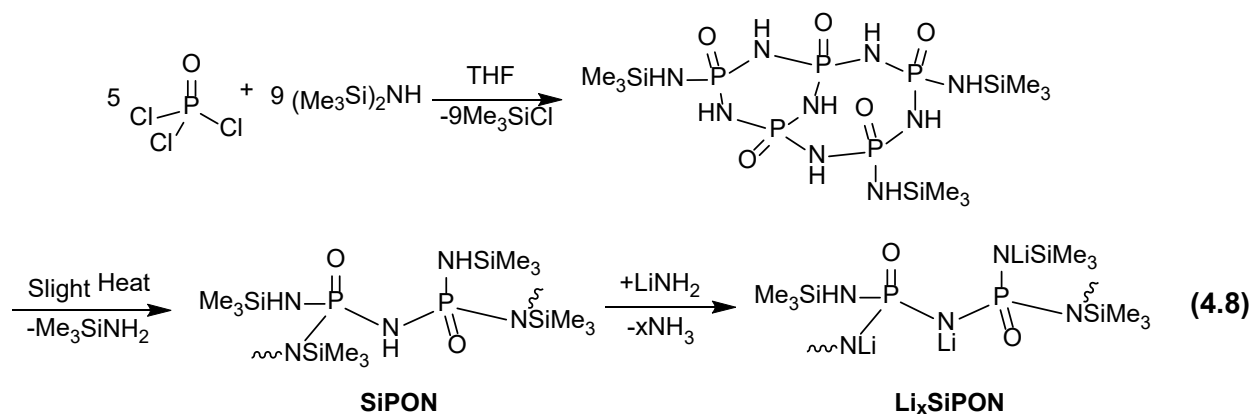
Thereafter, all precursors can be lithiated using controlled amounts of LiNH₂. The Li content in the LiPON-like precursors is readily controlled by the amount of LiNH₂ added, as confirmed by XPS studies below. In this work, the “x” in Li_xPON, Li_xSiPHN and Li_xSiPON, stands for the Li content based on the theoretical Li/P ratios used in the corresponding precursor syntheses.

One precursor design principle targets high ceramic yields (CYs) to minimize excessive volume changes associated with pyrolytic conversion precursors (average precursor density ≈ 1) to ceramic materials (ave. density >2.5).^{47–50,55} Higher CYs minimize pore formation from gaseous degradation products.

CYs typically improve with increases in MW.⁵⁵ For Li_xPON and Li_xSiPON systems, one approach to promote polymerization is to reduce the ratio of NaNH₂ or (Me₃Si)₂NH to OPCL₃ prior to lithiation, as suggested by reactions (4.6), (4.7). However, for the Li_xPON system, reducing the ratio of NaNH₂:OPCL₃ produces HCl [reaction (4.6)], resulting in an acidic environment which can be detrimental for lithiation and electrochemical performances.^{56,57}



In contrast, for Li_xSiPON system, where no HCl is produced; a reduced (Me₃Si)₂NH/OPCL₃ ratio of 1.8 is used, Scheme 4.4 [synthesis sequence (4.8)].



Scheme 4.4. Synthesis of Li_xSiPON precursors with $(\text{Me}_3\text{Si})_2\text{NH}/\text{OPCl}_3 = 1.8$.

In this section we characterize the reaction (4.3) derived Li_3PON and Li_6PON precursors. Similar results are presented for the Li_2SiPHN precursor from (4.5), and Li_3SiPON and Li_6SiPON precursors from (4.8).

Figure A.2 shows representative GPCs of the lithium-free PON, SiPHN and SiPON starting materials. The SiPHN and SiPON precursors show similar MWs of 0.2-2 kDa, while PON shows MWs of ≤ 0.5 kDa. Both SiPHN and SiPON precursors are soluble in THF forming clear solutions, while the PON precursor forms as a suspension. Since the GPC only analyzes soluble compounds, the actual MWs of the PON precursor are higher as demonstrated by MALDI-ToF.

MALDI of the lithiated precursors and their possible monomer structures are given in Figures A.3-A.8. A computer program was developed to check all the possible combinations as given in Appendix B. Negative-ion mode was used due to its higher resolution of LiPON-like precursors compared to the positive-ion mode. The ion source in negative-ion mode comes from the precursor itself which loses one Li^+ . Tables A.2-A.4 list example calculations leading to the proposed structures representative of the precursors (Li_xPON , Li_xSiPHN , and Li_xSiPON). Table 4.1 summarizes MWs and estimated compositions of the polymer precursors based on GPC and MALDI studies. Note that the Li_2SiPHN precursor consists of monomers with higher individual MWs (300-600

g/mol) than Li_xPON (80-150 g/mol) and Li_xSiPON (80-220 g/mol) precursors, thus Li_2SiPHN oligomers have lower average numbers of monomer units than the other precursors despite MALDI spectra in similar mass ranges.

Figure A.9 shows FTIR spectra of unlithiated PON, SiPHN and SiPON precursors. Table 4.2 summarizes literature reported FTIRs of LiPON glasses. Typically, the unlithiated precursors exhibit $\nu\text{N-H}$ ($\sim 3000\text{ cm}^{-1}$) and N-H overtone ($\sim 1500\text{ cm}^{-1}$), $\nu\text{P=O}$ (1150-1300 cm^{-1}), $\nu\text{P-O}^-$ (1000-1150 cm^{-1}), and $\nu\text{P-N=P}$ (800-900 cm^{-1}) absorption bands.^{40,58-61} For the SiPHN precursor, since no oxygen is present, peaks at ~ 1200 and $970\text{-}850\text{ cm}^{-1}$ can be assigned to $\nu\text{P-N}$ and $\nu\text{P-N=P}$, respectively.^{40,59,61}

The lithiated precursors were heated to 100-600 °C (10 °C/min) under vacuum or N_2 , Figure 4.1 shows the FTIR spectra of precursors at different temperatures (RT-600 °C). In general, precursors below 200 °C show spectra similar to the unlithiated precursors, $\nu\text{N-H}$ ($\sim 3000\text{ cm}^{-1}$, $\sim 1500\text{ cm}^{-1}$), $\nu\text{P=O}$ (1150-1300 cm^{-1}), $\nu\text{P-O}^-$ (1000-1150 cm^{-1}), $\nu\text{P-N=P}$ (800-900 cm^{-1}) and $\nu\text{P-O-P}$ (1150, 780-680 cm^{-1}).^{40,58-61} Additionally, Li_2SiPHN (Figure 4.1c) and Li_xSiPON (Figures 4.1d-e) precursors exhibit $\nu\text{C-H}$ at $\sim 2950\text{ cm}^{-1}$, which disappears at $\sim 300\text{ °C}$. Often, we observe $\nu\text{O-H}$ at $\sim 3400\text{ cm}^{-1}$, possibly from excess LiNH_2 that reacts with trace moisture during sample preparation forming LiOH.

In addition to the aforementioned adsorptions, a small peak at $\sim 2200\text{ cm}^{-1}$ is observed in some precursors, especially for the Li_3PON precursor. Pichonat *et al.*⁶¹ and Stallworth *et al.*⁶² suggest that peaks at 2200-2100 cm^{-1} may come from $\text{P-N}<^{\text{P}}$ or P-N=P bonds. In general, the intensity of this peak decreases as temperature increases and disappears at 300 °C, suggesting rearrangement or reaction of these bonds. The intensities of $\nu\text{O-H/N-H}$ bonds reduce as temperatures increase, the dominant peak at $\sim 1040\text{ cm}^{-1}$ at 600 °C can be assigned to $\nu\text{P-O}^-$.^{63,64}

Table 4.1. MWs and estimated compositions of polymer precursors.

Polymer precursor	MW ^a , kDa	No. monomer units ^b	Possible monomer structures ^c
Li ₃ PON	0.6-1.4	5-15	
Li ₆ PON	0.6-1.9	5-20	
Li ₂ SiPHN	0.7-1.5	2-4	
Li ₃ SiPON	0.5-1.0	5-13	
Li ₆ SiPON	0.7-1.5	6-15	

^aMW = molecular weight. ^bNumber of monomer units calculated based on MALDI (Figures A.3-A.8, Tables A.2-A.4). ^cIn the monomer structures, X = H or Li.

Table 4.2. Reported FTIR of LiPON glasses.

IR bands	Wavenumber, cm ⁻¹	Reference
P=O	1150-1300	40,58-61
P-O ⁻	950-1150	
P-O-P	1150, 780-680	
P-N=P	800-900	
P-N=P or P-N< _p	2200-2100	61,62
-NH ₂ /-NH	~3400	40
Li-O-P	450-550, 850-925, 1450-1500	58

Figure 4.2 compares representative TGA-DTA (800 °C/10 °C min⁻¹/N₂) of the vacuum dried (100 °C/1 h) precursors (Li_xPON, Li_xSiPHN, and Li_xSiPON). All precursors typically have 5 % mass loss temperatures (T_{5%}) ≥ 150 °C, and similar ceramic yields (CYs) of 50-60 wt.% at 800 °C. An endotherm at ~600 °C is exhibited for all the precursors, which suggests melting. This provides the potential of melt bonding for solid-state battery assembly.

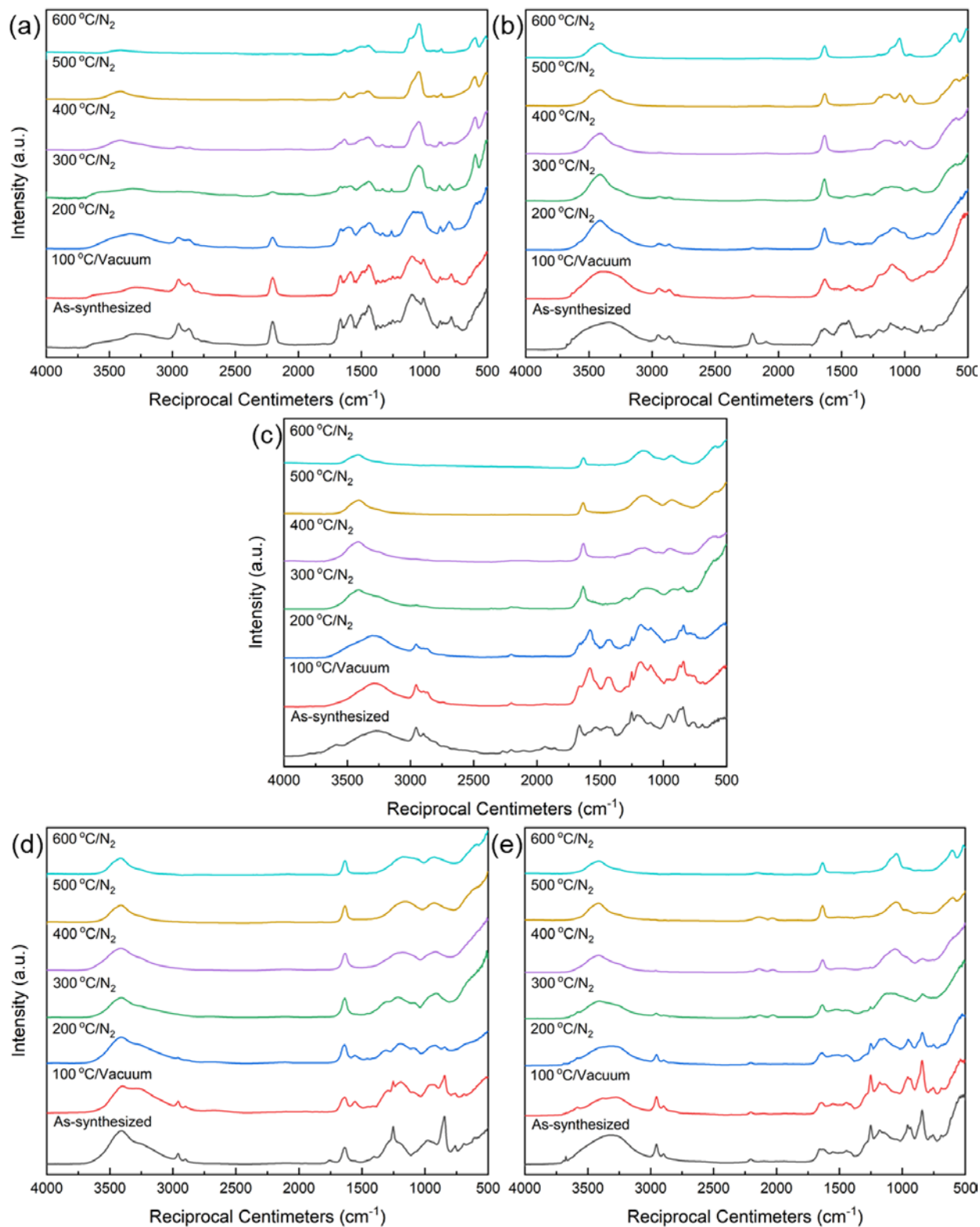


Figure 4.1. FTIR spectra of Li_3PON (a), Li_6PON (b), Li_2SiPHN (c), Li_3SiPON (d), and Li_6SiPON (e) precursors at different temperatures.

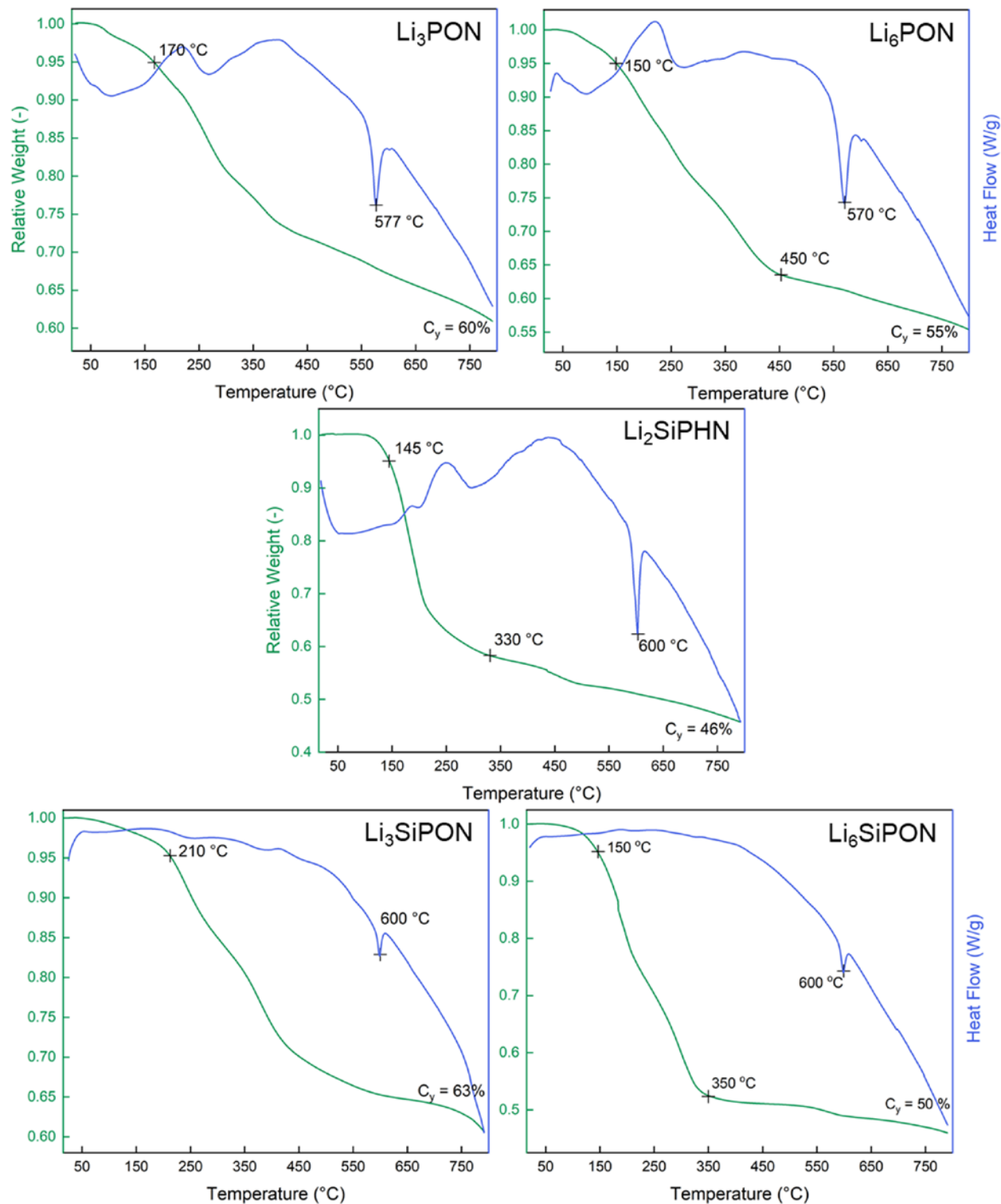


Figure 4.2. TGA-DTA (800 °C/10 °C min⁻¹/N₂) of Li₃PON, Li₆PON, Li₂SiPHN, Li₃SiPON and Li₆SiPON precursors.

Figure 4.3a compares ^7Li NMR (CDCl_3) of vacuum dried (RT) polymer precursors, the band width of Li_xSiPON precursors is qualitatively greater than found for the Li_xPON and Li_2SiPHN precursors suggesting these precursors may have several Li^+ chemical environments.

Based on the above proposed precursors structures, one can suggest possible Li^+ environments per Figure 4.3b. If we consider Li^+ bonded to N of (H)N-P as type **A**, typical for Li_xPON (marked as red in Figure 4.3b), and Li^+ bonded to an N between SiMe_3 and P as type **B**, typical for Li_xSiPHN (marked as green in Figure 4.3b), then Li_xSiPON precursors will have both types in agreement with the ^7Li NMRs for both Li_xPON and Li_2SiPHN precursors, which show single sharp peaks at different chemical shifts. In contrast, the Li_xSiPON precursors show broader peaks with chemical shifts similar to Li_2SiPHN due to the presence of SiMe_3 groups.

Of import, precursors with higher Li^+ contents also seem to show higher chemical shifts ($\text{Li}_6\text{PON} > \text{Li}_3\text{PON}$ and $\text{Li}_6\text{SiPON} > \text{Li}_3\text{SiPON}$) in agreement with See *et al.*⁶⁵ using a mixture of dioxolane and dimethoxyethane (DOL/DME, 1:1). This group found that ^7Li resonances shift to higher frequencies with increases in Li^+ concentration. These results may derive from increased numbers of solvated Li^+ ions causing a deshielding effect but may also be due to changes in the Li^+ coordination number.

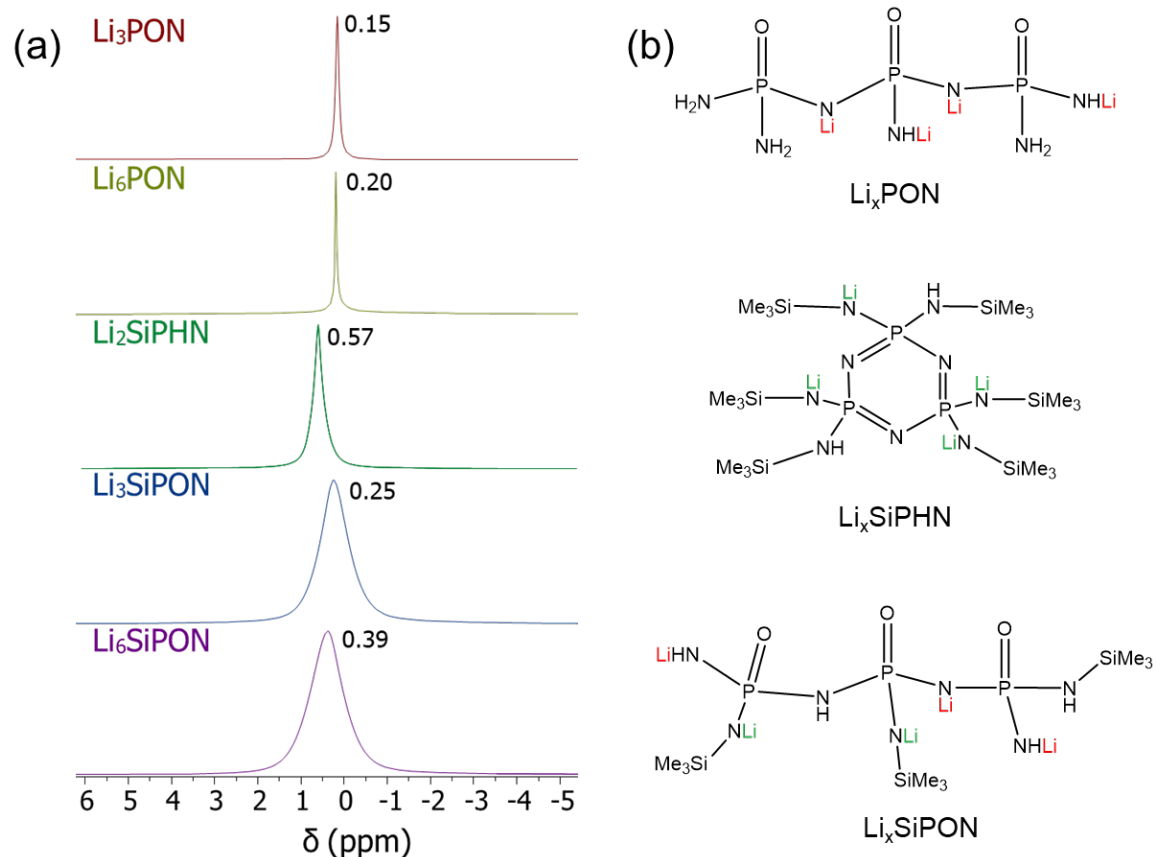


Figure 4.3a. ${}^7\text{Li}$ NMR of Li_3PON , Li_6PON , Li_2SiPHN , Li_3SiPON and Li_6SiPON precursors (RT/vacuum dried, dissolved in CDCl_3). **b.** Exemplary structures of Li_xPON , Li_xSiPHN and Li_xSiPON precursors with Li^+ highlighted.

Table 4.3 lists ${}^7\text{Li}$ NMR studies of various compounds in solution from the literature. Typically, a standard reference (0.1M or 1M LiCl in D_2O or THF-d_8) is used. In general, Li^+ in a complex structure with considerable electron shielding shows upfield chemical shifts. In contrast, Li^+ cations in the LiClO_4 solution are highly dissociated and show a large downfield chemical shift (2.12 ppm). The positive chemical shifts found for the Li_xPON , LiSiPHN , and Li_xSiPON precursors suggest the Li^+ ions are well solvated and dissociated which is in accord with our findings that they offer superior properties in a set polymer electrolyte batteries with Li-S cathodes and as ceramic precursors on ceramic electrolytes.^{51,54}

Additionally, N/P ratios may also influence chemical shifts (Table 4.4). As suggested by Muñoz *et al.*,⁶⁶ higher nitrogen contents (N/P ratios) lead to increases in the chemical shifts of the ⁷Li NMR resonances, related to decreases in average Li⁺ coordination numbers.^{66,67}

Table 4.3. ⁷Li NMR studies on various compounds in solution from the literature.

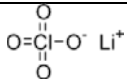
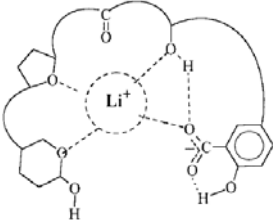
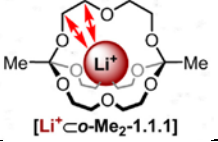
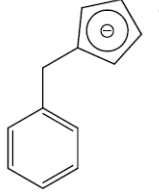
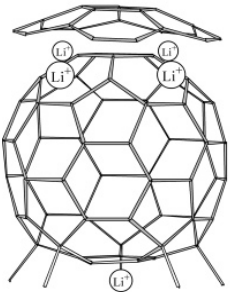
Compound	Structure	Solvent	Chemical shift δ (ppm)	Ref.
LiClO ₄		CD ₃ CN/CDCl ₃	2.12	68
Lasalocid lithium salt		CDCl ₃	-1.02	
[Li ⁺ c-o-Me ₂ -1.1.1]TPFPB ⁻		CDCl ₃	-1.85	69
Benzyl cyclopentadienyl lithium		THF-d ₈	-8.06	70
Me ₅ C ₆₀ ⁵⁻ /Cor ⁴⁺ /9Li ⁺		THF-d ₈	-5.91; -7.36	71

Table 4.4. ⁷Li NMR and atomic ratios based on XPS analyses for polymer precursors (RT/vacuum dried).

	Li ₃ PON	Li ₆ PON	Li ₂ SiPHN	Li ₃ SiPON	Li ₆ SiPON
⁷ Li NMR (ppm)	0.15	0.20	0.57	0.25	0.39
O/P	4.6	4.8	1.3	1.7	3.0
N/P	1.1	1.4	3.0	1.9	2.0
Li/N	1.0	2.0	0.3	0.95	1.4
Li/P	1.1	2.7	0.9	1.8	2.8

Figure **4.4a** shows ^{13}C NMRs of Li_2SiPHN and Li_xSiPON precursors (C-containing precursors). All precursors exhibit a peak at ~ 2.5 ppm similar to $(\text{Me}_3\text{Si})_2\text{NH}$ ($\delta_{\text{C}} = 2.64$ ppm), corresponding to carbons in the NH-SiMe_3 groups. However, this peak is slightly shifted upfield ($\Delta\delta = 0.10\text{-}0.15$ ppm). NMR chemical shifts are affected by electron density, when $(\text{Me}_3\text{Si})_2\text{NH}$ loses one SiMe_3 and bonds with P=O or P-N=P (see examples in Figure **4.3b**) in the polymer backbone, the carbon environment changes slightly (more shielded), causing a $\Delta\delta \approx 0.2$ ppm upfield shift.

Additionally, a small peak at ~ 2 ppm is exhibited in all precursors, which may be $\text{Me}_3\text{SiO-}$ group. As shown in Figure **A.10a**, $(\text{Me}_3\text{Si})_2\text{O}$ has a δ_{C} of 1.94 ppm.

Some precursors also show a small peak at ~ 3.9 ppm, which may be Me_3SiCl or Me_3SiNH_2 . As shown in Figure **A.10b**, Me_3SiCl has a δ_{C} of 3.26 ppm,⁷² slightly different from our observation. Therefore, the peak at ~ 3.9 ppm is likely Me_3SiNH_2 (NMR spectrum not found in literature).

Figure **4.4b** shows ^{29}Si NMRs of silicon-containing polymer precursors. All precursors show a peak at 2.3 ppm corresponding to NH-SiMe_3 groups, similar to the chemical shift of $(\text{Me}_3\text{Si})_2\text{NH}$ at 2.42 ppm. In accordance with ^{13}C NMR, the upfield shift ($\Delta\delta \approx 0.1$ ppm) suggests the silicon environment becomes more shielded when $(\text{Me}_3\text{Si})_2\text{NH}$ loses one $-\text{SiMe}_3$ and bonds to the polymer backbone.

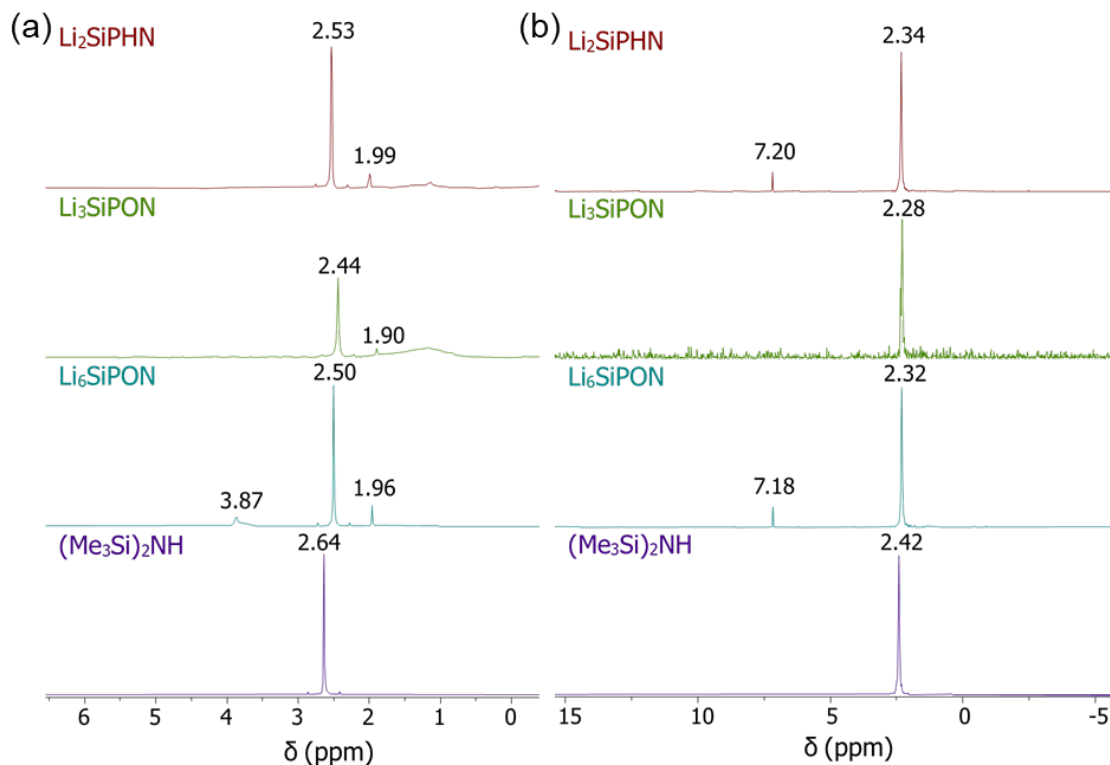


Figure 4.4. ^{13}C NMR (a) and ^{29}Si NMR (b) of Li_2SiPHN , Li_3SiPON and Li_6SiPON precursors (RT/vacuum dried, dissolved in CDCl_3) in comparison with $(\text{Me}_3\text{Si})_2\text{NH}$.

Some precursors also show a smaller peak at 7.2 ppm, which may be Me_3SiNH_2 or Me_3SiCl , as the silicon would be less electronically shielded (lower electron density near H and higher electronegativity with Cl) compared to $\text{P}=\text{O}-\text{NH}(\text{SiMe}_3)_2$ or $\text{P}-\text{N}=\text{P}-\text{NH}(\text{SiMe}_3)_2$. Table A.5 shows the electronegativity of selected elements. However, Me_3SiCl has a δ_{Si} of 31 ppm.^{72,73} Therefore, the corresponding compound at 7.2 ppm is likely Me_3SiNH_2 , which is in agreement with the δ_{C} at 3.9 ppm for ^{13}C NMR study.

Due to the lower sensitivity of ^{29}Si NMR, fewer peaks are observed compared to ^{13}C NMR.

Figure 4.5 shows ^1H NMRs of proton-containing polymer precursors and $(\text{Me}_3\text{Si})_2\text{NH}$. In general, protons from methyl groups and THF are observed. Since the precursors are dried at RT, there is a trace amount of THF left. All precursors show a large peak at 0.01 ppm, which is similar to

the -CH₃ groups from (Me₃Si)₂NH at 0.06 ppm, but slightly shifted to upfield, likely a result of polymerization causing a shielding effect in agreement with ¹³C and ²⁹Si NMR studies.

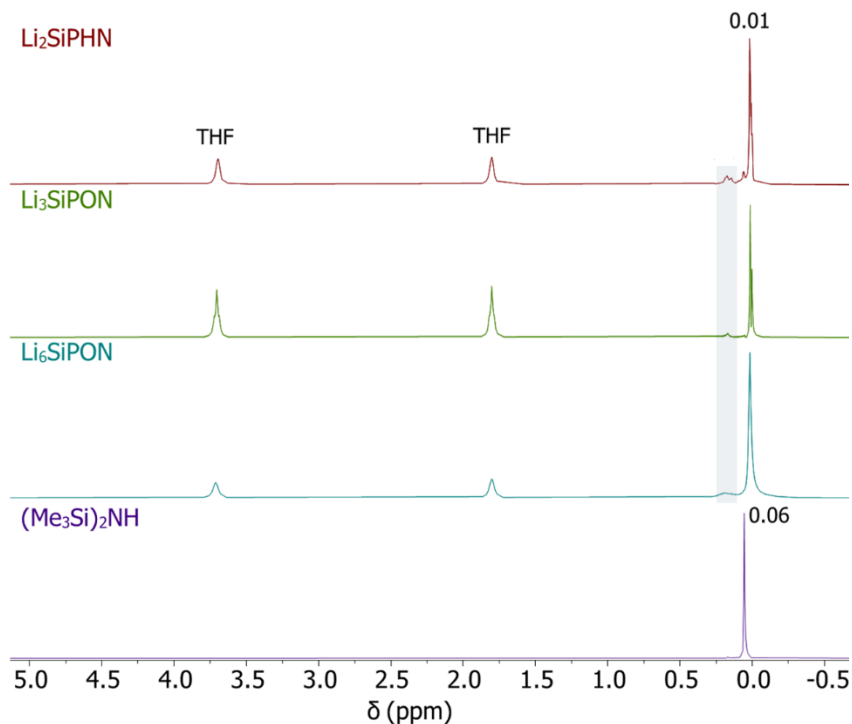


Figure 4.5. ¹H NMR of Li₂SiPHN, Li₃SiPON and Li₆SiPON precursors (RT/vacuum dried, dissolved in CDCl₃) in comparison with (Me₃Si)₂NH.

Additionally, small peaks at 0.15-0.2 ppm are exhibited. Figure A.11 shows ¹H NMR models of Me₃SiNH₂, (Me₃Si)₂O, and Me₃SiCl by ChemDraw, the main δ_H peaks are 0.08, 0.21 and 0.42 ppm respectively. The chemical shift at 0.15-0.2 ppm may be Me₃SiO- groups that shifted to upfield due to interaction with the polymer precursors.

Overall, only -SiMe₃ protons are observed, no proton migration is suggested by ¹H NMR.

Figures 4.6a-b show XRD patterns of Li_xPON pellets (5 ksi/RT/20 s, Φ = 13 mm) heated to 100-600 °C/2 h/N₂. The XRD of Li₃PON pellets heated to 100 °C shows a small peak near 35° 2θ, corresponding to Li₂O_{0.75}N_{0.25} phase (PDF-01-080-4542) with space group 225: Fm3m. However, it is mostly dominated by a broad peak 20° 2θ corresponding to amorphous nature of the material.

Three peaks at 30° , 33° , and 35° 2θ can be indexed to partially crystalline $\text{Li}_{2.88}\text{PN}_{0.14}\text{O}_{3.73}$, Li_2NH_2 , and $\text{Li}_2\text{O}_{0.75}\text{N}_{0.25}$ phases when the pellet is heated to 200-400 $^\circ\text{C}$. These peaks shift to 35° and 37° 2θ along with additional doublet peaks near 23° 2θ when the pellet is heated to 500 $^\circ$ and 600 $^\circ\text{C}$ corresponding to $\text{Li}_{2.88}\text{PN}_{0.14}\text{O}_{3.73}$. Similar peaks are present for Li_6PON pellets, Figure **4.6b**.

Figure **4.6c** shows XRD patterns of Li_2SiPHN pellets heated to 100-600 $^\circ\text{C}/2$ h/ N_2 . The XRD of Li_2SiPHN pellets heated to 100-300 $^\circ\text{C}$ is mostly dominated by a broad peak corresponding to poorly crystallized compound indicating amorphous nature of the pellet. Two main peaks at 22° and 29° 2θ can be indexed to partially crystalline $\text{Li}_4\text{P}_2\text{O}_7$ when heated to 500 $^\circ\text{C}$. The double peaks near 24° and 25° 2θ can be indexed to $\text{Li}_{6.6}\text{SiPO}_8$.

Figures **4.6d-e** show XRD patterns for Li_xSiPON pellets heated to 100-600 $^\circ\text{C}/2$ h/ N_2 . XRDs of Li_3SiPON pellets heated to 100-300 $^\circ\text{C}$ is dominated by a broad peak corresponding to poorly crystallized compound indicating an amorphous nature. Two main peaks at 22° and 29° 2θ can be indexed to partially crystalline $\text{Li}_4\text{P}_2\text{O}_7$ (PDF-01-084-7598) after heating to 400 $^\circ$ and 500 $^\circ\text{C}$. The single peak $\sim 29^\circ$ 2θ started to split in to double peaks when the pellet was heated above 500 $^\circ\text{C}$. The XRD of Li_3SiPON pellets heated 600 $^\circ\text{C}$ show sharp peaks matching $\text{Li}_4\text{P}_2\text{O}_7$ (PDF-01-083-9707) indicating loss of nitrogen doping.

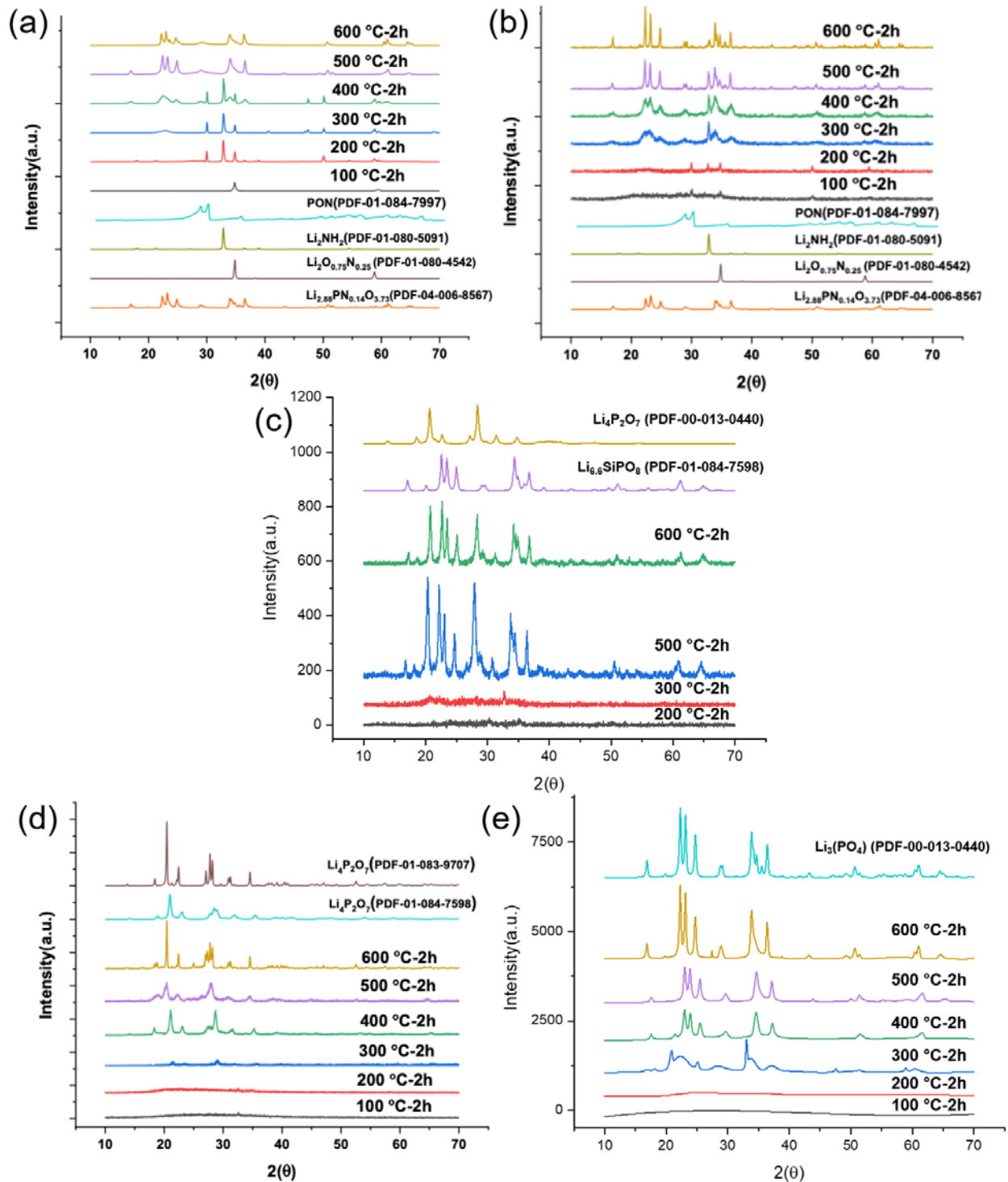


Figure 4.6. XRD plots of Li₃PON (a), Li₆PON (b), Li₂SiPHN (c), Li₃SiPON (d), and Li₆SiPON (e) heated to 100-600 °C/2 h/N₂.

XRDs of Li₆SiPON pellets heated to 100° and 200 °C are mostly dominated by broad peak (Figure 4.6e). The pellet heated to 300 °C showed doublet peaks ~20° and 30° 2θ indexed to partially crystalline Li₃PO₄. The XRD of Li₆SiPON pellets heated to 400-600 °C show sharp peaks matching Li₃PO₄ (PDF-04-007-2815) indicating loss of nitrogen doping.

XRD studies at 100 °C show mainly amorphous phase, hence this technique cannot detect the targeted elements nor quantify the components and or elemental ratios. Hence XPS studies were run on Li₃PON, Li₆PON, Li₂SiPHN, Li₃SiPON, and Li₆SiPON precursors dried under vacuum for 3 d/RT. The dried precursor (0.5 g) powders were pelletized using 13 mm diameter die/5 ksi/RT. XPS wide scan spectra and analyses are given in Figure A.12 and Table 4.5, respectively.

Table 4.5. XPS analyses of Li_xPON, Li₂SiPHN and Li_xSiPON pellets.

		Li ₃ PON	Li ₆ PON	Li ₂ SiPHN	Li ₃ SiPON	Li ₆ SiPON
Li 1s	B.E. ^a (eV)	52	52	52	53	53
	At.% ^b	7.0	12.6	6.7	13	17.6
P 2p	B.E. (eV)	130	130	130	131	130
	At. %	6.2	4.6	7.4	7.2	6.2
O 1s	B.E. (eV)	528	529	528	529	528
	At. %	28.7	22	9.5	12.3	18
N 1s	B.E. (eV)	396	396	395	396	396
	At. %	7.0	6.4	21.8	13.6	12.5
C 1s	B.E. (eV)	282	282	281	282	282
	At. %	43.5	47.6	44.5	37	40
Cl 2p	B.E. (eV)	195	195	195	196	196
	At. %	7.6	6.8	7.3	12.3	4.0
Si 2p	B.E. (eV)	-	-	98	98	98
	At. %	-	-	2.8	4.6	1.7

^aB.E. = binding energy. ^bAt.% = atomic percentage.

The Figure A.12a-b wide-scan XPS survey spectra of Li₃PON and Li₆PON pellets provides elemental compositions of Li₃PON and Li₆PON pellets confirming the signature elements, with minor peaks for C and Cl. The presence of chlorine likely arises from residual NaCl. Carbon is ubiquitous in XPS spectra but also may reflect brief exposure of the precursor to air forming Li₂CO₃ during pelletization. Results obtained from XPS are summarized in Tables 4.4 and 4.5.

They confirm the presence and incorporation of nitrogen into the pellets and reinforce the fact that the chemical makeup of the Li_3PON and Li_6PON pellets are similar to those found in previous studies of gas phase deposited materials.^{21,61,74}

The deduced atomic composition shows that the Li At.% increased from ~7 to 12.6 when LiNH_2 was doubled from Li_3PON to Li_6PON . Moreover, XPS analysis also provides information about bonding environments. The O 1s peak is attributed to the Li-O-Li, P-O-P, and P=O bonds. The N/P ratio (1.1-1.4) is higher than what is reported by gas phase deposition techniques (typically <1) which seems to be reflected in the higher Li^+ conductivities seen in the materials prepared here.^{61,75}

The Figure **A.12d-e** wide-scan survey XPS spectra of Li_3SiPON and Li_6SiPON pellets also present representative LiSiPON elemental signatures and minor peaks for C and Cl. The presence of chlorine might be from residual NaCl or Me_3SiCl . The presence of carbon can arise as noted above or from $(\text{Me}_3\text{Si})_2\text{NH}$. As shown in Table **4.5**, the Li At.% increased from ~13 to 18 when more LiNH_2 is introduced in synthesizing Li_6SiPON . In addition, the Li amount is higher than calculated for Li_3PON (7) and Li_6PON (12.6) pellets. This may be due to incorporation of silicon in the polymer precursor. It has been reported that partial substitution of P by Si in LiPO_4 results in an increase in Li^+ mobility by shortening the distance between adjacent positions for Li^+ hopping.⁷⁶

Furthermore, it has also been demonstrated that increases in N in LiSiPON films increases conductivity. The increase in the Si/P ratio has been hypothesized to improve the N content.³² The experimental ratio of N/P was calculated to be 3, the decrease in the ratio from XPS points to polymerization by loss of nitrogen. However, the N/P ratio (~2) is still higher than for Li_3PON and Li_6PON in Table **4.4**. The Li_6SiPON polymer electrolyte also shows the lowest Cl At.%.

The Figure **A.12c** wide-scan survey XPS of Li_2SiPHN presents the expected elemental signatures and minor peaks for C and Cl. The latter elements are likely sourced as noted above. The results obtained from XPS are summarized in Tables **4.4** and **4.5**.

The calculated atomic composition shows an Li/P ratio of 0.9 as listed in Table **4.4**. However, this ratio is smaller than what is calculated experimentally for Li_2SiPHN , the discrepancies are thought to arise from polymerization that reduces the number of sites that can be lithiated. Another explanation might be due to the fact that XPS could only be used to predict the composition of thin films and not bulk pellets.

SEM and EDX studies were conducted to characterize the microstructures and the composition of the polymer precursors. Figure **4.7** shows SEM fracture surface images of Li_3PON , Li_6PON , Li_2SiPHN , Li_3SiPON , and Li_6SiPON precursor pellets heated to 100-400 °C/2 h/ N_2 . The pellets heated to 100 °C in general showed a very smooth, uniform, and dense microstructure. This might be ascribed to the fact that these precursors show a very small mass loss before 200 °C as demonstrated by the TGA-DTA in Figure **4.2**. The pellets heated between 200-300 °C showed a 3D network of structures forming micro globules. When the heating schedule increased to 400 °C, the pellets showed porous microstructure ascribed to the loss of volatile and organic compounds, indicating the ceramization of the precursors as supported by the XRD in Figure **4.6**.

Figure **A.13** shows EDX map images of polymer precursor pellets heated to 100 °C/2 h/ N_2 . Well-distributed signature elements (N, O, P, and Si) are exhibited, and the presence of impurities such as Cl from the starting material and C from Li_2CO_3 is in good agreement with XPS data shown in Figure **A.12** and Table **4.5**. Quantitative EDX results are summarized in Table **A.6**. The N/P ratio seems to increase with the heating temperature of the polymer precursor pellets, which

might be ascribed to the loss of CO₂ during heating. The Li₆PON pellets showed a lower N/P ratio compared to Li₃PON, resulting in a lower ionic conductivity in the Li₆PON pellets.

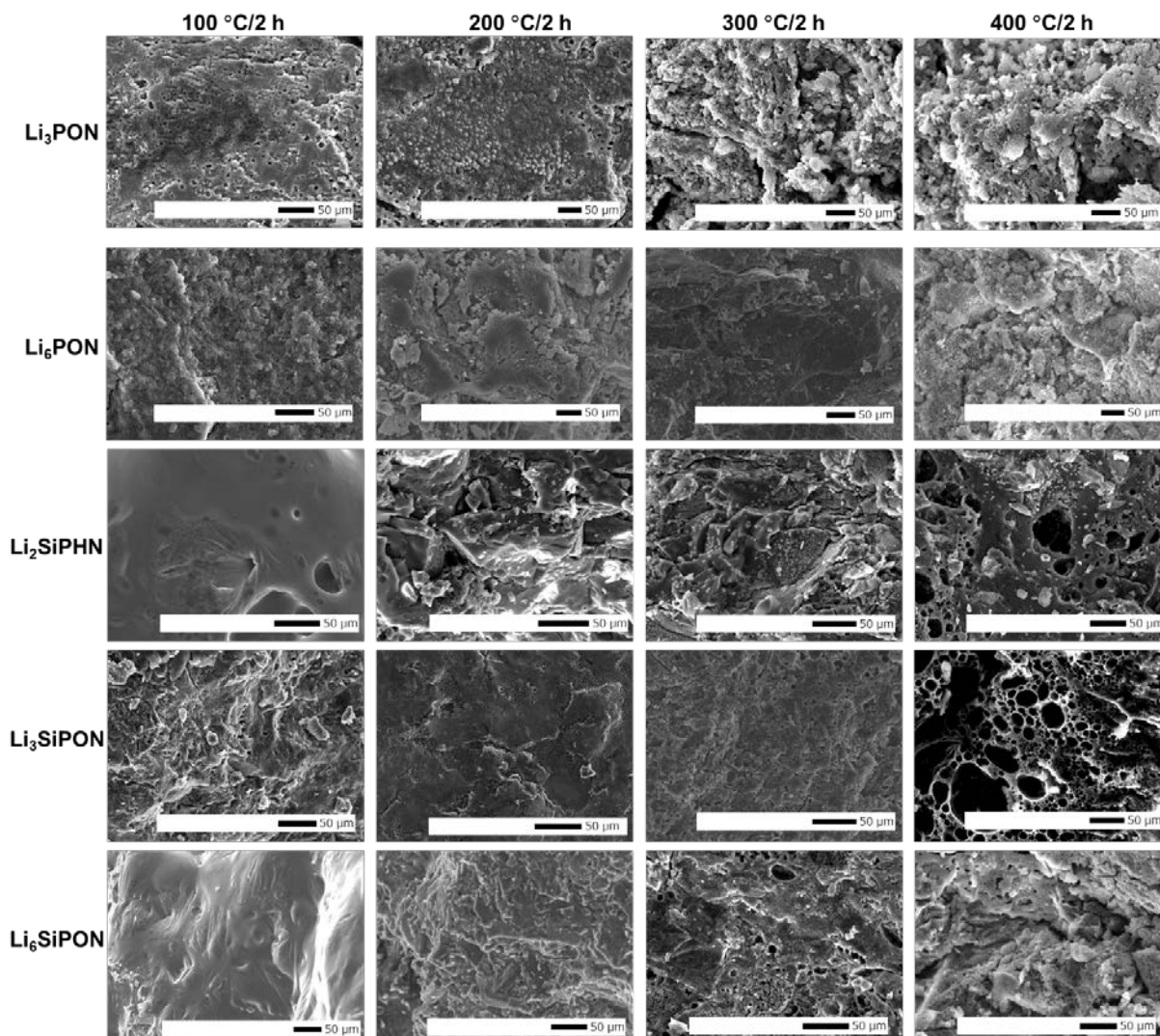


Figure 4.7. SEM fracture surface images of Li_xPON, Li₂SiPHN and Li_xSiPON pellets heated between 100-400 °C/2 h/N₂.

4.3.2 Li⁺ conductivity measurements

Conductivity measurements were run on compacted pellets rather than thin films as reported in complementary manuscripts.^{51,54} Figure 4.8 shows Nyquist plots of Li₃PON, Li₆PON, Li₂Si-PHN, Li₃SiPON, and Li₆SiPON pellets heated to 200-400 °C/2 h/N₂. All the measurements were conducted at RT.

Table 4.6 summarizes the total ambient conductivity of the polymer precursor pellets heated to 200-400 °C/2 h/ N₂. The highest conductivities are obtained on heating to 400 °C. The conductivity seems to improve with increasing temperature improving pathways for Li⁺ diffusion due to phase change as demonstrated by XRD plots in Figure 4.6. Li₂SiPHN shows the highest conductivity of 3×10^{-4} S/cm at 400 °C. This polymer precursor also shows the densest microstructure when compared to Li_xSiPON polymer precursors (Figure 4.7). The Li₃SiPON showed the lowest conductivity when heated to 400 °C ascribed to the increased porosity in the microstructure (Figure 4.7). The Li_xPON polymer precursors showed poor ionic conductivity compared to the Si based polymer precursors, these phenomena can be explained by the low N/P ratios (< 1.5) as well as the poor microstructure as shown in Table 4.4 and Figure 4.7, respectively.

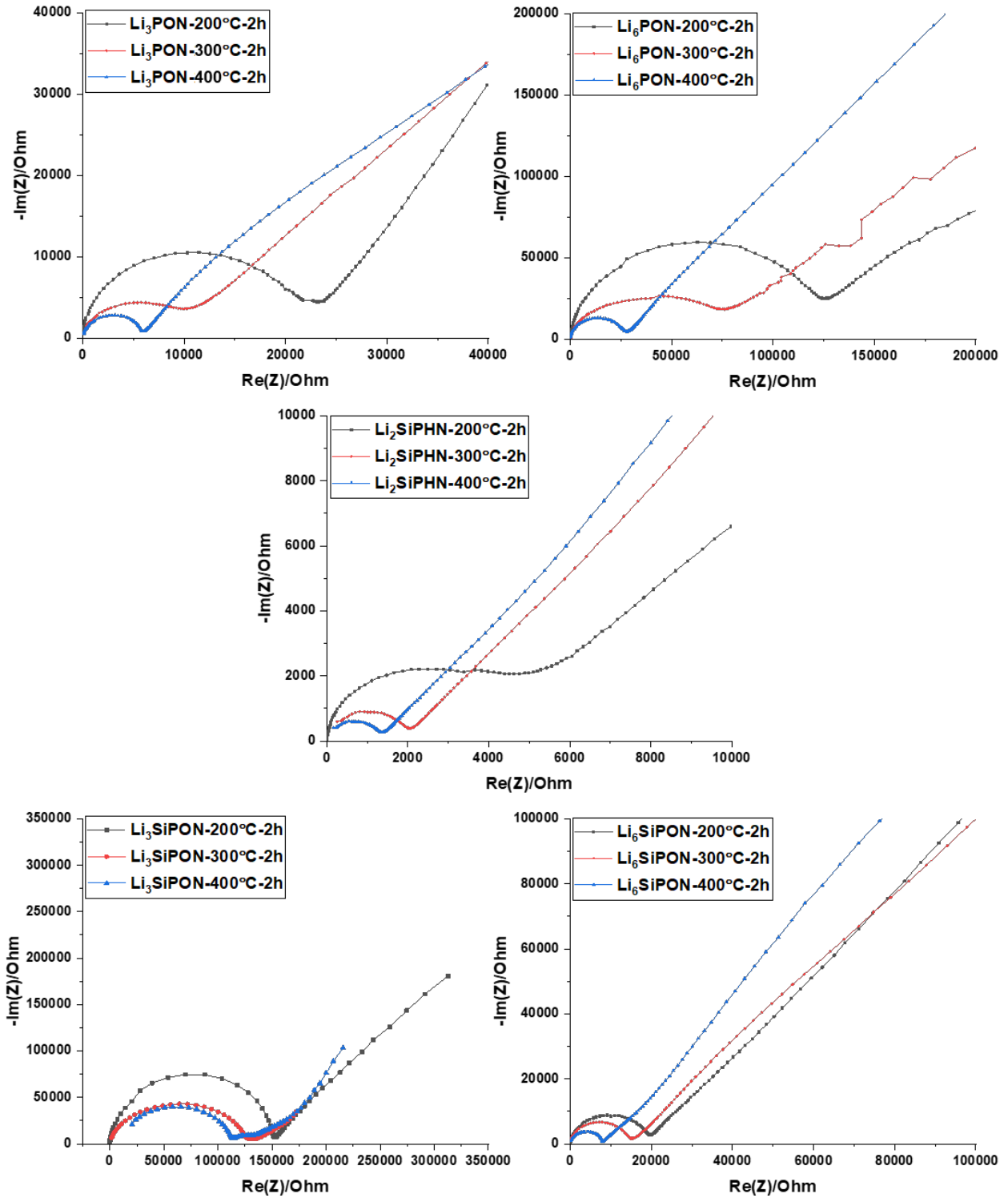


Figure 4.8. Nyquist plots of polymer precursor pellets heated to 200-400 °C/2 h/ N_2 .

Table 4.6. Total conductivities (σ_{RT}) of polymer precursor pellets heated to 200-400 °C/2 h/N₂.

Precursor pellets	Temp. (°C)	σ_{RT} (S/cm)
Li ₃ PON	200/2 h	1.1×10^{-5}
	300/2 h	1.8×10^{-5}
	400/2 h	4.5×10^{-5}
Li ₆ PON	200/2 h	1.9×10^{-6}
	300/2 h	5.3×10^{-6}
	400/2 h	1.2×10^{-5}
Li ₂ SiPHN	200/2 h	5.7×10^{-5}
	300/2 h	1.5×10^{-4}
	400/2 h	2.7×10^{-4}
Li ₃ SiPON	200/2 h	2.0×10^{-6}
	300/2 h	1.6×10^{-6}
	400/2 h	4.0×10^{-6}
Li ₆ SiPON	200/2 h	1.9×10^{-5}
	300/2 h	2.0×10^{-5}
	400/2 h	3.3×10^{-5}

4.3.3 Electrochemical performance of polymer precursor electrolytes

To further investigate electrochemical properties of these polymer precursors, Celgard separators were coated with polymer precursor solutions (0.05 g/mL in THF, 20 μ L) and heated to 90 °C/12 h/vacuum prior to cell assembly. SS/Celgard + polymer precursor/SS and Li/Celgard + polymer precursors/Li symmetrical cells and SPAN (sulfur-based cathode)/Celgard + polymer precursors/Li half cells were then assembled. Detailed cell fabrication procedure, characterization methods, results and discussion are reported elsewhere.⁵¹

Figure 4.9a shows the correlation of N/P ratio with ionic conductivities of SS/Celgard + polymer precursor/SS cells. Note that the N/P ratio is derived from XPS studies on polymer precursor pellets after heating to 90 °C/12 h/vacuum, slightly different results from values in Table 4.4. The increase in the N/P ratio results in a nearly linear increase in conductivity for coated Celgard. A maximum conductivity of 8.8×10^{-6} S/cm is achieved for the Celgard + Li₆SiPON polymer electrolyte with an N/P ratio of 2.4. The N/P ratio is very high compared to traditional gas-phase tech-

niques resulting in enhanced ionic conductivity.^{61,75} The positive correlation between ionic conductivity and the N/P ratio can be attributed to the decrease in electrostatic energy as adding more Na bridging and increased disorder that increases Li⁺ mobility.^{77,78}

Figure **4.9b** compares the average transference numbers (t_{Li^+}) of polymer precursor coated Celgards assembled in symmetric cell configuration (Li/Celgard + polymer precursor/Li). Overall, all polymer precursor coated Celgard electrolytes exhibit $t_{\text{Li}^+} \geq 0.7$, much higher than traditional polymer electrolytes (0.2-0.5).^{79,80} The Li₂SiPHN precursor showed an ideal transference number of ~ 0.9 comparable to solid-state electrolytes. The increase in the t_{Li^+} for the polymer electrolytes is indicative of a chemical interaction between Li and -PON, -SiPHN and -SiPON polymeric backbones, that in turn afforded high Li⁺ mobility and near single-ion conduction. From these preliminary results, the t_{Li^+} is in the order of Li₆SiPON < Li₃PON < Li₃SiPON < Li₆PON < Li₂SiPHN.

The electronic conductivities of polymer precursors coated Celgard coated measured by DC polarization experiments are given in Figure **4.9c**. Li₃PON and Li₆PON polymer electrolytes show an average electrical conductivity of ~ 3 and 2.6×10^{-10} S/cm, respectively. These values are higher than what is reported for Li_xPON systems (10^{-15} - 10^{-12} S/cm),^{27,81} but much lower than LLZO (10^{-8} - 10^{-7} S/cm)⁸² and Li₂S-P₂S₅ (10^{-9} - 10^{-8} S/cm)⁸³ solid electrolytes. The Li₂SiPHN polymer electrolyte exhibits an average electrical conductivity of $\sim 2.7 \times 10^{-9}$ S/cm, whereas Li₃SiPON and Li₆SiPON polymer electrolytes show lower average electronic conductivities of ~ 6.2 and 1.8×10^{-10} S/cm, respectively. The increase in Li⁺ concentration from Li₃SiPON to Li₆SiPON seems to reduce the electrical conductivity. Similar phenomena are observed when the Li concentration increased from Li₃PON to Li₆PON. It is also worth noting that the electrical conductivity measurements are done on the polymer precursor coated separators, the precursor by itself might have lower electronic conductivity.

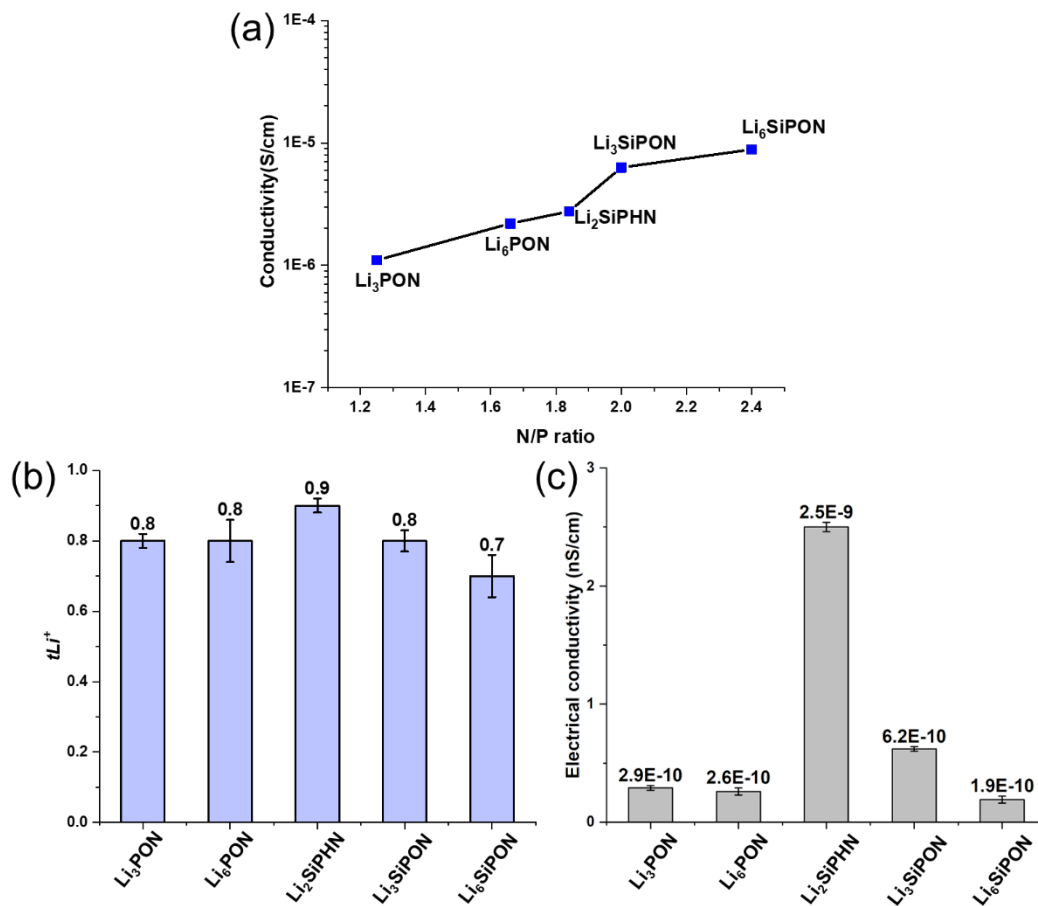


Figure 4.9a. Ionic conductivity vs. N/P ratio of SS/Celgard + polymer precursor/SS cells, **b.** t_{Li^+} and **c.** electrical conductivities of Li/Celgard + polymer precursor/Li cells.

Interestingly, the Li₆SiPON coated Celgard shows the lowest electrical conductivity, the highest ionic conductivity and high critical current density (3.75 mA/cm²).⁵¹ The Li₆SiPON polymer precursor electrolyte was then used to assemble a half cell with Li metal and SPAN cathode. Detailed synthesis and performance of SPAN cathodes can be found elsewhere.⁵² Figure 4.10a shows specific capacity of SPAN/Celgard + Li₆SiPON/Li half-cell cycled at 0.5 C rates for 220 h, from 1 to 3 V for 122 cycles. The Li-SPAN battery shows no polarization or voltage fluctuation during cycling. The half-cell showed an initial capacity ~2000 mAh/g_{sulfur}, higher than the theoretical capacity for sulfur (1672 mAh/g), suggesting that the π -conjugated pyridinic carbon framework of SPAN contributes to the initial capacity, which is likely a combination of Faradaic processes in

forming the SEI on carbon during the first cycle and a non-Faradaic pseudo-capacitance that may persist over subsequent cycles.^{52,84,85}

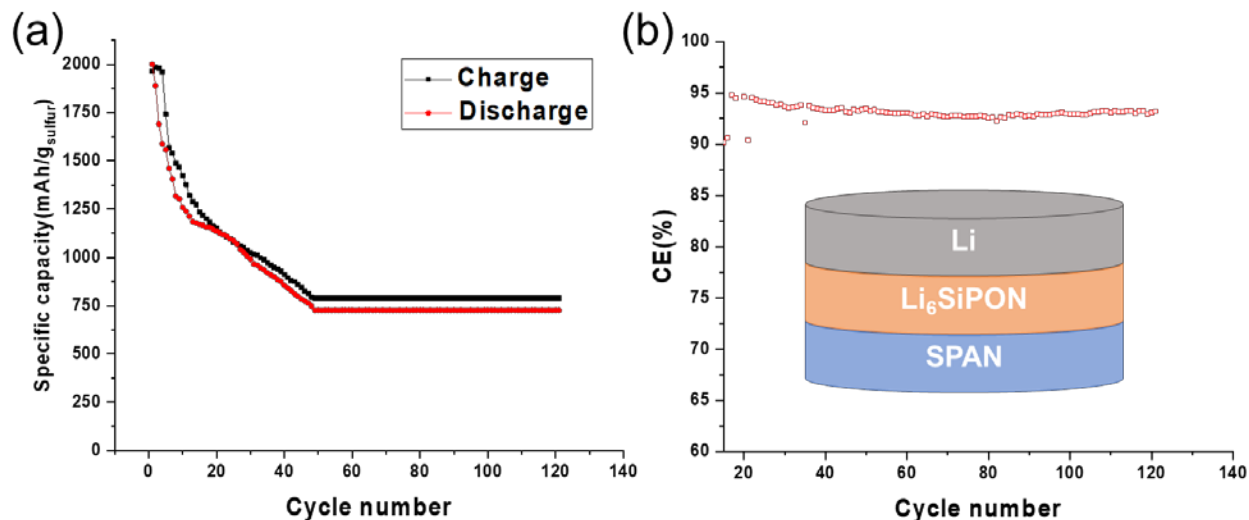


Figure 4.10. Specific capacity (a) and coulombic efficiency (b) vs. cycle number plots of SPAN/Celgard + Li₆SiPON/Li at 0.5 C.

The capacity decreases to 1000 mAh/g_{sulfur} after the 40th cycle and gradually to 750 mAh/g_{sulfur} thereafter, which is much improved compared to typical Li-S batteries assembled with polymer electrolytes (50-200 mAh/g_{sulfur}).^{51,86} The fast capacity fade for the first 40 cycles may be ascribed to the loss of electrical contact during cycling, which can also lead to a decrease in coulombic efficiency (Figure 4.10b). There may be a few causes for the electrical contact loss, including the formation of large particles of highly resistive sulfur or lithium sulfide, the migration of polysulfides away from the carbon phase, and the agglomeration of sulfur or carbon particles as a result of the pressure exerted on the cell.

Nevertheless, the half-cell with Li₆SiPON polymer electrolyte shows good electrochemical stability at 0.5 C for 122 cycles. As shown in Figure 4.10b, the coulombic efficiency shows a slight decrease from 95 to 92 % after the first 40 cycles and remains at ~92 % thereafter. The stability

and high performance of the nearly ASSB can be ascribed to the unique performance of SPAN and the polymer electrolyte. The most important feature of SPAN is that the sulfur is covalently bound to a polyaromatic backbone and forms different structural motifs that reduce detrimental polysulfide dissolution, which in turn minimizes capacity loss.^{52,87}

Future work will rely on the optimization of the electrical contact between the SPAN cathode and the polymer precursor electrolytes. The interfacial behavior directly dictates the lifespan, energy density, and safety of ASSBs. The reported polymer electrolytes bring potentials to lower the interfacial resistance and stabilize the interfacial performance of ASSBs.

4.3.4 LiPON-like polymer precursor solid solutions with PEO

In our efforts to develop Li_xPON , Li_xSiPON , and Li_xSiPHN polymer precursors, we realized that it might be possible to use these precursors as active fillers in PEO matrix forming polymer electrolytes (PEs), either as miscible or immiscible active second phases. As the polymer precursors turn into ceramics on heating as suggested by XRD studies above (Figure 4.6), it is anticipated that they offer flame retardance or resistance. More importantly, they exhibit high $t_{\text{Li}^+} \geq 0.7$, unlike most liquid or polymer electrolytes. Therefore, a systematic study was carried out on PEO/precursor composite properties.

PEO/precursor films were made by mixing PEO ($M_w = 900$ kDa) dissolved in acetonitrile with polymer precursor THF solution. After clear solutions formed, they were cast onto PTFE plates, and the solvent was allowed to evaporate at ambient for 24 h. The resulting transparent films were then dried at 65 °C/vacuum/24 h. In general, higher PEO concentrations result in poorer ionic conductivity, while lower PEO concentrations result in poorer mechanical properties. It was determined that solid solutions of polymer precursors form readily with 60 wt.% PEO, and such

compositions show good-to-excellent conductivities as discussed below, denoted as 60PEO/polymer precursor or PE films. Figure **A.14** shows optical images of dried 60PEO/PE films. Detailed fabrication procedure, characterization methods, results and discussion are reported elsewhere.⁵⁴

Table **4.7** summarizes N/P and Li/P ratios derived from XPS studies and measured conductivities of PE composite films at RT. XPS plots and Nyquist plots of PE films are given in Figure **A.15**. Based on XPS analyses (Figure **A.15a**), the resulting At.% suggests the Li/P ratio increases from ~1.1 to 1.3 with increasing amounts of LiNH₂ for the 60PEO/Li_xSiPON films. However, this ratio is smaller when compared to the Li₃PON (2.1) and Li₆PON (2.8) polymer composite films, which may be due to the introduction of silicon in Li_xSiPON. The deduced N/P ratio is smaller than what is experimentally calculated (3), which is associated with the loss of N by polymerization. Nevertheless, compared to gas-phase-deposited LiPON glasses (typically <1), the obtained N/P ratios (1-1.5) for the PE films are higher.^{61,75} The relation between the N/P ratio and ionic conductivity is discussed below.

Table 4.7. Calculated atomic compositions from XPS analyses and total conductivities (σ_{RT}) of PE composite films.

	Li ₃ PON	Li ₆ PON	Li ₂ SiPHN	Li ₃ SiPON	Li ₆ SiPON
N/P	1.1	1.1	1.5	1.2	1.0
Li/P	2.1	2.8	1.7	1.1	1.3
σ_{RT} (S/cm)	4.4×10^{-4}	3.7×10^{-4}	1.1×10^{-3}	2.8×10^{-3}	2.7×10^{-4}

Figure **4.11a** compares found melting temperatures (T_m) and percent crystallinities (χ_c) derived from DSC studies of PEO and polymer composite films (Figure **A.16**). χ_c is of the order Li₂SiPHN > Li₆PON > Li₃PON > Li₆SiPON > Li₃SiPON. T_m decreases with the introduction of the polymer precursors, suggesting that PEO crystallization is hindered. The crystallization temperature is also reduced from 40 °C for PEO to 38-30 °C for PE composite films (Figure **A.16**).

Figure **4.11b** demonstrates the relation between N/P ratio, χ_c , and ionic conductivity (at RT) of the PEs. As discussed above, the reported N/P ratios in this study are relatively high compared to the gas-phase-deposited Li_xPON electrolytes, resulting in significant improvements in the ionic conductivity. The 60PEO/ Li_2SiPHN showed the highest N/P ratio (1.5), resulting in a decrease in electrostatic energy; however, this alone did not result in fast ion mobility compared to the 60PEO/ Li_3SiPON thin film, which is ascribed to the fact that the 60PEO/ Li_2SiPHN film exhibits the highest crystallinity ($\chi_c \approx 56\%$). Similar relations are observed for the 60PEO/ Li_xPON PEs, suggesting the main limiting factor for fast Li^+ diffusion is the mobility of the PEO matrix. Although some reports show that crystalline PEO can offer fast ionic transport, prevailingly, the crystalline region inhibit ion transport due to the slower chain dynamics upon crystallization.⁸⁰

The decrease in the crystallinity of 60PEO/ Li_3SiPON ($\chi_c \approx 15\%$) along with the high N/P ratio resulted in superior ionic conductivity of 2.8×10^{-3} S/cm at ambient, much higher than gas-phase-deposited Li_xPON (typically 10^{-6} S/cm at ambient),^{20,21,28} and also higher than simple PEO/ Li^+ salt polymers.⁸⁰ This is ascribed to the solvation ability of the polymer backbone and homogenous miscibility of the polymer precursor in PEO, as shown in Figure **A.14**. In addition, the Li_xSiPON polymer precursor with high N contents seems to favor Li solvation better than the Li_xPON polymer precursors.

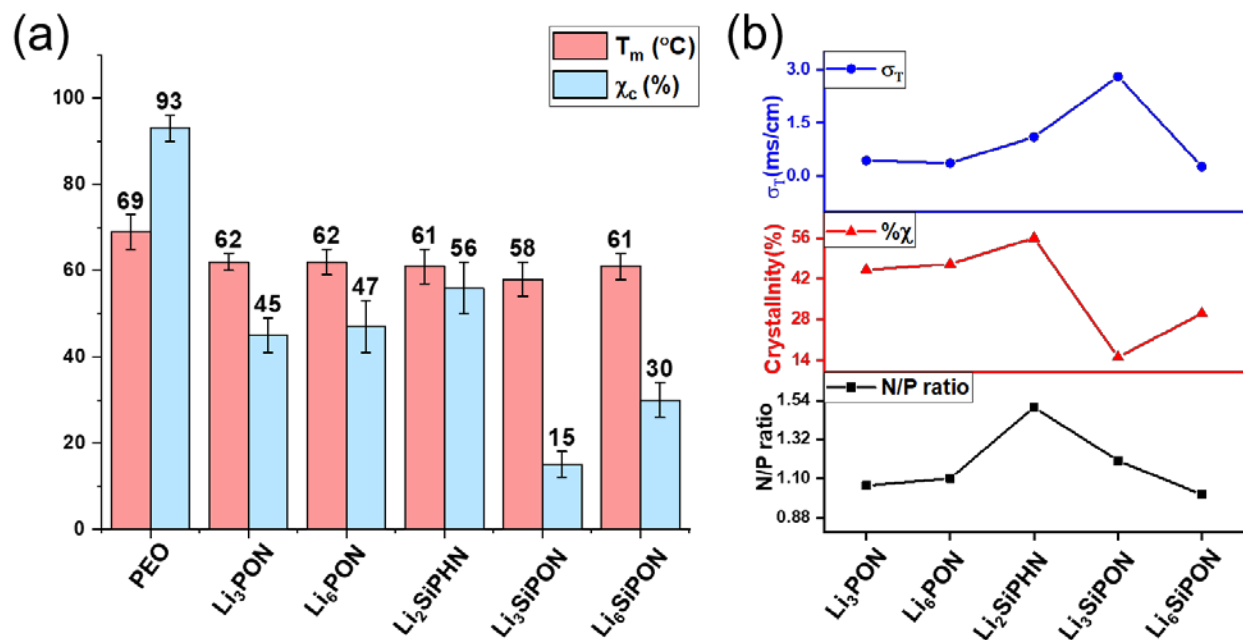


Figure 4.11a. Thermal properties of PEs and PEO films and **b.** correlation between the N/P ratio (black), crystallinity percentage (red), and ionic conductivity at RT of PEs (blue).

Figure 4.12a compares t_{Li^+} of PE films in Li/60PEO/PEs/Li cell configuration. All PEs show $t_{\text{Li}^+} \geq 0.5$, suggesting the interaction between Li^+ and polymeric -PON, -SiPON, and -SiPHN backbones results in fast Li^+ mobility, as discussed above. The 60PEO/ Li_2SiPHN film shows a high t_{Li^+} of ~ 0.8 , comparable to single-ion conducting polymer electrolytes.^{88,89} However, t_{Li^+} of the PEO/precursor films are lower compared to the above pristine LiPON-like polymer precursors ($t_{\text{Li}^+} > 0.7$). This might be a result of the increased mobility of both cations and anions in PE films due to high flexibility of the PEO segments. The increase in t_{Li^+} of Li_2SiPHN might be due to its cyclometric structure of -SiPHN (Figure 4.12a); the molecule is bulkier than -SiPON and -PON, hence lower anion mobility.

Galvanostatic cycling of Li/60PEO/PEs/Li at ambient are studied as reported elsewhere.⁵⁴ Among all PEs, 60PEO/ Li_6PON shows optimum performance at $\pm 1.5\text{-}7.5$ mA, Figure 4.12b. The symmetric cell shows a stable voltage response of 0.02 V for the first 40 h; the interfacial resistance

seems to increase indicated by the increase in voltage to 0.05 V after the 20th cycle. The 60PEO/Li₆PON film show stable voltage response (0.04 V) vs. Li metal at higher current densities (3.25 mAh/cm², active cross-sectional area = 2 cm²) compared to the traditional PEO/Li salt electrolytes (0.1 mA/cm²).⁹⁰ Furthermore, unlike most PEO/Li salt studies are performed at elevated temperatures (>65 °C),⁹¹ these symmetric cell studies are performed at RT. Most polymer/solid electrolytes are limited by the solid-solid diffusion at the interface, resulting in lower critical current densities.⁹² Here, we were able to enhance the interface between Li metal and the PE films by melt bonding PEs on the Li surface.

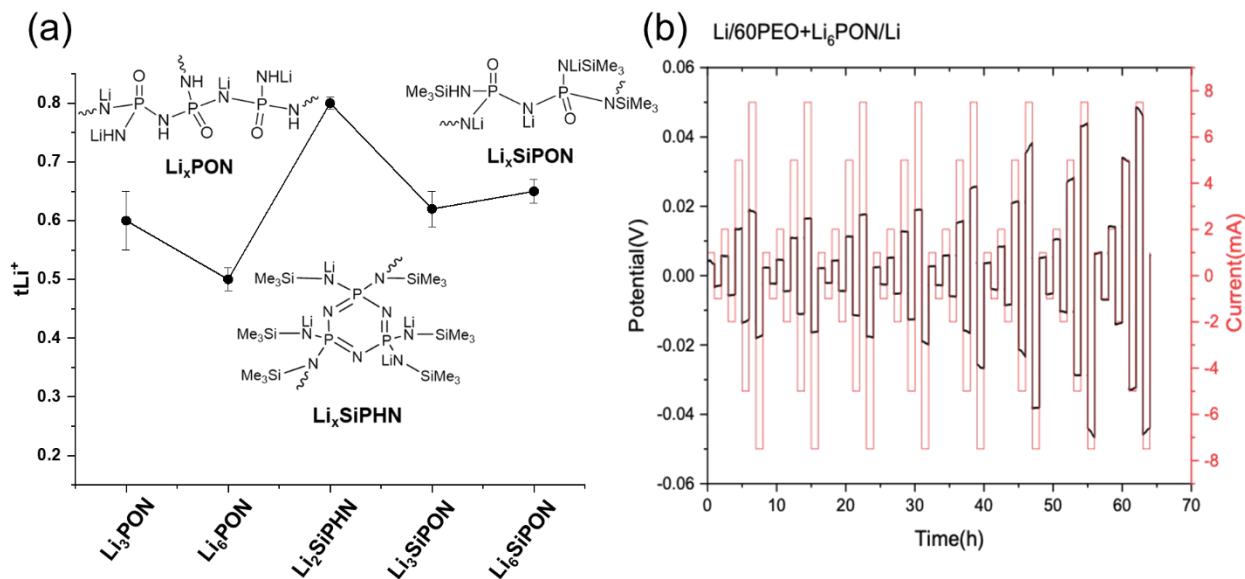


Figure 4.12a. t_{Li^+} of PE films in Li/60PEO/PEs/Li cell configuration and example precursor structures. **b.** Galvanostatic cycling of Li/60PEO/Li₆PON/Li at ± 1.5 -7.5 mA at RT.

Figure 4.13a shows the specific capacity of SPAN/60PEO/Li₆SiPON/Li half cells cycled at various C rates at 1 to 3 V for 100 cycles. Minimal voltage fluctuation was observed.⁵⁴ More specifically, the Li-S cell was cycled for 30 cycles at 0.25 C, 20 cycles at 0.5 and 1 C, and the last 20 cycles at 0.25 C. The half-cell showed initial discharge capacities of ~ 1800 mAh/g_{sulfur}, higher than the theoretical capacity for sulfur (1672 mAh/g), likely due to the C framework of SPAN that

irreversibly contributes to the initial capacity, similar to SPAN/Celgard + Li₆SiPON/Li above (Figure 4.10).^{84,85}

The half-cell charges and discharges to the targeted potentials with minimal polarization for 100 cycles at the desired C-rates. The capacity decreases to 1000 mAh/g_{sulfur} after the first cycle, and a slight decrease to 950 and 800 mAh/g_{sulfur} at 0.5 and 1 C is exhibited. However, the capacity was recovered when cycled back to 0.25 C. Overall, the Li/S cathode shows high capacity, high cycle stability, and high discharge/charge capacity. The 60PEO/Li₆SiPON polymer electrolyte also shows high electrochemical stability at high rates of 0.25, 0.5, and 0.1 C for 100 cycles. A coulombic efficiency of ~100 % was maintained throughout the cycle (Figure 4.13b).

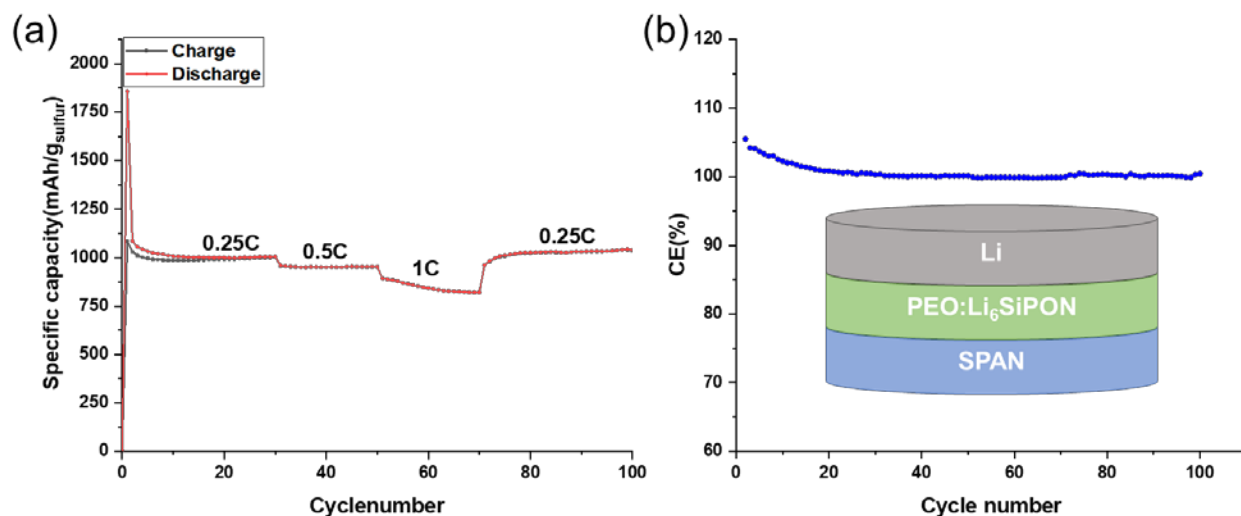


Figure 4.13. Specific capacity (a) and coulombic efficiency (b) vs. cycle number of SPAN/60PEO/Li₆SiPON/Li at selected C-rates.

4.4 Conclusions

In summary, we present here the synthesis of a set of polymers that emulate LiPON chemistries and that allow simple and extensive control of composition, degree of lithiation, and incorporation of silicon as well as exclusion of oxygen and understand their effects on the ionic conductivity.

The intent was to find a simple alternative to the equipment and energy intensive gas phase deposition methods. Our approach involves the synthesis of $\text{O}=\text{P}(\text{NH}_2)_3$ from OPCl_3 followed by lithiation with LiNH_2 . A detailed characterization of LiPON-like oligomer/polymer precursors are presented, including MALDI, FTIR, TGA-DTA, NMR, XRD, XPS, impedance and electrochemical studies. For all the precursors, the MWs are estimated to be $\approx 1\text{-}2$ kDa, and the CYs at 800°C are 50-60 %. They are thermally stable to $150\text{-}200^\circ\text{C}$. FTIR spectra fit well with typical LiPON glasses synthesized by gas phase methods.^{40,58-62} ^7Li NMR suggests that Li^+ ions in these precursors are well solvated and dissociated, which is beneficial for their electrochemical performances. The structures of Si (C) containing precursors were further investigated by ^1H , ^{13}C and ^{29}Si NMR studies, which suggests that Si doping was achieved by bonding NH-SiMe_3 with $\text{P}=\text{O}$ or $\text{P-N}=\text{P}$ onto the polymer backbone.

Crystalline phases of these polymer precursors at different temperatures ($100\text{-}600^\circ\text{C}$) were characterized by XRD. However, they are primarily amorphous at 100°C , hence XPS studies were performed to quantify the elemental composition of the precursors. Overall, all the precursors show higher N/P ratios (1-3) compared to traditional gas phase methods (<1), and there seems to be a correlation between the N/P ratio and ^7Li NMR chemical shift. All the polymer precursors show the highest ambient conductivity after treating at $400^\circ\text{C}/2$ h. In general, the conductivities of polymer precursor pellets seem to be $\text{Li}_2\text{SiPHN} > \text{Li}_6\text{SiPON} > \text{Li}_3\text{PON} > \text{Li}_6\text{PON} > \text{Li}_3\text{SiPON}$, and a maximum conductivity of 2.7×10^{-4} S/cm at RT is achieved for Li_2SiPHN after heating at $400^\circ\text{C}/2$ h/ N_2 .

For Celgard/polymer precursor electrolytes, the conductivity increases with increasing amounts of Li and N/P ratio. Maximum ambient conductivity of $\sim 1 \times 10^{-5}$ S/cm is achieved for the Li_6SiPON with an N/P ratio of 2.4. The Li_2SiPHN precursor showed an ideal transference

number of ~ 0.9 , comparable to SSEs. Furthermore, the Li_6SiPON polymer electrolyte was used to assemble a nearly all solid-state Li/SPAN battery. The stability and high performance of the half-cell was attributed to the unique performance of the SPAN and the polymer electrolyte.

For PEO/polymer precursor composite films, a maximum ionic conductivity of 2.8×10^{-3} S/cm is achieved for the 60PEO/ Li_3SiPON films at ambient, and all PE films show $t_{\text{Li}^+} \geq 0.5$. The enhancement in conductivity of this PE is ascribed to the suppression of the PEO crystallinity and the increase in the N/P ratio. The high Li^+ transference number of Li_2SiPHN ($t_{\text{Li}^+} \approx 0.8$) indicates that anion mobility is limited due to the polymer precursor bulky backbone. In addition to the enhanced ionic conductivities vs. traditional PEO electrolytes, these active polymer precursor fillers offer improved stability against Li metal at higher current densities. Galvanostatic cycling of the SPAN/PEs/Li cell shows discharge capacities of 1000 mAh/g_{sulfur} at 0.25 C and 800 mAh/g_{sulfur} at 1 C. The cell also shows high-capacity retention over 100 cycles with ~ 100 % coulombic efficiency.

References

1. Put, B.; Vereecken, P. M.; Meersschaut, J.; Sepúlveda, A.; Stesmans, A. Electrical Characterization of Ultrathin RF-Sputtered LiPON Layers for Nanoscale Batteries. *ACS Appl. Mater. Interfaces* **2016**, *8*, 7060–7069.
2. Oudenhoven, J. F. M.; Baggetto, L.; Notten, P. H. L. All-Solid-State Lithium-Ion Microbatteries: A Review of Various Three-Dimensional Concepts. *Adv. Energy Mater.* **2011**, *1*, 10–33.
3. Patil, A.; Patil, V.; Wook Shin, D.; Choi, J. W.; Paik, D. S.; Yoon, S. J. Issue and Challenges Facing Rechargeable Thin Film Lithium Batteries. *Mater. Res. Bull.* **2008**, *43* (8–9), 1913–1942.
4. Long, J. W.; Dunn, B.; Rolison, D. R.; White, H. S. Three-Dimensional Battery Architectures. *Chem. Rev.* **2004**, *104*, 4463–4492.
5. Rolison, D. R.; Long, J. W.; Lytle, J. C.; Fischer, A. E.; Rhodes, C. P.; McEvoy, T. M.; Bourg, M. E.; Lubers, A. M. Multifunctional 3D Nanoarchitectures for Energy Storage and Conversion. *Chem. Soc. Rev.* **2009**, *38*, 226–252.
6. Hartmann, P.; Leichtweiss, T.; Busche, M. R.; Schneider, M.; Reich, M.; Sann, J.; Adelhelm, P.; Janek, J. Degradation of NASICON-Type Materials in Contact with Lithium Metal: Formation of Mixed Conducting Interphases (MCI) on Solid Electrolytes. *J. Phys. Chem. C* **2013**, *117* (41), 21064–21074.
7. Manthiram, A.; Yu, X.; Wang, S. Lithium Battery Chemistries Enabled by Solid-State Electrolytes. *Nat. Rev. Mater.* **2017**, *2* (4), 16103.
8. Pitawala, H. M. J. C.; Dissanayake, M. A. K. L.; Seneviratne, V. A.; Mellander, B. E.; Albinsson, I. Effect of Plasticizers (EC or PC) on the Ionic Conductivity and Thermal Properties of the (PEO)₉LiTf: Al₂O₃ Nanocomposite Polymer Electrolyte System. *J. Solid State Electrochem.* **2008**, *12*, 783–789.
9. Imanishi, N.; Hasegawa, S.; Zhang, T.; Hirano, A.; Takeda, Y.; Yamamoto, O. Lithium Anode for Lithium-Air Secondary Batteries. *J. Power Sources* **2008**, *185* (2), 1392–1397.
10. Yu, X.; Bi, Z.; Zhao, F.; Manthiram, A. Polysulfide-Shuttle Control in Lithium-Sulfur Batteries with a Chemically/Electrochemically Compatible NaSICON-Type Solid Electrolyte. *Adv. Energy Mater.* **2016**, *6* (24), 1601392.
11. Wu, B.; Wang, S.; Lochala, J.; Desrochers, D.; Liu, B.; Zhang, W.; Yang, J.; Xiao, J. The Role of the Solid Electrolyte Interphase Layer in Preventing Li Dendrite Growth in Solid-State Batteries. *Energy Environ. Sci.* **2018**, *11* (7), 1803–1810.
12. Cheng, E. J.; Sharafi, A.; Sakamoto, J. Intergranular Li Metal Propagation through Polycrystalline Li_{6.25}Al_{0.25}La₃Zr₂O₁₂ Ceramic Electrolyte. *Electrochimica Acta* **2017**, *223* (1), 85–91.
13. Sharafi, A.; Meyer, H. M.; Nanda, J.; Wolfenstine, J.; Sakamoto, J. Characterizing the Li-Li₇La₃Zr₂O₁₂ Interface Stability and Kinetics as a Function of Temperature and Current Density. *J. Power Sources* **2016**, *302* (20), 135–139.
14. Li, G.; Monroe, C. W. Dendrite Nucleation in Lithium-Conductive Ceramics. *Phys. Chem. Chem. Phys.* **2019**, *21* (36), 20354–20359.
15. Yu, S.; Siegel, D. J. Grain Boundary Contributions to Li-Ion Transport in the Solid Electrolyte Li₇La₃Zr₂O₁₂ (LLZO). *Chem. Mater.* **2017**, *29* (22), 9639–9647.
16. Tian, H. K.; Xu, B.; Qi, Y. Computational Study of Lithium Nucleation Tendency in Li₇La₃Zr₂O₁₂ (LLZO) and Rational Design of Interlayer Materials to Prevent Lithium Dendrites. *J. Power Sources* **2018**, *392*, 79–86.

17. Lin, C. F.; Fan, X.; Pearse, A.; Liou, S. C.; Gregorczyk, K.; Leskes, M.; Wang, C.; Lee, S. B.; Rubloff, G. W.; Noked, M. Highly Reversible Conversion-Type FeOF Composite Electrode with Extended Lithium Insertion by Atomic Layer Deposition LiPON Protection. *Chem. Mater.* **2017**, *29* (20), 8780–8791.
18. Lin, C. F.; Qi, Y.; Gregorczyk, K.; Lee, S. B.; Rubloff, G. W. Nanoscale Protection Layers to Mitigate Degradation in High-Energy Electrochemical Energy Storage Systems. *Acc. Chem. Res.* **2018**, *51* (1), 97–106.
19. Westover, A. S.; Dudney, N. J.; Sacci, R. L.; Kalnaus, S. Deposition and Confinement of Li Metal along an Artificial Lipon-Lipon Interface. *ACS Energy Lett.* **2019**, *4* (3), 651–655.
20. Yu, X.; Bates, J. B.; Jellison, G. E.; Hart, F. X. A Stable Thin-Film Lithium Electrolyte: Lithium Phosphorus Oxynitride. *J. Electrochem. Soc.* **1997**, *144*, 524–532.
21. Bates, J. B.; Dudney, N. J.; Gruzalski, G. R.; Zuhr, R. A.; Choudhury, A.; Luck, C. F.; Robertson, J. D. Fabrication and Characterization of Amorphous Lithium Electrolyte Thin Films and Rechargeable Thin-Film Batteries. *J. Power Sources* **1993**, *43–44*, 103–110.
22. Neudecker, B. J.; Dudney, N. J.; Bates, J. B. “Lithium-Free” Thin-Film Battery with in Situ Plated Li Anode. *J. Electrochem. Soc.* **2000**, *147* (2), 517–523.
23. Bates, J. B.; Dudney, N. J.; Neudecker, B.; Ueda, A.; Evans, C. D. Thin-Film Lithium and Lithium-Ion Batteries. *Solid State Ion.* **2000**, *135* (1–4), 33–45.
24. Li, J.; Ma, C.; Chi, M.; Liang, C.; Dudney, N. J. Solid Electrolyte: The Key for High-Voltage Lithium Batteries. *Adv. Energy Mater.* **2015**, *5* (4), 1401408.
25. Han, F.; Westover, A. S.; Yue, J.; Fan, X.; Wang, F.; Chi, M.; Leonard, D. N.; Dudney, N. J.; Wang, H.; Wang, C. High Electronic Conductivity as the Origin of Lithium Dendrite Formation within Solid Electrolytes. *Nat. Energy* **2019**, *4* (3), 187–196.
26. Le Van-Jodin, L.; Ducroquet, F.; Sabary, F.; Chevalier, I. Dielectric Properties, Conductivity and Li⁺ Ion Motion in LiPON Thin Films. *Solid State Ion.* **2013**, *253* (15), 151–156.
27. Su, Y.; Falgenhauer, J.; Polity, A.; Leichtweiß, T.; Kronenberger, A.; Obel, J.; Zhou, S.; Schlettwein, D.; Janek, J.; Meyer, B. K. LiPON Thin Films with High Nitrogen Content for Application in Lithium Batteries and Electrochromic Devices Prepared by RF Magnetron Sputtering. *Solid State Ion.* **2015**, *282* (1), 63–69.
28. Bates, J. B.; Dudney, N. J.; Gruzalski, G. R.; Zuhr, R. A.; Choudhury, A.; Luck, C. F.; Robertson, J. D. Electrical Properties of Amorphous Lithium Electrolyte Thin Films. *Solid State Ion.* **1992**, *53*, 647–654.
29. Nimisha, C. S.; Rao, K. Y.; Venkatesh, G.; Rao, G. M.; Munichandraiah, N. Sputter Deposited LiPON Thin Films from Powder Target as Electrolyte for Thin Film Battery Applications. *Thin Solid Films* **2011**, *519*, 3401–3406.
30. Wang, Y.; Liu, B.; Li, Q.; Cartmell, S.; Ferrara, S.; Deng, Z. D.; Xiao, J. Lithium and Lithium Ion Batteries for Applications in Microelectronic Devices: A Review. *J. Power Sources* **2015**, *286*, 330–345.
31. Fujibayashi, T.; Kubota, Y.; Iwabuchi, K.; Yoshii, N. Highly Conformal and High-Ionic Conductivity Thin-Film Electrolyte for 3D-Structured Micro Batteries: Characterization of LiPON Film Deposited by MOCVD Method. *AIP Adv.* **2017**, *7* (8), 085110.
32. Lee, S. J.; Bae, J. H.; Lee, H. W.; Baik, H. K.; Lee, S. M. Electrical Conductivity in Li-Si-P-O-N Oxynitride Thin-Films. *J. Power Sources* **2003**, *123*, 61–64.
33. Lee, S. J.; Baik, H. K.; Lee, S. M. An All-Solid-State Thin Film Battery Using LISIPON Electrolyte and Si-V Negative Electrode Films. *Electrochem. Commun.* **2003**, *5*, 32–35.

34. Su, Y.; Falgenhauer, J.; Leichtweiß, T.; Geiß, M.; Lupó, C.; Polity, A.; Zhou, S.; Obel, J.; Schlettwein, D.; Janek, J.; Meyer, B. K. Electrochemical Properties and Optical Transmission of High Li⁺ Conducting LiSiPON Electrolyte Films. *Phys. Status Solidi B Basic Res.* **2017**, *254* (2), 1600088.
35. Famprakis, T.; Galipaud, J.; Clemens, O.; Pecquenard, B.; Le Cras, F. Composition Dependence of Ionic Conductivity in LiSiPO(N) Thin-Film Electrolytes for Solid-State Batteries. *ACS Appl. Energy Mater.* **2019**, *2* (7), 4782–4791.
36. Hamon, Y.; Douard, A.; Sabary, F.; Marcel, C.; Vinatier, P.; Pecquenard, B.; Levasseur, A. Influence of Sputtering Conditions on Ionic Conductivity of LiPON Thin Films. *Solid State Ion.* **2006**, *177*, 257–261.
37. Zhao, S.; Fu, Z.; Qin, Q. A Solid-State Electrolyte Lithium Phosphorus Oxynitride Film Prepared by Pulsed Laser Deposition. *Thin Solid Films* **2002**, *415*, 108–113.
38. Vereda, F.; Goldner, R. B.; Haas, T. E.; Zerigian, P. Rapidly Grown IBAD LiPON Films with High Li-Ion Conductivity and Electrochemical Stability. *Electrochem. Solid-State Lett.* **2002**, *5*, 239–241.
39. Kim, Y. G.; Wadley, H. N. G. Lithium Phosphorous Oxynitride Films Synthesized by a Plasma-Assisted Directed Vapor Deposition Approach. *J. Vac. Sci. Technol. Vac. Surf. Films* **2008**, *26*, 174–183.
40. Kim, H. T.; Mun, T.; Park, C.; Jin, S. W.; Park, H. Y. Characteristics of Lithium Phosphorous Oxynitride Thin Films Deposited by Metal-Organic Chemical Vapor Deposition Technique. *J. Power Sources* **2013**, *244*, 641–645.
41. Kozen, A. C.; Pearse, A. J.; Lin, C. F.; Noked, M.; Rubloff, G. W. Atomic Layer Deposition of the Solid Electrolyte LiPON. *Chem. Mater.* **2015**, *27* (15), 5324–5331.
42. Chantrell, P. G.; Popper, P. Inorganic Polymers and Ceramics. In *Special Ceramics*; 1965; pp 87–102.
43. Aylett, B. J. Silicon-Nitrogen Polymers. In *Special Ceramics*; 1964; p 105.
44. Wynne, K. J.; Rice, R. W. Ceramics via Polymer Pyrolysis. *Annu. Rev. Mater. Sci.* **1984**, *14* (1), 297–334.
45. Brinker, C. J.; Clark, D. E.; Ulrich, D. R. Better Ceramics Through Chemistry II. In *Materials Research Society Symposium Proceedings*; 1986.
46. Brinker, C. J.; Clark, D. E.; Ulrich, D. R. Better Ceramics Through Chemistry III. In *Materials Research Society Symposium Proceedings*; 1988.
47. Laine, R. M. *Transformation of Organometallics into Common and Exotic Materials: Design and Activation*; 1988.
48. Laine, R. M.; Sellinger, A. Si-Containing Ceramic Precursors. In *The Chemistry of Organic Silicon Compounds*; 2003.
49. Okamura, K. Ceramic Fibres from Polymer Precursors. *Composites* **1987**, *18*, 107–120.
50. Greil, P. Polymer Derived Engineering Ceramics. *Adv. Eng. Mater.* **2000**, *2* (6), 339–348.
51. Temeche, E.; Zhang, X.; Laine, R. M. Polymer Precursor Derived Li_xPON Electrolytes: Toward Li–S Batteries. *ACS Appl. Mater. Interfaces* **2020**, *12* (18), 20548–20562.
52. Warneke, S.; Zenn, R. K.; Lebherz, T.; Müller, K.; Hintennach, A.; Starke, U.; Dinnebier, R. E.; Buchmeiser, M. R. Hybrid Li/S Battery Based on Dimethyl Trisulfide and Sulfurized Poly(Acrylonitrile). *Adv. Sustain. Syst.* **2018**, *2* (2), 1700144.
53. Evans, J.; Vincent, C. A.; Bruce, P. G. Electrochemical Measurement of Transference Numbers in Polymer Electrolytes. *Polymer* **1987**, *28* (13), 2324–2328.

54. Temeche, E.; Zhang, X.; Laine, R. M. Solid Electrolytes for Li-S Batteries: Solid Solutions of Poly(Ethylene Oxide) with Li_xPON- and Li_xSiPON-Based Polymers. *ACS Appl. Mater. Interfaces* **2020**, *12* (27), 30353–30364.
55. Laine, R. M.; Babonneau, F. Pre-ceramic Polymer Routes to Silicon Carbide. *Chem. Mater.* **1993**, *5*, 260–279.
56. Li, L.; Dunn, J. B.; Zhang, X. X.; Gaines, L.; Chen, R. J.; Wu, F.; Amine, K. Recovery of Metals from Spent Lithium-Ion Batteries with Organic Acids as Leaching Reagents and Environmental Assessment. *J. Power Sources* **2013**, *233*, 180–189.
57. Zhang, P.; Yokoyama, T.; Itabashi, O.; Suzuki, T. M.; Inoue, K. Hydrometallurgical Process for Recovery of Metal Values from Spent Lithium-Ion Secondary Batteries. *Hydrometallurgy* **1998**, *47* (2–3), 259–271.
58. Larson, R. W.; Day, D. E. Preparation and Characterization of Lithium Phosphorus Oxynitride Glass. *J. Non-Cryst. Solids* **1986**, *88* (1), 97–113.
59. Mascaraque, N.; Fierro, J. L. G.; Durán, A.; Muñoz, F. An Interpretation for the Increase of Ionic Conductivity by Nitrogen Incorporation in LiPON Oxynitride Glasses. *Solid State Ion.* **2013**, *233*, 73–79.
60. Fleutot, B.; Pecquenard, B.; Martinez, H.; Letellier, M.; Levasseur, A. Investigation of the Local Structure of LiPON Thin Films to Better Understand the Role of Nitrogen on Their Performance. *Solid State Ion.* **2011**, *186* (1), 29–36.
61. Pichonat, T.; Lethien, C.; Tiercelin, N.; Godey, S.; Pichonat, E.; Roussel, P.; Colmont, M.; Rolland, P. A. Further Studies on the Lithium Phosphorus Oxynitride Solid Electrolyte. *Mater. Chem. Phys.* **2010**, *123* (1), 231–235.
62. Stallworth, P. E.; Vereda, F.; Greenbaum, S. G.; Haas, T. E.; Zerigian, P.; Goldner, R. B. Solid-State NMR Studies of Lithium Phosphorus Oxynitride Films Prepared by Nitrogen Ion Beam-Assisted Deposition. *J. Electrochem. Soc.* **2005**, *152* (3), A516–A522.
63. Manzi, J.; Curcio, M.; Brutti, S. Structural and Morphological Tuning of LiCoPO₄ Materials Synthesized by Solvo-Thermal Methods for Li-Cell Applications. *Nanomaterials* **2015**, *5* (4), 2212–2230.
64. Ait Salah, A.; Jozwiak, P.; Zaghbi, K.; Garbarczyk, J.; Gendron, F.; Mauger, A.; Julien, C. M. FTIR Features of Lithium-Iron Phosphates as Electrode Materials for Rechargeable Lithium Batteries. *Spectrochim. Acta - Part Mol. Biomol. Spectrosc.* **2006**, *65* (5), 1007–1013.
65. See, K. A.; Leskes, M.; Griffin, J. M.; Britto, S.; Matthews, P. D.; Emly, A.; Van Der Ven, A.; Wright, D. S.; Morris, A. J.; Grey, C. P.; Seshadri, R. Ab Initio Structure Search and in Situ ⁷Li NMR Studies of Discharge Products in the Li-S Battery System. *J. Am. Chem. Soc.* **2014**, *136* (46), 16368–16377.
66. Muñoz, F.; Durán, A.; Pascual, L.; Montagne, L.; Revel, B.; Rodrigues, A. C. M. Increased Electrical Conductivity of LiPON Glasses Produced by Ammonolysis. *Solid State Ion.* **2008**, *179* (15–16), 574–579.
67. Alam, T. M.; Conzone, S.; Brow, R. K.; Boyle, T. J. ⁶Li, ⁷Li Nuclear Magnetic Resonance Investigation of Lithium Coordination in Binary Phosphate Glasses. *J. Non-Cryst. Solids* **1999**, *258* (1–3), 140–154.
68. Pankiewicz, R.; Schroeder, G.; Gierczyk, B.; Wojciechowski, G.; Brzezinski, B.; Bartl, F.; Zundel, G. ⁷Li-NMR and FTIR Studies of Lithium, Potassium, Rubidium, and Cesium Complexes with Ionophore Lasalocid in Solution. *Biopolym. - Biospectroscopy Sect.* **2001**, *62* (3), 173–182.

69. Brachvogel, R. C.; Maid, H.; von Delius, M. NMR Studies on Li^+ , Na^+ and K^+ Complexes of Orthoester Cryptand o-Me₂-1.1.1. *Int. J. Mol. Sci.* **2015**, *16* (9), 20641–20656.
70. Foy, J. T.; Wilkes, E. B.; Aprahamian, I. Self-Assembly of Benzyl Cyclopentadienyl Lithium. *CrystEngComm* **2012**, *14* (19), 6126–6128.
71. Aprahamian, I.; Eisenberg, D.; Hoffman, R. E.; Sternfeld, T.; Matsuo, Y.; Jackson, E. A.; Nakamura, E.; Scott, L. T.; Sheradsky, T.; Rabinovitz, M. Ball-and-Socket Stacking of Supercharged Geodesic Polyarenes: Bonding by Interstitial Lithium Ions. *J. Am. Chem. Soc.* **2005**, *127* (26), 9581–9587.
72. Berger, S.; Bock, W.; Frenking, G.; Jonas, V.; Müller, F. NMR Data of Methyltitanium Trichloride and Related Organometallic Compounds. A Combined Experimental and Theoretical Study of $\text{Me}_n\text{XCl}_{4-n}$ ($n = 0-4$; $\text{X} = \text{C}, \text{Si}, \text{Sn}, \text{Pb}, \text{Ti}$). *J. Am. Chem. Soc.* **1995**, *117* (13), 3820–3829.
73. Arshadi, M.; Johnels, D.; Edlund, U.; Ottosson, C. H.; Cremer, D. Solvated Silylium Cations: Structure Determination by Nmr Spectroscopy and the Nmr/Ab Initio/Iglo Method. *J. Am. Chem. Soc.* **1996**, *118* (21), 5120–5131.
74. Roh, N. S.; Lee, S. D.; Kwon, H. S. Effects of Deposition Condition on the Ionic Conductivity and Structure of Amorphous Lithium Phosphorus Oxynitrate Thin Film. *Scr. Mater.* **1999**, *42* (1), 43–49.
75. Hu, Z.; Li, D.; Xie, K. Influence of Radio Frequency Power on Structure and Ionic Conductivity of LiPON Thin Films. *Bull. Mater. Sci.* **2008**, *31* (4), 681–686.
76. Albertus, P.; Babinec, S.; Litzelman, S.; Newman, A. Status and Challenges in Enabling the Lithium Metal Electrode for High-Energy and Low-Cost Rechargeable Batteries. *Nat. Energy* **2018**, *3* (1), 16–21.
77. Lacivita, V.; Arthith, N.; Ceder, G. Structural and Compositional Factors That Control the Li-Ion Conductivity in LiPON Electrolytes. *Chem. Mater.* **2018**, *30* (20), 7077–7090.
78. Li, J.; Lai, W. Structure and Ionic Conduction Study on Li_3PO_4 and LiPON (Lithium Phosphorous Oxynitride) with the Density-Functional Tight-Binding (DFTB) Method. *Solid State Ion.* **2020**, *351* (January), 115329.
79. Long, L.; Wang, S.; Xiao, M.; Meng, Y. Polymer Electrolytes for Lithium Polymer Batteries. *J. Mater. Chem. A* **2016**, *4* (26), 10038–10069.
80. Xue, Z.; He, D.; Xie, X. Poly(Ethylene Oxide)-Based Electrolytes for Lithium-Ion Batteries. *J. Mater. Chem. A* **2015**, *3* (38), 19218–19253.
81. Li, J.; Dudney, N. J.; Nanda, J.; Liang, C. Artificial Solid Electrolyte Interphase To Address the Electrochemical Degradation of Silicon Electrodes. *ACS Appl. Mater. Interfaces* **2014**, *6* (13), 10083–10088.
82. Chen, Y. T.; Jena, A.; Pang, W. K.; Peterson, V. K.; Sheu, H. S.; Chang, H.; Liu, R. S. Voltammetric Enhancement of Li-Ion Conduction in Al-Doped $\text{Li}_{7-x}\text{La}_3\text{Zr}_2\text{O}_{12}$ Solid Electrolyte. *J. Phys. Chem. C* **2017**, *121* (29), 15565–15573.
83. Shin, B. R.; Nam, Y. J.; Oh, D. Y.; Kim, D. H.; Kim, J. W.; Jung, Y. S. Comparative Study of $\text{TiS}_2/\text{Li-In}$ All-Solid-State Lithium Batteries Using Glass-Ceramic Li_3PS_4 and $\text{Li}_{10}\text{GeP}_2\text{S}_{12}$ Solid Electrolytes. *Electrochimica Acta* **2014**, *146*, 395–402.
84. Wei, S.; Ma, L.; Hendrickson, K. E.; Tu, Z.; Archer, L. A. Metal-Sulfur Battery Cathodes Based on PAN-Sulfur Composites. *J. Am. Chem. Soc.* **2015**, *137* (37), 12143–12152.
85. Cuisinier, M.; Hart, C.; Balasubramanian, M.; Garsuch, A.; Nazar, L. F. Radical or Not Radical: Revisiting Lithium-Sulfur Electrochemistry in Nonaqueous Electrolytes. *Adv. Energy Mater.* **2015**, *5* (16), 1401801.

86. Marmorstein, D.; Yu, T. H.; Striebel, K. A.; McLarnon, F. R.; Hou, J.; Cairns, E. J. Electrochemical Performance of Lithium/Sulfur Cells with Three Different Polymer Electrolytes. *J. Power Sources* **2000**, *89* (2), 219–226.
87. Frey, M.; Zenn, R. K.; Warneke, S.; Müller, K.; Hintennach, A.; Dinnebier, R. E.; Buchmeiser, M. R. Easily Accessible, Textile Fiber-Based Sulfurized Poly(Acrylonitrile) as Li/S Cathode Material: Correlating Electrochemical Performance with Morphology and Structure. *ACS Energy Lett.* **2017**, *2* (3), 595–604.
88. Matsumi, N.; Sugai, K.; Ohno, H. Ion Conductive Characteristics of Alkylborane Type and Boric Ester Type Polymer Electrolytes Derived from Mesitylborane. *Macromolecules* **2003**, *36* (7), 2321–2326.
89. Matsumi, N.; Sugai, K.; Ohno, H. Selective Ion Transport in Organoboron Polymer Electrolytes Bearing a Mesitylboron Unit. *Macromolecules* **2002**, *35* (15), 5731–5733.
90. Appetecchi, G. B.; Passerini, S. PEO-Carbon Composite Lithium Polymer Electrolyte. *Electrochimica Acta* **2000**, *45* (13), 2139–2145.
91. Bouchet, R.; Lascaud, S.; Rosso, M. An EIS Study of the Anode Li/PEO-LiTFSI of a Li Polymer Battery. *J. Electrochem. Soc.* **2003**, *150* (10), A1385–A1389.
92. Han, X.; Gong, Y.; Fu, K. (Kelvin); He, X.; Hitz, G. T.; Dai, J.; Pearse, A.; Liu, B.; Wang, H.; Rubloff, G.; Mo, Y.; Thangadurai, V.; Wachsman, E. D.; Hu, L. Negating Interfacial Impedance in Garnet-Based Solid-State Li Metal Batteries. *Nat. Mater.* **2017**, *16* (5), 572–579.

Chapter 5 Li_xSiON ($x = 2, 4, 6$), A Novel Solid Electrolyte System Derived from Agricultural Waste

Published: Zhang, X.; Temeche, E.; Laine, R. M. *Green Chem.* **2020**, 22 (21), 7491–7505.

5.1 Introduction

To reduce the consumption of traditional energy sources, i.e., fossil fuels, and emission of greenhouse gases, researchers have long sought to replace combustion-based energy technologies. Electrochemical energy storage/conversion systems, including lithium-ion batteries (LIBs), have become subjects of great interest.^{1–3} Although LIBs are now used intensely in applications ranging from simple replacements for traditional batteries in toys, medical devices, portable electronics and are instrumental in the commercialization of electric vehicles; the use of organic solvent based liquid electrolytes with inadequate electrochemical and thermal stabilities introduces inherent safety risks and restrains operating temperatures.^{4–7} Non-flammable, solid-state electrolytes offer an escape from such problems offering potential for both wider operating temperatures coincident with higher energy-densities.^{4–6,8} The potential to formulate solid-state electrolytes from agricultural waste (e.g. rice hull ash, RHA) therefore offers two exciting opportunities. One is to valorize the waste of a commodity product (rice hull ash) and the potential to coincidentally reduce the carbon footprint of extensively used battery materials. This then is the motivation for work reported here.

Li^+ -containing oxynitride amorphous thin films are promising materials for electrochemical applications as solid electrolytes due to their high ionic conductivity, mechanical stability and

chemical durability. Most studies focus on LiPON thin films as suggested by the extensive literature on this topic.⁹⁻³⁵ There are a few reports on borate analogs, lithium boron oxynitrides (LiBON).³⁶⁻³⁹ However, the ionic conductivity (at ambient) for LiBON (10^{-8} S/cm) is much lower than LiPON (10^{-6} S/cm).⁹⁻¹² Studies on other Li-containing oxynitrides are also reported including lithium sulfur oxynitride (LiSON) with ambient conductivities of 10^{-6} - 10^{-5} S/cm,^{40,41} and lithium vanadium oxynitride (LiVON) with conductivities of 10^{-4} - 10^{-5} S/cm at 330 °C.^{42,43}

A number of research groups have explored MSiON (M = Li, Na) glass-ceramics with respect to their crystallization and bonding arrangements,⁴⁴⁻⁴⁸ mechanical properties,^{44,47} chemical durability and conductivities.^{49,50} Typically, such glasses are prepared by melt mixing Li₂O or Na₂O, SiO₂ and Si₃N₄ at 1400-1500 °C/1-3 h in BN crucibles under N₂.^{45,46,48-50} The conductivity for MSiON is attributed to alkali ion transport, which increases with increasing N content.^{49,50} The literature explanation for this behavior suggests that Si-N bonds are more covalent (less ionic) than Si-O bonds, the electrostatic force exerted on alkali ions decreases upon nitridation resulting in reduced activation energy (E_a).⁴⁴⁻⁵⁰ A similar N for O effect is found for LiPON glasses.¹³⁻¹⁸ However, the ambient conductivities of M-Si-O-N glasses remain at 10^{-8} - 10^{-7} S/cm.

A doctoral thesis by Jarkaneh⁴³ describes novel Li⁺ oxynitride conductors including Li_{3+x}PO_{4-x}N_x, Li_{3+x}VO_{4-x}N_x, Li_{2+y}ZnSiO_{4-y}N_y and Li_{2+y}MgSiO_{4-y}N_y solid solutions. N-doping of all compositions generates a γ -phase, except in Li₃VO₄ which generates a β -phase. The γ -phase structures are typical for Li⁺ superionic conductors (LISICON), where cations are tetrahedrally coordinated.

As shown in Table 5.1, N-doping improves conductivities by up to two orders of magnitude in N-doped Li₃(P,V)O₄ and 4-6 orders in N-doped Li₂(Zn,Mg)SiO₄. The E_a decreases by about 0.3 eV in N-doped Li₃(P,V)O₄ and 0.6-0.7 eV in N-doped Li₂(Zn,Mg)SiO₄. Higher ionic conductivities and lower E_a in N-doped samples are attributed to higher numbers of interstitial Li⁺ created as

a result of substitution of N for O. Therefore, it is reasonable to envision that N-doping of other γ -structured materials, including Li_4SiO_4 , can be expected to improve ionic conductivity.

Table 5.1. Ionic conductivities (σ) and activation energies (E_a) for $\text{Li}_{3+x}\text{PO}_{4-x}\text{N}_x$, $\text{Li}_{3+x}\text{VO}_{4-x}\text{N}_x$, $\text{Li}_{2+y}\text{ZnSiO}_{4-y}\text{N}_y$ and $\text{Li}_{2+y}\text{MgSiO}_{4-y}\text{N}_y$ solid solutions.⁴³

Solid solution system	Composition	σ (S/cm) at T °C	E_a (eV)
$\text{Li}_{3+x}\text{PO}_{4-x}\text{N}_x$	Li_3PO_4	1.0×10^{-18} (25)	1.18
	$\text{Li}_{3.2}\text{PO}_{3.8}\text{N}_{0.2}$	9.6×10^{-15} (25)	0.92
	$\text{Li}_{3.4}\text{PO}_{3.6}\text{N}_{0.4}$	2.5×10^{-14} (25)	0.91
	$\text{Li}_{3.6}\text{PO}_{3.4}\text{N}_{0.6}$	2.0×10^{-16} (25)	1.20
	$\text{Li}_{3.8}\text{PO}_{3.2}\text{N}_{0.8}$	1.6×10^{-16} (25)	1.18
$\text{Li}_{3+x}\text{VO}_{4-x}\text{N}_x$	Li_3VO_4	2.0×10^{-7} (360)	1.29
	$\text{Li}_{3.2}\text{VO}_{3.8}\text{N}_{0.2}$	4.0×10^{-4} (330)	1.00
	$\text{Li}_{3.4}\text{VO}_{3.6}\text{N}_{0.4}$	1.2×10^{-5} (330)	1.01
	$\text{Li}_{3.6}\text{VO}_{3.4}\text{N}_{0.6}$	3.0×10^{-5} (330)	1.02
$\text{Li}_{2+y}\text{ZnSiO}_{4-y}\text{N}_y$	$\text{Li}_2\text{ZnSiO}_4$	8.0×10^{-8} (390)	1.14
	$\text{Li}_{2.2}\text{ZnSiO}_{3.8}\text{N}_{0.2}$	8.0×10^{-8} (115)	0.99
	$\text{Li}_{2.4}\text{ZnSiO}_{3.6}\text{N}_{0.4}$	4.0×10^{-6} (125)	0.44
	$\text{Li}_{2.6}\text{ZnSiO}_{3.4}\text{N}_{0.6}$	2.0×10^{-6} (70)	0.55
$\text{Li}_{2+y}\text{MgSiO}_{4-y}\text{N}_y$	$\text{Li}_2\text{MgSiO}_4$	4.0×10^{-8} (420)	1.39
	$\text{Li}_{2.2}\text{MgSiO}_{3.8}\text{N}_{0.2}$	4.0×10^{-7} (115)	0.80
	$\text{Li}_{2.4}\text{MgSiO}_{3.6}\text{N}_{0.4}$	1.0×10^{-6} (130)	0.87
	$\text{Li}_{2.6}\text{MgSiO}_{3.4}\text{N}_{0.6}$	7.0×10^{-6} (130)	0.83
	$\text{Li}_{2.8}\text{MgSiO}_{3.2}\text{N}_{0.8}$	5.0×10^{-7} (110)	0.79

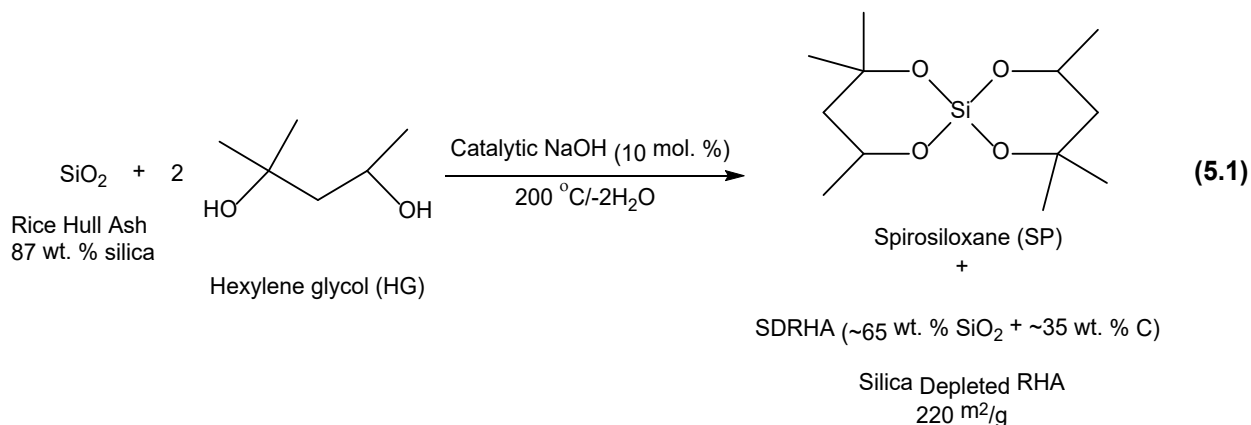
Indeed, studies show that Li_4SiO_4 may offer utility as a solid electrolyte. Wu *et al.*^{51,52} synthesized Li_4SiO_4 powders (particle sizes ≈ 100 nm) via sol-gel processing using SiO_2 (aerosil) and $\text{LiOH}\cdot\text{H}_2\text{O}$ as the starting materials and citric acid ($\text{C}_6\text{H}_8\text{O}_7\cdot\text{H}_2\text{O}$) as the chelating agent. Li_4SiO_4 pellets ($\Phi = 10$ mm, thickness = 2 mm) sintered at 1000 °C/4 h exhibited bulk conductivities of $\sim 10^{-3}$ S/cm at 400 °C. Similarly, Adnan *et al.*⁵³ prepared Li_4SiO_4 powders by sol-gel, then pelletized and sintered at 600-750 °C/4 h finding a bulk conductivity of $\sim 3 \times 10^{-6}$ S/cm at ambient, suggesting potential use as LISICON structured solid electrolytes for low-temperature applications.

Furthermore, various studies have described Li_4SiO_4 -based solid electrolytes, including the binary and ternary systems: $\text{Li}_4\text{SiO}_4\text{-Li}_3\text{XO}_4$ ($X = \text{V, As, P, etc.}$),⁵⁴⁻⁵⁹ and $\text{Li}_2\text{S-SiS}_2\text{-Li}_4\text{SiO}_4$.⁶⁰⁻⁶⁴

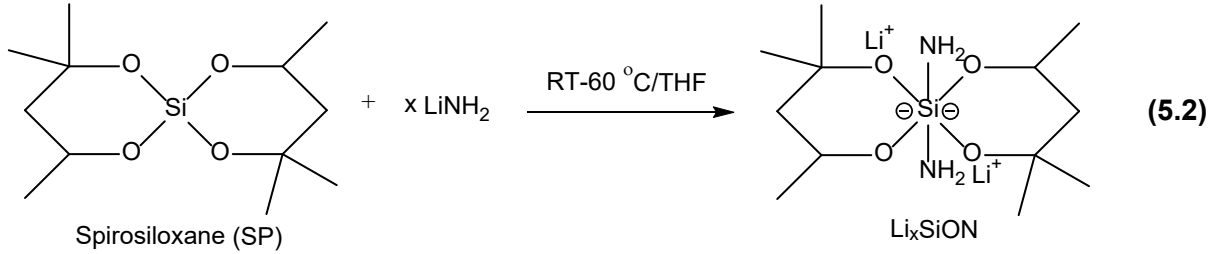
For the binary system, compositions with 40-60 mol.% Li_4SiO_4 typically give the highest ionic conductivities of $\sim 10^{-6}$ S/cm at 20 °C.^{55,57-59} For the ternary system, the composition $(1-z)[0.6\text{Li}_2\text{S}-0.4\text{SiS}_2]-z\text{Li}_4\text{SiO}_4$ ($z = 0-10$ mol.%) exhibits an ambient conductivity of $10^{-4}-10^{-3}$ S/cm.⁶⁰⁻⁶³

The above studies suggest that Li_4SiO_4 is a reasonable candidate for solid electrolyte applications. However, to the best of our knowledge, there have been no reports on N-doped Li_4SiO_4 (or Li_xSiON) as solid electrolytes. Given our previous success in developing polymer precursor derived Li_xPON -like electrolytes,⁶⁵⁻⁶⁷ we present here a novel and green approach to Li_xSiON oligomer/polymer precursors ($x = \text{Li/Si}$ mole ratio).

Recently, we reported processing “green” hybrid Li^+ capacitors (LICs) electrodes using the plentiful agricultural waste, RHA, as the starting material.⁶⁸ The basis for this report was the use of silica depleted RHA (SDRHA, ≈ 65 wt.% SiO_2 , 35 wt.% C); a carbon/silica nanocomposite. This nanocomposite derives from SiO_2 extraction from RHA by simple distillation of the spiro-siloxane $[(\text{C}_6\text{H}_{14}\text{O}_2)_2\text{Si}, \text{SP}]$ at 200 °C, as illustrated in reaction (5.1):



We report here that this spiro-siloxane “byproduct” provides the starting point for a series of Li^+ conducting polymer precursors on reaction with LiNH_2 , generically illustrated by reaction (5.2). Such a synthetic approach provides environmental advantages including green source, low cost, low temperature, low energy consumption, emission-free, and scalable features.



5.2 Experimental section

Density measurement. Masses (m) and dimensions (thickness t , and diameter Φ) of polymer precursor pellets (pelletized hydraulically at 5 ksi/20 sec with a $\Phi = 13$ mm die) heated to different temperatures (60-400 $^\circ\text{C}$) were measured. Density is calculated by the equation $\rho = 4m/(\pi\Phi^2t)$.

Electrochemical impedance spectroscopy (EIS). AC impedance data were collected with a broadband dielectric spectrometer (Biologics) in a frequency range of 7 MHz to 1 Hz at 10 mV. “EIS spectrum analyser” software was used for extracting total resistance. For Li_xSiON precursor pellets, concentric Au/Pd electrodes ($\Phi = 3$ mm) were deposited using an SPI sputter coater on both surfaces of polymer precursor pellets using a deposition mask. For Celgard/ Li_xSiON electrolytes, Li_xSiON THF solutions (0.05 g/mL) were coated on Celgard separators (18 mm \times 25 μm) and assembled between stainless steel (SS) disks ($\Phi = 8$ mm) forming symmetrical cells.

An equivalent circuit consisting of $(R_{total}Q_{total})(Q_{electrode})$ was used to measure the ionic resistivity. R and Q denote resistance and constant phase element, respectively. The total conductivity (σ) was calculated using the equation $\sigma_t = t/(A \times R)$, where t is the thickness of the polymer precursor pellet (0.2-0.3 mm) or coated Celgard PE, A is the active area, and R is the total resistivity obtained from the Nyquist plots.

Li^+ transference numbers (t_{Li^+}) of polymer electrolytes were calculated by chronoamperometric studies, using eq (5.3) as suggested by Evans *et al.*,⁶⁹ and were further confirmed by using data from the DC polarization experiments per eq (5.4).

$$t_{Li^+} = I_{SS}(U-Z_0 * I_0) / I_0(U-Z_{SS} * I_{SS}) \quad (5.3)$$

$$t_{Li^+} = \sigma_{Li^+} / (\sigma_e + \sigma_{Li^+}) \quad (5.4)$$

where σ_{Li^+} is the ionic conductivity of the polymer electrolytes and the σ_e is the electrical conductivity obtained from the DC polarization studies reported elsewhere.⁷⁰

Cyclic voltammetry (CV) and galvanostatic cycling tests were conducted using SP-300 potentiostats/galvanostat (Bio-Logic Science Instruments, Knoxville, TN). Detailed cell fabrication procedures and cycling conditions are reported elsewhere.^{70,71}

Detailed synthetic methods for Li_xSiON precursors, processing techniques, and other characterization procedures are given above in Chapter 2. Figure 2.2 shows optical images of representative Li_xSiON precursor powders dried at 60 °C/1 h/vacuum and pellets pressed hydraulically at 5 ksi/20 sec with a 13 mm diameter die.

5.3 Results and discussion

Our objectives in this work were first to carefully verify that the prepared precursors contain nitrogen and form oligomers as the first step in exploring their utility as $LiSiON$ precursors. Once having demonstrated well-defined compositions, the next step was to explore their properties as electrolytes. For clarity and simplicity, the precursors are simply labeled as Li_xSiON ($x = 2, 4, 6$) rather than including a complete chemical formula for reasons that become apparent below.

The apparent structures and chemical compositions of Li_xSiON precursors were analyzed using FTIR, MALDI-ToF, multi-nuclear NMR, TGA-DTA, XRD, XPS, SEM and EDX, followed by EIS for ionic conductivity measurements.

To further study electrochemical properties, Celgard separators were impregnated with Li_xSiON polymer precursors forming polymer electrolytes (PEs). These PEs were subjected to EIS, CV, and galvanostatic cycling to evaluate ionic conductivity, stability, and critical current

density. Additionally, a half-cell was assembled using a sulfur-based cathode (SPAN), Celgard/Li₆SiON PE and Li metal anode, and its stability was investigated by galvanostatic cycling.

Finally, in an attempt to improve electrochemical properties of Li₄Ti₅O₁₂ (LTO) anode, LTO nanopowders (NPs) prepared by liquid-feed flame spray pyrolysis (LF-FSP) were mixed with selected amounts (5 and 10 wt.%) of LiAlO₂ NPs and Li₆SiON polymer precursor forming LTO-composite anodes. Comparison of their discharge capacities and effects of LiAlO₂ NPs and Li₆SiON precursor are discussed.

5.3.1 Characterization of Li_xSiON precursors

Figure 5.1a shows representative FTIRs of Li_xSiON (dried at 60 °C/1 h/vacuum) compared to SP.

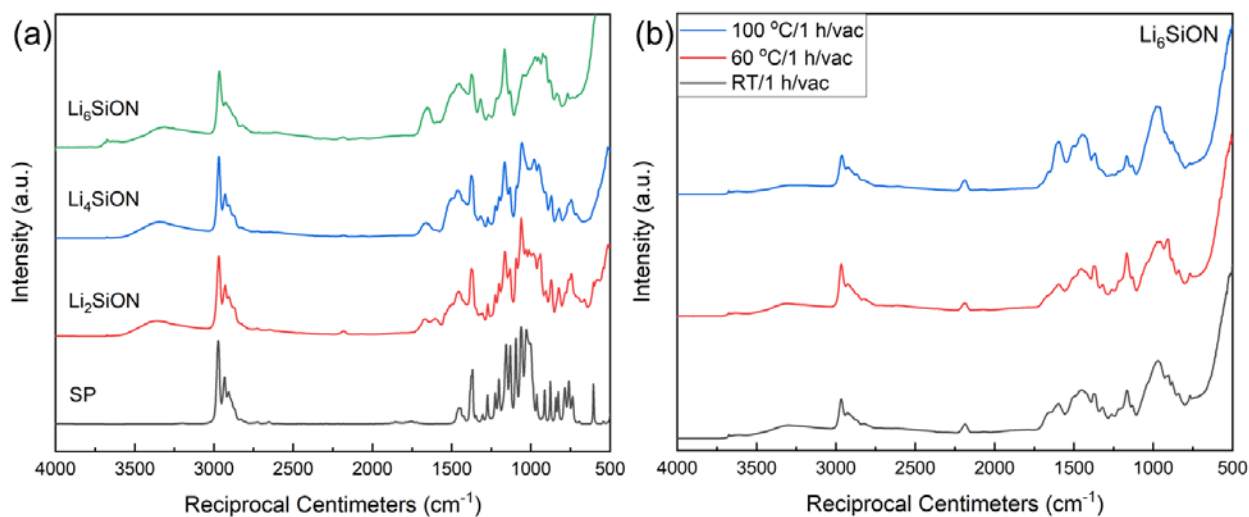


Figure 5.1. FTIRs of **a.** Li_xSiON precursors (60 °C/1 h/vacuum) and SP (60 °C/12 h/vacuum), **b.** Li₆SiON dried at RT, 60 and 100 °C/1 h/vacuum.

All precursors show similar SP peaks; in addition, the broad peak at ~3400 cm⁻¹ is ascribed to νN-H, with N-H overtones at ~1600 cm⁻¹. The Li₄SiON and Li₆SiON precursors exhibit a small νN-H peak at ~3600 cm⁻¹ evident of residual, unreacted LiNH₂ (Figure A.17) as excess LiNH₂ was

used to synthesize both Li_4SiON and Li_6SiON precursors. Li_xSiON precursors dried at temperatures ≤ 100 °C show similar FTIRs as illustrated by the **5.1b** FTIRs of Li_6SiON dried at RT-100 °C/vacuum. Likewise, as discussed below, very similar XRD patterns are also observed for precursors dried at low temperatures (≤ 100 °C).

Precursor MWs as well as possible compositions were analyzed using both positive- and negative-ion MALDIs, as done previously for Li_xPON and Li_xSiPON precursors.^{65,67} The ion source in the negative-ion mode comes from the precursor itself which loses Li^+ ; for the positive-ion mode, the ion source is Ag^+ from AgNO_3 and there is no loss of Li^+ . With the assistance of a Python program (see SI), calculations based on MALDI provide insights into the materials' possible compositions and structures.

Figure **5.2** shows positive-ion mode MALDIs of Li_xSiON precursors and possible compositions of selected peaks. Negative-ion mode MALDIs are given in Figure **A.18**; the complete composition calculations are listed in Table **A.7**. Table **5.2** records calculated properties of Li_xSiON precursors derived from MALDI peaks and their intensities.

In general, the Li_xSiON precursors show similar peaks with each peak consisting of different combinations of SP, $-\text{NH}_2$ and Li^+ . With higher Li content, the maximum MW (highest m/z) increases; all precursors formed oligomers with $\text{SP} = 3-5$ (Table **5.2**). Composition calculations (Figure **5.2** and Table **A.7**) suggest that there are typically 5-10 $-\text{NH}_2$ groups and 8-13 Li^+ in each precursor structure with only 1-5 SP units, which is much higher than available sites for LiNH_2 [two for each SP, see reaction (5.2)]. One possible explanation is that some Li^+ containing species exist as clusters in addition to those that interact with SP. It is also possible that ring-opening leads to the formation of more Si-NH bonds and Li-O-HG bonds, NMR data below do not support such conclusions but in fact also do not disprove the possibility.

A similar pattern is observed for both ion modes: precursors show peaks in separate groups, the difference between every two peaks in each group is typically 7 or 14 Da, which corresponds to one or two Li^+ (7 Da). In some cases, the distance of two peaks is 15-16 Da, which fits better with $-\text{NH}_2$ (16 Da). It is likely that each group of peaks corresponds to a certain structure, and each peak in that group corresponds to different numbers of Li^+ and $-\text{NH}_2$. The composition calculations listed in Table A.7 also indicates such pattern.

Additionally, similar or the same peaks are observed in both positive/negative-ion modes, but the start/end peaks of each group in the positive-ion mode generally shift higher ($\text{integer} \times 7 \text{ m/z} = \text{different numbers of } \text{Li}^+$) as there is no loss of Li^+ .

Atomic percentages (At.%) of N and Li calculated from possible compositions (Table A.7) are also given in Table 5.2. Since the composition calculation derived from MALDI gives mathematical combinations and multiple possible results are generated for each peak; for convenience, only one is chosen that may not reflect the true structure. Therefore, the At.% calculated from MALDI is meant solely to give a qualitative idea of N contents. As discussed below, XPS and EDX studies were performed to deduce the elemental At.% makeup of the Li_xSiON precursors.

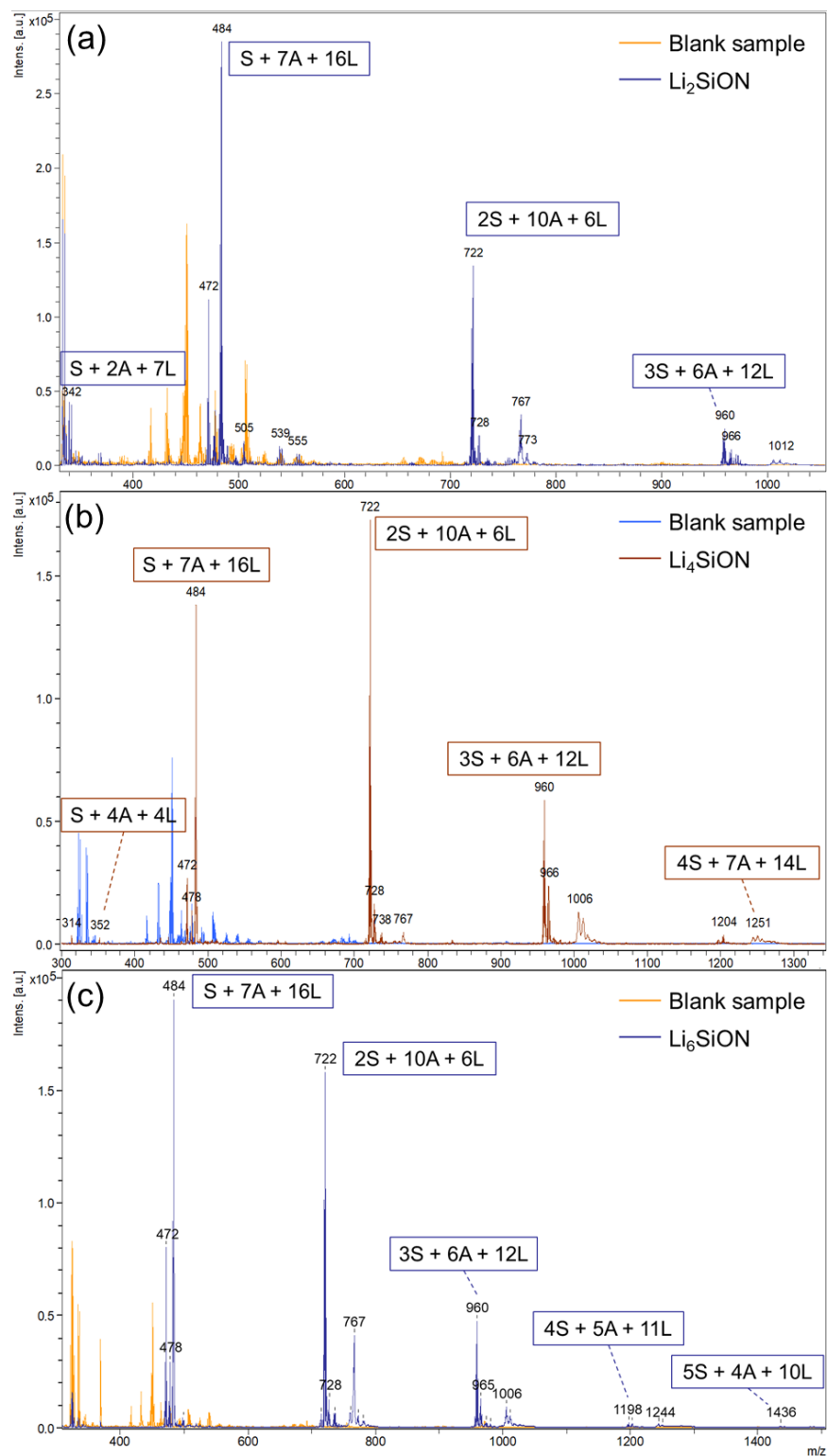


Figure 5.2. Positive-ion MALDI of blank vs. Li_xSiON precursors, **a.** Li_2SiON , **b.** Li_4SiON and **c.** Li_6SiON , and possible compositions of selected peaks. S = SP, A = $-\text{NH}_2$, L = Li^+ .

Table 5.2. Properties of Li_xSiON precursors derived from MALDI.

Precursor	Max. MW (m/z) ^a	Max. monomer units ^b	N At. % ^c	Li At. % ^c
Li_2SiON	1012 (P)	3 (P)	7.7 ± 3.0 (w. H)	8.3 ± 4.6 (w. H)
	946 (N)	3 (N)	17.4 ± 6.7 (wo. H)	18.2 ± 8.7 (wo. H)
Li_4SiON	1251 (P)	4 (P)	8.5 ± 2.8 (w. H)	9.7 ± 5.1 (w. H)
	1002 (N)	3 (N)	18.9 ± 6.2 (wo. H)	20.9 ± 9.7 (wo. H)
Li_6SiON	1436 (P)	5 (P)	8.4 ± 2.9 (w. H)	9.2 ± 4.7 (w. H)
	1196 (N)	4 (N)	18.6 ± 6.5 (wo. H)	21.1 ± 8.6 (wo. H)

^aMaximum molecular weights. P = positive-ion mode, N = negative-ion mode. ^bMaximum monomer units = maximum number of SP by calculation. ^cCalculated N/Li atomic percentages. “w. H”: including H as part of the calculation; “wo. H” excluding H, providing comparison to XPS studies below.

The chemical environments and structures for Li_xSiON precursors, were further elucidated using NMR. Dried Li_xSiON powders (0.05 g, RT/1 h/vacuum) were dissolved in 1 mL CDCl_3 .

Figure A.19 compares the ^1H NMRs of the Li_xSiON precursors (RT/1 h/vacuum), THF and SP. All Li_xSiON precursors show peaks at 3.7 and 1.8 ppm in addition to SP peaks, which are ascribed to residual THF. Unlike Li_4SiON and Li_2SiON precursors, Li_6SiON shows no original SP peaks but a broad peak at 1-1.5 ppm ($-\text{CH}_3/\text{CH}_2$) indicating fluxional behavior.^{72,73}

To eliminate residual THF, Li_xSiON precursors were further dried at 60 °C/24 h/vacuum in a vacuum oven. The dried solids (0.05 g each) were added to 1 mL CDCl_3 , respectively. All formed suspensions after stirring overnight/RT, suggesting reduced solubility after prolonged drying.

Figure 5.3 compares the ^1H NMRs of the Li_xSiON precursors (60 °C/24 h/vacuum) and SP, no THF peaks (3.7 and 1.8 ppm) are observed. Similar to precursors dried at RT/1 h/vacuum (Figure A.19), Li_6SiON (60 °C/24 h/vacuum) shows only a small and broad $-\text{CH}_3/\text{CH}_2$ peak at 1.2-1.3 ppm, suggesting fluxional behavior.

Both Li_4SiON and Li_2SiON precursors show a peak at 4.2 ppm, likely the $-\text{CHO}$ group from SP that shifts due to interaction with Li^+ , suggesting Li^+ interacts more directly with O lone electron pairs from SP. The same $-\text{CH}_3$ peaks from SP are observed in Li_4SiON and Li_2SiON precursors, but the intensity is reduced for Li_4SiON , suggesting there may be partial fluxional behavior for the Li_4SiON precursor.

Li₆SiON

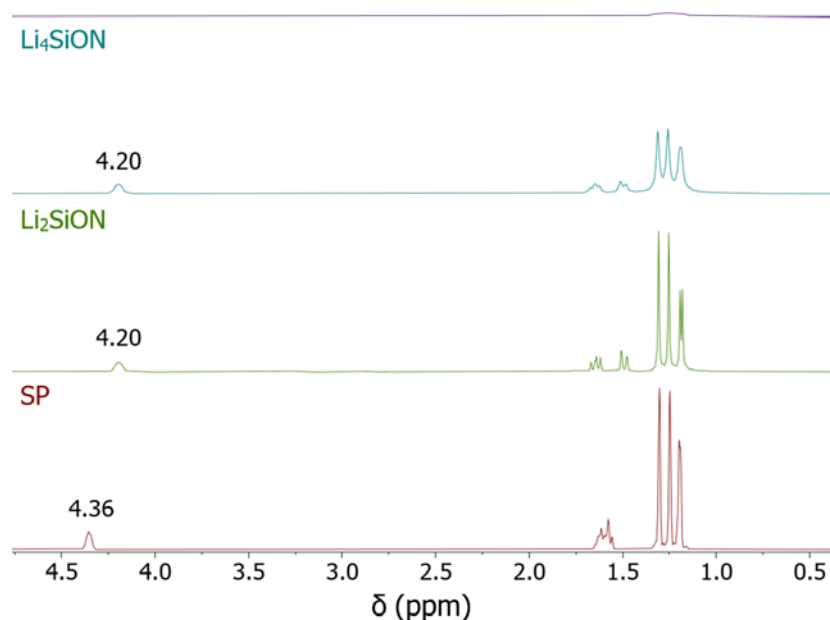


Figure 5.3. ¹H NMRs of Li_xSiON precursors (60 °C/24 h/vacuum) and SP.

Similarly, ¹³C NMRs of the Li_xSiON precursors dried at RT/1 h/vacuum exhibit THF peaks at 68.1 and 25.7 ppm (Figure A.20), but no THF peaks are observed for Li_xSiON precursors dried at 60 °C/24 h/vacuum (Figure 5.4). Both Li₄SiON and Li₂SiON (60 °C/24 h/vacuum) show small SP peaks that shift due to interaction with Li⁺, and the -CO and -CHO show higher $\Delta\delta_c$ (qualitative, blue dash lines in Figure 5.4) than -CH₂ and -CH₃ peaks, suggesting Li⁺ likely interacts with the O from SP, in agreement with the ¹H NMR.

The disappearance of SP peaks for the Li₆SiON precursor (Figures 5.4 and A.20) again reflects fluxional behavior pointing to rapid exchange of Li⁺ in associated clusters. Lee *et al.*⁷⁴ studied exchange dynamics in Li⁺ liquid electrolytes of 1.0 M LiPF₆ in DEC and PC/DMC (1:1 vol.). Ultrafast fluxional behavior of Li⁺-carbonate complexes is observed (electrostatic interactions forming and breaking in picoseconds) as proven by coherent 2-D infrared spectroscopy, suggesting

macroscopic Li^+ transport may be related to microscopic fluctuation of solvation. We can suggest that fast chemical exchange dynamics will also play an important role in solvation and de-solvation of Li^+ in solid polymer electrolytes.

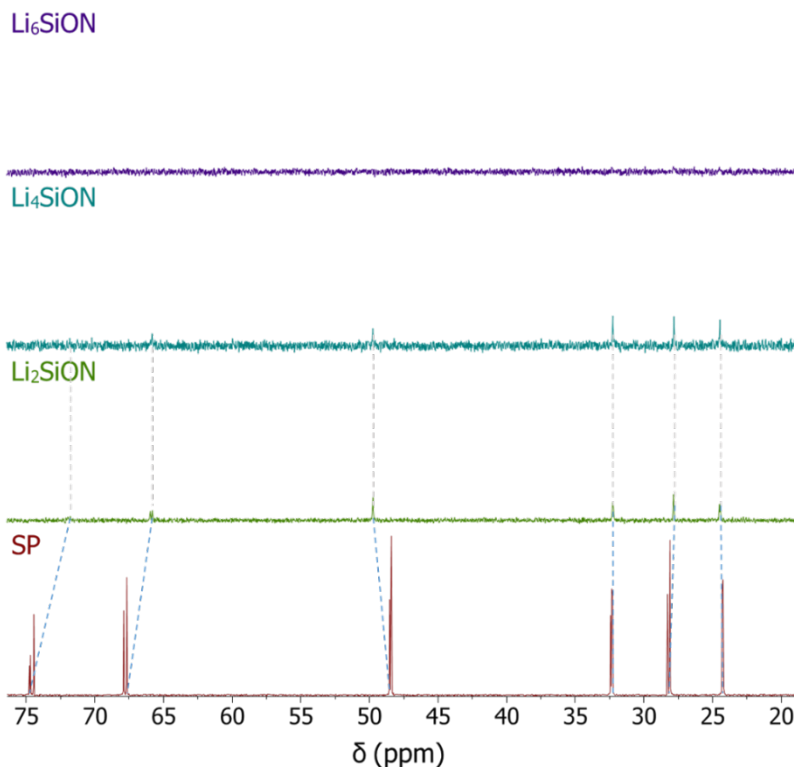


Figure 5.4. ^{13}C NMRs of Li_xSiON precursors (60 °C/24 h/vacuum) and SP.

Figure 5.5 compares the ^7Li NMRs of Li_xSiON precursors (RT/1 h/vacuum), the δ_{Li} shifts downfield with increasing Li content, especially for the Li_6SiON precursor suggesting Li^+ ions are well solvated. The excess Li^+ likely forms clusters in agreement with work of See *et al.*⁷⁵ where δ_{Li} shifts to higher frequencies as Li^+ concentration increases (LiTFSI in DOL/DME), as also found in our previous studies on Li_xPON -like polymer precursors.⁶⁵ These results suggest the downfield shift is due to deshielding of Li^+ (reduced electron density around Li^+), i.e., increased numbers of Li^+ interacting with one SP molecule (coordination numbers change).

However, broad ^7Li bands with low intensities centered at ~ 0 ppm are observed for Li_xSiON precursors dried at $60\text{ }^\circ\text{C}/24\text{ h/vacuum}$ due to low solubility (Figure A.21), suggesting that THF aids in dissolution of Li^+ .

^{29}Si NMRs of Li_xSiON precursors and SP are presented in Figure A.22. For precursors dried at RT/1 h/vacuum (Figure A.22a), similar to ^1H and ^{13}C studies, no SP peaks were found for the Li_6SiON precursor, while Li_2SiON and Li_4SiON precursors show the same δ_{Si} at -81.3 ppm as SP, suggesting no chemical environment change on the O-Si-O bonds for Li_2SiON and Li_4SiON precursors, but fluxional behavior for the Li_6SiON precursor.

However, no ^{29}Si signals are observed for Li_xSiON precursors dried at $60\text{ }^\circ\text{C}/24\text{ h/vacuum}$ (Figure A.22b), likely due to reduced solubility, in agreement with ^7Li NMR above.

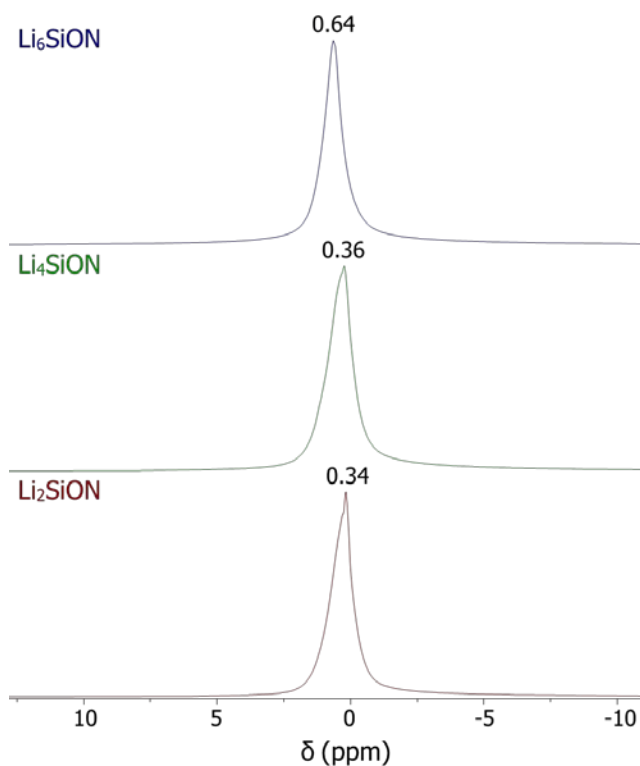


Figure 5.5. ^7Li NMRs of Li_xSiON precursors (RT/1 h/vacuum).

The thermal stability of Li_xSiON precursors were investigated by TGA-DTA studies. Figure 5.6 compares representative TGA-DTAs ($800\text{ }^\circ\text{C}/10\text{ }^\circ\text{C min}^{-1}/\text{N}_2$) of Li_xSiON precursors (dried at $60\text{ }^\circ\text{C}/1\text{ h}/\text{vacuum}$). All precursors typically show 5 % mass loss temperatures ($T_{5\%}$) $>100\text{ }^\circ\text{C}$; the major mass loss (from $\sim 100\text{ }^\circ\text{C}$ to $\sim 300\text{-}450\text{ }^\circ\text{C}$) is associated with evaporation and/or decomposition of organics. Additionally, the Li_6SiON precursor exhibits a second mass loss at $\sim 650\text{ }^\circ\text{C}$, associated with excess LiNH_2 decomposition.⁷⁶ Overall, the CYs ($800\text{ }^\circ\text{C}$) of Li_xSiON precursors are $\text{Li}_6\text{SiON} > \text{Li}_4\text{SiON} > \text{Li}_2\text{SiON}$ in $\sim 10\text{ wt.}\%$ increments (Figure 5.6) correlated with MWs (Figure 5.2 and Table 5.2) and Li contents.

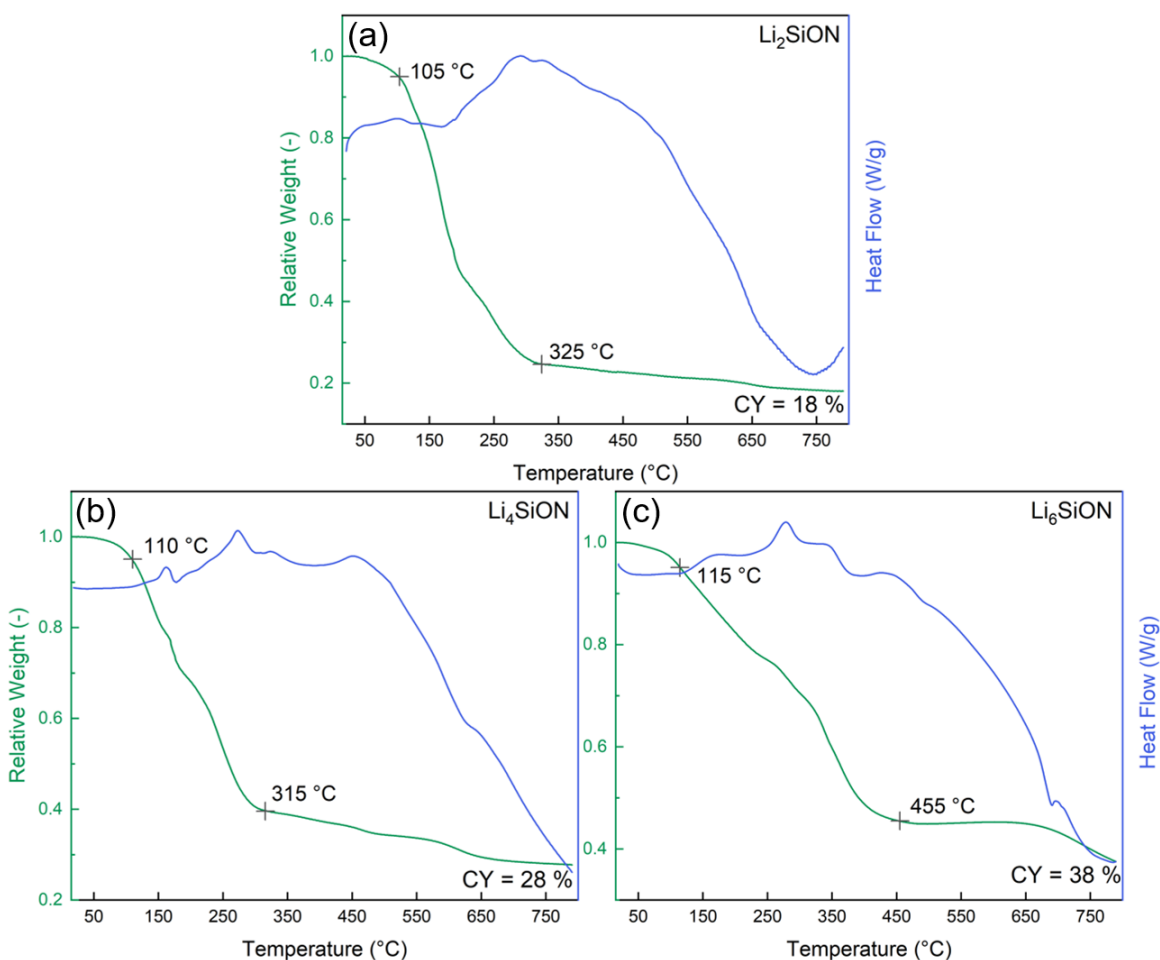


Figure 5.6. TGA-DTAs ($800\text{ }^\circ\text{C}/10\text{ }^\circ\text{C min}^{-1}/\text{N}_2$) of **a.** Li_2SiON , **b.** Li_4SiON and **c.** Li_6SiON precursors dried at $60\text{ }^\circ\text{C}/1\text{ h}/\text{vacuum}$.

Unlike the Li_xSiON precursors, SP evaporates/distills fully at $\sim 100\text{-}200\text{ }^\circ\text{C}$ (Figure A.23) due to its high vapor pressure. Consequently, added LiNH_2 promotes formation of oligomers/polymers with higher MWs and stable polymer precursors and eventually ceramics form at higher temperatures as demonstrated below.

Figure 5.7a compares the XRDs of Li_xSiON (dried at $60\text{ }^\circ\text{C}/1\text{ h}/\text{vacuum}$) and SP. SP exhibits various crystalline peaks that are indexed to space group 10: P2/m by Expo2014, while the Li_xSiON precursors show a broad peak at $\sim 20^\circ 2\theta$ suggesting amorphous materials, indicating that SP reacts fully. As mentioned above, when dried at temperatures $\leq 100\text{ }^\circ\text{C}$, Li_xSiON precursors show similar XRD patterns, see Figure 5.7b comparing XRDs of Li_6SiON dried at RT- $100\text{ }^\circ\text{C}/\text{vacuum}$ as an example. It's noteworthy that there is a small peak at $33^\circ 2\theta$ in the XRD corresponding to $\text{Li}(\text{OH})(\text{H}_2\text{O})$, likely due to brief interactions with atmospheric moisture during sample preparation, but the intensity is very low.

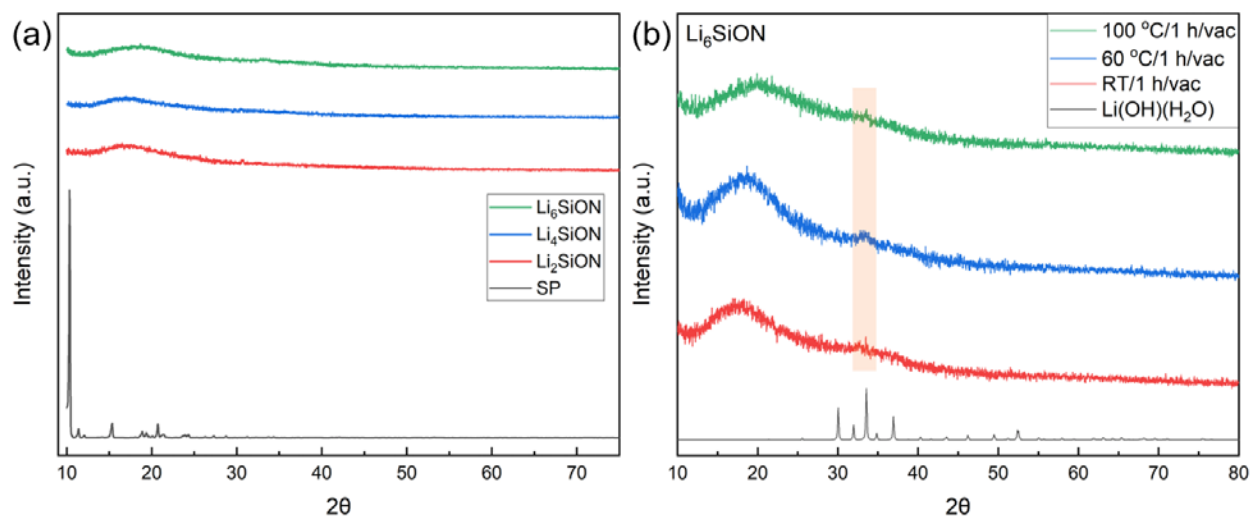


Figure 5.7. XRDs of **a.** Li_xSiON precursors ($60\text{ }^\circ\text{C}/1\text{ h}/\text{vacuum}$) and SP ($60\text{ }^\circ\text{C}/12\text{ h}/\text{vacuum}$), **b.** Li_6SiON dried at RT, 60 and $100\text{ }^\circ\text{C}/1\text{ h}/\text{vacuum}$.

To study XRDs of Li_xSiON precursors heated to higher temperatures ($>100\text{ }^\circ\text{C}$), dried polymer precursor powders ($60\text{ }^\circ\text{C}/24\text{ h/vacuum}$, $0.1\text{-}0.2\text{ g}$) were compacted into pellets using a 13 mm diameter die at 5 ksi/RT (Figure 2.2). The resulting pellets were heated between Al_2O_3 disks to $100\text{-}400\text{ }^\circ\text{C}/2\text{ h}$ at $1\text{ }^\circ\text{C}/\text{min}$ under $120\text{ mL}/\text{min}$ N_2 flow.

Figure 5.8 presents XRD patterns of Li_xSiON pellets heated to $100\text{-}400\text{ }^\circ\text{C}/2\text{ h}/\text{N}_2$. XRD of Li_2SiON pellet (Figure 5.8a) heated to $100\text{ }^\circ\text{C}$ exhibits small peaks at $\sim 20^\circ$ and $30^\circ\ 2\theta$, corresponding to LiSi_2N_3 (PDF-01-086-6830) with space group $\text{Cmc}21$. The pellet also exhibits a large broad peak from $\sim 30\text{-}40^\circ\ 2\theta$ with a central and shoulder peaks at 35° and $38^\circ\ 2\theta$ associated with an amorphous phase. The small peak $\sim 30^\circ\ 2\theta$ disappears when the Li_2SiON pellet is heated to $200\text{-}300\text{ }^\circ\text{C}$. The broad peak seems to shift to lower diffraction angles ($20\text{-}30^\circ\ 2\theta$) when the pellet is heated to $400\text{ }^\circ\text{C}$.

Figure 5.8b shows that Li_4SiON pellets present a broad peak similar to Li_2SiON after heating to $100\text{ }^\circ\text{C}$. No apparent sharp peaks appear on heating to $200\text{-}300\text{ }^\circ\text{C}$ confirming the absence of any ordered crystalline structure. At $400\text{ }^\circ\text{C}$, the amorphous peak shifts to lower diffraction angles with a shoulder peak at $\sim 32^\circ\ 2\theta$, suggesting that the lattice is expanding. This might be ascribed to nitrogen loss which results in a change in composition and structure.

The XRD of Li_6SiON pellets (Figure 5.8c) at $100\text{ }^\circ\text{C}$ is dominated by a broad peak corresponding to a poorly crystallized material, indicating an amorphous nature. The sharp peak at $35^\circ\ 2\theta$ can be indexed to partially crystalline Li_4SiO_4 (PDF-01-084-7600) after heating to $200\text{ }^\circ\text{C}$. The single peak at $\sim 22^\circ\ 2\theta$ starts to split into doublets when the Li_6SiON pellet is heated above $300\text{ }^\circ\text{C}$. The doublets at $\sim 30^\circ\ 2\theta$ for the pellet heated to $400\text{ }^\circ\text{C}$ corresponds to Li_2CO_3 (PDF-04-0101-7186). Since the Li_6SiON precursor contains a slight LiNH_2 component, it is quite likely to form Li_2CO_3 during the decomposition process, which will generate CO_2 .

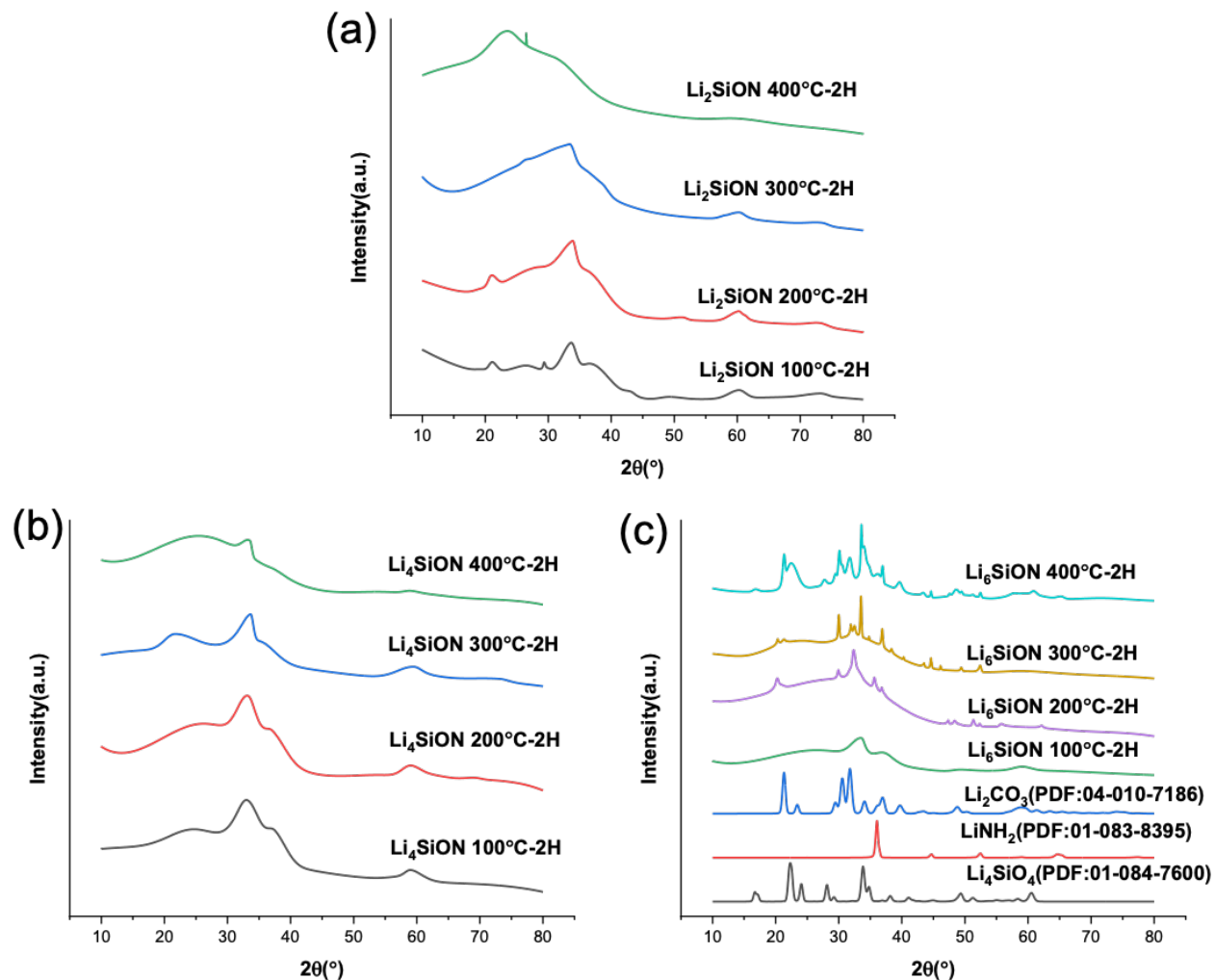


Figure 5.8. XRDs of **a.** Li_2SiON , **b.** Li_4SiON , **c.** Li_6SiON pellets heated to 100-400 °C/2 h/ N_2 .

The amorphous nature of the Li_xSiON precursors ≤ 100 °C by XRD fails to reveal elemental compositions of as-synthesized materials. Hence, Li_xSiON precursors (dried at ≤ 100 °C, powders) were characterized by XPS. For each sample, a wide-scan survey was done on three separate points for better accuracy. As shown in Figure 5.9, all precursors show peaks for O, C and Li, small amounts of N and Si, and little difference is observed at different drying temperatures. SP, on the other hand, only shows peaks for O, C, and Si with higher intensity (Figure A.24).

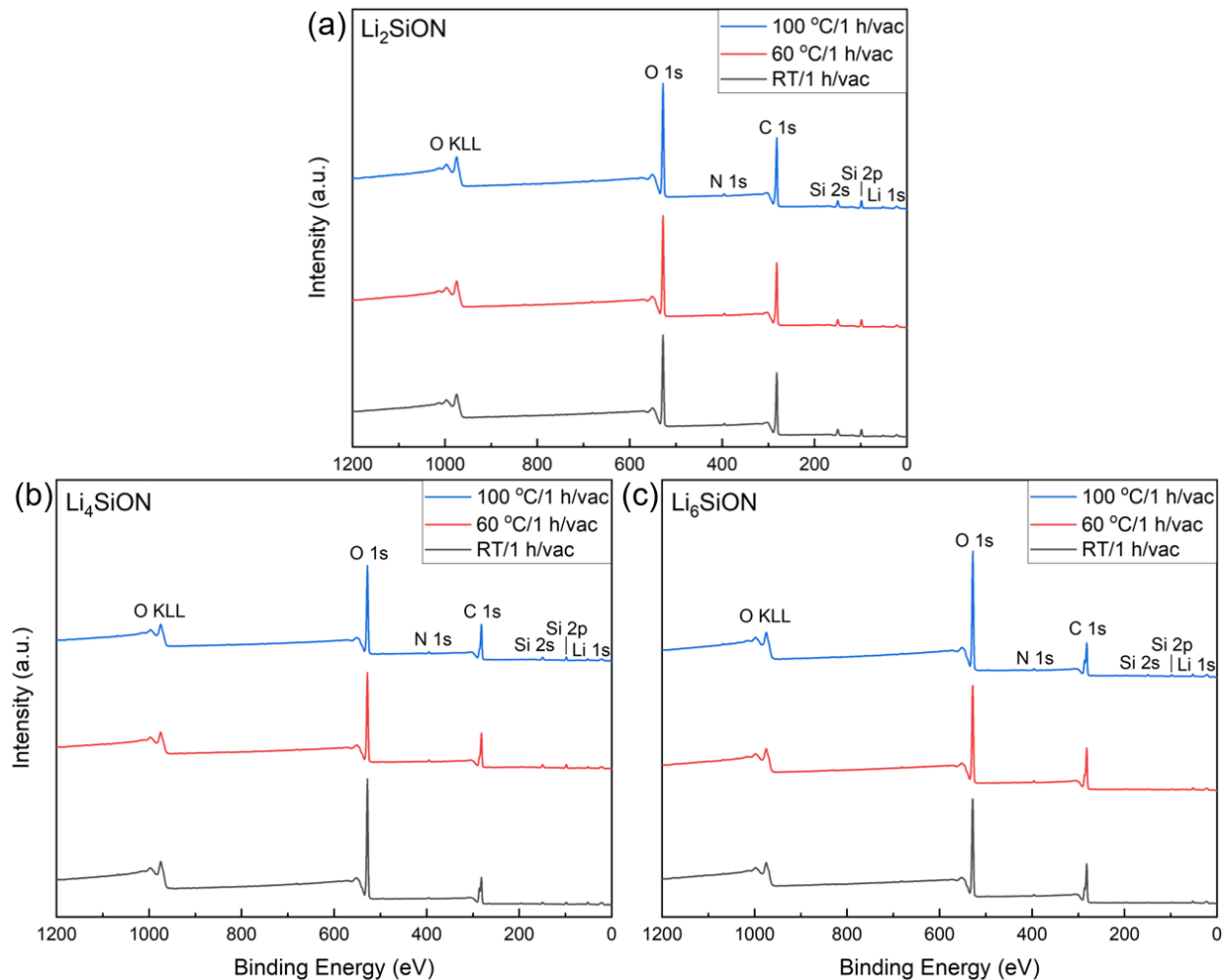


Figure 5.9. Wide-scan survey XPS spectra of Li_2SiON (a), Li_4SiON (b) and Li_6SiON (c) precursors dried at RT, 60 and 100 °C/1 h/vacuum respectively.

Table 5.3 summarizes the average At.% for Li_xSiON precursors dried at different temperatures compared to SP. In general, Li_xSiON precursors show lower C and Si contents compared to SP as expected, but the O content increases which may be LiOH and/or Li_2CO_3 formed due to brief exposure in air.

The At.% for all Li_xSiON precursors stay nearly the same after drying at different temperatures under vacuum. The Li content increases with the amount of added LiNH_2 as expected, but the

increase from Li₄SiON to Li₆SiON is smaller than the increase from Li₂SiON to Li₄SiON, suggesting that Li content saturation is likely reached for the Li₆SiON precursor. The fluxional nature of this one precursor belies the large excess of LiNH₂ originally added and strongly suggests novel chemistry for this system since, we originally assumed that only two amide groups might be accommodated based on equation (5.2). Unfortunately, this same fluxional nature means that NMR characterization was not possible at least at ambient.

For Li₂SiON and Li₄SiON precursors, C and Si contents decrease with increasing Li content, but the O content shows the opposite trend. As mentioned above, this is likely a result of LiOH and/or Li₂CO₃ forming, and a higher Li content leads to a higher O content.

For the Li₆SiON precursor, C and O contents are similar to the Li₄SiON precursor, which may be related to the similar Li contents. However, after drying at 100 °C/1 h/vacuum, we can see a significant decrease in the C content and increases in the Li, O and Si contents. C may come from adsorbed organics during sample preparation that are volatile and removed on drying at a higher temperature resulting in increased percentages for the other elements.

Table 5.3. Average atomic percentage (At.%) of Li_xSiON precursors dried at different temperatures in comparison with SP (60 °C/12 h/vacuum), analyzed by CasaXPS.

Compound	Condition	Li 1s	C 1s	N 1s	O 1s	Si 2p
SP	60 °C/12 h/vacuum	-	80.0	-	14.1	5.0
Li ₂ SiON	RT/1 h/vacuum	13.0	56.3	0.8	23.3	6.7
	60 °C/1 h/vacuum	12.9	55.5	0.8	24.3	6.5
	100 °C/1 h/vacuum	13.3	54.6	0.8	25.0	6.2
Li ₄ SiON	RT/1 h/vacuum	24.9	40.3	0.7	31.8	2.3
	60 °C/1 h/vacuum	23.9	42.8	1.0	28.0	4.2
	100 °C/1 h/vacuum	22.1	45.0	0.8	28.2	3.9
Li ₆ SiON	RT/1 h/vacuum	23.8	46.5	0.7	28.4	0.6
	60 °C/1 h/vacuum	25.2	46.0	0.9	27.2	0.7
	100 °C/1 h/vacuum	31.5	36.9	0.7	29.4	1.5

However, the N content ranges between 0.7-0.9 at.% for all precursors. Since all samples were kept under vacuum overnight prior to XPS scans (10⁻⁹-10⁻⁷ Torr), -NH₂ is likely eliminated as NH₃,

and the residual or “stable” N is similar for all precursors. In contrast, the MALDI studies on Li_xSiON solution droplets dried *in vacuo* for only a few minutes retained $-\text{NH}_2$ groups presenting much higher N contents ($\sim 5\text{-}30$ at.% N excluding H) as suggested by composition calculations (Table 5.2). It is also worth mentioning that the At.% analyzed by XPS may not be accurate as XPS only characterizes the sample surface to depths ≤ 10 nm.

Representative N 1s and Si 2p core-level XPS spectra of Li_xSiON precursors (dried at $60^\circ\text{C}/1$ h/vacuum) are given in Figure 5.10. All Li_xSiON precursors show an N 1s peak at $\sim 396\text{-}397$ eV (Figure 5.10a), which can be ascribed to Li-NH from LiNH_2 . Due to the low N content, the N 1s intensity is low for all precursors. It is noticeable that the N 1s peak shifts to lower binding energy (BE) as the Li content increases, i.e., BE of the N 1s peak (BE_N) follows $\text{Li}_2\text{SiON} > \text{Li}_4\text{SiON} > \text{Li}_6\text{SiON}$, with a ΔBE of $0.4\text{-}0.5$ eV. Since the BE is related to electron density, as the electronegativity (EN) of surrounding atoms decreases, electron density increases for the base element and BE decreases. For Li_xSiON precursors, as the Li (low EN) content increases, Li^+ concentration increases but the “stable” N content stays at ~ 1 at.% for all precursors (Table 5.3), resulting in increased electron density around N and thus lower BE.

For Si 2p XPS spectra (Figure 5.10b), all Li_xSiON precursors exhibit Si $2p_{1/2}$ and $2p_{3/2}$ peaks ascribed to Si-O from SP. Similar to N 1s peaks, the Si 2p peak shifts to lower BE as the Li content increases (BE_Si : $\text{SP} > \text{Li}_2\text{SiON} > \text{Li}_4\text{SiON} > \text{Li}_6\text{SiON}$), which is likely due to the increased number of Li^+ that interact with the O from SP as suggested by NMR studies.

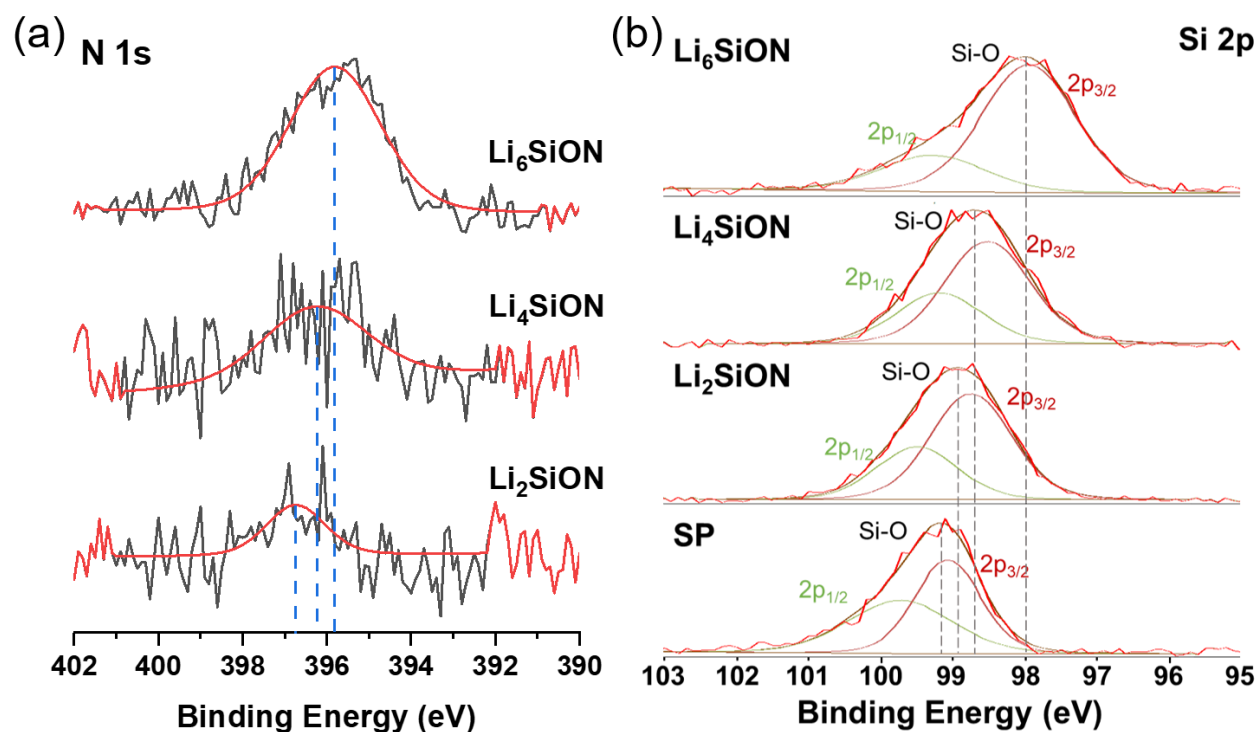


Figure 5.10. N 1s core-level XPS spectra of Li_xSiON precursors (60 °C/1 h/vacuum). **b.** Si 2p XPS core-level spectra of Li_xSiON precursors (60 °C/1 h/vacuum) compared to SP (60 °C/12 h/vacuum).

To study high temperature compositions of Li_xSiON precursors, precursor pellets (Figure A.30) were heated to 800 °C/1 h/ N_2 in a tube furnace and characterized by FTIR, XRD and XPS. Figure 5.11a compares the FTIRs of Li_xSiON heated to 800 °C/1 h/ N_2 . Peaks at $\sim 1450\text{ cm}^{-1}$ are present for all precursors, which may be carbonate and/or silicate peaks. The peaks at $\sim 1000\text{--}800\text{ cm}^{-1}$ are likely $\nu\text{Si-O}$ ($\sim 1050\text{ cm}^{-1}$) and possibly some $\nu\text{Si-N}$ ($960\text{--}840\text{ cm}^{-1}$),^{77–81} or silicate peaks.

Figure 5.11b compares the XRDs of Li_4SiON (800 °C/1 h/ N_2) and Li_4SiO_4 as an example. Both the pellets and ground powder show the same diffraction peaks, suggesting phase uniformity of the bulk surface and interior. These peaks fit well with monoclinic Li_4SiO_4 , in agreement with FTIR analyses in Figure 5.11a.

Figure 5.11c compares the XPS spectra of Li_4SiON treated at RT/1 h/vacuum and 800 °C/1 h/ N_2 . Both spectra show the same main peaks for O, C, Si and Li. Only trace amounts of N are found in Li_4SiON treated at RT/1 h/vacuum, and no N in Li_4SiON treated at 800 °C/1 h/ N_2 .

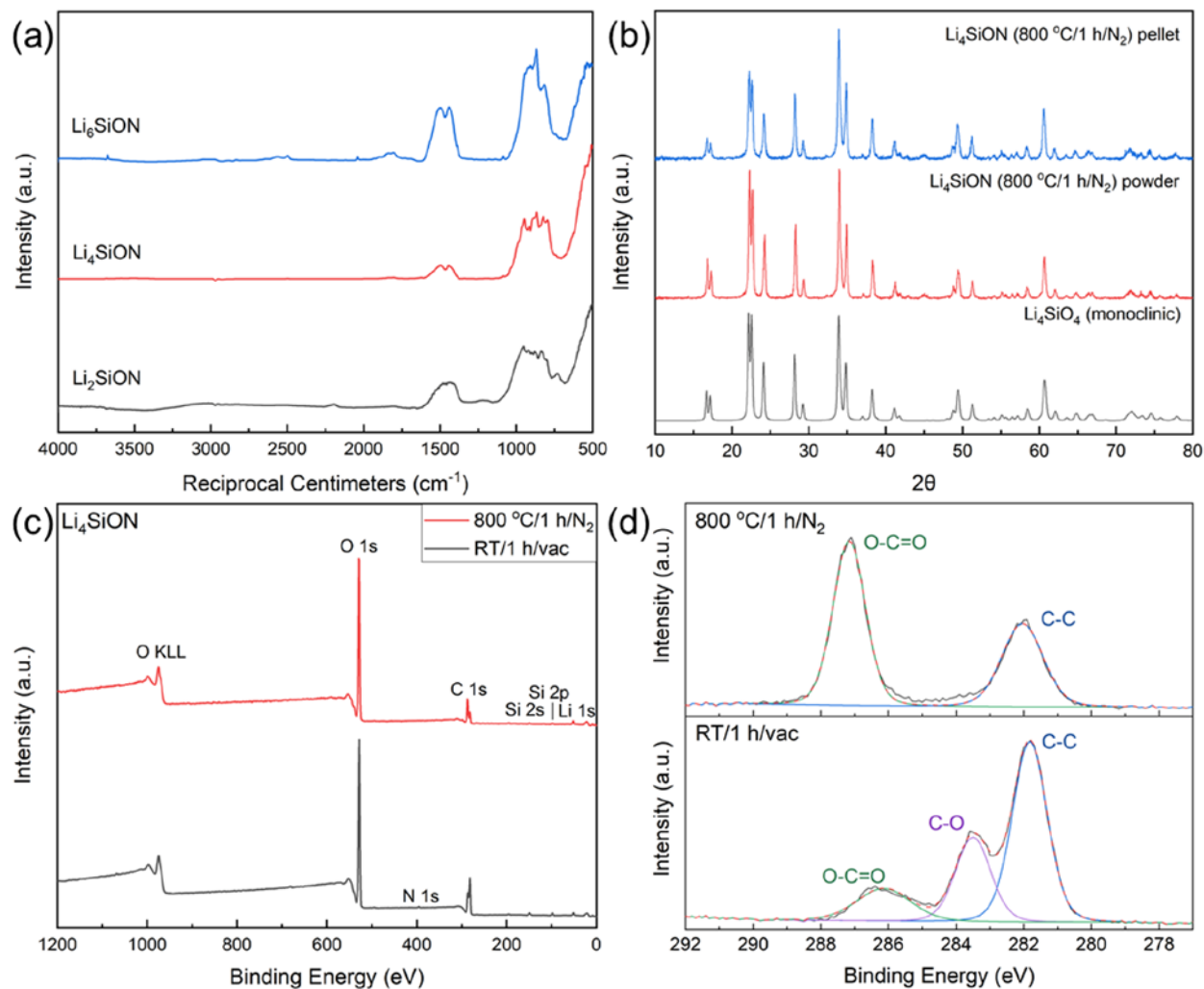


Figure 5.11a. FTIRs of Li_xSiON pellets heated to 800 °C/1 h/ N_2 . **b.** XRDs of Li_4SiON (800 °C/1 h/ N_2) pellet and powder compared to Li_4SiO_4 (monoclinic). **c.** Wide-scan survey XPS spectra of Li_4SiON treated at RT/1 h/vacuum and 800 °C/1 h/ N_2 . **d.** C 1s core-level spectra of Li_4SiON treated at RT/1 h/vacuum and 800 °C/1 h/ N_2 .

Table 5.4 summarizes the XPS analyses of Li₄SiON treated at different temperatures. Li and O contents increase after heating to 800 °C while C and N contents decrease due to decomposition of organic groups.

As for the binding energy, all elements remain mostly the same after heating to 800 °C except for C per Table 5.4. Figure 5.11d compares C 1s core-level spectra of Li₄SiON treated at RT/1 h/vacuum and 800 °C/1 h/N₂. The as-synthesized Li₄SiON (RT/1 h/vacuum) show three different C 1s peaks, corresponding to O-C=O from carbonate, and C-O and C-C from SP. After heating to 800 °C, as the organic components decompose, C-O disappears and the intensity of C-C drops (residual carbon), leaving a large carbonate peak (O-C=O) that also corresponds to the band at ~1450 cm⁻¹ in the FTIR (Figure 5.11a). Overall, after heating to 800 °C/1 h/N₂, the precursors form stable crystalline Li₄SiO₄ and small amounts of Li₂CO₃.

Table 5.4. XPS analyses (by CasaXPS) of the Li₄SiON precursor treated at different temperatures.

	Condition	Li 1s	C 1s	N 1s	O 1s	Si 2p
Binding energy (eV)	RT/1 h/vacuum	52	282, 284, 286	396	529	99
	800 °C/1 h/N ₂	52	282, 287	-	529	98
Average At. %	RT/1 h/vacuum	24.9	40.3	0.7	31.8	2.3
	800 °C/1 h/N ₂	36.6	25.3	-	37.0	1.2

To further characterize the composition and microstructures of the Li_xSiON precursors, SEM and EDX were conducted on precursor pellets (Figure 2.2), respectively.

Figure 5.12 shows SEM fracture surface images of Li₂SiON, Li₄SiON, and Li₆SiON precursor pellets heated to 100-400 °C/2 h/N₂. The Li₄SiON and Li₆SiON pellets heated between 100-200 °C, in general, show a smooth, uniform, and dense microstructure, typical for polymeric materials, which can be ascribed to the fact that these precursors show a relatively small mass loss (20 wt.%) before 250 °C. The densification at 200 °C for the Li₄SiON and Li₆SiON pellets might be due to

rearrangement between the polymeric chains during heat treatment; it may be also associated with a phase change as suggested by XRD for Li_6SiON (Figure 5.8c). In comparison to pellets with high Li content, the microstructure of Li_2SiON pellet reveals porous structures on heating between 100-200 °C, attributed to the large mass loss (50 wt.%) before 250 °C (Figure 5.6a).

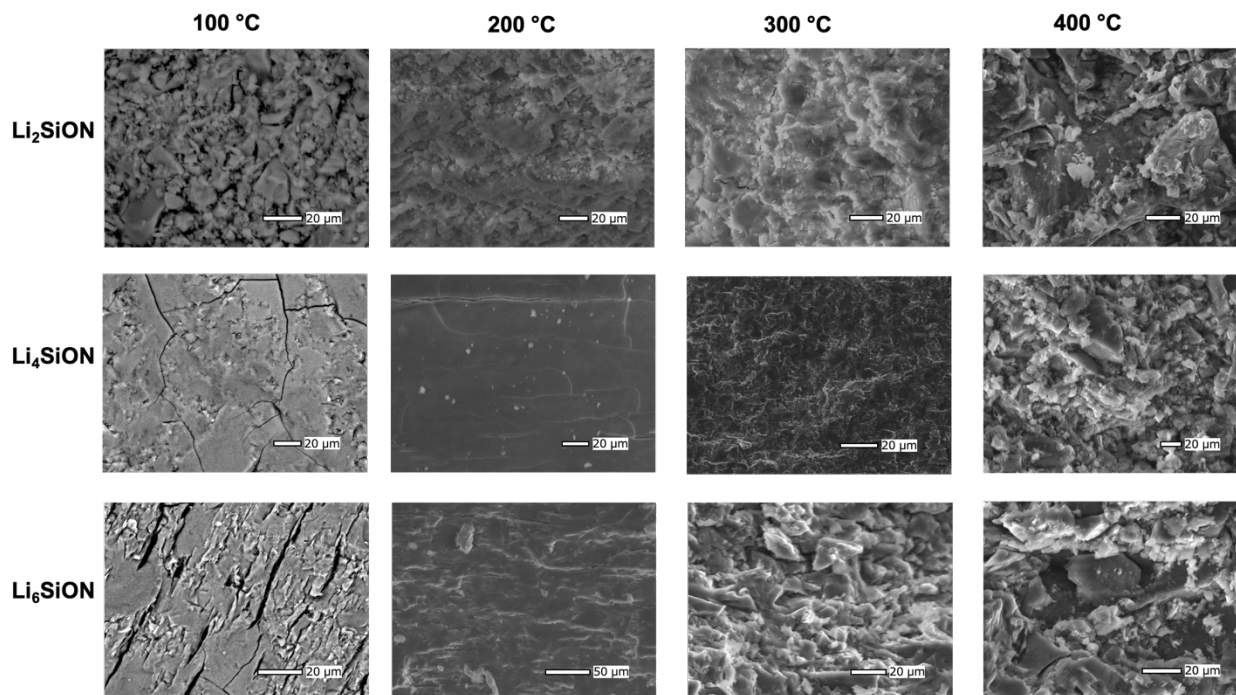


Figure 5.12. SEM fracture surface images of Li_xSiON pellets heated to 100-400 °C/2 h/ N_2 .

The pellets heated between 300-400 °C exhibit crystalline features with uneven fracture surface (grain boundary fractures) as well as micropores associated with the loss of volatile and organic compounds and ceramization of the precursors.

Table 5.5 lists densities of Li_xSiON precursor pellets treated under different conditions. The as-synthesized precursors (dried at 60 °C/1 h/vacuum) show densities close to 1 g/cm^3 , which is typical for polymeric materials. After heat treatment to 100-400 °C/2 h/ N_2 , all precursors show increased densities, which may be arised from polymeric structural rearrangements, and ceramization at higher temperatures (≥ 300 °C, Figure 5.12). In general, the density increases with

temperature, but Li₂SiON and Li₄SiON precursors show decreased density when the temperature increased from 300° to 400 °C, likely due to decomposition of organic compounds, consistent with SEM (Figure 5.12) and TGA-DTA studies (Figure 5.6). The Li₆SiON precursor shows better thermal stability as suggested by TGA-DTA (Figure 5.6), therefore its density increases after heating to 400 °C.

Table 5.5. Densities (g/cm³) of Li_xSiON precursors treated under different conditions.

	Li ₂ SiON	Li ₄ SiON	Li ₆ SiON
60 °C/1 h/vacuum	0.96 ± 0.06	1.04 ± 0.04	1.11 ± 0.06
100 °C/2 h/N ₂	1.09 ± 0.03	1.35 ± 0.06	1.17 ± 0.07
200 °C/2 h/N ₂	1.23 ± 0.03	1.39 ± 0.05	1.31 ± 0.04
300 °C/2 h/N ₂	1.23 ± 0.03	1.46 ± 0.03	1.37 ± 0.05
400 °C/2 h/N ₂	1.21 ± 0.04	1.29 ± 0.03	1.41 ± 0.04

Figures A.25-A.27 show EDX map images of Li_xSiON pellets heated to 100-400 °C/2 h/ N₂. The EDX map of pellets heated to 100 °C shows well-distributed signature elements (N, O, and Si) as well as C from the starting material (SP) in good agreement with XPS per Figure 5.9 and Table 5.3. Quantitative EDX results are summarized in Table A.8. In general, the N content decreases with increasing temperature. This is likely due to loss of -NH₂ (Table 5.3). In addition, the C content also decreases as pellets are heated to 400 °C, also ascribed to decomposition of volatile and absorbed organic compounds (Figure 5.6).

5.3.2 Ionic conductivity measurements

Figure 5.13 shows Nyquist plots of Li₂SiON, Li₄SiON, and Li₆SiON pellets heated to 100-400 °C/2 h/N₂. All the measurements were conducted at RT.

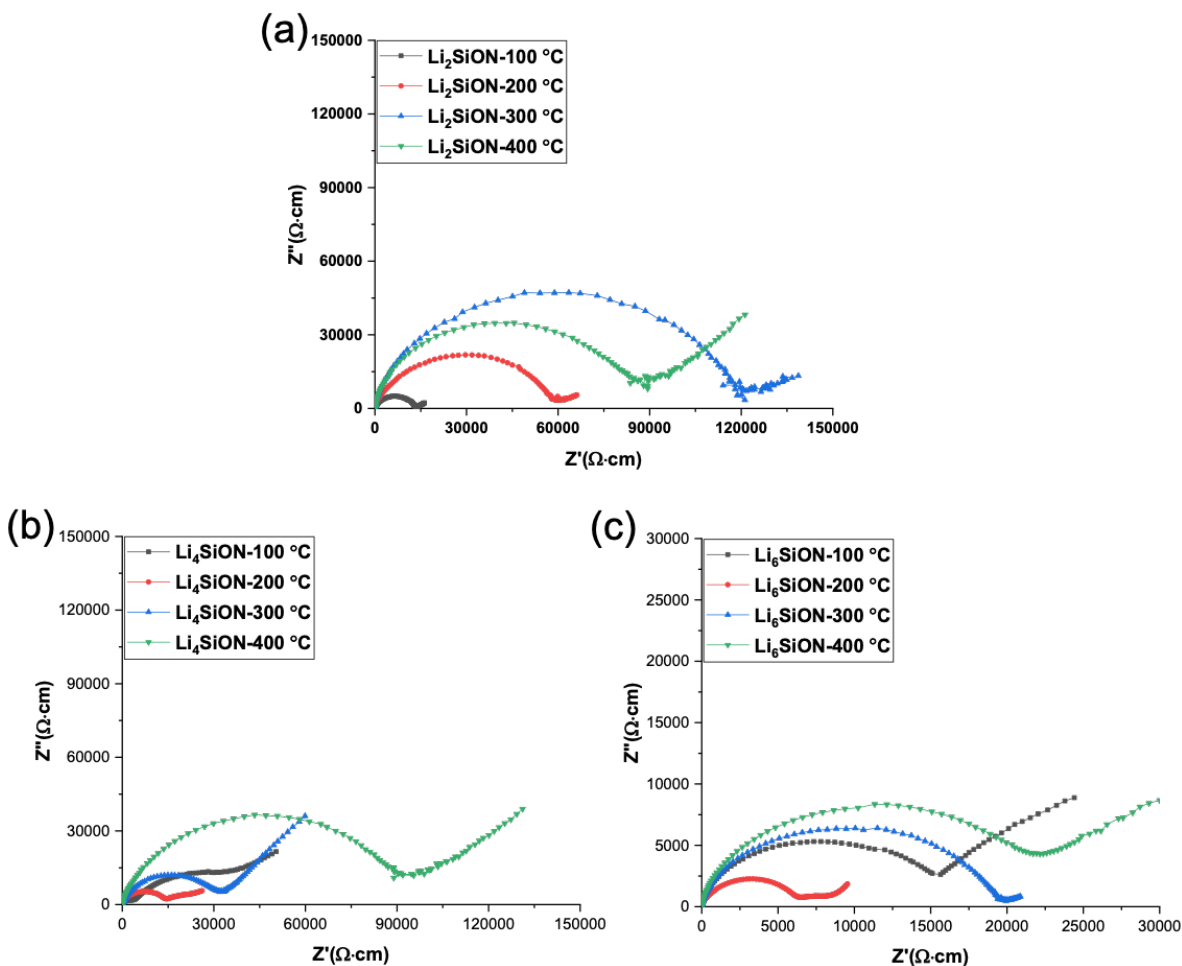


Figure 5.13. Nyquist plots of Li_xSiON pellets heated to 100-400 °C/2 h/ N_2 .

Table 5.6 summarizes total conductivities of the polymer precursor pellets heated to 100-400 °C/2 h/ N_2 . The Li_2SiON pellet showed the highest conductivity when heated to 100 °C as shown in Figure 5.13a. Conductivities decrease with increasing temperature to 300 °C, likely as a result of N loss per EDX in Figure A.25. The slight increase in ionic conductivity at 400 °C for the Li_2SiON pellet might be a consequence of lower C contents. There seems to be a tradeoff between the loss of N and decreases in C content when the pellets are heated to higher temperatures (i.e. >300 °C) per Table A.8. The decrease in C content is desirable as it decreases the electronic conductivity of the electrolyte.

Li₄SiON and Li₆SiON pellets show the highest conductivities of 9×10^{-7} and 8.5×10^{-6} S/cm at 200 °C, respectively. The increase in conductivity is associated with the denser microstructures of both precursors at 200 °C, Figure 5.12. Conductivities then decrease on heating to 300-400 °C, a likely result of the decrease in N contents.

Table 5.6. Total conductivities (σ_{RT}) of Li_xSiON pellets heated to 100-400 °C/2 h/N₂.

Precursor pellet	Temp. (°C)	σ_{RT} (S/cm)
Li ₂ SiON	100/2h	7.4×10^{-7}
	200/2h	2.5×10^{-7}
	300/2h	1.4×10^{-8}
	400/2h	2.0×10^{-8}
Li ₄ SiON	100/2h	2.3×10^{-7}
	200/2h	9.0×10^{-7}
	300/2h	4.6×10^{-7}
	400/2h	1.1×10^{-7}
Li ₆ SiON	100/2h	5.8×10^{-6}
	200/2h	8.5×10^{-6}
	300/2h	4.3×10^{-6}
	400/2h	2.7×10^{-6}

Table 5.7 compares the ionic conductivities of Li₄SiO₄ and LiSiON systems with different synthesis/processing methods in literature. Reported Li₄SiO₄ conductivities are typically measured at elevated temperatures (>100 °C). In general, Li₄SiO₄ sintered from sol-gel processed NPs show higher conductivities compared to Li₄SiO₄ prepared via solid-state reaction. Adnan *et al.*⁵³ reported a high ambient bulk conductivity of $\sim 3 \times 10^{-6}$ S/cm for Li₄SiO₄ by sol-gel processing and sintering at 750 °C/4 h, which is still lower than the highest ambient conductivity of 8.5×10^{-6} S/cm for Li₆SiON heated to 200 °C/2 h. For N-doped systems, the only LiSiON glass ionic conductivity measurement found in the literature records a low value of 2.5×10^{-8} at 40 °C.⁵⁰

Furthermore, compared to other synthesis and processing methods listed in Table 5.7, the polymer precursor synthesis is easily scalable; dense microstructures (Figure 5.12) and optimum conductivities (Table 5.6) are obtained for Li_xSiON (x = 4, 6) pellets when heated only to 200 °C/2 h/N₂, which significantly reduces processing steps, temperatures, and cost.

Table 5.7. Comparison of ionic conductivities (σ) of Li_4SiO_4 and LiSiON systems with different synthesis/processing methods in the literature.

Composition/phase	Synthesis/processing method	σ (S/cm) at T °C	Thickness (mm)*	Ref.
Li_4SiO_4 (monoclinic)	Sol-gel and sintering (1000 °C/4 h)	$\sim 10^{-5}$ (250)	~ 2	51
Li_4SiO_4 (monoclinic)	Sol-gel and sintering (750 °C/4 h)	$\sim 3 \times 10^{-6}$ (RT); $\sim 10^{-4}$ (100)	-	53
Li_4SiO_4 (monoclinic)	Solid state reaction (1000-1050 °C/18-24 h)	$\sim 10^{-7}$ (150)	-	55,57
Li_4SiO_4 (monoclinic)	Solid state reaction (1200 °C/10 h)	2.5×10^{-6} (300)	-	59
$30\text{Si}_2\text{O} \cdot 61\text{SiO}_2 \cdot 3\text{Si}_3\text{N}_4$ (LiSiON glass)	Melt mixing (1400-1450 °C/ N_2)	2.5×10^{-8} (40)	~ 1	50
Li_6SiON (amorphous)	Polymer precursor synthesis and heating to 200 °C/2 h/ N_2	8.5×10^{-6} (RT)	0.2-0.3	This work

*All conductivities are measured on pellets; thicknesses are not provided in some work.

5.3.3 Electrochemical characterization of Celgard/ Li_xSiON electrolytes

Figure 5.14 presents Nyquist plots and correlation between ionic conductivity and the Li/Si ratio of SS/Celgard + Li_xSiON /SS symmetric cells. The total ionic conductivities are calculated similarly to conventional, liquid electrolytes-soaked separators. Detail procedures can be found elsewhere.⁶⁷ The Celgard/ Li_6SiON electrolyte exhibits the highest Li^+ conductivity of $\sim 6.5 \times 10^{-6}$ S/cm, which shows an order of magnitude improvement compared to Celgard/ Li_2SiON (6.2×10^{-7} S/cm), suggesting the conductivity increases with Li content, consistent with Li_xSiON pellets above (Table 5.6). As shown in Figure 5.14b, the ionic conductivity seems to increase linearly with the Li/Si ratio.

The amorphous nature (Figure 5.7) of the polymer electrolyte likely provides isotropic Li^+ conduction, eliminating grain boundary resistivities. Nakagawa *et al.*⁸² reported that Li_4SiO_4 amorphous film deposited by pulsed laser deposition (PLD) shows an ionic conductivity of $\sim 4 \times 10^{-7}$ S/cm at ambient. The N-doped Li_4SiO_4 polymer electrolyte on Celgard presented here exhibits conductivity an order of magnitude higher compared to the amorphous thin film fabricated by gas-phase deposition techniques. In addition, AC impedance measurements at -15° to 85°C suggests

an E_a of 0.28 eV for the Li_6SiON electrolyte,⁷⁰ lower than the reported E_a of amorphous Li_4SiO_4 is 0.62 eV.⁸²

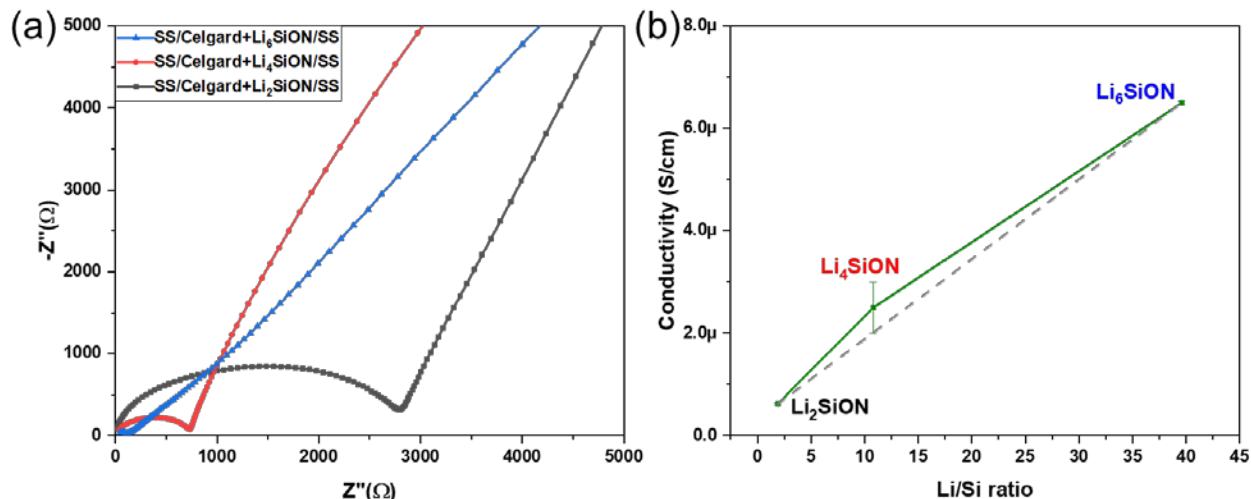


Figure 5.14a. Nyquist plots of SS/Celgard + $\text{Li}_x\text{SiON}/\text{SS}$ symmetric cells and **b.** Li/Si ratio vs. ionic conductivity at ambient.

As shown in Table 5.8, the calculated t_{Li^+} for the Li_xSiON electrolytes using both chronoamperometric studies and DC polarization are in good agreement. The Li-SiON chemical interaction seems to facilitate higher Li^+ mobility as indicated by high $t_{\text{Li}^+} > 0.7$ for the Li_xSiON polymer electrolytes. In traditional liquid electrolytes and PEs, both the cations and anions are mobile species resulting in a decreased t_{Li^+} of < 0.5 , which can lead to electro-polarization from anion buildup, and can further result in a decrease in the overall electrochemical performance due to high internal resistances, voltage losses, and dendrite growth. As Li_xSiON precursors possess bulky anion groups with polymeric features leading to hindered anion mobility, Celgard/ Li_xSiON electrolytes show high t_{Li^+} (~ 0.75 -1) that can overcome such challenges faced by liquid electrolytes and PEs.

Table 5.8. Comparison of t_{Li^+} calculated using eq (5.3) and eq (5.4).

Sample	t_{Li^+} from eq (5.3)	t_{Li^+} from eq (5.4)
Li_2SiON	0.9 ± 0.03	1 ± 0.02
Li_4SiON	0.8 ± 0.06	0.79 ± 0.04
Li_6SiON	0.73 ± 0.08	0.76 ± 0.06

Figure **5.15a** presents CV plots for the Li/Celgard + Li₆SiON/SS half-cells between potential ranges of -1 to 6 V at 1 mV/sec. The Li plating and stripping phenomena are demonstrated by the anodic and cathodic peaks ~ 0 V, indicating that the Li⁺ ions diffuse through the Celgard/Li₆SiON PE and plate onto the working electrode. Good electrochemical stability is demonstrated by the small current response at high voltage (~ 4.5) vs Li/Li⁺. The current response difference between the polymer electrolyte may be due to variance in electronegativity of the Li_xSiON framework (Figure **A.28**). The increase in Li/Si ratio of the polymer precursor is postulated to decrease the covalency of Li-N framework, resulting in a decrease of the antibonding energy state.⁶⁷

Li⁺ plating/stripping behavior by charging/discharging the Li/Celgard + Li_xSiON/Li symmetric cells at ambient was investigated by galvanostatic cycling with constant current densities of 0.75-3.75 mA/cm², as shown in Figures **5.15b** and **A.29**. The Li/Celgard + Li₆SiON/Li symmetric cell (Figure **5.15b**) follows Ohmic behavior at both low and high critical current densities, delivering an average interfacial resistance of 8 $\Omega \cdot \text{cm}^2$. The voltage response is stable at high current density of 3.75 mA/cm², meeting the requirement of electrolytes to enable the assembly of ASSBs,^{83,84} and is significantly higher than typical inorganic SEs with higher ionic conductivities (0.1 mS/cm) at ambient. Irrespective of the use of numerous engineering processes, *i.e.*, polishing, grinding, surface modification, and melting of metallic Li to bind with electrolyte surfaces, can lead to voids/pores, grain boundaries, and surface impurities in most oxide-based inorganic solid electrolytes.⁸⁵ These surface impurities provide pathways for Li dendrites growth and penetration, resulting in low critical current densities (< 0.5 mA/cm).⁸⁵

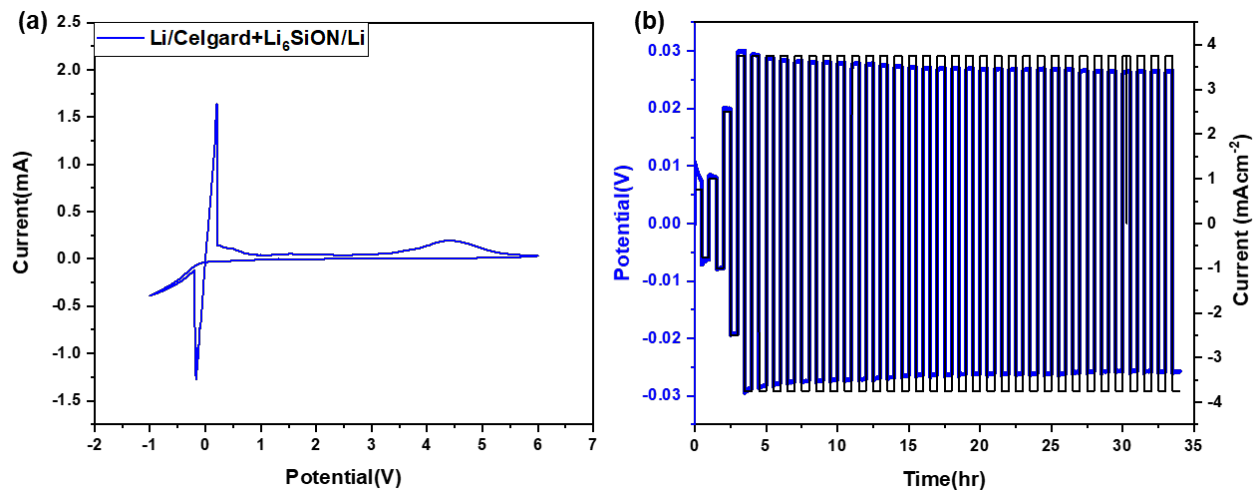


Figure 5.15a. CV plot of Li/Celgard + Li₆SiON/SS at sweep rate of 1 mV/sec and **b.** galvanostatic cycling of Li/Celgard + Li₆SiON/Li symmetric cell at ambient.

Li-S batteries have drawn intense attention as candidates for next generation energy storage technologies owing to their high theoretical capacity (1672 mAh/g) and specific energy (2600 Wh/kg).⁸⁶ In addition, sulfur possesses low-cost, abundant, and environmental features, making it a promising cathode material.⁸⁷ Due to its structural framework, SPAN cathodes are known to suppress polysulfide shuttle effects and facilitate fast charging capabilities.^{86,88} Therefore, the stability of the Celgard/Li₆SiON electrolyte with SPAN cathode and metallic Li anode was investigated. As shown in Figure 5.16, the SPAN/Celgard + Li₆SiON/Li half-cell delivers an initial discharge capacity ~1300 mAh/g_{sulfur} at ambient, and a reversible capacity of ~850 mAh/g_{sulfur} at 0.25 C, which gradually decreases to 765 mAh/g_{sulfur} after 30 cycles. Fast cycling at 0.5 C results in reversible capacity of 725 mAh/g_{sulfur} for the rest of 20 cycles, which is about double the capacity attained for conventional Li-ion batteries with graphite anode and high voltage oxide cathode (372 mAh/g).⁸⁹ The half-cell maintained high coulombic efficiency of ~100 % attributed to the high t_{Li^+} and optimal ionic conductivity of the Celgard/Li₆SiON polymer electrolyte.

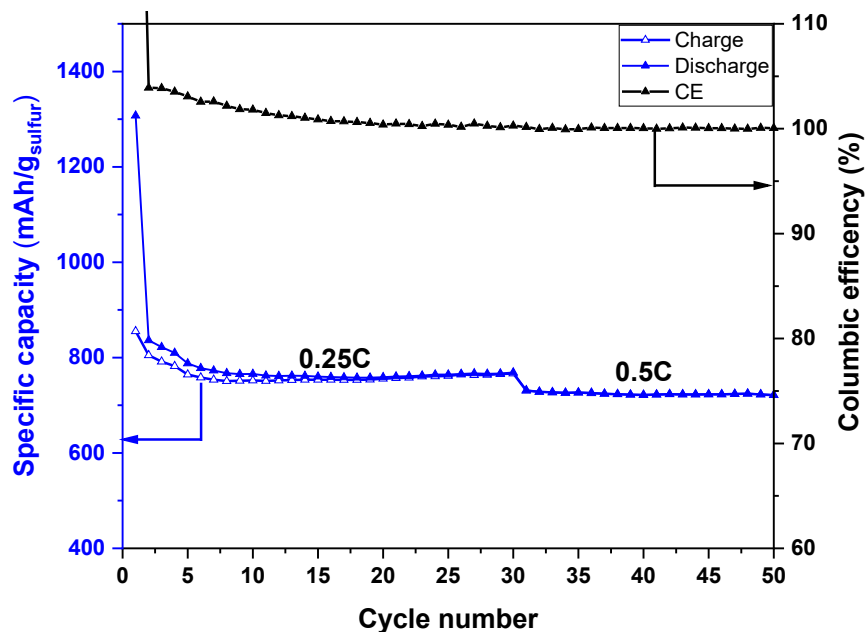


Figure 5.16. Cycle number vs. specific capacity and coulombic efficiency of SPAN/Celgard + Li₆SiON/Li half-cell cycled between 1-3 V at ambient.

5.3.4 Li₄Ti₅O₁₂ composite anodes with addition of LiAlO₂ and Li₆SiON

Li₄Ti₅O₁₂ (LTO) is a promising alternate anode material for high power density batteries for large scale applications due to its excellent thermal stability, high structural stability, good cyclability at high current densities, and negligible irreversible capacity.^{90,91} In addition, spinel LTO anodes can facilitate up to three Li⁺ ions per formula unit and deliver theoretical capacities ~175 mAh/g without significant volume changes (<1%) when cycled.^{92,93} In contrast, graphite anodes expand up to 10 vol.% during charging.⁹⁰ However, LTO suffers from poor Li⁺ diffusivity (10⁻⁹-10⁻¹⁴ cm²/s) and poor electronic conductivity (10⁻¹³ S/cm), resulting in capacity loss and poor rate performance.^{94,95}

To improve electrochemical properties of LTO, a facile synthesis of LTO NPs was used via LF-FSP, providing high surface area (~38 m²/g) with average particle sizes (APSs) of 45 nm. Pristine LTO-Li half-cells exhibit reversible capacity of 70 mAh/g at 10 C.⁷¹ Furthermore, as

shown in Figures 5.17 and A.30, by mixing LiAlO_2 NPs (5 and 10 wt.%) and Li_6SiON polymer precursor (5 and 10 wt.%) with pristine LTO via ball-milling and ultrasonication, homogeneous composite powders with APSs <60 nm were obtained. Followed by tape casting, enhanced LTO electrochemical performance was achieved for these LTO-composite anodes. Detailed fabrication procedure, characterization methods, results and discussion are reported elsewhere.⁷¹

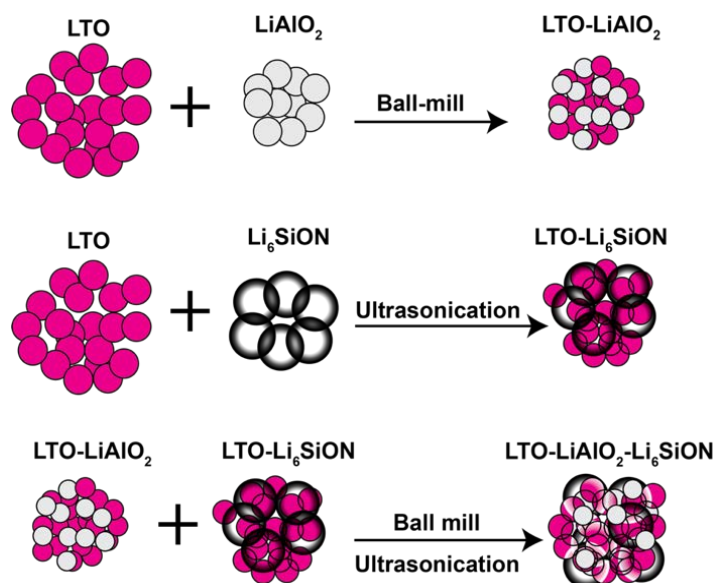


Figure 5.17. Preparation of LTO-composite anodes.

Figure 5.18 demonstrates the rate capability of LTO-pristine and LTO composite-Li half cells cycled between 0.01 and 2.5 V at various current densities. The LTO-pristine-Li half-cell delivers average specific capacities of 202 and 120 mAh/g at 0.5 and 5 C, respectively. The reversible capacities at 0.5 C for LTO-5 LiAlO_2 -10 Li_6SiON (260 mAh/g) and LTO-10 Li_6SiON (231 mAh/g) are much higher than those of LTO-pristine electrodes (202 mAh/g). At 10 C, the LTO-10 Li_6SiON shows the highest discharge capacity of 190 mAh/g. The LTO-5 LiAlO_2 also delivered a high specific capacity of 174 mAh/g at 10 C, which is more than double the capacity obtained for the pristine LTO (70 mAh/g).

However, LTO-10LiAlO₂-5Li₆SiON and LTO-10LiAlO₂-10Li₆SiON composite electrodes show poor discharge capacities compared to the pristine LTO electrode. LTO-10LiAlO₂ also shows slightly lower capacities compared to LTO-5LiAlO₂, which can be ascribed to larger APSs for LTO-10LiAlO₂ that agglomerates likely formed (Figure A.30). Hence, it is important that the optimal content of LiAlO₂ (5 wt.%) is introduced to achieve superior cell performance. Compared to pristine LTO, Li₄Ti₅O₁₂-LiAlO₂ (5 wt.%),⁹⁶ and Li₄Ti₅O₁₂-Li_{0.33}La_{0.56}TiO₃ (5 wt.%)⁹⁷ composites prepared by solid-state reactions, the rate capability of LF-FSP derived by LTO-5LiAlO₂-10Li₆SiON composite electrodes is much higher in the range of 0.01-2.5 V at higher C-rates (Table 5.9). This clearly indicates that moderate modification of LTO particle surfaces is substantially beneficial to rate performance.

Overall, the introduction of appropriate amounts of LiAlO₂ NPs shortens diffusion distances for Li⁺ and electrons, increases the contact interface with electrolyte, and provides abundant surface Li⁺ storage sites or excess near-surface Li⁺ storage.⁷¹ The introduction of Li₆SiON polymer precursor enhances the rate performance of the LTO-composite electrodes, especially for the LTO-5LiAlO₂-10Li₆SiON electrode, which also shows a long-term cycling stability over 500 cycles delivering reversible capacity of ~217 mAh/g at 5 C (Figure A.31). Such improvement can be attributed to (1) an optimal amounts of LiAlO₂ (5 wt.%) and Li₆SiON (10 wt.%) between or on the LTO particle surfaces enhancing the ionic conductivity shown by the increase in Li⁺ diffusivity (Table A.9); (2) Li₆SiON reorganizing LTO surface bonding, resulting in an increase in the electronic conductivity due to the local charge imbalance;⁷¹ (3) diminishing electrode polarization, via introduction of appropriate LiAlO₂ and Li₆SiON electrolyte contents (Figure A.32), and (4) uniform particle morphology (Figure A.30) and high surface area of LTO NPs.⁷¹

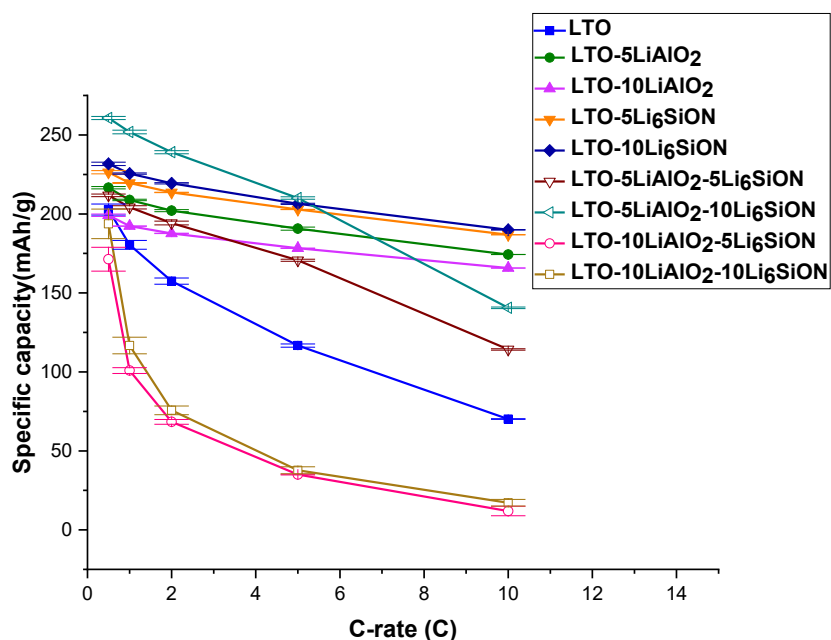


Figure 5.18. Comparison of discharge capacities of the various electrodes cycled between 0.01 and 2.5 V at selected C-rates.

Table 5.9. Comparison of discharge capacities of LTO-composite anode materials at 5 C.

Electrodes	Discharge capacities (mAh/g)	Ref
LTO-LiAlO ₂ (5 wt.%)	127	96
LTO-LiAlO ₂ (10 wt.%)	~50	96
LTO-Li _{0.33} La _{0.56} TiO ₃ (5 wt.%)	146	97
LTO-Li _{0.33} La _{0.56} TiO ₃ (10 wt.%)	137	97
Li ₄ Ti _{4.9} La _{0.1} O ₁₂	181	98
LTO-TiO ₂	117	99
LTO-TiO ₂ /C	140	100
LTO-5LiAlO ₂	190	This work
LTO-10Li ₆ SiON	206	This work
LTO-5LiAlO ₂ -10Li ₆ SiON	210	This work

5.4 Conclusions

In summary, we present here the green synthesis and detailed characterization of Li_xSiON oligomer/polymer precursors, including FTIR, MALDI-ToF, NMR, TGA-DTA, XRD, XPS, EDX, SEM and impedance studies. XPS shows that the Li content increases with LiNH₂ amounts, which also correlates with MWs and CYs. ⁷Li NMR suggests that Li⁺ ions are well solvated and dissoci-

ated, and excess Li^+ may exist in clusters, which is beneficial for their electrochemical performances. When $x = 6$, the Li content reaches a saturation level suggested by XPS; ^1H , ^{13}C and ^{29}Si NMRs indicate fluxional motion. Li_xSiON precursors start to decompose at $\sim 100^\circ\text{C}$ due to organic portions. When dried at $\leq 100^\circ\text{C}$, XRD patterns show amorphous phase; when heated to 800°C , Li_4SiO_4 forms, suggesting a polymer to ceramic conversion at higher temperatures. SEM and impedance studies show that dense microstructures and optimum conductivities are obtained after heating to $200^\circ\text{C}/2\text{ h}/\text{N}_2$ for Li_xSiON ($x = 4, 6$) pellets. In general, conductivities of precursor pellets increase with Li content: $\text{Li}_6\text{SiON} > \text{Li}_4\text{SiON} > \text{Li}_2\text{SiON}$.

When coated with Celgard separators, the PEs show an optimal conductivity for Celgard/ Li_6SiON ($\sim 6.5 \times 10^{-6}\text{ S/cm}$) at ambient and low E_a (0.28 eV), which can be ascribed to the high Li content and nitridation of the Li_6SiON precursor. Celgard/ Li_xSiON PEs also exhibit high t_{Li^+} of $\sim 0.7-1$ attributed to the polymer framework with low anion mobility. Furthermore, the Celgard/ Li_6SiON PE enables the assembly of Li symmetric cells with high critical current density of 3.75 mAh/cm , making it desirable for fast charging applications. Finally, the SPAN/Celgard + $\text{Li}_6\text{SiON}/\text{Li}$ half-cell delivers a reversible capacity of $\sim 725\text{ mAh/g}$ at 0.5 C over 50 cycles.

In a separate set of studies, we show that a facile LF-FSP method enables the synthesis of high surface area ($\sim 38\text{ m}^2/\text{g}$), phase pure LTO NPs. Pristine LTO was mixed with LiAlO_2 and Li_6SiON electrolytes to improve the ionic and electronic conductivities by simple ball-milling and ultrasonication methods. The microstructure studies show that the composite powders are homogeneous with APSs $< 60\text{ nm}$. The LTO-composite electrodes with optimal LiAlO_2 (5 wt.%) and Li_6SiON (10 wt.%) electrolyte additives exhibit excellent rate performance delivering reversible capacity of 260 and 140 mAh/g at 0.5 and 10 C, respectively.

References

1. Yuan, C.; Wu, H. B.; Xie, Y.; Lou, X. W. (David). Mixed Transition-Metal Oxides: Design, Synthesis, and Energy-Related Applications. *Angew. Chem. Int. Ed.* **2014**, *53* (6), 1488–1504.
2. Peterson, S. B.; Michalek, J. J. Cost-Effectiveness of Plug-in Hybrid Electric Vehicle Battery Capacity and Charging Infrastructure Investment for Reducing US Gasoline Consumption. *Energy Policy* **2013**, *52*, 429–438.
3. Gaines, L. L.; Dunn, J. B. Lithium-Ion Battery Environmental Impacts. In *Lithium-Ion Batteries*; Pistoia, G., Ed.; Elsevier: Amsterdam, 2014; pp 483–508.
4. Jiang, T.; He, P.; Wang, G.; Shen, Y.; Nan, C. W.; Fan, L. Z. Solvent-Free Synthesis of Thin, Flexible, Nonflammable Garnet-Based Composite Solid Electrolyte for All-Solid-State Lithium Batteries. *Adv. Energy Mater.* **2020**, *10* (12), 1903376.
5. Manthiram, A.; Yu, X.; Wang, S. Lithium Battery Chemistries Enabled by Solid-State Electrolytes. *Nat. Rev. Mater.* **2017**, *2* (4), 1–16.
6. Fergus, J. W. Ceramic and Polymeric Solid Electrolytes for Lithium-Ion Batteries. *J. Power Sources* **2010**, *195* (15), 4554–4569.
7. Xu, K. Nonaqueous Liquid Electrolytes for Lithium-Based Rechargeable Batteries. *Chem. Rev.* **2004**, *104* (10), 4303–4418.
8. Cheng, X. B.; Zhang, R.; Zhao, C. Z.; Wei, F.; Zhang, J. G.; Zhang, Q. A Review of Solid Electrolyte Interphases on Lithium Metal Anode. *Adv. Sci.* **2016**, *3* (3), 1500213.
9. Nimisha, C. S.; Rao, K. Y.; Venkatesh, G.; Rao, G. M.; Munichandraiah, N. Sputter Deposited LiPON Thin Films from Powder Target as Electrolyte for Thin Film Battery Applications. *Thin Solid Films* **2011**, *519*, 3401–3406.
10. Yu, X.; Bates, J. B.; Jellison, G. E.; Hart, F. X. A Stable Thin-Film Lithium Electrolyte: Lithium Phosphorus Oxynitride. *J. Electrochem. Soc.* **1997**, *144*, 524–532.
11. Bates, J. B.; Dudney, N. J.; Gruzalski, G. R.; Zuhr, R. A.; Choudhury, A.; Luck, C. F.; Robertson, J. D. Fabrication and Characterization of Amorphous Lithium Electrolyte Thin Films and Rechargeable Thin-Film Batteries. *J. Power Sources* **1993**, *43–44*, 103–110.
12. Reyes Jiménez, A.; Nölle, R.; Wagner, R.; Hüsker, J.; Kolek, M.; Schmich, R.; Winter, M.; Placke, T. A Step towards Understanding the Beneficial Influence of a LiPON-Based Artificial SEI on Silicon Thin Film Anodes in Lithium-Ion Batteries. *Nanoscale* **2018**, *10*, 2128–2137.
13. Hu, Z.; Li, D.; Xie, K. Influence of Radio Frequency Power on Structure and Ionic Conductivity of LiPON Thin Films. *Bull. Mater. Sci.* **2008**, *31* (4), 681–686.
14. Lee, S. J.; Bae, J. H.; Lee, H. W.; Baik, H. K.; Lee, S. M. Electrical Conductivity in Li-Si-P-O-N Oxynitride Thin-Films. *J. Power Sources* **2003**, *123*, 61–64.
15. Muñoz, F.; Durán, A.; Pascual, L.; Montagne, L.; Revel, B.; Rodrigues, A. C. M. Increased Electrical Conductivity of LiPON Glasses Produced by Ammonolysis. *Solid State Ion.* **2008**, *179* (15–16), 574–579.
16. Stallworth, P. E.; Vereda, F.; Greenbaum, S. G.; Haas, T. E.; Zerigian, P.; Goldner, R. B. Solid-State NMR Studies of Lithium Phosphorus Oxynitride Films Prepared by Nitrogen Ion Beam-Assisted Deposition. *J. Electrochem. Soc.* **2005**, *152* (3), A516–A522.
17. Fleutot, B.; Pecquenard, B.; Martinez, H.; Letellier, M.; Lévassieur, A. Investigation of the Local Structure of LiPON Thin Films to Better Understand the Role of Nitrogen on Their Performance. *Solid State Ion.* **2011**, *186* (1), 29–36.

18. Mascaraque, N.; Fierro, J. L. G.; Durán, A.; Muñoz, F. An Interpretation for the Increase of Ionic Conductivity by Nitrogen Incorporation in LiPON Oxynitride Glasses. *Solid State Ion.* **2013**, *233*, 73–79.
19. Bates, J. B.; Dudney, N. J.; Gruzalski, G. R.; Zuhr, R. A.; Choudhury, A.; Luck, C. F.; Robertson, J. D. Electrical Properties of Amorphous Lithium Electrolyte Thin Films. *Solid State Ion.* **1992**, *53*, 647–654.
20. Wang, B.; Kwak, B. S.; Sales, B. C.; Bates, J. B. Ionic Conductivities and Structure of Lithium Phosphorus Oxynitride Glasses. *J. Non-Cryst. Solids* **1995**, *183*, 297–306.
21. Put, B.; Vereecken, P. M.; Meersschaut, J.; Sepúlveda, A.; Stesmans, A. Electrical Characterization of Ultrathin RF-Sputtered LiPON Layers for Nanoscale Batteries. *ACS Appl. Mater. Interfaces* **2016**, *8*, 7060–7069.
22. Hamon, Y.; Douard, A.; Sabary, F.; Marcel, C.; Vinatier, P.; Pecquenard, B.; Levasseur, A. Influence of Sputtering Conditions on Ionic Conductivity of LiPON Thin Films. *Solid State Ion.* **2006**, *177*, 257–261.
23. Zhao, S.; Fu, Z.; Qin, Q. A Solid-State Electrolyte Lithium Phosphorus Oxynitride Film Prepared by Pulsed Laser Deposition. *Thin Solid Films* **2002**, *415*, 108–113.
24. Liu, W. Y.; Fu, Z. W.; Li, C. L.; Qin, Q. Z. Lithium Phosphorus Oxynitride Thin Film Fabricated by a Nitrogen Plasma-Assisted Deposition of E-Beam Reaction Evaporation. *Electrochem. Solid-State Lett.* **2004**, *7*, J36–J40.
25. Vereda, F.; Goldner, R. B.; Haas, T. E.; Zerigian, P. Rapidly Grown IBAD LiPON Films with High Li-Ion Conductivity and Electrochemical Stability. *Electrochem. Solid-State Lett.* **2002**, *5*, 239–241.
26. Kim, Y. G.; Wadley, H. N. G. Lithium Phosphorous Oxynitride Films Synthesized by a Plasma-Assisted Directed Vapor Deposition Approach. *J. Vac. Sci. Technol. Vac. Surf. Films* **2008**, *26*, 174–183.
27. Nowak, S.; Berkemeier, F.; Schmitz, G. Ultra-Thin LiPON Films - Fundamental Properties and Application in Solid State Thin Film Model Batteries. *J. Power Sources* **2015**, *275*, 144–150.
28. Kim, H. T.; Mun, T.; Park, C.; Jin, S. W.; Park, H. Y. Characteristics of Lithium Phosphorous Oxynitride Thin Films Deposited by Metal-Organic Chemical Vapor Deposition Technique. *J. Power Sources* **2013**, *244*, 641–645.
29. Xu, F.; Dudney, N. J.; Veith, G. M.; Kim, Y.; Erdonmez, C.; Lai, W.; Chiang, Y. M. Properties of Lithium Phosphorus Oxynitride (LiPON) for 3D Solid-State Lithium Batteries. *J. Mater. Res.* **2010**, *25* (8), 1507–1515.
30. Kozen, A. C.; Pearse, A. J.; Lin, C. F.; Noked, M.; Rubloff, G. W. Atomic Layer Deposition of the Solid Electrolyte LiPON. *Chem. Mater.* **2015**, *27* (15), 5324–5331.
31. Wang, B.; Chakoumakos, B. C.; Sales, B. C.; Kwak, B. S.; Bates, J. B. Synthesis, Crystal Structure, and Ionic Conductivity of a Polycrystalline Lithium Phosphorus Oxynitride with the γ -Li₃PO₄ Structure. *J. Solid State Chem.* **1995**, *115* (2), 313–323.
32. Roh, N. S.; Lee, S. D.; Kwon, H. S. Effects of Deposition Condition on the Ionic Conductivity and Structure of Amorphous Lithium Phosphorus Oxynitrate Thin Film. *Scr. Mater.* **1999**, *42* (1), 43–49.
33. Meda, L.; Maxie, E. E. Lipon Thin Films Grown by Plasma-Enhanced Metalorganic Chemical Vapor Deposition in a N₂-H₂-Ar Gas Mixture. *Thin Solid Films* **2012**, *520* (6), 1799–1803.
34. Le Van-Jodin, L.; Ducroquet, F.; Sabary, F.; Chevalier, I. Dielectric Properties, Conductivity and Li⁺ Ion Motion in LiPON Thin Films. *Solid State Ion.* **2013**, *253* (15), 151–156.

35. Su, Y.; Falgenhauer, J.; Polity, A.; Leichtweiß, T.; Kronenberger, A.; Obel, J.; Zhou, S.; Schlettwein, D.; Janek, J.; Meyer, B. K. LiPON Thin Films with High Nitrogen Content for Application in Lithium Batteries and Electrochromic Devices Prepared by RF Magnetron Sputtering. *Solid State Ion.* **2015**, *282* (1), 63–69.
36. Birke, P.; Chu, W. F.; Weppner, W. Materials for Lithium Thin-Film Batteries for Application in Silicon Technology. *Solid State Ion.* **1996**, *93* (1–2), 1–15.
37. Birke, P.; Weppner, W. Electrochemical Analysis of Thin Film Electrolytes and Electrodes for Application in Rechargeable All Solid State Lithium Microbatteries. *Electrochimica Acta* **1997**, *42* (97), 3375–3384.
38. Hamon, Y.; Vinatier, P.; Kamitsos, E. I.; Dussauze, M.; Varsamis, C. P. E.; Zielniok, D.; Roesser, C.; Roling, B. Nitrogen Flow Rate as a New Key Parameter for the Nitridation of Electrolyte Thin Films. *Solid State Ion.* **2008**, *179* (21–26), 1223–1226.
39. Dussauze, M.; Kamitsos, E. I.; Johansson, P.; Matic, A.; Varsamis, C. P. E.; Cavagnat, D.; Vinatier, P.; Hamon, Y. Lithium Ion Conducting Boron-Oxynitride Amorphous Thin Films: Synthesis and Molecular Structure by Infrared Spectroscopy and Density Functional Theory Modeling. *J. Phys. Chem. C* **2013**, *117* (14), 7202–7213.
40. Joo, K. H.; Sohn, H. J.; Vinatier, P.; Pecquenard, B.; Levasseur, A. Lithium Ion Conducting Lithium Sulfur Oxynitride Thin Film. *Electrochem. Solid-State Lett.* **2004**, *7* (8), 256–259.
41. Yang, W.; Yang, W.; Sun, B.; Di, S.; Yan, K.; Wang, G.; Shao, G. Mixed Lithium Oxynitride/Oxysulfide as an Interphase Protective Layer to Stabilize Lithium Anodes for High-Performance Lithium-Sulfur Batteries. *ACS Appl. Mater. Interfaces* **2018**, *10* (46), 39695–39704.
42. Dong, B.; Jarkaneh, R.; Hull, S.; Reeves-McLaren, N.; Biendicho, J. J.; West, A. R. Synthesis, Structure and Electrical Properties of N-Doped Li₃VO₄. *J. Mater. Chem. A* **2015**, *4* (4), 1408–1413.
43. Jarkaneh, R. Novel Oxynitride Lithium Ion Conductors, 2015.
44. Unuma, H. Molecular Dynamics Study of Na-Si-O-N Oxynitride Glasses. *J. Am. Ceram. Soc.* **1993**, *76* (5), 1308–1312.
45. Unuma, H.; Kokubo, T.; Sakka, S. Crystallization of Li-Si-O-N Oxynitride Glasses. *J. Mater. Sci.* **1988**, *23* (12), 4399–4405.
46. Wójcik, N. A.; Jonson, B.; Möncke, D.; Kamitsos, E. I.; Segawa, H.; Karczewski, J.; Ali, S. The Effect of Nitrogen on the Structure and Thermal Properties of Beryllium-Containing Na-(Li)-Si-O-N Glasses. *J. Non-Cryst. Solids* **2019**, *522*, 119585.
47. Sakka, S. Structure, Properties and Application of Oxynitride Glasses. *J. Non-Cryst. Solids* **1995**, *181* (3), 215–224.
48. Unuma, H.; Suzuki, Y.; Furusaki, T.; Ishizuka, Y.; Kodaira, K. Phase Separation in Li-Si-O-N Oxynitride Glasses. *J. Ceram. Soc. Jpn.* **1989**, *97* (3), 376–379.
49. Unuma, H.; Sakka, S. Electrical Conductivity in Na-Si-O-N Oxynitride Glasses. *J. Mater. Sci. Lett.* **1987**, *6* (9), 996–998.
50. Unuma, H.; Komori, K.; Sakka, S. Electrical Conductivity and Chemical Durability in Alkali-Silicate Oxynitride Glasses. *J. Non-Cryst. Solids* **1987**, *95*, 913–920.
51. Wu, X.; Wen, Z.; Xu, X.; Wang, X.; Lin, J. Synthesis and Characterization of Li₄SiO₄ Nano-Powders by a Water-Based Sol-Gel Process. *J. Nucl. Mater.* **2009**, *392* (3), 471–475.
52. Wu, X.; Wen, Z.; Xu, X.; Liu, Y. Fabrication of Li₄SiO₄ Pebbles by a Sol-Gel Technique. *Fusion Eng. Des.* **2010**, *85* (2), 222–226.

53. Adnan, S. B. R. S.; Mohamed, N. S.; Norwati, K. A. Li₄SiO₄ Prepared by Sol-Gel Method as Potential Host for LISICON Structured Solid Electrolytes. *Int. J. Eng. Math. Phys. Sci.* **2011**, *5* (2), 183–186.
54. West, A. R. Ionic Conductivity of Oxides Based on Li₄SiO₄. *J. Appl. Electrochem.* **1973**, *3* (4), 327–335.
55. Khorassani, A.; West, A. R. Li⁺ Ion Conductivity in the System Li₄SiO₄-Li₃VO₄. *J. Solid State Chem.* **1984**, *53* (3), 369–375.
56. Tao, Y.; Yi, D.; Li, J. Electrochemical Formation of Crystalline Li₃VO₄/Li₄SiO₄ Solid Solutions Film. *Solid State Ion.* **2008**, *179* (40), 2396–2398.
57. Khorassani, A.; West, A. R. New Li⁺ Ion Conductors in the System Li₄SiO₄-Li₃AsO₄. *Solid State Ion.* **1982**, *7*, 1–8.
58. Sakurai, Y.; Sakuda, A.; Hayashi, A.; Tatsumisago, M. Preparation of Amorphous Li₄SiO₄-Li₃PO₄ Thin Films by Pulsed Laser Deposition for All-Solid-State Lithium Secondary Batteries. *Solid State Ion.* **2011**, *182* (1), 59–63.
59. Deng, Y.; Eames, C.; Chotard, J. N.; Laleire, F.; Seznec, V.; Emge, S.; Pecher, O.; Grey, C. P.; Masquelier, C.; Islam, M. S. Structural and Mechanistic Insights into Fast Lithium-Ion Conduction in Li₄SiO₄-Li₃PO₄ Solid Electrolytes. *J. Am. Chem. Soc.* **2015**, *137* (28), 9136–9145.
60. Hirai, K.; Tatsumisago, M.; Minami, T. Thermal and Electrical Properties of Rapidly Quenched Glasses in the Systems Li₂S-SiS₂-Li_xMO_y (Li_xMO_y = Li₄SiO₄, Li₂SO₄). *Solid State Ion.* **1995**, *78* (95), 269–273.
61. Kawakami, Y.; Ikuta, H.; Uchida, T.; Wakihara, M. Ionic Conduction of Lithium in Li₂S-SiS₂-Li₄SiO₄ Glass System. *Thermochim. Acta* **1997**, *299* (1–2), 7–12.
62. Morimoto, H.; Yamashita, H.; Tatsumisago, M.; Minami, T. Mechanochemical Synthesis of the High Lithium Ion Conductive Amorphous Materials in the Systems Li₂S-SiS₂ and Li₂S-SiS₂-Li₄SiO₄. *J. Ceram. Soc. Jpn.* **2000**, *108* (2), 128–131.
63. Tatsumisago, M.; Morimoto, H.; Yamashita, H.; Minami, T. Preparation of Amorphous Solid Electrolytes in the System Li₂S-SiS₂-Li₄SiO₄ by Mechanical Milling. *Solid State Ion.* **2000**, *136–137*, 483–488.
64. Ikeda, Y.; Kitade, T.; Kohjiya, S.; Hayashi, A.; Matsuda, A.; Tatsumisago, M.; Minami, T. Ion Conducting Composites from Li₂S-SiS₂-Li₄SiO₄ Oxysulfide Glass and Poly(Oxyethylene)s. *Polymer* **2001**, *42*, 7225–7228.
65. Zhang, X.; Temeche, E.; Laine, R. M. Design, Synthesis, and Characterization of Polymer Precursors to Li_xPON and Li_xSiPON Glasses: Materials That Enable All-Solid-State Batteries (ASBs). *Macromolecules* **2020**, *53*, 2702–2712.
66. Temeche, E.; Zhang, X.; Laine, R. M. Solid Electrolytes for Li-S Batteries: Solid Solutions of Poly(Ethylene Oxide) with Li_xPON- and Li_xSiPON-Based Polymers. *ACS Appl. Mater. Interfaces* **2020**, *12* (27), 30353–30364.
67. Temeche, E.; Zhang, X.; Laine, R. M. Polymer Precursor Derived Li_xPON Electrolytes: Toward Li-S Batteries. *ACS Appl. Mater. Interfaces* **2020**, *12* (18), 20548–20562.
68. Temeche, E.; Yu, M.; Laine, R. M. Silica Depleted Rice Hull Ash (SDRHA), an Agricultural Waste, as a High-Performance Hybrid Lithium-Ion Capacitor. *Green Chem.* **2020**, *22* (14), 4656–4668.
69. Evans, J.; Vincent, C. A.; Bruce, P. G. Electrochemical Measurement of Transference Numbers in Polymer Electrolytes. *Polymer* **1987**, *28* (13), 2324–2328.

70. Temeche, E.; Zhang, X.; Laine, R. M. Electrochemical Performance of Li_xSiON Polymer Electrolytes Derived from an Agriculture Waste Product, Rice Hull Ash. *ACS Appl. Polym. Mater.* **2021**, *3* (4), 2144–2152.
71. Temeche, E.; Buch, E.; Zhang, X.; Brandt, T.; Hintennach, A.; Laine, R. M. Improved Electrochemical Properties of $\text{Li}_4\text{Ti}_5\text{O}_{12}$ Nanopowders (NPs) via Addition of LiAlO_2 and Li_6SiON Polymer Electrolytes, Derived from Agricultural Waste. *ACS Appl. Energy Mater.* **2021**.
72. Cotton, F. A. Fluxional Organometallic Molecules. *Acc. Chem. Res.* **1968**, *1* (9), 257–265.
73. Arvidsson, P. I.; Ahlberg, P.; Hilmersson, G. Intraaggregate Fluxional Lithium and Carbanion Exchanges in a Chiral Lithium Amide/*n*-Butyllithium Mixed Tetramer Directly Observed by Multinuclear NMR. *Chem. - Eur. J.* **1999**, *5* (4), 1348–1354.
74. Lee, K. K.; Park, K.; Lee, H.; Noh, Y.; Kossowska, D.; Kwak, K.; Cho, M. Ultrafast Fluxional Exchange Dynamics in Electrolyte Solvation Sheath of Lithium Ion Battery. *Nat. Commun.* **2017**, *8* (1), 1–9.
75. See, K. A.; Leskes, M.; Griffin, J. M.; Britto, S.; Matthews, P. D.; Emly, A.; Van Der Ven, A.; Wright, D. S.; Morris, A. J.; Grey, C. P.; Seshadri, R. Ab Initio Structure Search and in Situ ^7Li NMR Studies of Discharge Products in the Li-S Battery System. *J. Am. Chem. Soc.* **2014**, *136* (46), 16368–16377.
76. Zhang, J.; Hu, Y. H. Decomposition of Lithium Amide and Lithium Imide with and without Anion Promoter. *Ind. Eng. Chem. Res.* **2011**, *50* (13), 8058–8064.
77. Scardera, G.; Puzzer, T.; Conibeer, G.; Green, M. A. Fourier Transform Infrared Spectroscopy of Annealed Silicon-Rich Silicon Nitride Thin Films. *J. Appl. Phys.* **2008**, *104* (10), 104310.
78. San Andrés, E.; Del Prado, A.; Martínez, F. L.; Mártel, I.; Bravo, D.; López, F. J. Rapid Thermal Annealing Effects on the Structural Properties and Density of Defects in SiO_2 and SiN_x :H Films Deposited by Electron Cyclotron Resonance. *J. Appl. Phys.* **2000**, *87* (3), 1187–1192.
79. Diniz, J. A.; Tatsch, P. J.; Pudenzi, M. A. A. Oxynitride Films Formed by Low Energy NO^+ Implantation into Silicon. *Appl. Phys. Lett.* **1996**, *69* (15), 2214–2215.
80. Ono, H.; Ikarashi, T.; Miura, Y.; Hasegawa, E.; Ando, K.; Kitano, T. Bonding Configurations of Nitrogen Absorption Peak at 960 cm^{-1} in Silicon Oxynitride Films. *Appl. Phys. Lett.* **1999**, *74* (2), 203–205.
81. Viard, J.; Beche, E.; Perarnau, D.; Berjoan, R.; Durand, J. XPS and FTIR Study of Silicon Oxynitride Thin Films. *J. Eur. Ceram. Soc.* **1997**, *17* (15–16), 2025–2028.
82. Nakagawa, A.; Kuwata, N.; Matsuda, Y.; Kawamura, J. Thin Film Lithium Battery Using Stable Solid Electrolyte Li_4SiO_4 Fabricated by PLD. *ECS Trans.* **2010**, *25* (36), 155–161.
83. Flatscher, F.; Philipp, M.; Ganschow, S.; R. Wilkening, H. M.; Rettenwander, D. The Natural Critical Current Density Limit for $\text{Li}_7\text{La}_3\text{Zr}_2\text{O}_{12}$ Garnets. *J. Mater. Chem. A* **2020**, *8* (31), 15782–15788.
84. Raj, R.; Wolfenstine, J. Current Limit Diagrams for Dendrite Formation in Solid-State Electrolytes for Li-Ion Batteries. *J. Power Sources* **2017**, *343*, 119–126.
85. Wu, B.; Wang, S.; Iv, W. J. E.; Z. Deng, D.; Yang, J.; Xiao, J. Interfacial Behaviours between Lithium Ion Conductors and Electrode Materials in Various Battery Systems. *J. Mater. Chem. A* **2016**, *4* (40), 15266–15280.
86. Warneke, S.; Zenn, R. K.; Lebherz, T.; Müller, K.; Hintennach, A.; Starke, U.; Dinnebier, R. E.; Buchmeiser, M. R. Hybrid Li/S Battery Based on Dimethyl Trisulfide and Sulfurized Poly(Acrylonitrile). *Adv. Sustain. Syst.* **2018**, *2* (2), 1700144.
87. Wang, H.; Cao, X.; Liu, W.; Sun, X. Research Progress of the Solid State Lithium-Sulfur Batteries. *Front. Energy Res.* **2019**, *7*, 112.

88. Frey, M.; Zenn, R. K.; Warneke, S.; Müller, K.; Hintennach, A.; Dinnebier, R. E.; Buchmeiser, M. R. Easily Accessible, Textile Fiber-Based Sulfurized Poly(Acrylonitrile) as Li/S Cathode Material: Correlating Electrochemical Performance with Morphology and Structure. *ACS Energy Lett.* **2017**, *2* (3), 595–604.
89. Asenbauer, J.; Eisenmann, T.; Kuenzel, M.; Kazzazi, A.; Chen, Z.; Bresser, D. The Success Story of Graphite as a Lithium-Ion Anode Material – Fundamentals, Remaining Challenges, and Recent Developments Including Silicon (Oxide) Composites. *Sustain. Energy Fuels* **2020**, *4* (11), 5387–5416.
90. Sun, X.; Radovanovic, P. V.; Cui, B. Advances in Spinel $\text{Li}_4\text{Ti}_5\text{O}_{12}$ Anode Materials for Lithium-Ion Batteries. *New J. Chem.* **2014**, *39* (1), 38–63.
91. Zhao, B.; Ran, R.; Liu, M.; Shao, Z. A Comprehensive Review of $\text{Li}_4\text{Ti}_5\text{O}_{12}$ -Based Electrodes for Lithium-Ion Batteries: The Latest Advancements and Future Perspectives. *Mater. Sci. Eng. R Rep.* **2015**, *98*, 1–71.
92. Zhang, Q.; Li, X. Recent Developments in the Doped- $\text{Li}_4\text{Ti}_5\text{O}_{12}$ Anode Materials of Lithium-Ion Batteries for Improving the Rate Capability. *Int. J. Electrochem. Sci.* **2013**, *8*, 8.
93. Mukai, K.; Kato, Y.; Nakano, H. Understanding the Zero-Strain Lithium Insertion Scheme of $\text{Li}[\text{Li}_{1/3}\text{Ti}_{5/3}]\text{O}_4$: Structural Changes at Atomic Scale Clarified by Raman Spectroscopy. *J. Phys. Chem. C* **2014**, *118* (6), 2992–2999.
94. Zhao, L.; Hu, Y. S.; Li, H.; Wang, Z.; Chen, L. Porous $\text{Li}_4\text{Ti}_5\text{O}_{12}$ Coated with N-Doped Carbon from Ionic Liquids for Li-Ion Batteries. *Adv. Mater.* **2011**, *23* (11), 1385–1388.
95. Han, J. P.; Zhang, B.; Wang, L. Y.; Zhu, H. L.; Qi, Y. X.; Yin, L. W.; Li, H.; Lun, N.; Bai, Y. J. $\text{Li}_{1.3}\text{Al}_{0.3}\text{Ti}_{1.7}(\text{PO}_4)_3$ Behaving as a Fast Ionic Conductor and Bridge to Boost the Electrochemical Performance of $\text{Li}_4\text{Ti}_5\text{O}_{12}$. *ACS Sustain. Chem. Eng.* **2018**, *6* (6), 7273–7282.
96. Fang, Z. K.; Zhu, Y. R.; Yi, T. F.; Xie, Y. $\text{Li}_4\text{Ti}_5\text{O}_{12}$ - LiAlO_2 Composite as High Performance Anode Material for Lithium-Ion Battery. *ACS Sustain. Chem. Eng.* **2016**, *4* (4), 1994–2003.
97. Zhu, Y. R.; Yuan, J.; Zhu, M.; Hao, G.; Yi, T. F.; Xie, Y. Improved Electrochemical Properties of $\text{Li}_4\text{Ti}_5\text{O}_{12}$ - $\text{Li}_{0.33}\text{La}_{0.56}\text{TiO}_3$ Composite Anodes Prepared by a Solid-State Synthesis. *J. Alloys Compd.* **2015**, *646*, 612–619.
98. Yi, T. F.; Xie, Y.; Wu, Q.; Liu, H.; Jiang, L.; Ye, M.; Zhu, R. High Rate Cycling Performance of Lanthanum-Modified $\text{Li}_4\text{Ti}_5\text{O}_{12}$ Anode Materials for Lithium-Ion Batteries. *J. Power Sources* **2012**, *214*, 220–226.
99. Rahman, M. M.; Wang, J. Z.; Hassan, M. F.; Chou, S.; Wexler, D.; Liu, H.-K. Basic Molten Salt Process—A New Route for Synthesis of Nanocrystalline $\text{Li}_4\text{Ti}_5\text{O}_{12}$ - TiO_2 Anode Material for Li-Ion Batteries Using Eutectic Mixture of LiNO_3 - LiOH - Li_2O_2 . *J. Power Sources* **2010**, *195* (13), 4297–4303.
100. Wang, J.; Zhao, H.; Yang, Q.; Wang, C.; Lv, P.; Xia, Q. $\text{Li}_4\text{Ti}_5\text{O}_{12}$ - TiO_2 Composite Anode Material for Lithium-Ion Batteries. *J. Power Sources* **2013**, *222*, 196–201.

Chapter 6 Conclusions and Future Work

6.1 Summaries

In this dissertation, we first explore oxysilylation reactions as a means to synthesize nanocomposites with 3-D ordered architectures by reaction of $[\text{HSiMe}_2\text{OSiO}_{1.5}]_8$ (OHS) linked via different diepoxides, including DEB, DEO, DGEBA and ECHX, as discussed in Chapter 3. In principle, the linkages formed by ring-opening of epoxy groups contain EO segments that may facilitate Li^+ transport, while the 3-D ordered organic-inorganic hybrid structure offers mechanical stability. Transparent and flexible films were successfully cast for the 1:1 DEO:OHS system, but when incorporated with LiClO_4 , a common Li salt for PEs, the resulting films failed to show ionic conductivity, likely due to the highly crosslinked rigid structure. Despite the failed attempt to form novel SPE systems, we were able to establish a method of synthesizing self-reinforced epoxy resin nanocomposites via oxysilylation that avoids the use of polyamines while showing the potential to control MWs and extent of reaction by changing the catalyst concentrations and solvent volumes. These epoxy resins and nanocomposites interconnected by Si-O bonds with retained Si-H groups also exhibit unexpected hydrolytic stability.

In Chapter 4, we explore a new synthetic approach to Li_xPON , Li_xSiPON ($x = 3, 6$) and $\text{Li}_2\text{Si-PHN}$ inorganic polymer precursors by reacting OPCl_3 and $\text{Cl}_6\text{N}_3\text{P}_3$ with MNH_2 ($\text{M} = \text{Li}/\text{Na}$) or $(\text{Me}_3\text{Si})_2\text{NH}$ followed by lithiation with controlled amounts of LiNH_2 . These oligomer/polymers serve as precursors to LiPON-like glasses and ceramics offering considerable advantages over

traditional gas phase deposition methods including low cost, low-temperature syntheses and scalable features. In particular, the Li_6SiPON and Li_2SiPHN precursors show high ambient conductivities of 3.3×10^{-5} and 2.7×10^{-4} S/cm after treating at $400^\circ\text{C}/2$ h, respectively. We were also able to demonstrate that the precursor Li content can be controlled by controlling initial quantities of LiNH_2 used in the synthesis. This is quite difficult to achieve using gas phase deposition methods.

In addition, the N/P ratios of different precursors can be varied based on synthesis stoichiometry used, with all values well above LiPON glasses obtained by gas phase deposition, which is beneficial for Li^+ conduction. These polymers can be used in an intact form by impregnating Celgard separators, or as solid solutions with PEO as SSEs in nearly ASSBs that exhibits discharge capacities of 1000 mAh/g_{sulfur} at 0.25 C and 800 mAh/g_{sulfur} at 1 C retaining coulombic efficiency of ~100 % over 100 cycles.

In Chapter 5, we present a novel and green synthetic approach to oligo- and polysiloxane based Li^+ conducting materials using a spiro-siloxane (SP) distilled directly from rice hull ash (RHA), which is a plentiful agricultural waste. The novel Li^+ electrolyte system also provides a green, low cost, low temperature, and scalable solution for ASSBs. The distilled SP can be lithiated and nitrated by LiNH_2 producing Li_xSiON ($x = 2, 4$ and 6) precursors, and the Li content can be easily controlled by LiNH_2 amounts. Overall, conductivities of Li_xSiON precursors increase with the Li content: $\text{Li}_6\text{SiON} > \text{Li}_4\text{SiON} > \text{Li}_2\text{SiON}$. Specifically, Li_6SiON pellets show the highest ambient conductivity of 8.5×10^{-6} S/cm after treating at $200^\circ\text{C}/2$ h. Similar to LiPON-like polymer precursors, as-synthesized Li_xSiON oligomer/polymers can be used in an intact form through impregnation of Celgard separators showing an optimal ambient conductivity for Celgard/ Li_6SiON ($\sim 6.5 \times 10^{-6}$ S/cm), low E_a (0.28 eV), and high t_{Li^+} of ~0.7-1 are exhibited for all Celgard/PEs. The nearly

ASSB of SPAN/Celgard + Li₆SiON/Li half-cell delivers a reversible capacity of ~725 mAh/g at 0.5 C over 50 cycles.

In conclusion, we demonstrate novel solid electrolyte systems with desirable electrochemical performance derived from polymer precursor syntheses. Traditional gas phase deposition methods have the advantage of precise control, offering impurity-free and uniform thin electrolyte films, but their slow production rate and requirement for specialized equipment limit mass production at commodity scales. In contrast, although higher impurity contents are expected for polymer precursor syntheses, they are easily scalable and comparatively fast, providing low-cost and low-temperature fabrication procedures, allowing commodity scale production. More importantly, Li_x-PON-like precursors exhibit about two orders of magnitude improvement on ionic conductivity compared to traditional LiPON glasses ($\sim 10^{-4}$ vs. 10^{-6} S/cm). In addition, our ability to synthesize Li_xSiON precursors from agricultural waste avoids the use of toxic starting materials such as OPCl₃ and (Me₃Si)₂NH for Li_xPON, and it also reduces the chance of impurity inclusion as no byproduct is produced from the lithiation of SP. Moreover, it provides a carbon-neutral synthesis method for SSEs, contributing to our fight against global warming.

6.2 Future work

While this dissertation focuses on the syntheses of polymeric solid electrolytes, our ultimate goal is to assemble ASSBs through low-cost, scalable and environmentally friendly methods that can be commercialized. The following sections discuss our near-future research objectives on the syntheses, applications and improvement for electrolytes derived from polymer syntheses that might lead us one step forward.

6.2.1 Li_xSiON polymer precursor solid solutions with PEO

As discussed in Chapter 5, Li_xSiON oligomers/polymers can be used to coat Celgard separators showing good cycling stability and high-capacity retention between SPAN/Li electrodes, similar to Li_xPON-like precursors in Chapter 4. We also studied Li_xPON-PEO composite electrolyte films in Chapter 4, which exhibited even higher ionic conductivities ($\sim 10^{-3}$ vs. 10^{-5} S/cm) and higher capacity retention (~ 1000 vs. 750 mAh/g_{sulfur}) compared to the Li_xPON/Celgard system. Therefore, it is reasonable to also investigate the Li_xSiON-PEO composite electrolyte system.

Similar to the study on LiPON-like polymer precursor solid solutions with PEO in Chapter 4, Li_xSiON-PEO solid solution PE films can be made by mixing Li_xSiON precursor with 60 wt.% PEO ($M_w = 900$ kDa). As shown in Figure 6.1, transparent and dense films form, especially for 60PEO/Li₄SiON and Li₆SiON PE films.

As listed in Table 6.1, melting temperature (T_m) and crystallinity ($\chi_c, \%$) decrease for 60PEO/Li_xSiON PE films compared to pristine PEO. The 60PEO/Li₆SiON films show the highest conductivity of $\sim 10^{-4}$ S/cm at ambient temperature, despite higher T_m and crystallinity compared to 60PEO/Li₂SiON and Li₄SiON films, which can be ascribed to its higher Li content.

Future work will focus on electrochemical characterization of 60PEO/Li_xSiON PE films assembled in symmetrical and half cell forms towards ASSBs.

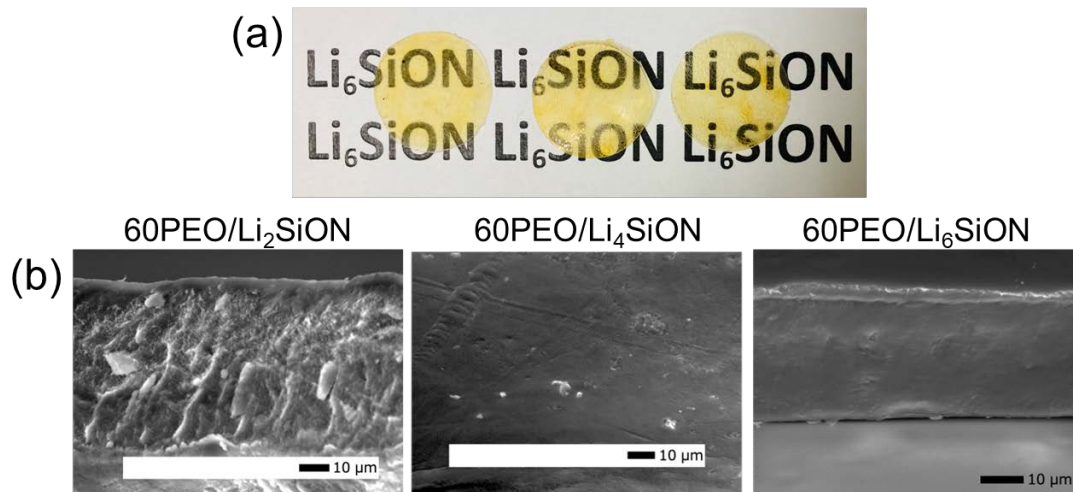


Figure 6.1. Optical images of 60PEO/Li₆SiON (a) and SEM fracture surface images of 60PEO/Li_xSiON PE films (b) heated to 65 °C/24 h/vacuum.

Table 6.1. Selected properties of 60PEO/Li_xSiON PE films.

Electrolyte	T _m (°C)	Percent crystallinity (χ _c ,%)	σ _{RT} (S/cm)
PEO	69	93	-
60PEO/Li ₂ SiON	55	55	1.0 ± 0.3 × 10 ⁻⁵
60PEO/Li ₄ SiON	55	43	7.1 ± 0.4 × 10 ⁻⁵
60PEO/Li ₆ SiON	58	67	1.4 ± 0.1 × 10 ⁻⁴

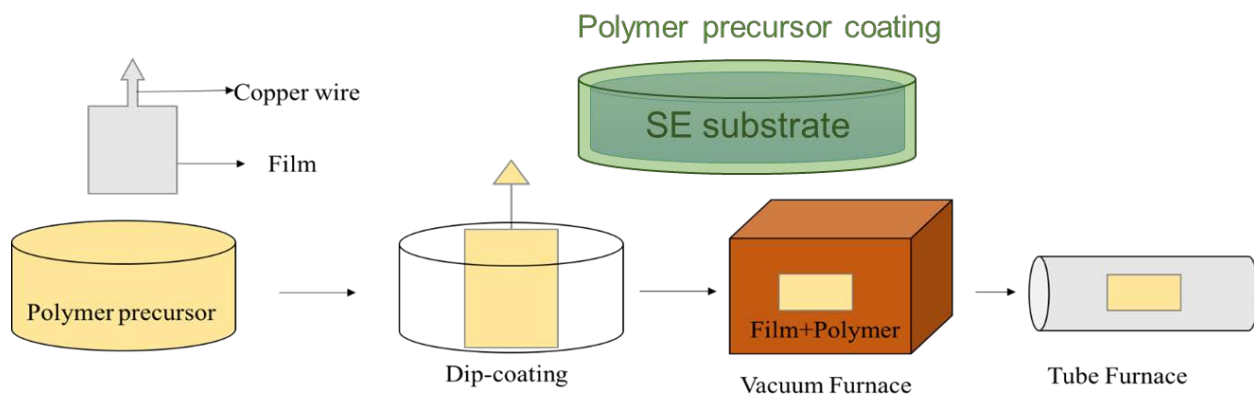
6.2.2 Polymer precursor coated solid-state electrolyte thin films

Li metal dendrite formation resulting from nonuniform Li deposition is a well-established problem when cycling LIBs, which can lead to short circuiting wherein the dendrites penetrate the electrolyte layer and bridge to the cathode.^{1,2} Inorganic (ceramic) SSEs were originally thought to offer a mechanical solution by blocking dendrite growth, including NASICON-type LATP [Li_{1.3}Al_{0.3}Ti_{1.7}(PO₄)₃] and garnet-type LLZO (Li₇La₃Zr₂O₁₂).³⁻⁷ However, they generally suffer from low fracture toughness and ductility, resulting in poor interfacial contact with electrodes.⁸⁻¹¹ Moreover, LATP undergoes irreversible reduction during cycling,⁷ and LLZO is susceptible to dendrite penetration along grain boundaries, which also leads to short-circuiting.¹²

One solution to these problems is LiPON glasses, which appear to resist dendrite penetration and wet with Li metal.^{13,14} However, LiPON glasses typically suffer from poor conductivities (10^{-8} - 10^{-6} S/cm)¹⁵⁻¹⁷ compared to LATP ($\sim 3 \times 10^{-3}$ S/cm for bulk)³⁻⁵ or LLZO (10^{-4} - 10^{-3} S/cm)^{6,7,12,18} such that they must be introduced as interface materials at thicknesses of 50-200 nm to offer practical Li⁺ cycling. Consequently, LiPON thin films are typically fabricated through gas phase deposition methods including radio frequency magnetron sputtering (RFMS).¹⁵⁻¹⁷

As discussed in detail in Chapter 4, LiPON-like precursors were synthesized via polymer syntheses, offering a facile, low-cost alternative for the application of thin ceramic films. Furthermore, polymer precursors can be applied in a liquid format, e.g., be used as a coating material. This provides us the opportunity to optimize scalable LiPON-like polymer precursors as coating materials that act as binder/or adhesives for ceramic electrolytes, offering the potential to serve as an interface buffer layer between electrolyte and electrode.

To test the utility of synthesized precursors, it is also important to have a set of substrates qualified for testing the efficacy of the coatings and processing conditions explored. To this end, we chose a series of substrates produced in our laboratories, including LiAlO₂ thin films (20-30 μm thick)¹⁹ and LATSP (Li_{1.7}Al_{0.3}Ti_{1.7}Si_{0.4}P_{2.6}O₁₂, ~ 25 μm thick)³ derived from flame-synthesized NPs as solid electrolyte substrates. As shown in Scheme 6.1, these sintered substrates were dip-coated in the desired LiPON-like precursor solution (~ 0.1 g/mL in THF) using copper wire to suspend the sample. The coated films were dried (100 °C/12 h/vacuum), followed by heating to selected temperatures under N₂.



Scheme 6.1. Coating procedure of LiPON-like polymer precursors on SE substrates.

Figures 6.2 and A.33 show SEM fracture surface images of coated LiAlO_2 and LATSP films after heating to 400° , 500° and $600^\circ \text{C}/2 \text{ h}/\text{N}_2$, respectively. Coated LiAlO_2 films generally show dense and uniform coatings ($\sim 4 \mu\text{m}$) with a well-defined interface between the coating and the substrate. When heated to 500° and 600°C , the coating thickness decreases, corresponding to melting of the coating material as suggested by TGA-DTA studies in Chapter 4.

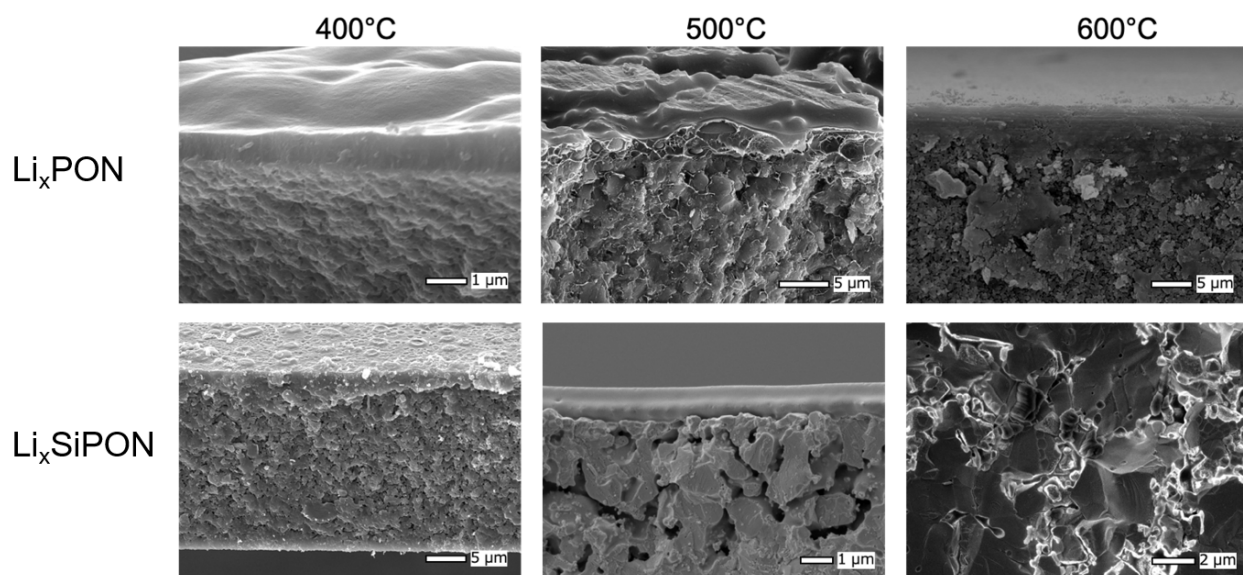


Figure 6.2. SEM fracture surface images of $\text{LiAlO}_2 + \text{LiPON}$ -like precursor films heated to 400° , 500° and $600^\circ \text{C}/2 \text{ h}/\text{N}_2$.

Similarly, coated LATSP films (Figure A.33) generally present uniform coatings and well-defined interfaces with an average coating thickness of 5 μm . Additionally, some coated films show LiPON-like precursor percolating into the LATSP substrate, resulting in a denser microstructure.

Conductivity measurements were conducted at room temperature as described in previous chapters. Table 6.2 summarizes total conductivities of LiPON-like polymer precursor coated SE films after heating to 400°, 500° and 600 °C/2 h/N₂.

Table 6.2. Total ambient conductivities (σ_{RT}) of LiPON-like precursor coated SE films after heating to selected temperatures.

Substrate	Polymer coating	Temperature (°C/2 h/N ₂)	σ_{RT} (S/cm)
Pristine LiAlO ₂ ¹⁹		-	1.6×10^{-8}
LiAlO ₂	Li ₃ PON	400	$6.6 \pm 0.1 \times 10^{-5}$
		500	$4.5 \pm 0.4 \times 10^{-5}$
		600	$3.8 \pm 1.6 \times 10^{-5}$
	Li ₃ SiPON	400	$1.4 \pm 0.2 \times 10^{-5}$
		500	$5.8 \pm 1.4 \times 10^{-5}$
		600	$4.1 \pm 0.3 \times 10^{-5}$
	Li ₆ SiPON	400	$1.4 \pm 2.5 \times 10^{-4}$
		500	$0.5 \pm 0.6 \times 10^{-4}$
		600	$1.5 \pm 0.3 \times 10^{-5}$
Pristine LATSP ³		-	4.3×10^{-4}
LATSP	Li ₃ PON	400	$2.6 \pm 0.8 \times 10^{-5}$
		500	$2.4 \pm 1.5 \times 10^{-5}$
		600	$3.3 \pm 1.6 \times 10^{-5}$
	Li ₃ SiPON	400	$1.8 \pm 0.8 \times 10^{-4}$
		500	$2.8 \pm 0.3 \times 10^{-4}$
		600	$8.0 \pm 0.8 \times 10^{-5}$
	Li ₆ SiPON	400	$3.7 \pm 0.5 \times 10^{-5}$
		500	$1.6 \pm 1.8 \times 10^{-5}$
		600	$1.7 \pm 1.4 \times 10^{-5}$

In general, all coated films show conductivities of 10^{-5} - 10^{-4} S/cm, similar to Chapter 4, LiPON-like polymer precursor pellets suggesting a dominant contribution of Li⁺ conduction from LiPON-like precursors, which may arise from coatings that “encircle” the sample via film edges. A more probable explanation is that the coating penetrates pores introducing Li⁺ conducting pathways not

available before coating. Note that coatings heated $>700\text{ }^{\circ}\text{C}$ lose N_2 forming Li_xPO_y and offer low conductivities expected of crystalline lithium phosphates (10^{-10} - 10^{-9} S/cm).

Although LiPON-like precursor coatings reduce the conductivity of LATSP by an order of magnitude, significant improvement in conductivity (up to four orders of magnitude) for LiAlO_2 is exhibited. This is important as LiAlO_2 substrates are less costly substitutes for LATP and LLZO.¹⁹

The interfacial behavior directly dictates the lifespan, energy density and safety of ASSBs. Polymer precursor coatings might offer improved interfacial properties that lower interfacial resistance and stabilize the interfacial performance of ASSBs. Future studies will focus on the use of these polymer precursors for bonding between thin film ceramics and to assemble symmetrical and half-cells for electrochemical performance.

The Figure 6.3 shows SEM microstructures for LTO/ Li_3SiPON / LiAlO_2 heated to $400\text{ }^{\circ}\text{C}/2\text{ h}/\text{N}_2$ as an example demonstration. Clear bonding between the SE LiAlO_2 substrate and the anode LTO via Li_3SiPON precursor coating is observed, and the resulting coating interface appears dense and uniform. This interposed Li_3SiPON buffer layer might reduce cathode/SSE impedance in space charge regions. Electrochemical characterization of the anolyte with Li metal remains as future work.

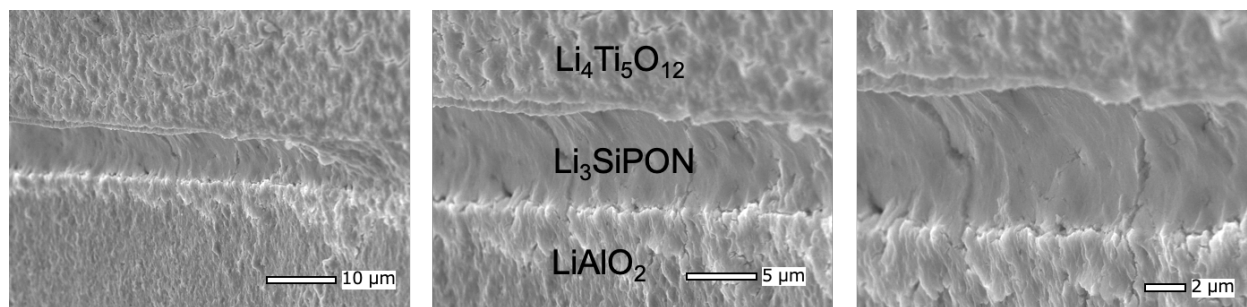


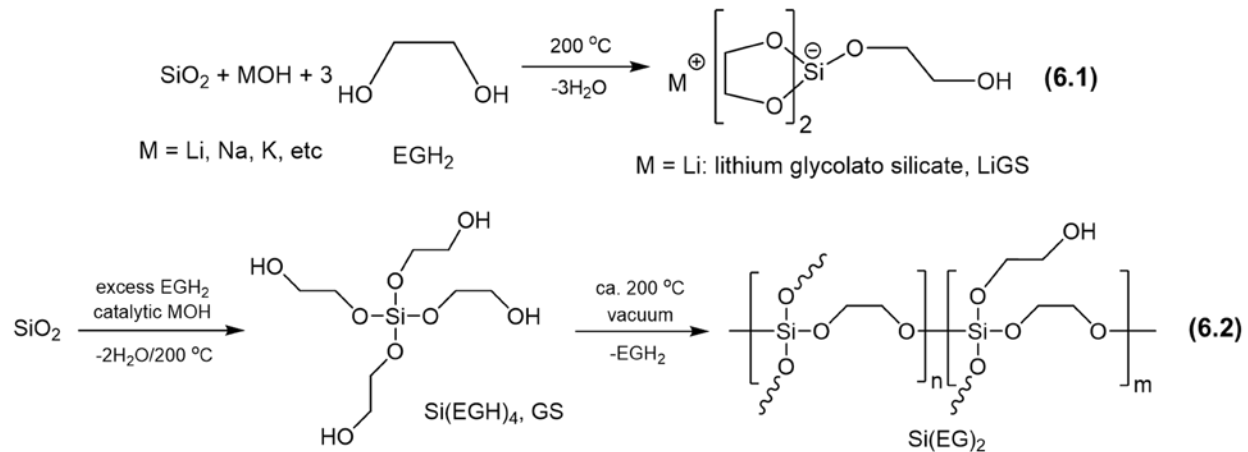
Figure 6.3. SEM fracture surface images of Li_3SiPON precursor bonding interface between LTO and LiAlO_2 thin films (sample heated to $400\text{ }^{\circ}\text{C}/2\text{ h}/\text{N}_2$).

6.2.3 Silica dissolution with ethylene glycol

In Chapter 5, we present a green synthesis method for a novel electrolyte system, Li_xSiON , by reacting SP distilled from RHA with LiNH_2 . The reaction between SiO_2 in RHA with a sterically hindered diol, hexylene glycol, in the presence of catalytic amount of an alkali base forms distillable SP with a spirocyclic structure.

Previously, our group reported similar reactions of fumed silica with ethylene glycol (EGH₂) and an alkali base, as illustrated in reactions (6.1) and (6.2).^{20,21} One can envision that if an intermediate amount of alkali base is used, e.g., 40 mol. % of SiO_2 , a mixture of metal glycolate silicate salt with $\text{Si}(\text{EG})_2$ polymer will form, which is analogous to a SPE system. Therefore, a set of reactions are explored using selected amounts of LiOH (20, 40 and 60 mol.% to SiO_2), and they are denoted as Li_xSiO ($\text{Li}/\text{Si} = x = 0.2, 0.4$ and 0.6).

In general, a selected amount of LiOH was first dissolved in an excess amount of EGH₂ (~200 °C/1 d/ N_2) followed by addition of fumed SiO_2 . The mixture was kept at >200 °C/ N_2 in a standard Pyrex distillation setup for 3-5 d to distill EGH₂ and byproduct water. As distillation continues, additional EGH₂ was added to retain the total reaction volume. Once a clear solution forms, a portion of the reaction mixture was dried at ~120 °C/1-3 d under vacuum. The dried products were ground into powders with an alumina mortar pestle, and pelletized at 100 °C/5 ksi/5 min.



As shown in Figure 6.4a, Li_xSiO ($x = 0.2$ and 0.4) gave light brown powders and opaque and brittle pellets that crack easily, likely due to a low polymer content and/or polymers with low MWs.

To improve mechanical properties of the pellets, triethanolamine (TEA, 5 mol. %) was added during Li_xSiO syntheses to promote polymerization by introducing crosslinking. As a result, brown solids and brown translucent pellets were obtained for Li_xSiO -5TEA (Figure 6.4b). These pellets also appear to be flexible suggesting improved mechanical properties (Figure A.34).

It is noteworthy that after adding TEA, the products generally need longer drying time (up to 5 d). Since TEA is less volatile than EGH_2 , there may be unreacted and trapped TEA that can't be easily removed. In addition, by replacing 5 mol. % EG bonds, TEA introduces crosslinking, and there may be EGH_2 trapped in between the polymer chains that are harder to remove. Consequently, there may still be liquid phase in the final products after drying, resulting in gel polymer electrolytes (GPEs).

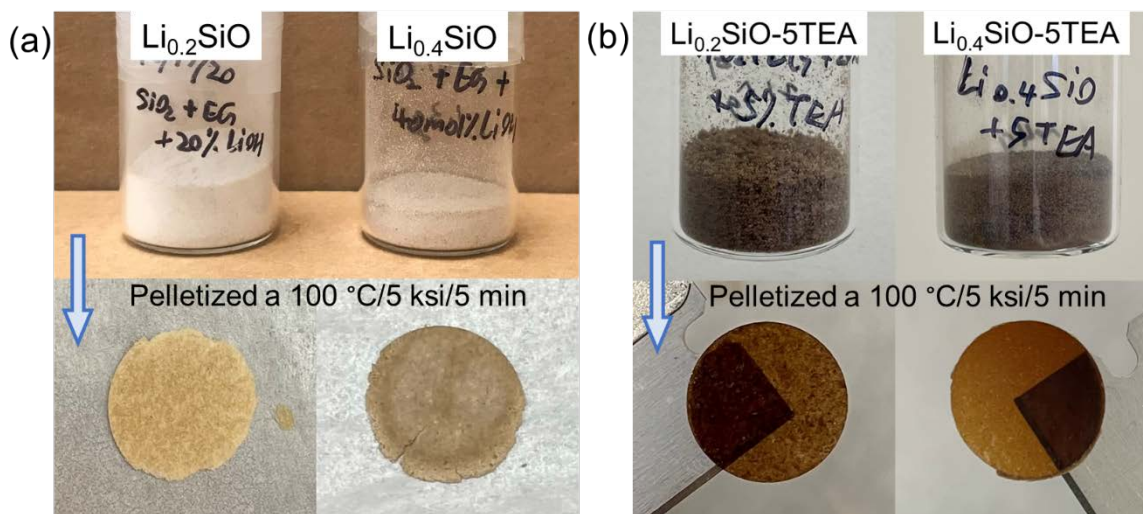


Figure 6.4. Optical images of **a.** Li_xSiO ($x = 0.2$ and 0.4) dried products and pellets, and **b.** Li_xSiO -5TEA ($x = 0.2$ and 0.4) dried products and pellets.

Overall, Li_xSiO and $\text{Li}_x\text{SiO-5TEA}$ ($x = 0.2$ and 0.4) syntheses formed clear solutions, suggesting complete SiO_2 dissolution. In contrast, the synthesis of $\text{Li}_{0.6}\text{SiO}$ gave a suspension, which may be ascribed to insoluble products with higher MWs. Another explanation is that based on reactions (6.1) and (6.2), the products should be a mixture of lithium glycolato silicate (LiGS) and $\text{Si}(\text{EG})_2$, and as the LiOH content increases to 60 mol.%, more LiGS forms, which might have lower solubility.

The dried $\text{Li}_{0.6}\text{SiO}$ suspension gives light brown powders and opaque pellets, while the dried soluble part gave dark brown solid and translucent pellets (Figure 6.5), similar to $\text{Li}_x\text{SiO-5TEA}$ ($x = 0.2$ and 0.4) above.

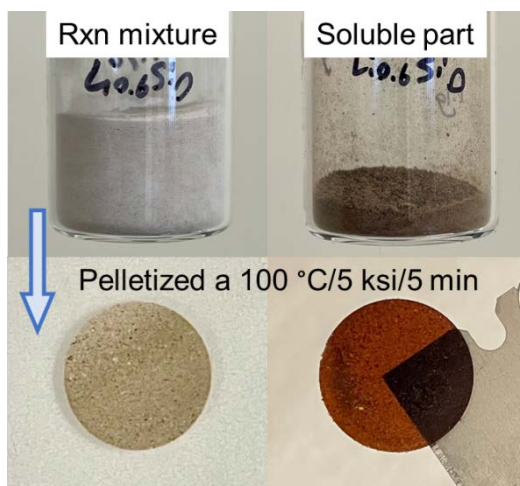


Figure 6.5. Optical images of $\text{Li}_{0.6}\text{SiO}$ powders and pellets from the suspension mixture and soluble portion.

Conductivity measurements were conducted on pressed pellets at room temperature as described in previous chapters. Figure 6.6a compares representative Nyquist plots of Li_xSiO ($x = 0.2, 0.4$ and 0.6) pellets ($100\text{ °C}/5\text{ ksi}/5\text{ min}$). The resistivity of $\text{Li}_{0.6}\text{SiO}$ from the suspension mixture is much higher than $\text{Li}_{0.2}\text{SiO}$ and $\text{Li}_{0.4}\text{SiO}$ pellets, but $\text{Li}_{0.6}\text{SiO}$ from the soluble part shows similar resistivity to $\text{Li}_{0.4}\text{SiO}$.

Figure 6.6b compares ambient conductivities (S/cm) of Li_xSiO ($x = 0.2, 0.4$ and 0.6) and Li_xSiO -5TEA pellets. Overall, conductivity increase with increasing Li content from 0.2 to 0.4, but $\text{Li}_{0.6}\text{SiO}$ from the suspension mixture shows a low conductivity of $\sim 3 \times 10^{-8}$ S/cm. In contrast, $\text{Li}_{0.6}\text{SiO}$ from the soluble part shows a higher conductivity of $\sim 4 \times 10^{-7}$ S/cm, similar to Li_xSiO -5TEA ($x = 0.2$ and 0.4) pellets, ascribing to higher polymer contents that enhances Li^+ mobility. $\text{Li}_{0.4}\text{SiO}$ without TEA shows the highest conductivity of $\sim 10^{-6}$ S/cm.

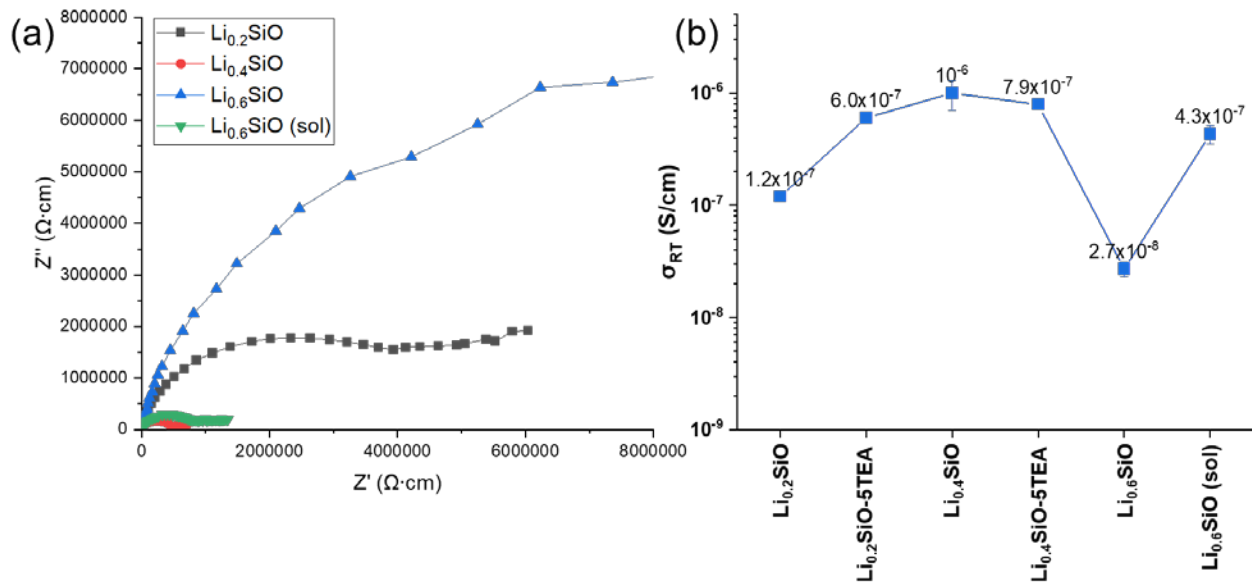


Figure 6.6. Representative Nyquist plots (a) and summarized conductivities (b) of Li_xSiO ($x = 0.2, 0.4$) and $\text{Li}_{0.6}\text{SiO}$ pellets ($100^\circ\text{C}/5 \text{ ksi}/5\text{min}$) from the soluble part and suspension mixture.

Overall, the Li_xSiO system shows limited ionic conductivities ($\leq 10^{-6}$ S/cm). Improving the conductivity and fabricating processable solid electrolyte membranes for ASSBs assembly remain as future work. It is also important to optimize the synthesis procedure so that RHA can be used as the starting material, achieving a green synthetic method similar to the Li_xSiON SE system.

References

1. Liu, Y.; Zhou, G.; Liu, K.; Cui, Y. Design of Complex Nanomaterials for Energy Storage: Past Success and Future Opportunity. *Acc. Chem. Res.* **2017**, *50* (12), 2895–2905.
2. Lin, C.-F.; Qi, Y.; Gregorczyk, K.; Lee, S. B.; Rubloff, G. W. Nanoscale Protection Layers To Mitigate Degradation in High-Energy Electrochemical Energy Storage Systems. *Acc. Chem. Res.* **2018**, *51* (1), 97–106.
3. Yi, E.; Wang, W.; Mohanty, S.; Kieffer, J.; Tamaki, R.; Laine, R. M. Materials That Can Replace Liquid Electrolytes in Li Batteries: Superionic Conductivities in $\text{Li}_{1.7}\text{Al}_{0.3}\text{Ti}_{1.7}\text{Si}_{0.4}\text{P}_{2.6}\text{O}_{12}$. Processing Combustion Synthesized Nanopowders to Free Standing Thin Films. *J. Power Sources* **2014**, *269* (10), 577–588.
4. Zhao, E.; Ma, F.; Guo, Y.; Jin, Y. Stable LATP/LAGP Double-Layer Solid Electrolyte Prepared: Via a Simple Dry-Pressing Method for Solid State Lithium Ion Batteries. *RSC Adv.* **2016**, *6*, 92579–92585.
5. Wang, S.; Ding, Y.; Zhou, G.; Yu, G.; Manthiram, A. Durability of the $\text{Li}_{1+x}\text{Ti}_{2-x}\text{Al}_x(\text{PO}_4)_3$ Solid Electrolyte in Lithium-Sulfur Batteries. *ACS Energy Lett.* **2016**, *1* (6), 1080–1085.
6. Murugan, R.; Thangadurai, V.; Weppner, W. Fast Lithium Ion Conduction in Garnet-Type $\text{Li}_7\text{La}_3\text{Zr}_2\text{O}_{12}$. *Angew. Chem. Int. Ed.* **2007**, *46* (41), 7778–7781.
7. Ohta, S.; Kobayashi, T.; Asaoka, T. High Lithium Ionic Conductivity in the Garnet-Type Oxide $\text{Li}_{7-x}\text{La}_3(\text{Zr}_{2-x}\text{Nb}_x)\text{O}_{12}$ ($X=0-2$). *J. Power Sources* **2011**, *196* (6), 3342–3345.
8. Jiang, T.; He, P.; Wang, G.; Shen, Y.; Nan, C. W.; Fan, L. Z. Solvent-Free Synthesis of Thin, Flexible, Nonflammable Garnet-Based Composite Solid Electrolyte for All-Solid-State Lithium Batteries. *Adv. Energy Mater.* **2020**, *10* (12), 1903376.
9. Chen, R. J.; Zhang, Y. B.; Liu, T.; Xu, B. Q.; Lin, Y. H.; Nan, C. W.; Shen, Y. Addressing the Interface Issues in All-Solid-State Bulk-Type Lithium Ion Battery via an All-Composite Approach. *ACS Appl. Mater. Interfaces* **2017**, *9* (11), 9654–9661.
10. Chen, L.; Li, Y.; Li, S. P.; Fan, L. Z.; Nan, C. W.; Goodenough, J. B. PEO/Garnet Composite Electrolytes for Solid-State Lithium Batteries: From “Ceramic-in-Polymer” to “Polymer-in-Ceramic.” *Nano Energy* **2018**, *46*, 176–184.
11. Zhou, W.; Wang, S.; Li, Y.; Xin, S.; Manthiram, A.; Goodenough, J. B. Plating a Dendrite-Free Lithium Anode with a Polymer/Ceramic/Polymer Sandwich Electrolyte. *J. Am. Chem. Soc.* **2016**, *138* (30), 9385–9388.
12. Yi, E.; Wang, W.; Kieffer, J.; Laine, R. M. Key Parameters Governing the Densification of Cubic- $\text{Li}_7\text{La}_3\text{Zr}_2\text{O}_{12}$ Li^+ conductors. *J. Power Sources* **2017**, *352*, 156–164.
13. Yu, X.; Bates, J. B.; Jellison, G. E.; Hart, F. X. A Stable Thin-Film Lithium Electrolyte: Lithium Phosphorus Oxynitride. *J. Electrochem. Soc.* **1997**, *144*, 524–532.
14. Han, F.; Westover, A. S.; Yue, J.; Fan, X.; Wang, F.; Chi, M.; Leonard, D. N.; Dudney, N. J.; Wang, H.; Wang, C. High Electronic Conductivity as the Origin of Lithium Dendrite Formation within Solid Electrolytes. *Nat. Energy* **2019**, *4* (3), 187–196.
15. Yu, X.; Bates, J. B.; Jellison, G. E.; Hart, F. X. A Stable Thin-Film Lithium Electrolyte: Lithium Phosphorus Oxynitride. *J. Electrochem. Soc.* **1997**, *144*, 524–532.
16. Bates, J. B.; Dudney, N. J.; Gruzalski, G. R.; Zuhr, R. A.; Choudhury, A.; Luck, C. F.; Robertson, J. D. Electrical Properties of Amorphous Lithium Electrolyte Thin Films. *Solid State Ion.* **1992**, *53*, 647–654.

17. Bates, J. B.; Dudney, N. J.; Gruzalski, G. R.; Zuhr, R. A.; Choudhury, A.; Luck, C. F.; Robertson, J. D. Fabrication and Characterization of Amorphous Lithium Electrolyte Thin Films and Rechargeable Thin-Film Batteries. *J. Power Sources* **1993**, *43–44*, 103–110.
18. Yi, E.; Wang, W.; Kieffer, J.; Laine, R. M. Flame Made Nanoparticles Permit Processing of Dense, Flexible, Li⁺ Conducting Ceramic Electrolyte Thin Films of Cubic-Li₇La₃Zr₂O₁₂ (c-LLZO). *J. Mater. Chem. A* **2016**, *4* (33), 12947–12954.
19. Temeche, E.; Indris, S.; Laine, R. M. LiAlO₂/LiAl₅O₈ Membranes Derived from Flame-Synthesized Nanopowders as a Potential Electrolyte and Coating Material for All-Solid-State Batteries. *ACS Appl. Mater. Interfaces* **2020**, *12* (41), 46119–46131.
20. Laine, R. M.; Blohowiak, K. Y.; Robinson, T. R.; Hoppe, M. L.; Nardi, P.; Kampf, J.; Uhm, J. Synthesis of Pentacoordinate Silicon Complexes from SiO₂. *Nature* **1991**, *353* (6345), 642–644.
21. Laine, R. M.; Furgal, J. C.; Doan, P.; Pan, D.; Popova, V.; Zhang, X. Avoiding Carbothermal Reduction: Distillation of Alkoxysilanes from Biogenic, Green, and Sustainable Sources. *Angew. Chem. - Int. Ed.* **2016**, *55* (3), 1065–1069.

Appendix A. Supplemental Data

Table A.1. GPC data for oxysilylation of DEB with OHS.

Reaction time	Mn (kDa)	Mw (kDa)	PDI
30 min	6.5	14.1	2.2
1 d	6.3	13.5	2.1

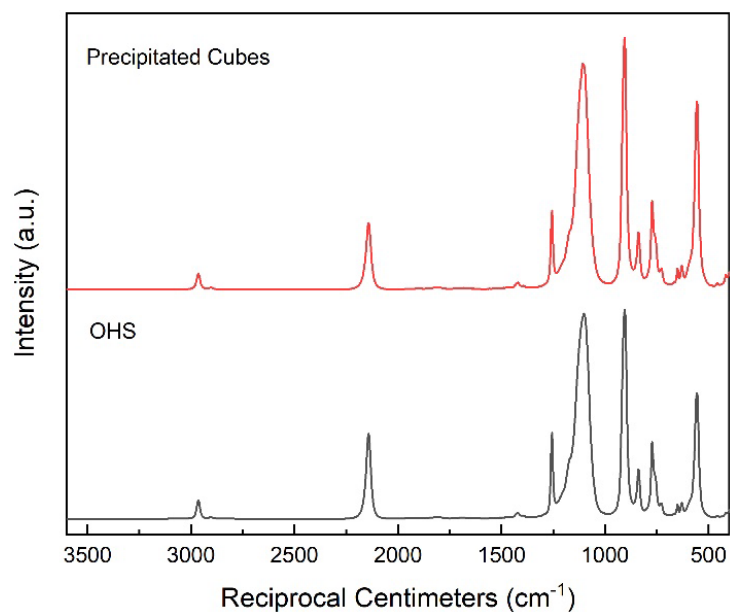


Figure A.1. Representative FTIRs of OHS (bottom) and precipitated cubes in diepoxide oxysilylation with TMDS + (5-20 mol.%) OHS.

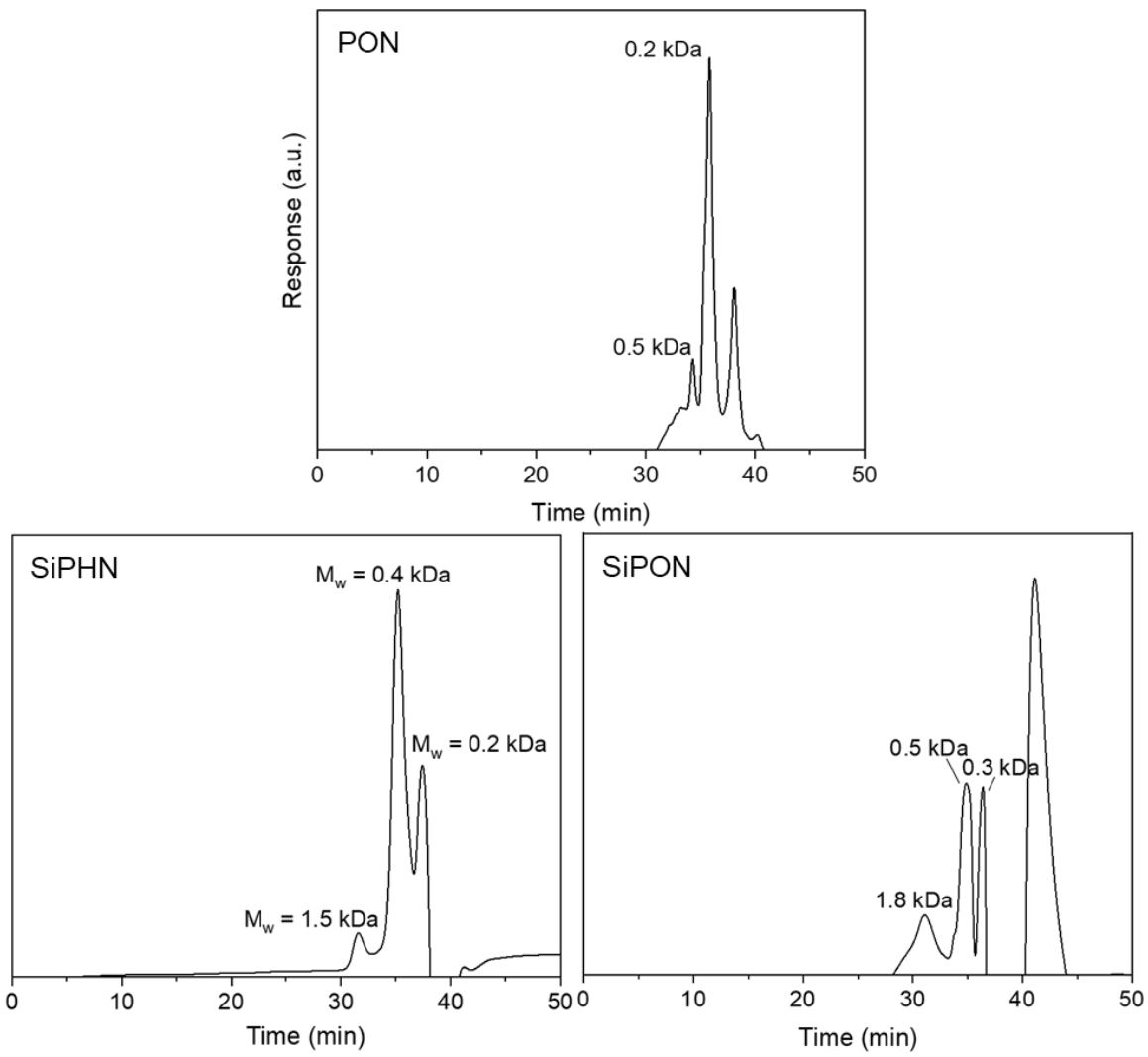


Figure A.2. GPC of unlithiated PON, SiPHN and SiPON precursors.

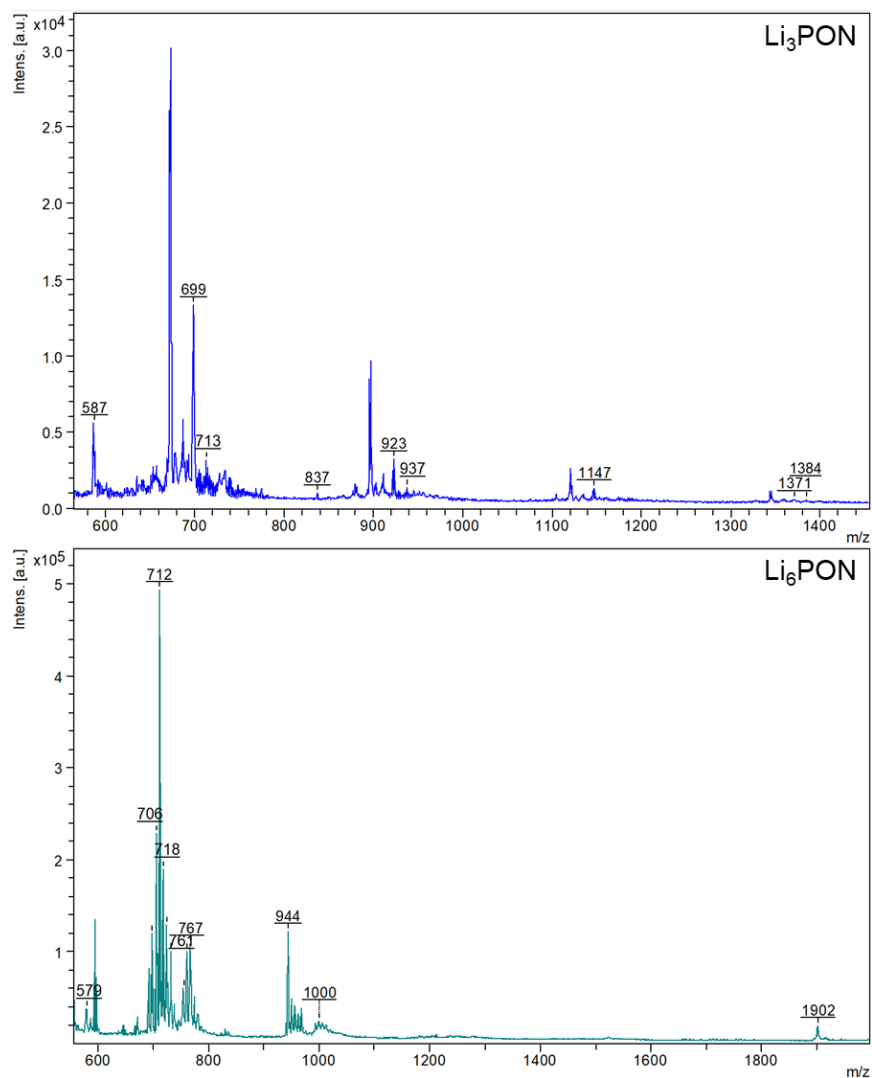


Figure A.3. Negative-ion mode MALDI of Li_3PON (left) and Li_6PON (right) precursors.

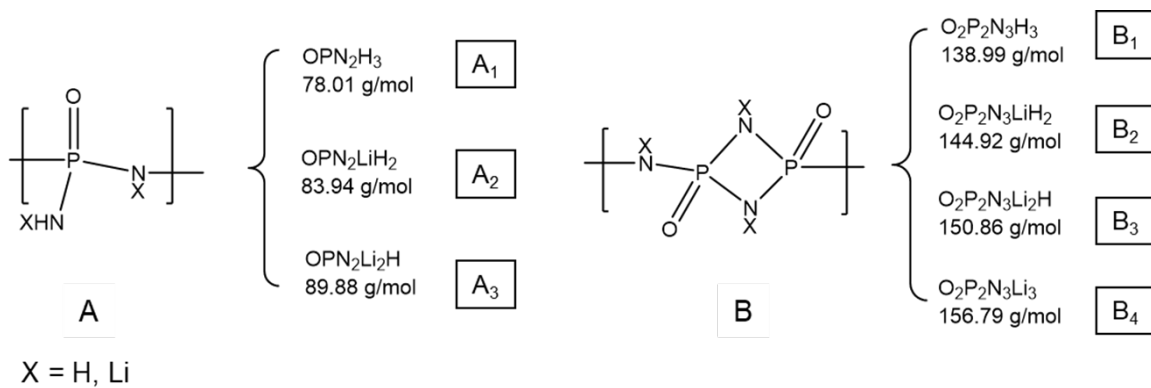


Figure A.4. Possible Li_xPON monomer structures.

Table A.2. Possible compositions of Li_xPON precursors based on Figures A.3-A.4.

Li_3PON		Li_6PON	
m/z, Da	Possible compositions	m/z, Da	Possible compositions
587	$A_2 + 2A_3 + 2B_4 + -H + -\text{NH}_2 - \text{Li}^+ = 3A_3 + B_3 + B_4 + -H + -\text{NH}_2 - \text{Li}^+ = 587.4$	579	$4A_1 + 2A_2 + A_3 + -H + -\text{NH}_2 - \text{Li}^+ = 579.9$
699	$A_1 + B_1 + 3B_4 + -H + -\text{NH}_2 - \text{Li}^+ = A_1 + B_2 + B_3 + 2B_4 + -H + -\text{NH}_2 - \text{Li}^+ = 697.5$ $A_2 + 6A_3 + B_4 + -H + -\text{NH}_2 - \text{Li}^+ = 700.2$	706	$4A_1 + A_2 + B_2 + B_4 + -H + -\text{NH}_2 - \text{Li}^+ = 707.8$
713	$3A_1 + 3B_4 + -H + -\text{NH}_2 - \text{Li}^+ = 2A_1 + A_2 + C_3 + 2C_4 + -H + -\text{NH}_2 - \text{Li}^+ = 714.5$	712	$4B_1 + B_2 + -H + -\text{NH}_2 - \text{Li}^+ = 711.0$ $6A_1 + A_2 + B_3 + -H + -\text{NH}_2 - \text{Li}^+ = 713.0$
837	$A_1 + 2B_1 + 3B_4 + -H + -\text{NH}_2 - \text{Li}^+ = 836.5$	718	$3B_1 + 2B_2 + -H + -\text{NH}_2 - \text{Li}^+ = 716.9$ $6A_1 + A_2 + B_4 + -H + -\text{NH}_2 - \text{Li}^+ = 718.9$
923	$3A_1 + 2A_2 + A_3 + 2B_1 + B_2 + -H + -\text{NH}_2 - \text{Li}^+ = 924.7$	761	$A_2 + 4A_3 + B_3 + B_4 + -H + -\text{NH}_2 - \text{Li}^+ = 761.2$
937	$2A_1 + 2A_2 + 2A_3 + 2B_1 + B_2 + -H + -\text{NH}_2 - \text{Li}^+ = 936.7$	767	$A_2 + 4A_3 + 2B_4 + -H + -\text{NH}_2 - \text{Li}^+ = 767.1$
1147	$3A_1 + 2A_2 + 2B_1 + B_2 + 2B_4 + -H + -\text{NH}_2 - \text{Li}^+ = 1148.5$	944	$A_1 + 3A_3 + 2B_1 + B_3 + B_4 + -H + -\text{NH}_2 - \text{Li}^+ = 943.4$
1371	$3A_1 + 3A_2 + 3B_1 + B_2 + 2B_4 + -H + -\text{NH}_2 - \text{Li}^+ = 1371.4$	1000	$A_2 + 2A_3 + 3B_1 + B_3 + B_4 + -H + -\text{NH}_2 - \text{Li}^+ = 998.4$ $5B_1 + B_2 + B_3 + -H + -\text{NH}_2 - \text{Li}^+ = 1000.8$
1384	$A_1 + A_2 + 11A_3 + 2B_4 + -H + -\text{NH}_2 - \text{Li}^+ = 1384.4$	1902	$12A_1 + 5A_2 + A_3 + B_1 + B_3 + B_4 + -H + -\text{NH}_2 - \text{Li}^+ = 1902.4$

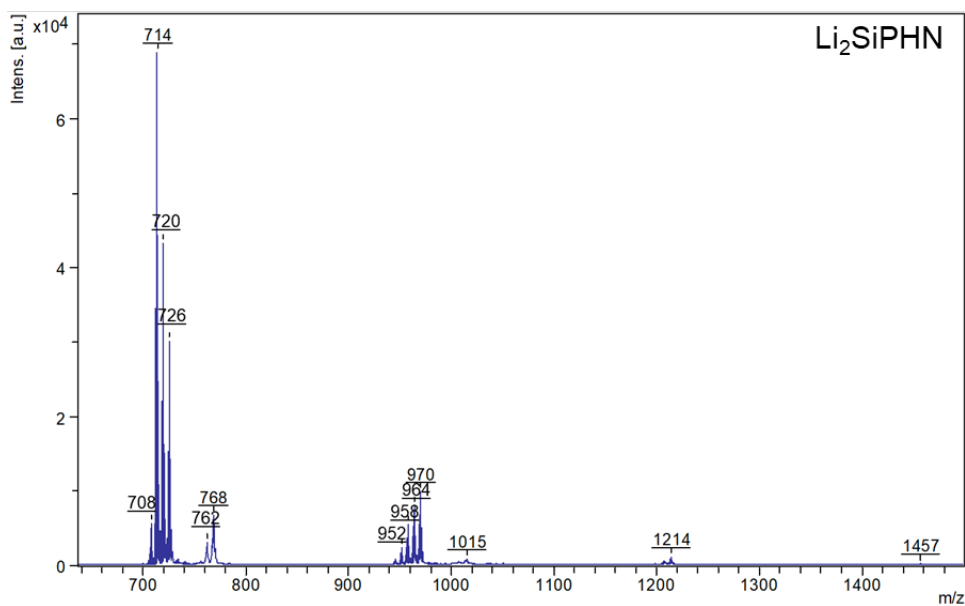


Figure A.5. Negative-ion mode MALDI of the Li_2SiPHN precursor.

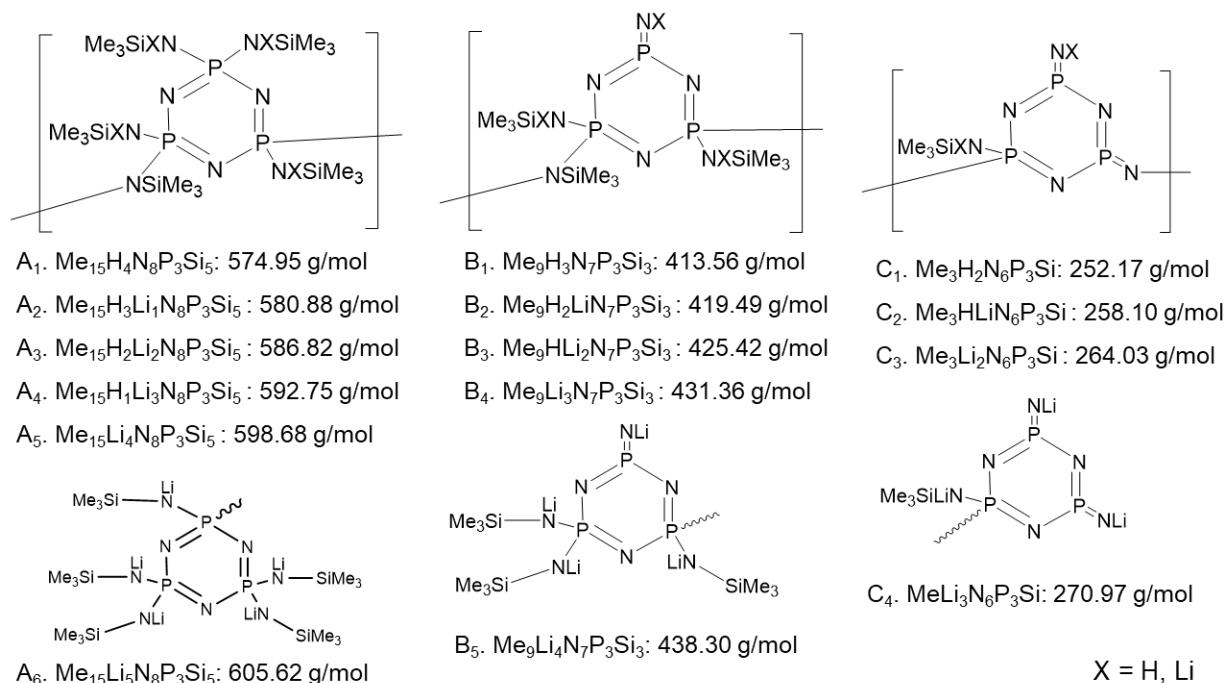


Figure A.6. Possible monomer structures of Li₂SiPHN precursor.

Table A.3. Possible compositions of Li₂SiPHN precursor based on Figures A.5-A.6.

m/z, Da	Possible compositions
708	C ₂ + C ₄ + D ₂ - Li ⁺ = 707.0
714	2C ₃ + D ₃ + -H - Li ⁺ = C ₂ + C ₄ + D ₃ - Li ⁺ = 712.9
720	C ₃ + C ₄ + D ₃ - Li ⁺ = 718.8
726	2C ₄ + D ₃ - Li ⁺ = 726.8
762	2C ₁ + C ₃ + H - Li ⁺ = C ₁ + 2C ₂ - Li ⁺ = 761.4
768	A ₄ + D ₁ - Li ⁺ = A ₃ + D ₂ - Li ⁺ = 765.7 B ₃ + C ₃ + -H + -NHSiMe ₃ - Li ⁺ = B ₄ + C ₂ + -H + -NHSiMe ₃ - Li ⁺ = 771.8
952	A ₆ + C ₃ + -NHSiMe ₃ - Li ⁺ = B ₄ + B ₅ + -NHSiMe ₃ - Li ⁺ = 950.9 B ₃ + C ₃ + C ₄ - -H - Li ⁺ = B ₅ + C ₂ + C ₅ - -H - Li ⁺ = 952.4
958	C ₁ + C ₃ + C ₄ + D ₁ - Li ⁺ = C ₁ + C ₂ + C ₄ + D ₂ - Li ⁺ = 959.2
964	C ₂ + C ₃ + C ₄ + D ₁ - Li ⁺ = 965.1
970	3C ₃ + D ₂ - Li ⁺ = 970.0
1015	A ₁ + C ₃ + D ₁ + H - Li ⁺ = B ₁ + C ₁ + C ₃ + -H + -NHSiMe ₃ - Li ⁺ = 1012.0 A ₁ + C ₂ + D ₃ - Li ⁺ = B ₁ + B ₃ + D ₂ - Li ⁺ = 1016.9
1214	A ₅ + B ₄ + D ₃ + -H - Li ⁺ = A ₅ + B ₅ + D ₂ - Li ⁺ = 1214.9
1457	A ₂ + B ₄ + C ₃ + D ₂ + H - Li ⁺ = A ₃ + C ₁ + C ₃ + C ₄ + -NHSiMe ₃ - Li ⁺ = B ₁ + B ₅ + C ₁ + C ₄ - -H + -NHSiMe ₃ - Li ⁺ = 1455.2

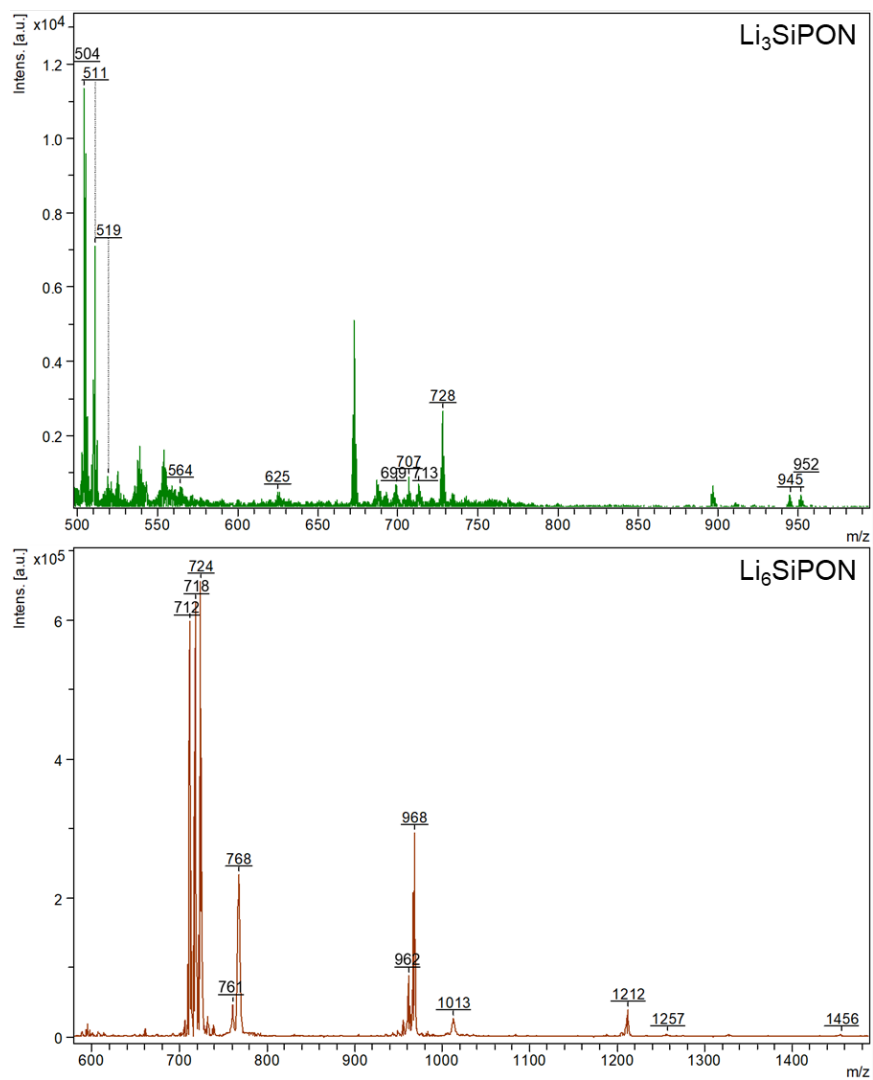


Figure A.7. Negative-ion mode MALDI of Li_3SiPON (left) and Li_6SiPON (right) precursors.

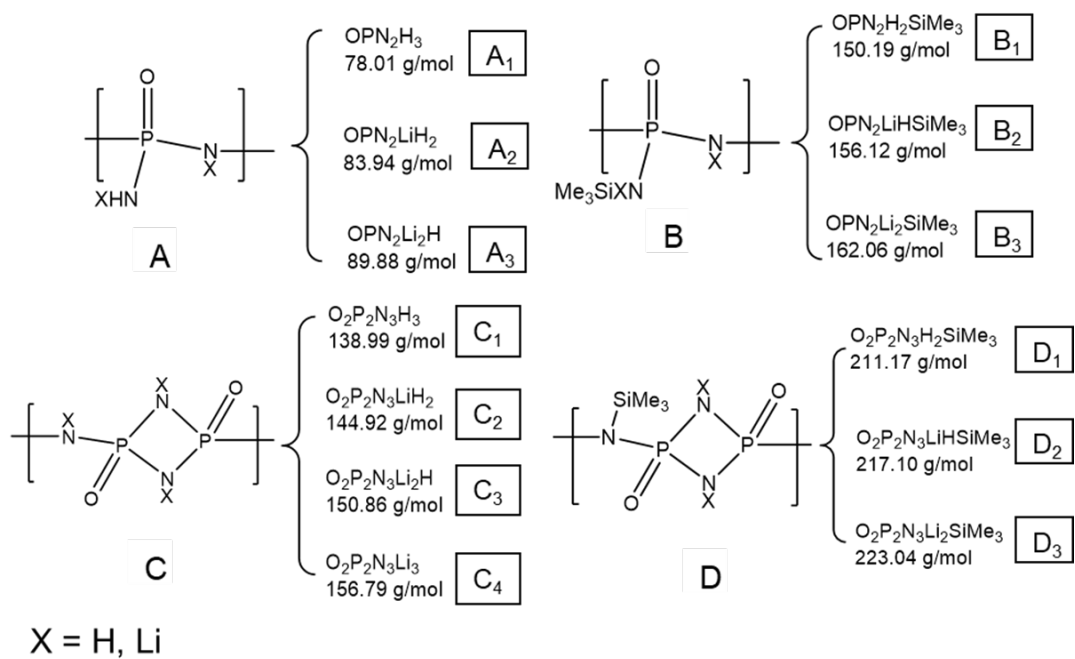


Figure A.8. Possible Li_xSiPON monomer structures.

Table A.4. Possible compositions of Li_xSiPON precursors based on Figures A.7-A.8.

Li ₃ SiPON		Li ₆ SiPON	
m/z, Da	Possible compositions	m/z, Da	Possible compositions
504	$2A_1 + 2A_3 + C_4 + -H + -NH_2 - Li^+ = A_1 +$ $2A_2 + A_3 + C_4 + -H + -NH_2 - Li^+ = 502.7$ $A_2 + 2A_3 + C_4 + -H + -NHSiMe_3 - Li^+ =$ 502.8	712	$A_1 + A_2 + 6A_3 + -H + -NH_2 - Li^+ = 711.3$ $3A_1 + A_2 + A_3 + D_3 + -H + -NHSiMe_3 - Li^+ =$ 713.2
511	$A_1 + 2C_1 + C_2 + -H + -NH_2 - Li^+ = 511.0$ $A_1 + C_1 + D_1 + -H + -NHSiMe_3 - Li^+ = B_1 +$ $2C_1 + -H + -NHSiMe_3 - Li^+ = 510.5$	718	$8A_1 + A_2 + -H + -NH_2 - Li^+ = 718.2$ $5A_1 + 2A_2 + B_1 + -H + -NH_2 - Li^+ = 718.3$
519	$2A_1 + A_2 + 3A_3 + -H + -NH_2 - Li^+ = 519.7$ $2A_2 + 2A_3 + B_3 + -H + -NH_2 - Li^+ = 519.8$	724	$4A_1 + 2A_2 + A_3 + C_2 + -H + -NH_2 - Li^+ =$ 724.8 $3A_1 + A_2 + 2A_3 + C_2 + -H + -NHSiMe_3 - Li^+$ $= 725.0$
564	$A_1 + 2A_3 + C_3 + C_3 + -H + -NH_2 - Li^+ =$ 563.6 $A_2 + A_3 + C_3 + C_4 + -H + -NHSiMe_3 - Li^+ =$ 563.8	761	$A_1 + A_2 + 3A_3 + B_3 + C_4 + -H + -NH_2 - Li^+ =$ 760.5
625	$A_3 + B_2 + C_1 + C_4 + -H + -NHSiMe_3 - Li^+ =$ 624.1 $A_2 + A_3 + C_1 + 2C_3 + -H + -NH_2 - Li^+ =$ 624.6	768	$A_1 + A_2 + B_1 + B_2 + C_1 + C_3 + -H + -NH_2 -$ $Li^+ = 768.3$ $A_1 + B_2 + B_3 + C_1 + C_3 + -H + -NHSiMe_3 -$ $Li^+ = 768.4$
699	$A_1 + 3A_2 + 4A_3 + -H + -NH_2 - Li^+ = 699.5$	962	$5A_1 + 3C_1 + C_2 + -H + -NH_2 - Li^+ = 962.0$ $2A_1 + B_1 + 2C_1 + C_2 + D_3 + -H + -NH_2 - Li^+$ $= 962.2$
707	$3A_1 + 2A_2 + D_3 + -H + -NHSiMe_3 - Li^+ =$ 707.3	968	$2A_1 + A_2 + B_2 + 3C_1 + C_2 + -H + -NH_2 - Li^+$ $= 968.1$ $2A_1 + B_2 + 2C_1 + C_2 + D_3 + -H + -NH_2 - Li^+$ $= 968.2$
713	$2A_1 + 2A_2 + A_3 + C_1 + C_3 + -H + -NH_2 - Li^+$ $= 713.8$	1013	$A_1 + 3C_1 + 2C_2 + D_2 + -H + -NH_2 - Li^+ =$ 1012.0
728	$2A_1 + 3C_1 + C_2 + -H + -NH_2 - Li^+ = A_1 +$ $2C_1 + C_2 + D_2 + -H + -NH_2 - Li^+ = 728.0$ $B_1 + 2C_1 + 2C_2 + -H + -NH_2 - Li^+ = A_1 +$ $2C_1 + C_3 + D_1 + -H + -NH_2 - Li^+ = 728.2$	1212	$2A_1 + A_2 + 6A_3 + 2C_1 + C_2 + -H + -NH_2 -$ $Li^+ = 1212.2$
945	$3A_1 + 4C_1 + C_2 + -H + -NH_2 - Li^+ = 945.0$	1257	$3A_1 + B_1 + B_3 + 4C_1 + C_2 + -H + -NH_2 - Li^+$ $= 1257.3$
952	$11A_1 + A_2 + -H + -NH_2 - Li^+ = 952.2$ $6A_1 + 2A_2 + B_1 + B_2 + -H + -NH_2 - Li^+ =$ 952.4	1456	$A_1 + A_2 + 4A_3 + 3C_1 + 2C_2 + D_2 + -H + -$ $NH_2 - Li^+ = 1455.5$ $2A_1 + 2A_2 + 10A_3 + D_3 + -H + -NH_2 - Li^+ =$ 1455.8

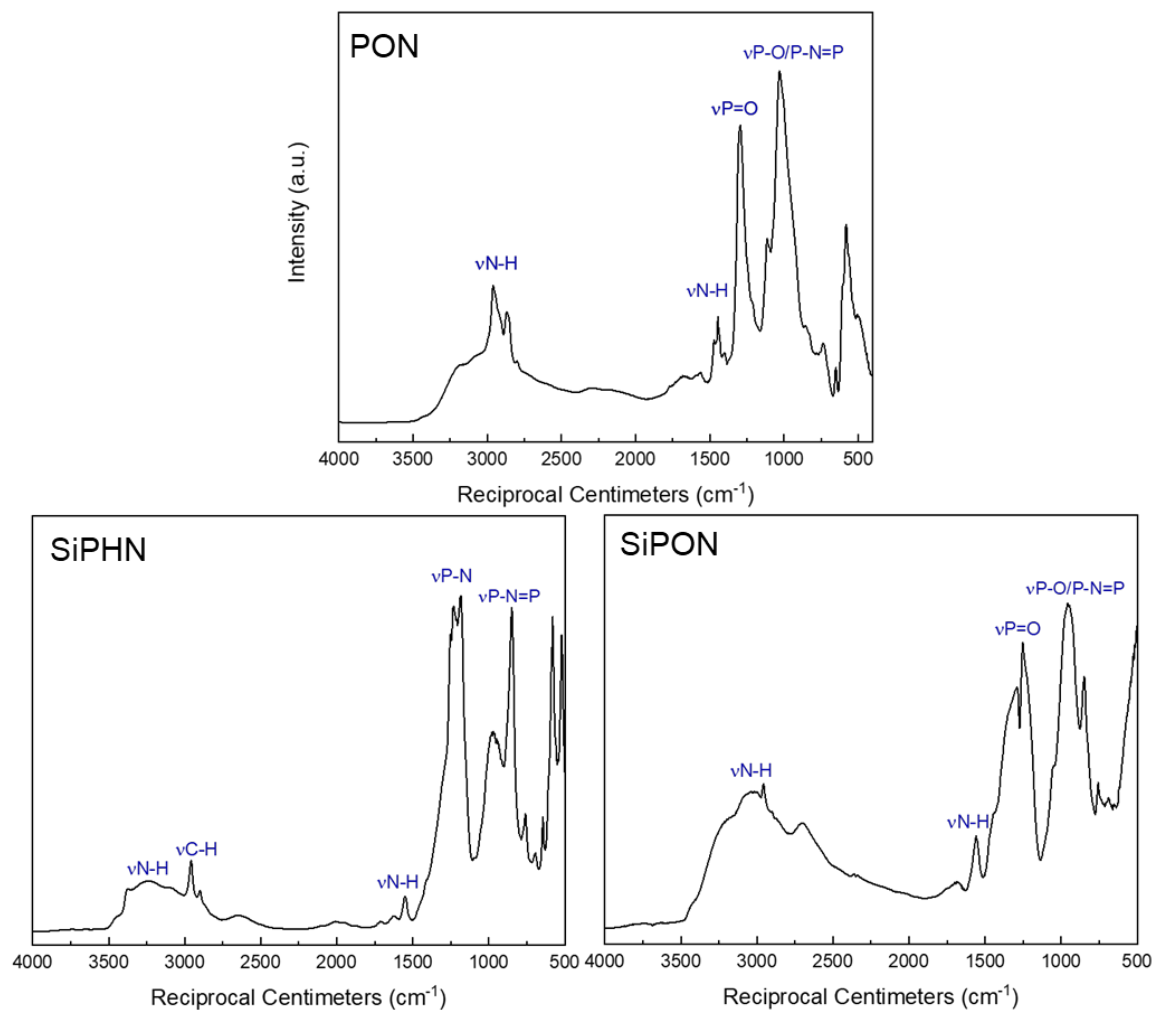


Figure A.9. FTIR spectra of un lithiated PON, SiPHN and SiPON precursors.

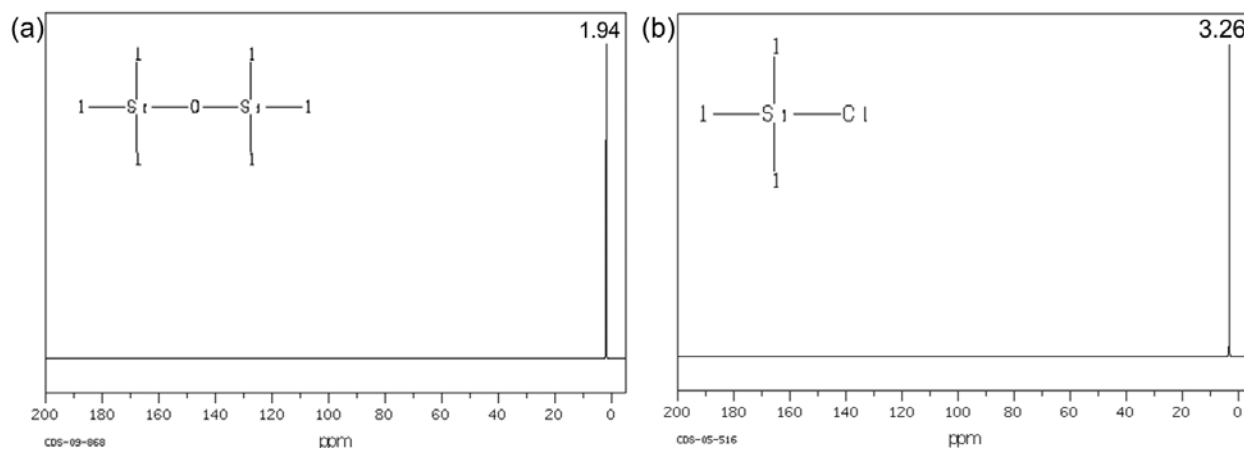


Figure A.10. ^{13}C NMR of **a.** $(\text{Me}_3\text{Si})_2\text{O}$ and **b.** Me_3SiCl from Chemical Book database. Solvent: CDCl_3 .

Table A.5. Electronegativity of selected elements.

Element	Electronegativity
H	2.20
Li	0.98
C	2.55
N	3.04
O	3.44
Si	1.90
P	2.19
Cl	3.16

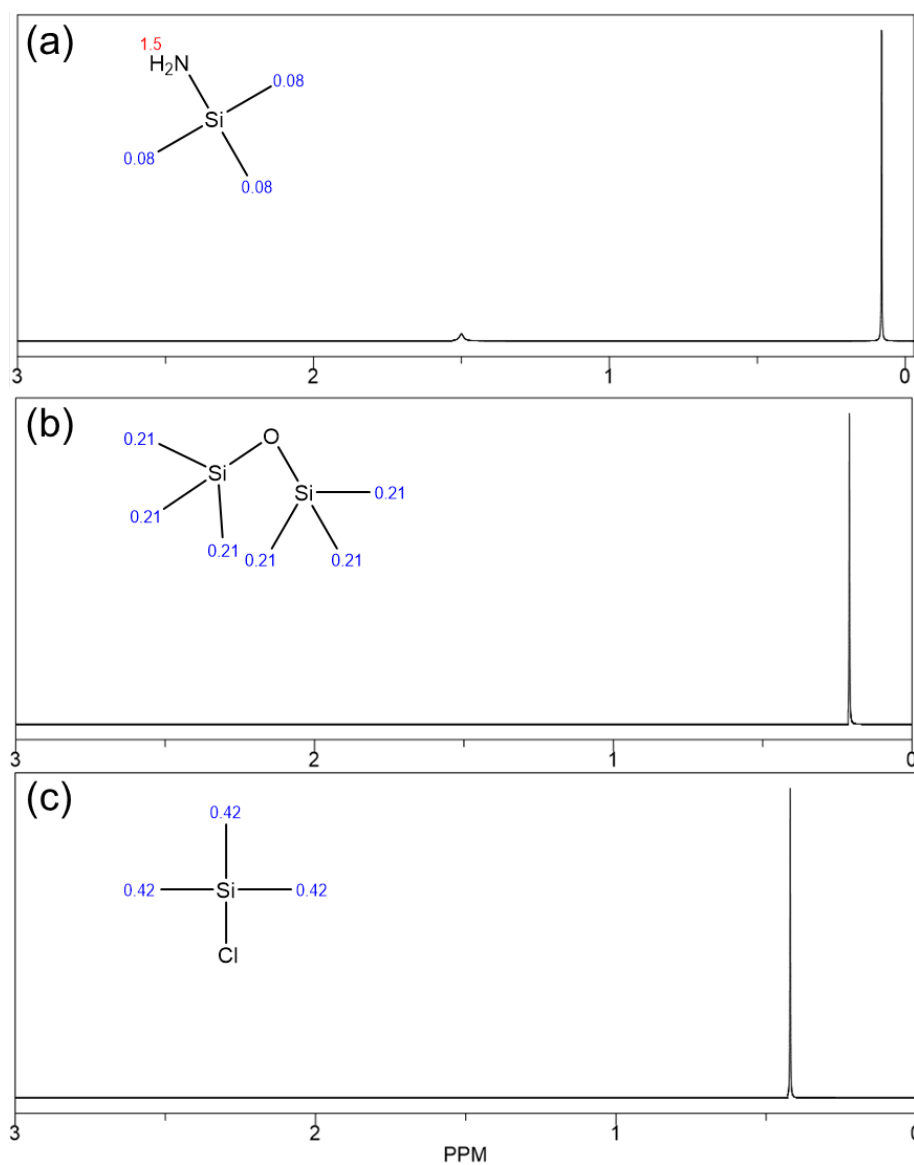


Figure A.11. ^1H NMR models of **a.** Me_3SiNH_2 , **b.** $(\text{Me}_3\text{Si})_2\text{O}$, and **c.** Me_3SiCl by ChemDraw.

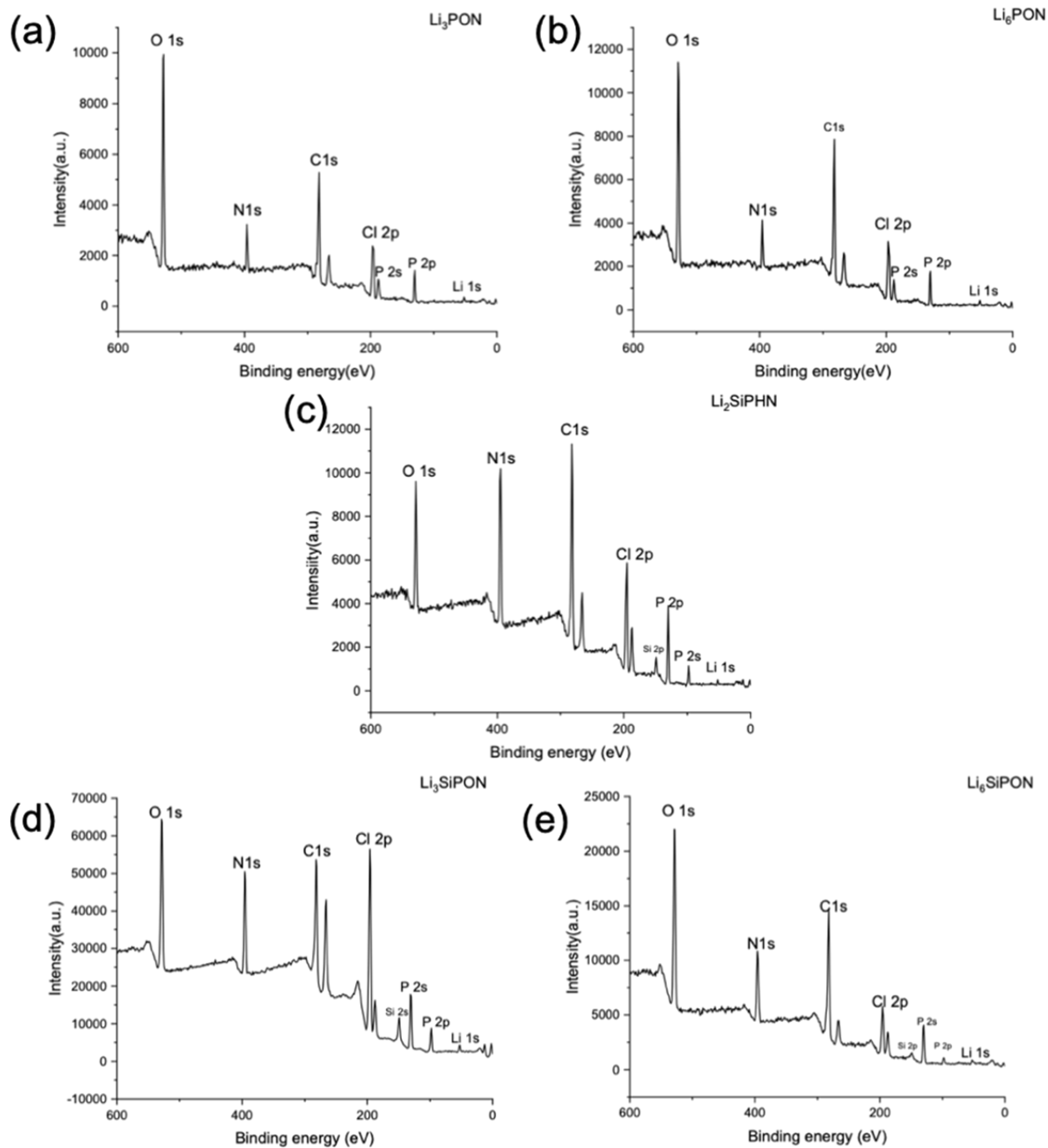


Figure A.12. Wide-scan survey XPS spectra (600 to 0 eV) of Li_3PON (a), Li_6PON (b), Li_2SiPHN (c), Li_3SiPON (d), and Li_6SiPON (e) pellets (RT/vacuum dried).

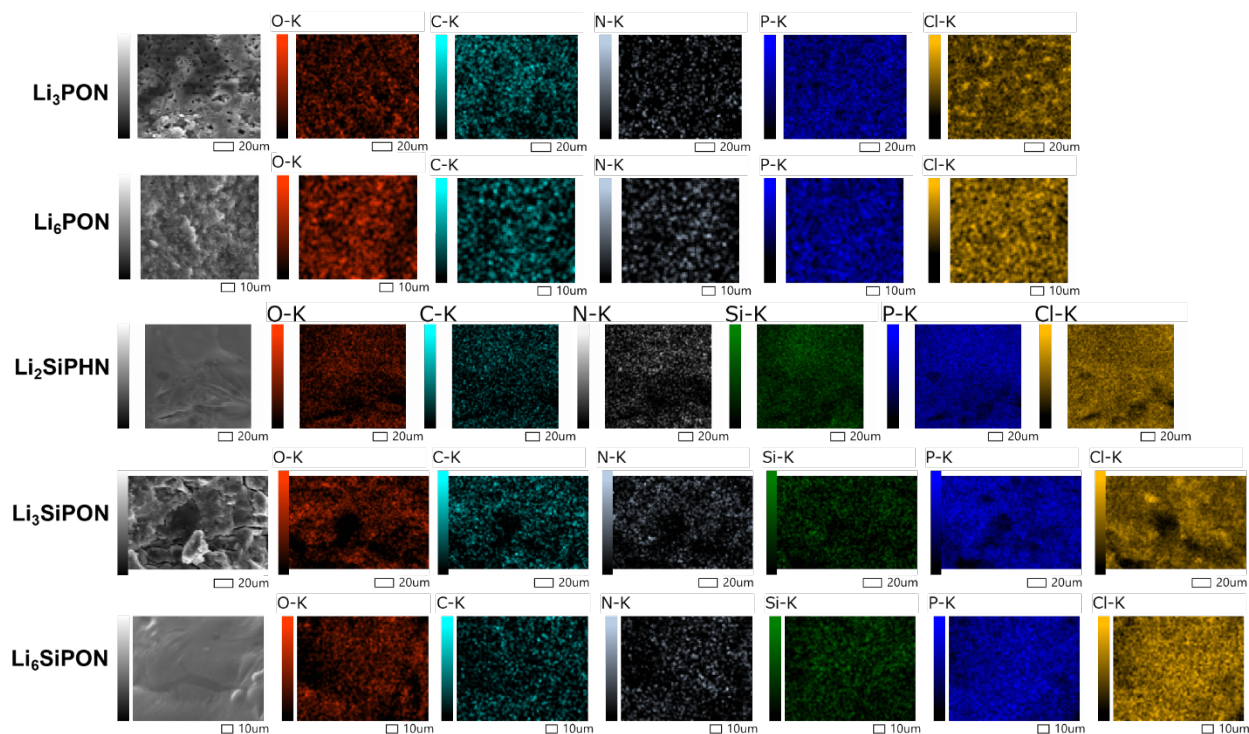


Figure A.13. EDX map images of Li_xPON , Li_2SiPHN and Li_xSiPON pellets heated to $100\text{ }^\circ\text{C}/2\text{ h}/\text{N}_2$.

Table A.6. Atomic ratios based on EDX analyses for Li_xPON , Li_2SiPHN and Li_xSiPON after heating to various temperatures for 2 h.

Heating temp. ($^\circ\text{C}$)	Li_3PON		Li_6PON		Li_2SiPHN		Li_3SiPON		Li_6SiPON	
	O/P	N/P	O/P	N/P	Si/P	N/P	Si/P	N/P	Si/P	N/P
100	7.7 ± 0.03	1 ± 0.04	5.9 ± 0.04	1.8 ± 0.06	0.4 ± 0.03	3.5 ± 0.01	0.2 ± 0.06	2.6 ± 0.03	0.3 ± 0.04	2.8 ± 0.06
200	6.2 ± 0.1	2.6 ± 0.07	3.7 ± 0.03	2.2 ± 0.07	0.3 ± 0.08	4.2 ± 0.04	0.1 ± 0.03	2.4 ± 0.05	0.2 ± 0.07	3.7 ± 0.08
300	3.5 ± 0.08	3.6 ± 0.02	2.4 ± 0.09	2.8 ± 0.04	0.1 ± 0.08	4.5 ± 0.02	0.05 ± 0.02	3.4 ± 0.04	0.1 ± 0.02	4.1 ± 0.1
400	2.8 ± 0.05	4.2 ± 0.04	6.4 ± 0.02	3.7 ± 0.04	0.1 ± 0.03	4.8 ± 0.05	0.01 ± 0.02	4.1 ± 0.04	0.08 ± 0.04	4.4 ± 0.02



Figure A.14. Optical image of PEO (60 wt.%) / polymer precursor films.

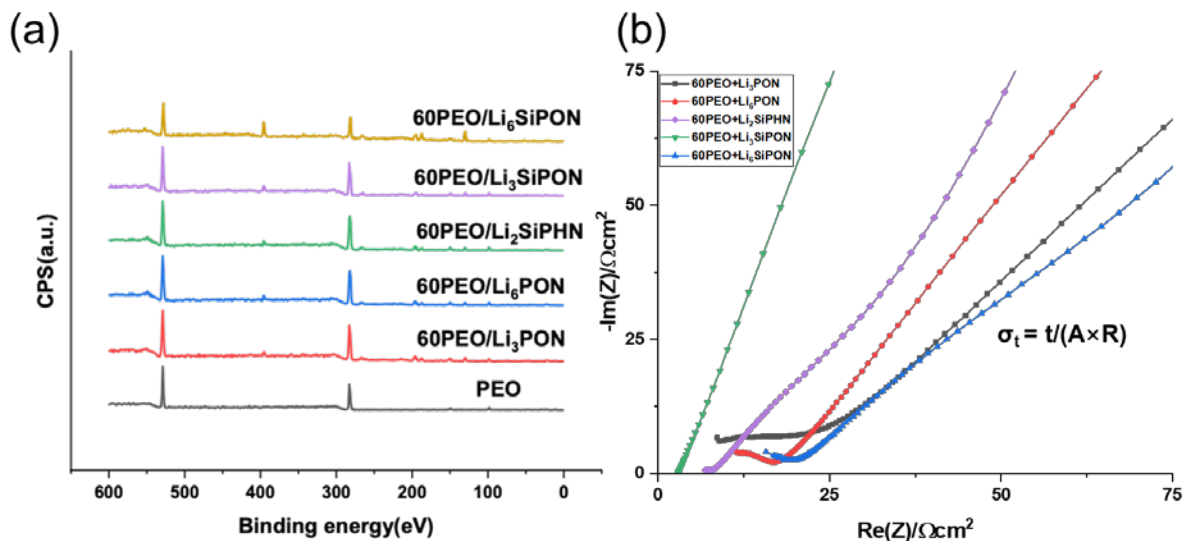


Figure A.15a. XPS Spectra (600 to 0 eV) of PEs and the PEO film, and b. Nyquist plots of PEs at ambient.

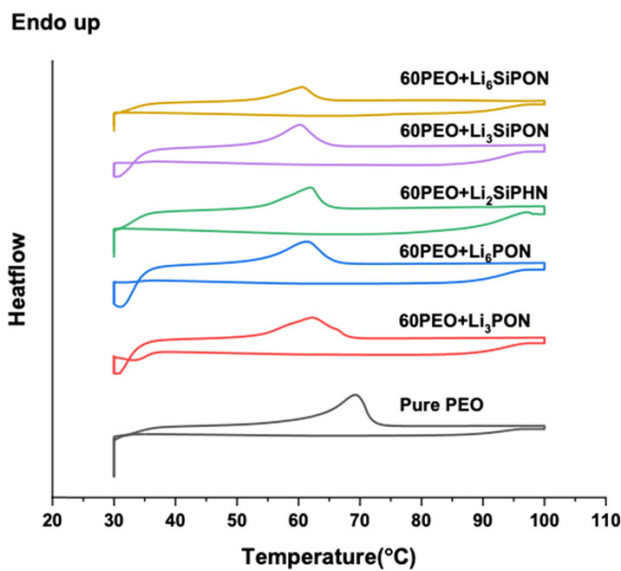


Figure A.16. DSC thermograms of pristine PEO and PE films after the 3rd cycle.

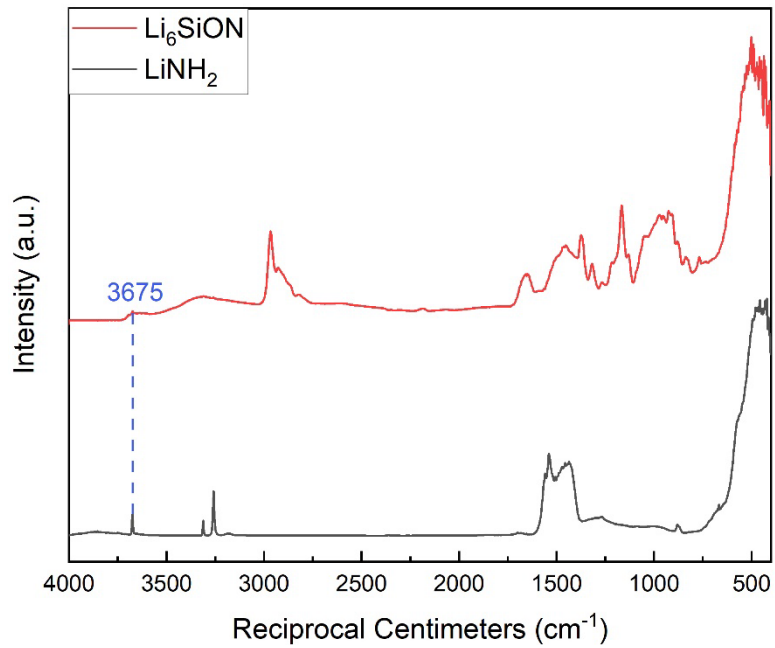


Figure A.17. FTIRs of Li_6SiON (dried at 60 °C/1 h/vacuum) and LiNH_2 .

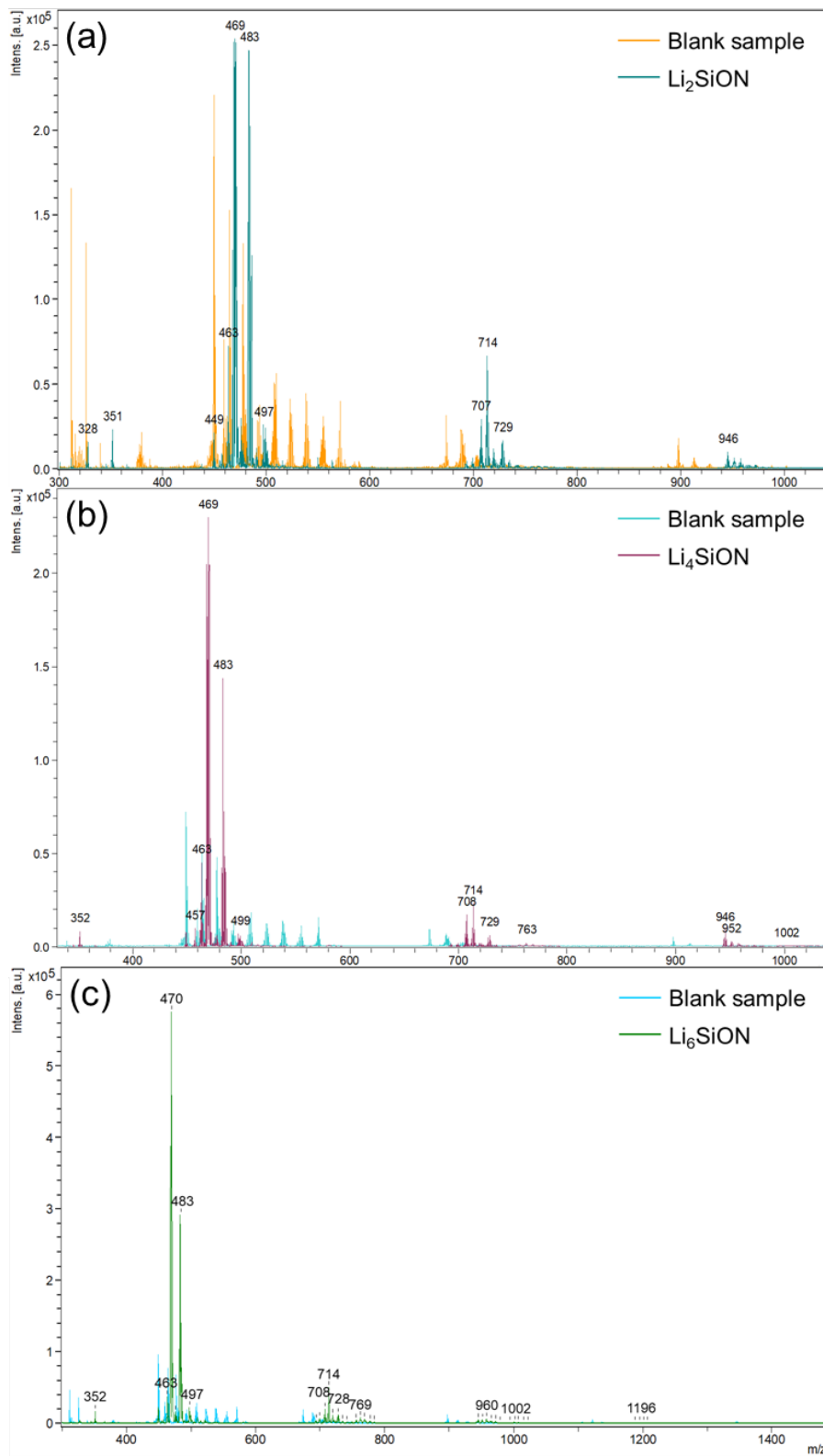


Figure A.18. Negative-ion mode MALDI of blank vs Li_xSiON precursors, **a.** Li_2SiON , **b.** Li_4SiON and **c.** Li_6SiON .

Table A.7. Possible compositions of Li_xSiON precursors based on MALDI.[†]

Precursor	Positive-ion mode			Negative-ion mode		
	Group	m/z	Calculation	Group	m/z	Calculation
Li_2SiON	I	342	$\text{S} + 2\text{A} + 7\text{L} = 341.0$	I	328	$\text{S} + 2\text{A} + 5\text{L} = 327.2$
		472	$\text{S} + 8\text{A} + 12\text{L} = 471.8$		351	$\text{S} + 3\text{A} + 6\text{L} = 350.1$
	II	484	$\text{S} + 7\text{A} + 16\text{L} = 483.6$	II	449	$\text{S} + 10\text{A} + 4\text{L} = 448.4$
		505	$\text{S} + 11\text{A} + 10\text{L} = 506.1$		463	$\text{S} + 7\text{A} + 13\text{L} = 462.8$
		539	$\text{S} + 10\text{A} + 17\text{L} = 538.6$		469	$\text{S} + 10\text{A} + 7\text{L} = 469.2$
		555	$\text{S} + 11\text{A} + 17\text{L} = 554.6$		483	$\text{S} + 10\text{A} + 9\text{L} = 483.1$
	III	722	$2\text{S} + 10\text{A} + 6\text{L} = 722.7$	III	497	$\text{S} + 10\text{A} + 11\text{L} = 497.0$
		728	$2\text{S} + 9\text{A} + 9\text{L} = 727.5$		707	$2\text{S} + 9\text{A} + 6\text{L} = 706.6$
		767	$2\text{S} + 11\text{A} + 10\text{L} = 766.5$		714	$2\text{S} + 9\text{A} + 7\text{L} = 713.6$
		773	$2\text{S} + 11\text{A} + 11\text{L} = 773.4$		729	$2\text{S} + 10\text{A} + 7\text{L} = 729.6$
	IV	960	$3\text{S} + 6\text{A} + 12\text{L} = 960.6$	IV	946	$3\text{S} + 9\text{A} + 3\text{L} = 946.2$
		966	$3\text{S} + 5\text{A} + 15\text{L} = 965.4$			
		1012	$3\text{S} + 7\text{A} + 17\text{L} = 1011.4$			
Li_4SiON	I	314	$\text{S} + 2\text{A} + 3\text{L} = 313.3$	I	352	$\text{S} + 4\text{A} + 4\text{L} = 352.2$
		352	$\text{S} + 4\text{A} + 4\text{L} = 352.2$		457	$\text{S} + 8\text{A} + 10\text{L} = 458.0$
	II	472	$\text{S} + 8\text{A} + 12\text{L} = 471.8$	II	463	$\text{S} + 7\text{A} + 13\text{L} = 462.8$
		478	$\text{S} + 8\text{A} + 13\text{L} = 478.8$		469	$\text{S} + 10\text{A} + 7\text{L} = 469.2$
		484	$\text{S} + 7\text{A} + 16\text{L} = 483.6$		483	$\text{S} + 10\text{A} + 9\text{L} = 483.1$
		722	$2\text{S} + 10\text{A} + 6\text{L} = 722.7$		499	$\text{S} + 11\text{A} + 9\text{L} = 499.1$
	III	728	$2\text{S} + 9\text{A} + 9\text{L} = 727.5$	III	708	$2\text{S} + 6\text{A} + 13\text{L} = 707.2$
		738	$2\text{S} + 11\text{A} + 6\text{L} = 738.7$		714	$2\text{S} + 9\text{A} + 7\text{L} = 713.6$
		767	$2\text{S} + 11\text{A} + 10\text{L} = 766.5$		729	$2\text{S} + 10\text{A} + 7\text{L} = 729.6$
		960	$3\text{S} + 6\text{A} + 12\text{L} = 960.6$		763	$2\text{S} + 9\text{A} + 14\text{L} = 762.2$
	IV	966	$3\text{S} + 5\text{A} + 15\text{L} = 965.4$	IV	946	$3\text{S} + 9\text{A} + 3\text{L} = 946.2$
		1006	$3\text{S} + 8\text{A} + 14\text{L} = 1006.6$		952	$3\text{S} + 5\text{A} + 13\text{L} = 951.6$
		1204	$4\text{S} + 8\text{A} + 5\text{L} = 1204.5$		1002	$3\text{S} + 9\text{A} + 11\text{L} = 1001.8$
	V	1251	$4\text{S} + 7\text{A} + 14\text{L} = 1250.9$			
Li_6SiON	I	472	$\text{S} + 8\text{A} + 12\text{L} = 471.8$	I	352	$\text{S} + 4\text{A} + 4\text{L} = 352.2$
		478	$\text{S} + 8\text{A} + 13\text{L} = 478.8$		463	$\text{S} + 7\text{A} + 13\text{L} = 462.8$
		484	$\text{S} + 7\text{A} + 16\text{L} = 483.6$		470	$\text{S} + 10\text{A} + 7\text{L} = 469.2$
	II	722	$2\text{S} + 10\text{A} + 6\text{L} = 722.7$	II	483	$\text{S} + 10\text{A} + 9\text{L} = 483.1$
		728	$2\text{S} + 9\text{A} + 9\text{L} = 727.5$		497	$\text{S} + 10\text{A} + 11\text{L} = 497.0$
		767	$2\text{S} + 11\text{A} + 10\text{L} = 766.5$		708	$2\text{S} + 6\text{A} + 13\text{L} = 707.2$
	III	960	$3\text{S} + 6\text{A} + 12\text{L} = 960.6$	III	714	$2\text{S} + 9\text{A} + 7\text{L} = 713.6$
		965	$3\text{S} + 8\text{A} + 8\text{L} = 964.9$		728	$2\text{S} + 9\text{A} + 9\text{L} = 727.5$
		1006	$3\text{S} + 8\text{A} + 14\text{L} = 1006.6$		769	$2\text{S} + 9\text{A} + 15\text{L} = 769.1$
		1198	$4\text{S} + 5\text{A} + 11\text{L} = 1198.1$		960	$3\text{S} + 6\text{A} + 12\text{L} = 960.6$
	IV	1244	$4\text{S} + 7\text{A} + 13\text{L} = 1244.0$	IV	1002	$3\text{S} + 9\text{A} + 11\text{L} = 1001.8$
		1436	$5\text{S} + 4\text{A} + 10\text{L} = 1435.5$		V	1196

[†] S = spiroxiloxane, A = $-\text{NH}_2$, L = Li^+ . All possible compositions are calculated by Python program *MALDI-Calculaton* (see Appendix B): <https://github.com/haveamission/MALDI-Calculaton>.

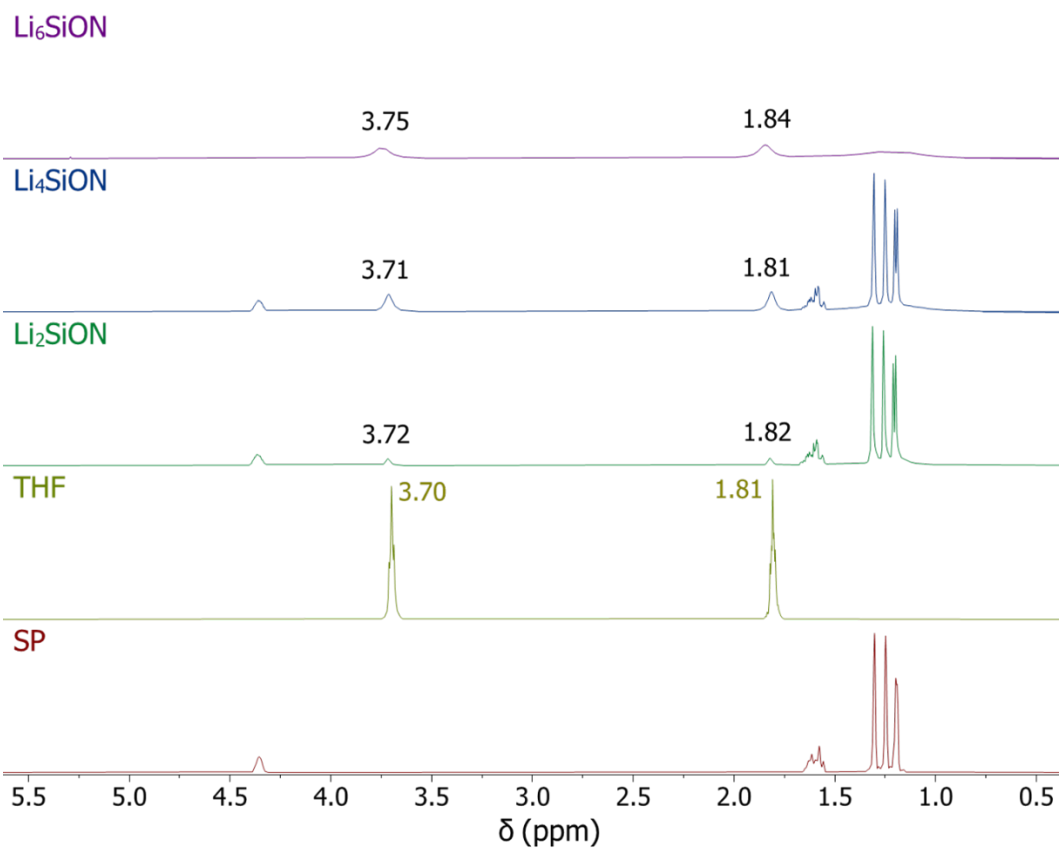


Figure A.19. ^1H NMRs of Li_xSiON precursors (RT/1 h/vacuum), THF and SP.

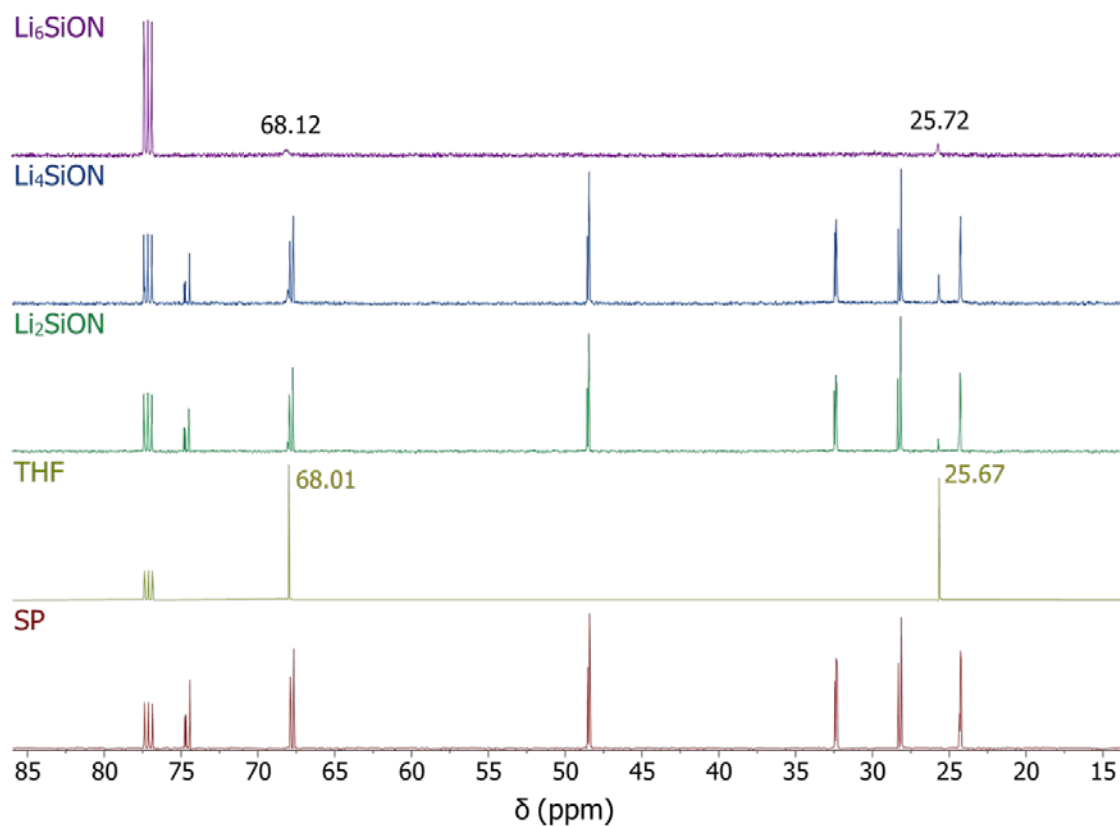


Figure A.20. ^{13}C NMRs of Li_xSiON precursors (RT/1 h/vacuum), THF and SP.

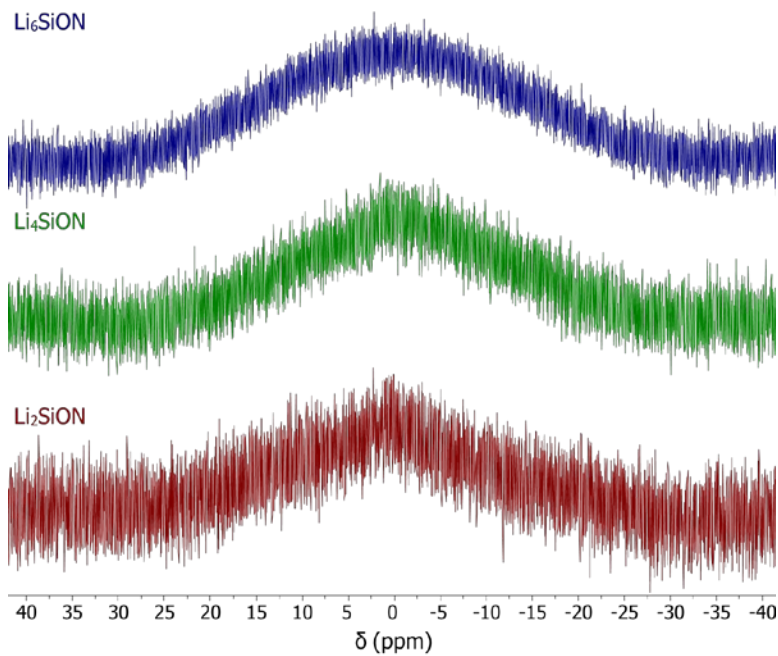


Figure A.21. ^7Li NMRs of Li_xSiON precursors (60 °C/24 h/vacuum).

(a) Li_6SiON

(b) Li_6SiON

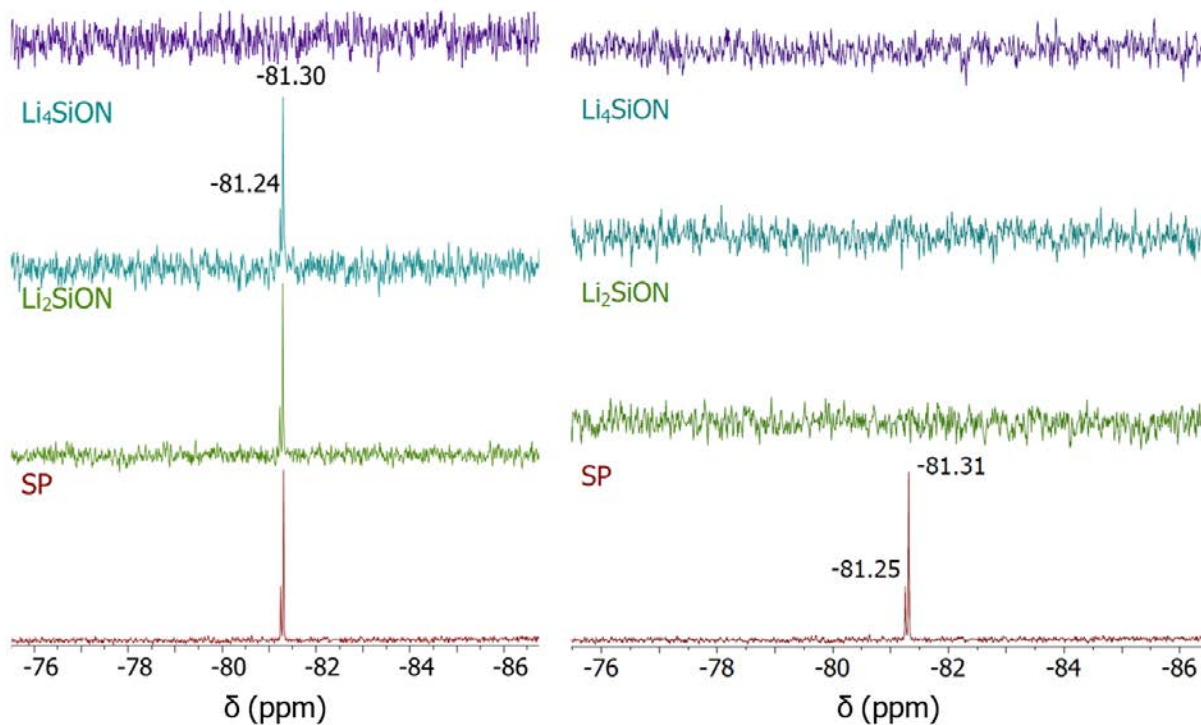


Figure A.22. ^{29}Si NMRs of Li_xSiON precursors dried at **a.** RT/1 h/vacuum and **b.** 60 °C/24 h/vacuum.

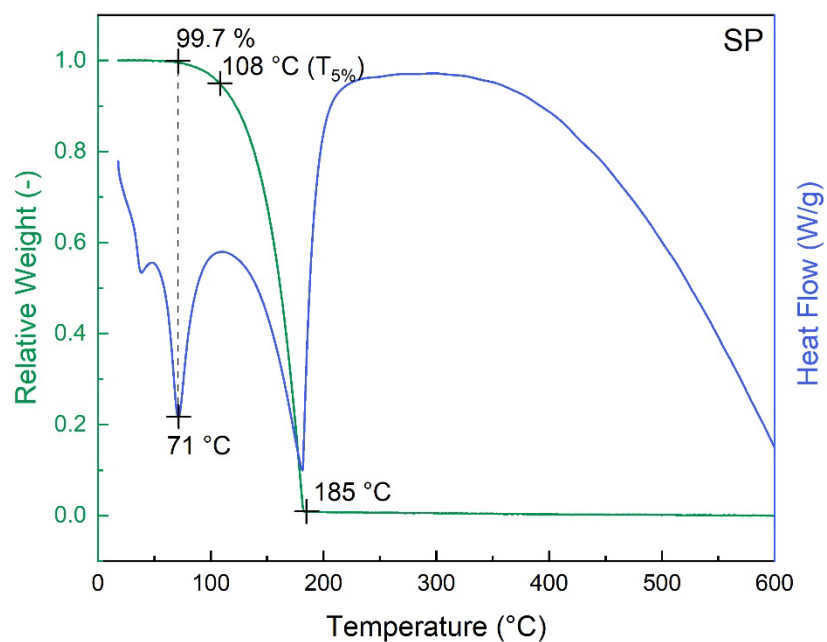


Figure A.23. TGA-DTA (600 °C/10 °C $\text{min}^{-1}/\text{N}_2$) of SP (60 °C/12 h/vacuum).

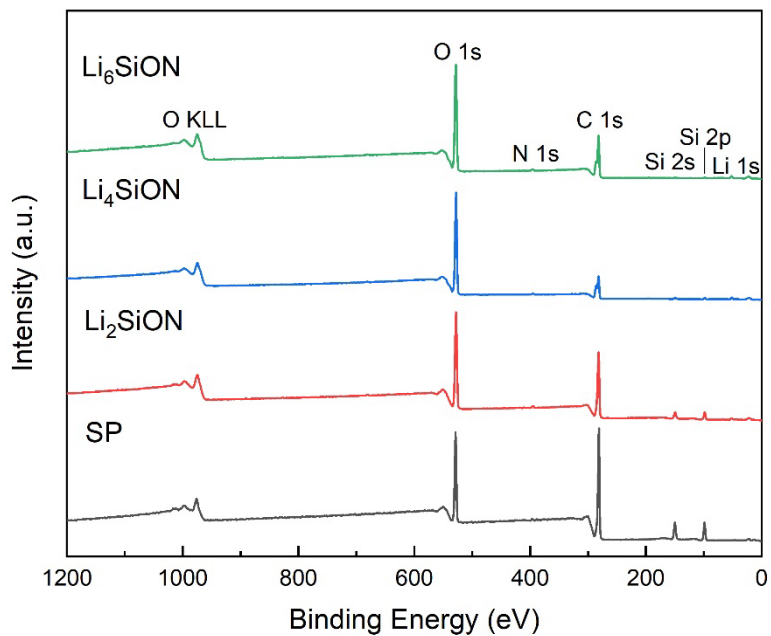


Figure A.24. Wide-scan survey XPS spectra of Li_xSiON precursors dried at RT/1 h/vacuum compared to SP (60 °C/12 h/vacuum).

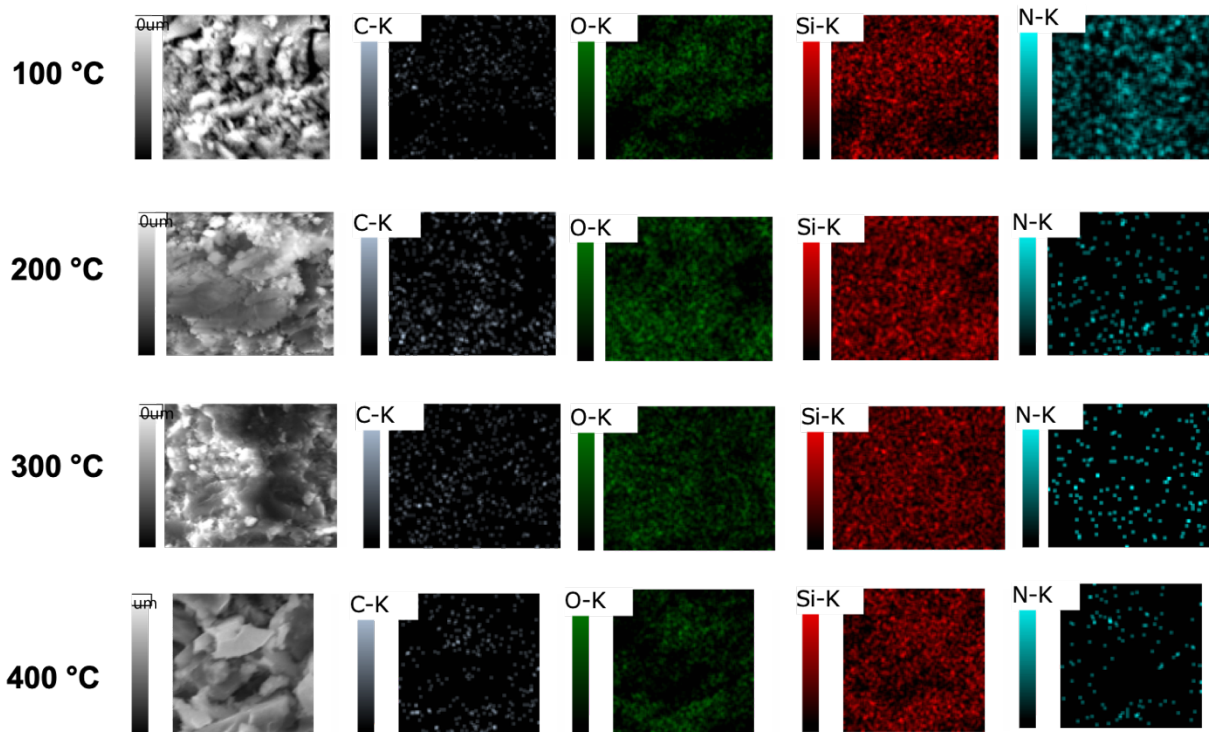


Figure A.25. EDX map of Li_2SiON pellets heated to 100-400 °C/2 h/ N_2 .

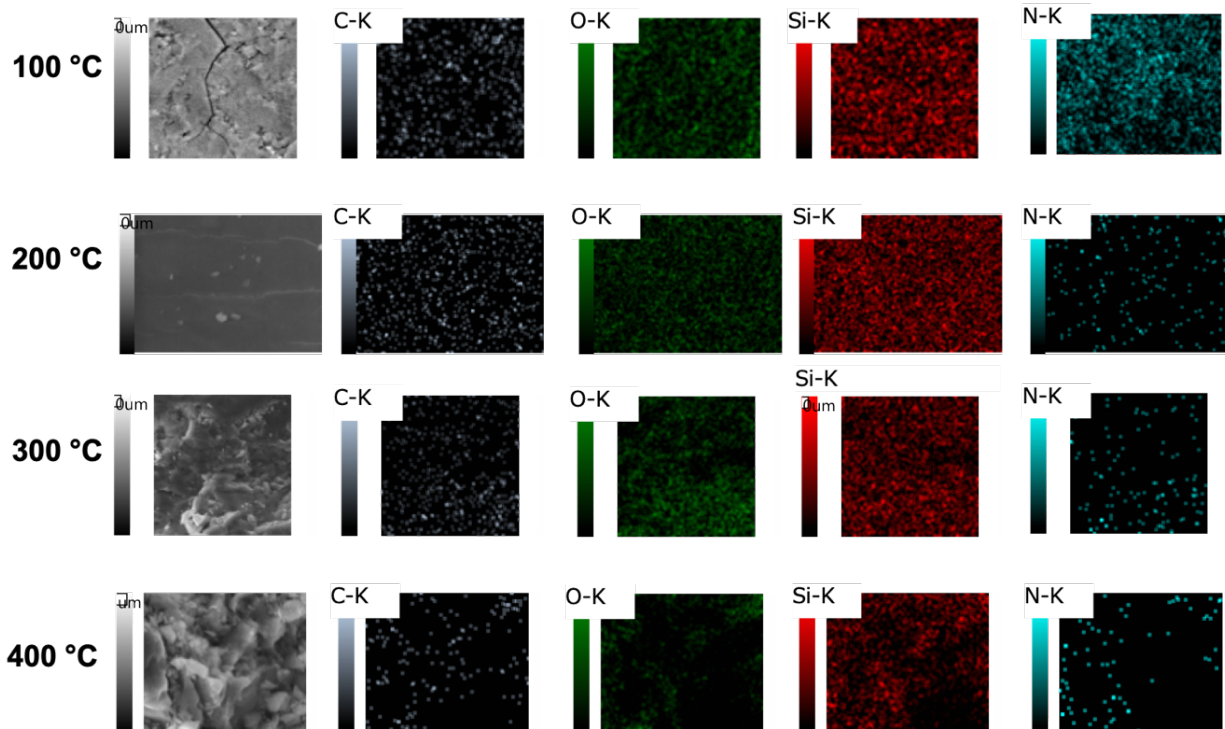


Figure A.26. EDX map of Li_4SiON pellets heated to 100-400 °C/2 h/ N_2 .

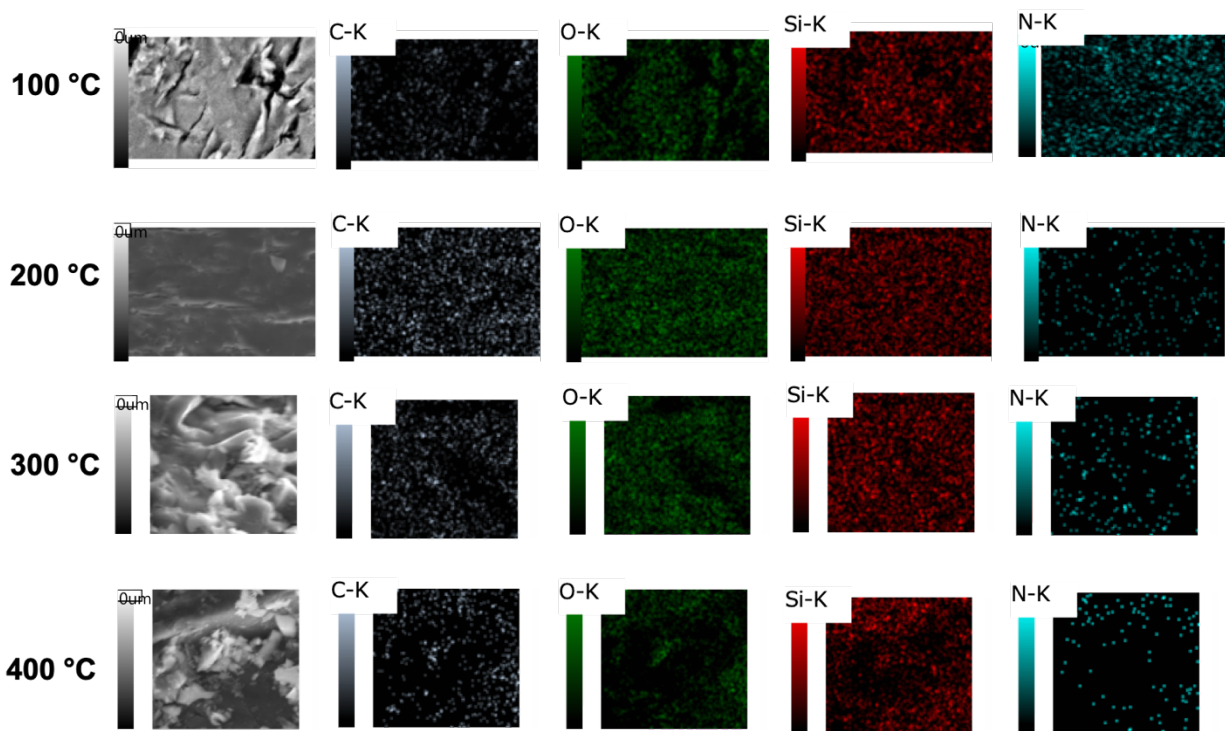


Figure A.27. EDX map of Li_6SiON pellets heated to 100-400 °C/2 h/ N_2 .

Table A.8. Average atomic percentage (At.%) of Li_xSiON pellets based on EDX analyses.

Precursor pellet	Temp. ($^{\circ}\text{C}/2\text{ h}$)	At. %			
		C	N	O	Si
Li_2SiON	100	23.2	1.8	65.2	9.8
	200	22.3	1.2	67.5	9.0
	300	21.7	1.0	67.0	10.3
	400	19.7	0.5	67.4	12.4
Li_4SiON	100	27.5	1.7	64.2	6.6
	200	27.2	1.0	62.7	8.9
	300	23.6	0.5	67.5	8.4
	400	21.6	0.2	68.0	10.2
Li_6SiON	100	31.6	1.1	61.6	5.7
	200	31.4	1.3	62.0	5.3
	300	30.1	0.7	64.8	4.4
	400	28.5	0.2	65.0	6.3

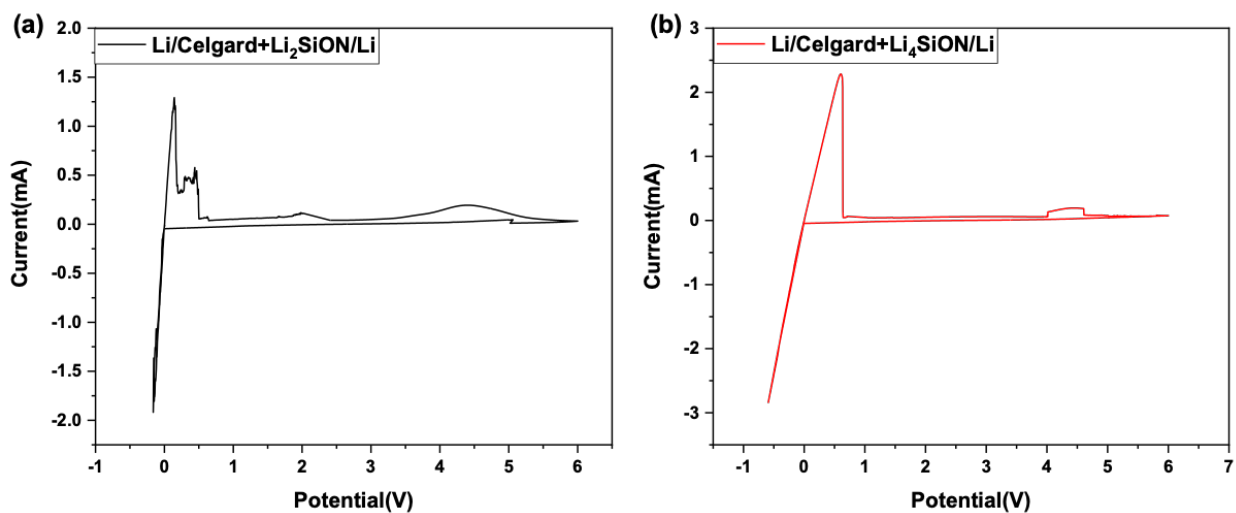


Figure A.28. CV plots of **a.** Li/Celgard + $\text{Li}_2\text{SiON}/\text{SS}$ and **b.** Li/Celgard + $\text{Li}_4\text{SiON}/\text{SS}$ at sweep rate of 1 mV/sec.

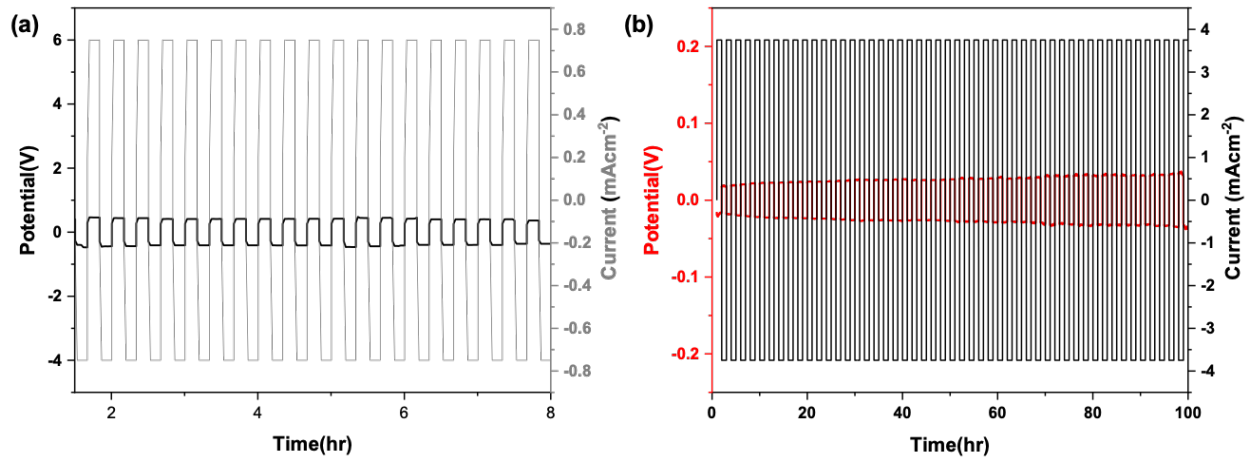


Figure A.29. Galvanostatic cycling of **a.** Li/Celgard + $\text{Li}_2\text{SiON}/\text{Li}$ and **b.** Li/Celgard + $\text{Li}_4\text{SiON}/\text{Li}$ at ambient.

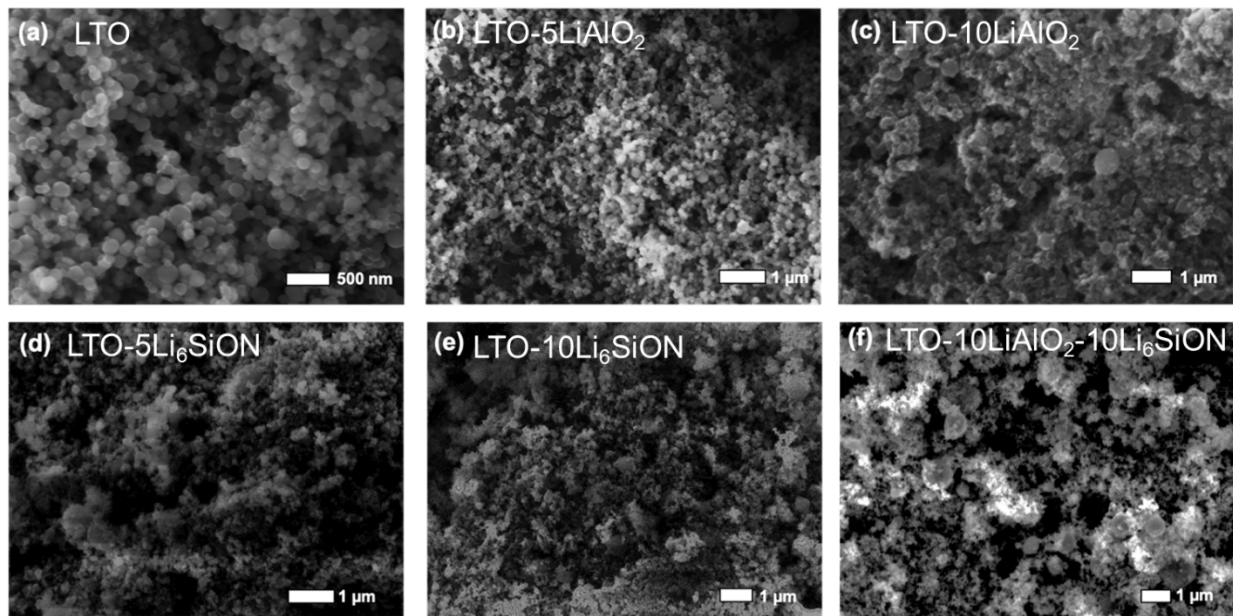


Figure A.30. SEM images of LTO and LTO-composite powders.

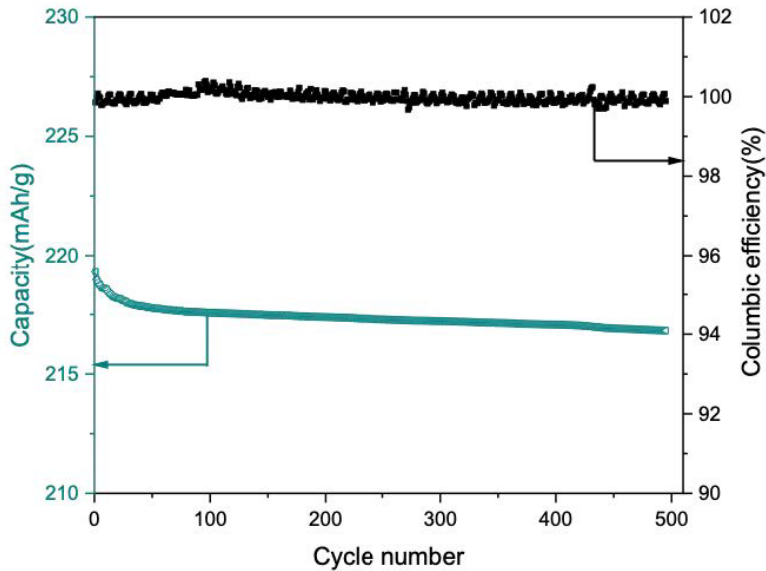


Figure A.31. Long-term cycling stability of LTO-5LiAlO₂-10Li₆SiON/Li half-cell at 5 C.

Table A.9. Diffusivities and potential gap for pristine and composite LTO electrodes.

Electrodes	D_{Li} (cm ² /s)	$\Delta\phi_p$ (mV)
LTO-pristine	$4.6 \pm 0.5 \times 10^{-14}$	400
LTO-5LiAlO ₂	$6.1 \pm 0.7 \times 10^{-13}$	340
LTO-10LiAlO ₂	$4.8 \pm 0.2 \times 10^{-14}$	410
LTO-5Li ₆ SiON	$6.7 \pm 0.6 \times 10^{-14}$	380
LTO-10Li ₆ SiON	$1.2 \pm 0.3 \times 10^{-12}$	320
LTO-5LiAlO ₂ - 5Li ₆ SiON	$2.3 \pm 0.3 \times 10^{-13}$	300
LTO-5LiAlO ₂ - 10Li ₆ SiON	$2.7 \pm 0.3 \times 10^{-12}$	290
LTO-10LiAlO ₂ - 5Li ₆ SiON	$3.0 \pm 0.5 \times 10^{-14}$	350
LTO-10LiAlO ₂ - 10Li ₆ SiON	$1.3 \pm 0.6 \times 10^{-14}$	370

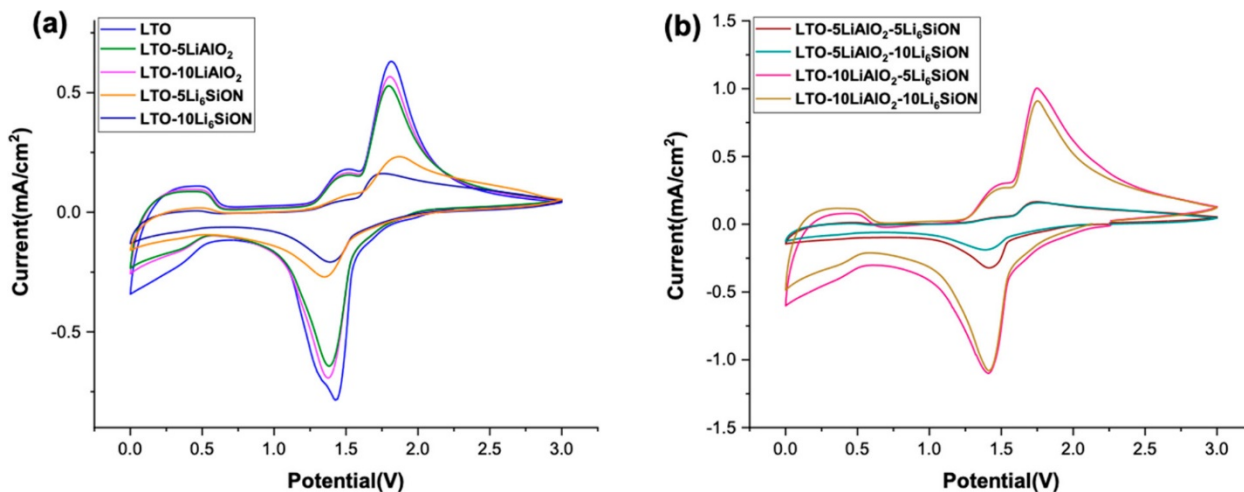


Figure A.32. CV plots of the LTO-pristine, LTO-LiAlO₂, and LTO-Li₆SiON (a) and LTO-LiAlO₂-Li₆SiON (b) half-cells.

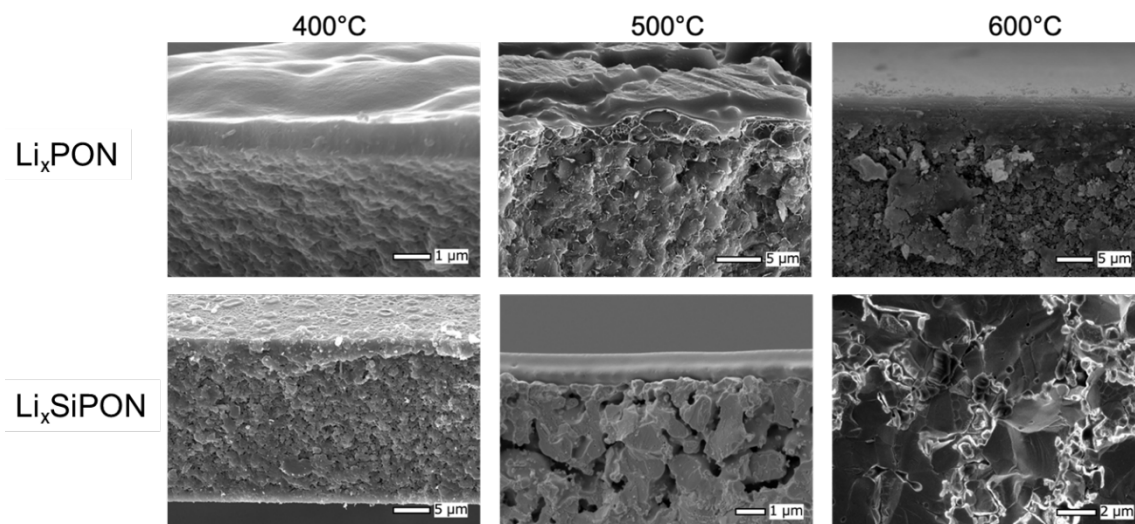


Figure A.33. SEM fracture surface images of LATSP + LiPON -like precursor films heated to 400°, 500° and 600 °C/2 h/ N_2 .

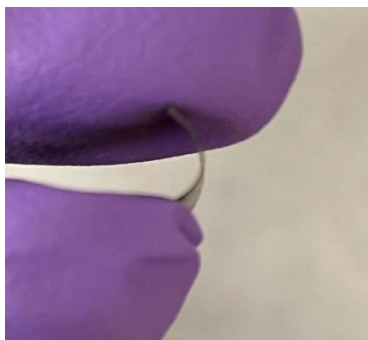


Figure A.34. Example optical image of a $\text{Li}_x\text{SiO-5TEA}$ pellet.

Appendix B. MALDI-Calculatation

The below Python program was developed by Andrew Alexander as a tool to calculate polymer precursor structures based on MALDI-ToF study. Two files are included, one is the configuration and data set (JSON format) which needs manual inputs according to the polymer structures, the other one is the program file.

An example structural calculation of a Li₃PON peak from MALDI-ToF is given below. Please note that this program is under constant improvement; the newest version and instructions can be found at: <https://github.com/haveamission/MALDI-Calculatation>.

The program is licensed under Creative Commons Non-Commercial ShareAlike 4.0 International; third party contributions are welcomed.

File 1, configuration and data set:

```
{  
    "monomer_weight": {"A1": 78.01, "A2": 83.94, "A3": 89.88, "C1": 138.99, "C2":  
144.92, "C3": 150.86, "C4": 156.79},  
    "polymer_weight": [699],  
    "range_bottom": 2,  
    "range_top": 7,  
    "error_number": 3  
}
```

File 2, main program:

```
import itertools
```

```
import json
```

```
class MolecularWeight:
```

```
    def __init__(self):
```

```
        filename = input("Enter filename: ")
```

```
        if filename:
```

```
            datastore = self.load_file(filename)
```

```
        else:
```

```
            datastore = self.load_file("default_dataset.json")
```

```
        self.monomer_weight = datastore["monomer_weight"]
```

```
        self.monomer_weight_keys = self.monomer_weight.keys()
```

```
        self.polymer_weight = datastore["polymer_weight"]
```

```
        self.range_bottom = datastore["range_bottom"]
```

```
        self.range_top = datastore["range_top"]
```

```
        self.error_number = datastore["error_number"]
```

```
        self.main()
```

```
    def load_file(self, filename):
```

```

with open(filename, 'r') as f:

    datastore = json.load(f)

    return datastore

def check_list(self, number, final_alpha):

    result = {}

    for monomer_weight_num in self.polymer_weight:

        if abs(monomer_weight_num - number) < self.error_number:

            result[number] = final_alpha

            return result

        else:

            pass

def use_iter(self, range_num):

    product_list = list(itertools.combinations_with_replacement(self.mono-
mer_weight_keys, range_num))

    return product_list

def combinations_generator(self):

    steps = []

    for range_num in range(self.range_bottom, self.range_top):

        step = self.use_iter(range_num)

        steps.extend(step)

```

```
return steps
```

```
def result_calculator(self, combination):
```

```
    final_value = 0
```

```
    final_alpha = ""
```

```
    for item in combination:
```

```
        value = self.monomer_weight[item]
```

```
        final_value += value
```

```
        final_alpha += item
```

```
    result = self.check_list(final_value, final_alpha)
```

```
    return result
```

```
def main(self):
```

```
    combinations = self.combinations_generator()
```

```
    for combination in combinations:
```

```
        result = self.result_calculator(combination)
```

```
        if result:
```

```
            print(result)
```

MolecularWeight()

Appendix C. Incorporation of LiClO₄ to 1:1 DEO:OHS

Synthesis of 1:1 DEO:OHS. In a 50 mL round bottom flask equipped with a magnetic stir bar, OHS (1.5 g, 1.5 mmol) and DEO (0.8 g, 5.9 mmol) were dissolved in a mixture of 10 ml DCM and 10 ml hexane. The solution was stirred at 40 °C/5 min, then B(C₆F₅)₃ (3 mg, 6 μmol) dissolved in 500 μL of DCM was added using a syringe. The solution was then kept stirring magnetically at 40 °C/48 h.

1:1 DEO:OHS + (1 wt.%) LiClO₄ film. Thereafter, to the 1:1 DEO:OHS reaction mixture was added 10 mL of LiClO₄ acetonitrile solution (2.5 mg/mL) and kept running for another 48 h at 40 °C. The mixture stayed transparent. The solution was then cast onto a PTFE plate and placed into a desiccator for drying. The lid of the desiccator was left slightly open to promote evaporation. After 2 d of drying, a viscous thin layer formed. It was then moved to a vacuum oven for further drying at RT/2 d, and another 5 h at ~100 °C/vacuum.

The dried film appears translucent, flat, and brittle. However, precipitates are observed, which is likely LiClO₄ (Figure C.1a). The film was cut into small sizes (lateral length ≈ 1 cm) and both sides of the films were sputter coated with concentric Au/Pd electrodes ($\Phi = 3$ mm) using a deposition mask (Figure C.1b). EIS impedance measurement was then performed on the sputter coated films. Unfortunately, no semi-circle was shown in the Nyquist plots suggesting poor ionic conductivity. This can be ascribed to the high crosslinking density of the 1:1 DEO:OHS rigid structure that leads to little to no chain mobility, and therefore restrained Li⁺ transport.

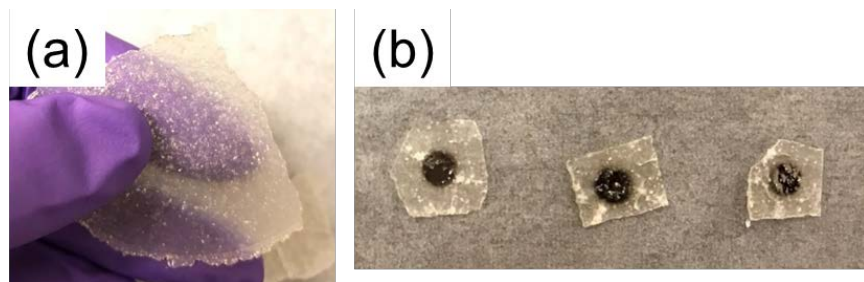


Figure C.1. Optical images of **a.** dried 1:1 DEO:OHS + LiClO₄ film and **b.** after sputter coating.

Appendix D. *t*-ZrO₂ Toughened Al₂O₃ Free-standing Films and as Oxidation Mitigating Thin Films on Silicon Nitride via Colloidal Processing of Flame Made Nanopowders

Published: Zhang, X.; Cheng, X.; Jansohn, M.; Niedermaier, M.; Lenk, T.; Britting, S.; Schmidt, K.; Laine, R. M. *J. Am. Ceram. Soc.* **2021**, *104* (3), 1281–1296.

D.1 Introduction

Alumina (Al₂O₃) is a widely studied structural ceramic with applications as grinding media, for cutting tools, high-temperature engine components, prosthetic implants, and substrates for power electronics due to its high melting point, excellent mechanical strength, hardness and chemical stability as well as its widespread abundance.¹⁻¹⁷ However, applications using pure α -Al₂O₃ are limited by its low resistance to crack propagation, i.e., poor fracture toughness (4-5 MPa m^{1/2})^{18,19} that can lead to catastrophic failure.¹⁻³ To enhance Al₂O₃ fracture toughness, a common practice involves incorporating additives such as tetragonal zirconia (*t*-ZrO₂) to increase toughness while maintaining the hardness and chemical resistance of Al₂O₃, commonly referred to as zirconia toughened aluminas (ZTAs).^{2-6,20-29}

Room temperature stabilized *t*-ZrO₂ will transform to monoclinic (*m*-ZrO₂) if subjected to mechanical stress. This transformation is accompanied by a 4 % volume expansion creating a compressive stress field in the surrounding grains, which opposes crack propagation.^{2-4,20-24} In this process some fraction of the energy needed for crack propagation is consumed promoting the *t*→*m*, transformation, the operative mechanism that inhibits crack propagation.²¹⁻²⁴ Unfortunately, *t*-

ZrO₂ typically transforms to *m*-ZrO₂ at 950-1000 °C on cooling making it unstable at lower temperatures.^{2-4,20-24} A resolution to this problem is to stabilize *t*-ZrO₂ by introducing dopants with cationic radii close to that of Zr⁴⁺ (0.8-1 Å, e.g. Y³⁺, Ca²⁺, Mg²⁺ and related rare earth ions).^{2,6-8,21-23,26,30-33} Table **D.1** compares various ZTA compositions synthesized/sintered using different methods and their selected properties. In general, yttria (Y³⁺) is the most common dopant, stabilizing *t*-ZrO₂ after sintering at 1600 °C/1-5 h/air (Table **D.1**).^{2,6,21}

Table D.1. Comparison of ZTA ceramics in literature and this work.

ZrO ₂ (%) ^a	t (%) ^b	Powder processing/synthesis	Sintering condition (°C/h)	AGS (µm) ^c	Relative density (%)	Mechanical properties ^d	Ref.
5-20 vol.	10-90	Ball milling	1500/2, hot-pressing	0.4-5	-	K _{1C} : 6-8 H _v : 10-12	20
5-30 vol. (3Y)	50-100	Ball milling	1600/1/air	0.3-3	96-99	E: 340-390 σ: 400-950	21
5 mol.	75	Sol-gel	1550/4/air	0.1-4	98	E: 370 K _{1C} : 5 H _v : 17	4,5
30 wt. (3Y)	100	GCHAS ^e	1600/1/air	0.6-4	92	K _{1C} : 5.5 H _v : 14-15 σ: 610	6
20 wt. (10M)	25	Ball milling	1600/2/air	~1	94.5	K _{1C} : 11.5 H _v : 16.4	23
10-30 wt. (3Y)	8-25	Co-precipitation	1600/5/air	0.5-3	96-98	K _{1C} : 8-8.5	2
54 mol.	100	LF-FSP	1120/6/air	~0.2	99	-	27-29
10 mol. ^f	100	LF-FSP	1500/5/N ₂ /H ₂	0.5-1	97-99	K _{1C} : 24	This work

^aZrO₂ content, *t*-ZrO₂ stabilizing additives: 3Y = 3 mol.% Y₂O₃, 10M = 10 wt.% MgO. ^b*t*-ZrO₂ content in sintered ceramics at room temperature. ^cAverage grain sizes of both Al₂O₃ and ZrO₂. ^dK_{1C}: fracture toughness (MPa m^{1/2}); H_v: Vickers hardness (GPa); E: elastic modulus (GPa); σ: flexural strength (MPa). ^eGel casting hydrolysis-assisted solidification. ^fOne example is given: 10 mol.% ZrO₂ doped Al₂O₃ films (≈200 µm thick) with MgO and TiO₂ (1 wt.% each).

Previously, we demonstrated that it is possible to sinter flame made NPs (average particle sizes, APSs: 40-60 nm) consisting of particles of *t*-ZrO₂ encapsulated within δ-Al₂O₃ shells to fully dense (*t*-ZrO₂)_{0.54}(α-Al₂O₃)_{0.46} pellets (Φ = 13 mm, thickness = 1.4 mm) with AGSs ≤200 nm at 1120 °C/6 h/air. The encapsulation process seems to stabilize the *t*-ZrO₂ without the need for additives likely due to rapid quenching of the flame made NPs (liquid feed flame spray pyrolysis, LF-FSP)

to kinetically rather than thermodynamically stable phases produced using traditional processing methods.²⁷⁻²⁹

We have recently returned to these flame made NPs, demonstrating their utility as a simple and scalable route to functional ceramic thin films (<100 μm thick) for applications such as capacitors, solid electrolytes and electrodes for solid-state batteries.³⁴⁻³⁶ Coincidentally, we reported processing dense and flexible $\alpha\text{-Al}_2\text{O}_3$ thin films (<10 μm).¹⁰

Our success with $\alpha\text{-Al}_2\text{O}_3$ thin films prompted efforts to extend our new approach to $t\text{-ZrO}_2$ doped $\alpha\text{-Al}_2\text{O}_3$ thin films targeting mechanical properties superior to $\alpha\text{-Al}_2\text{O}_3$ for applications including electronic substrates and protective coatings.

In the first part of the present work, we explored sintering $(\text{ZrO}_2)_x(\text{Al}_2\text{O}_3)_{1-x}$ thin films ($x = 0\text{-}50$ mol.%, ≈ 40 μm thick) using a select set of conditions (1120-1500 $^\circ\text{C}/5$ h in O_2 or 95% $\text{N}_2/5\%$ H_2) from NPs by LF-FSP to optimize ZrO_2 content, sinterability and microstructures. Similar to our previous work,²⁷⁻²⁹ all films retain $t\text{-ZrO}_2$ at RT with AGSs of 0.1-1 μm .

Although no $t\text{-ZrO}_2$ stabilizing additives are needed due to rapid quenching of LF-FSP, additives such as TiO_2 and MgO were found to be effective in tailoring final grain sizes and sinterability; permitting us to optimize the ZTA composite properties. Studies show that TiO_2 doping enhances densification and reduces ZTA sintering temperatures on substituting Al^{3+} by Ti^{4+} which generates vacancies, thereby improving diffusion.^{7,37-40} Additionally, Chen *et al.*^{7,8} report formation of a liquid phase at ZTA grain boundaries with TiO_2 contents ≥ 4 wt.% which also promotes densification. Unfortunately, TiO_2 doping sometimes coincides with excessive grain growth leading to a reduced elastic modulus and hardness.^{7,8,37} Consequently, we sought to eliminate this issue by introducing MgO , which is quite useful in limiting grain sizes in the $\alpha\text{-Al}_2\text{O}_3$ thin films.

MgO is known to be an effective additive in inhibiting grain growth during sintering through segregation of MgO-Al₂O₃ solid solutions (solubility limit \approx 500 ppm MgO) and/or pinning through formation of fine spinel particles (MgAl₂O₄) at grain boundaries resulting in reduced grain boundary mobility.^{10,40–51} It has also been suggested that the dominant densification mechanism is via surface diffusion for MgO doping levels of 0.1-0.3 wt.%, and grain boundary diffusion for MgO concentrations of 0.5-1.0 wt%.^{47,48} In this work, both TiO₂ and MgO additives (\approx 1 wt.% each) were used to optimize sinterability and final microstructures.

While thin films are suitable for applications such as electronic devices and protective coatings, for other structural applications such as wear components, dental composites and prosthetic implants, bulk materials are also highly desirable. At the interface between bulk and thin films, intermediate thicknesses, e.g. up to \sim 300 μ m are used as electrically insulating layers as well as high-strength substrates for piezoresistive sensors and power electronics.^{11–14} Finally, to test ZTA mechanical properties, greater thicknesses are preferred to prevent cracking caused simply by handling.

These issues provided the motivation to expand our approach to ZTA films up to \sim 200 μ m thick and up to \sim 2 \times 2 cm². To our surprise, \sim 200 μ m thick ZTA films doped with MgO and TiO₂ (1 wt.% each) show a fracture toughness of 24 MPa m^{1/2} using single-edged precracked beam tests (SEPB), which is 2-4 times higher than reported values (Table **D.1**), suggesting potential application as electronic substrates with improved mechanical properties.

Similar to ZTA films, silicon nitride (Si₃N₄) films (\approx 300 μ m thick) are also commonly used in structural applications due to their good chemical, physical and thermal stabilities, and mechanical properties.^{15,16,52–58} For electronic substrates, Si₃N₄ films exhibit superior thermal conductivity (κ)

of ~ 90 W/mK (at RT) and a K_{IC} of 6.5-7 MPa m^{1/2} compared to ZTA films (typically $\kappa = 28$ W/mK and $K_{IC} \approx 5$ MPa m^{1/2}) providing better thermal conductivity and reliability.^{15,57}

Unfortunately, Si₃N₄ is susceptible to oxidation even at ambient and may deteriorate over time.⁵²⁻⁵⁵ Although a surface oxide/oxynitride layer that forms can protect against further oxidation,^{52,53} to withstand high-temperature oxidation and/or active oxidation environments, additional protection is needed. In the present work, we find that sintered ZTA coatings (<5 μ m) adhere well to Si₃N₄ substrates (≈ 300 μ m thick) providing physical protection against oxidation after heating to 1500 °C/1 h/O₂ as characterized by scanning electron microscope (SEM).

D.2 Experimental section

Precursor syntheses

Nanopowders (NPs) were produced by liquid feed-flame spray pyrolysis (LF-FSP), which was invented in the Laine group at the University of Michigan. It is a single-step continuous synthesis method for producing ceramic NPs. Typical metalloorganic precursors in this work include metal-carboxylates and metal-atrane compounds; detailed synthesis procedures are reported elsewhere.^{10,27-29,34-36,59-62} Representative examples are given below.

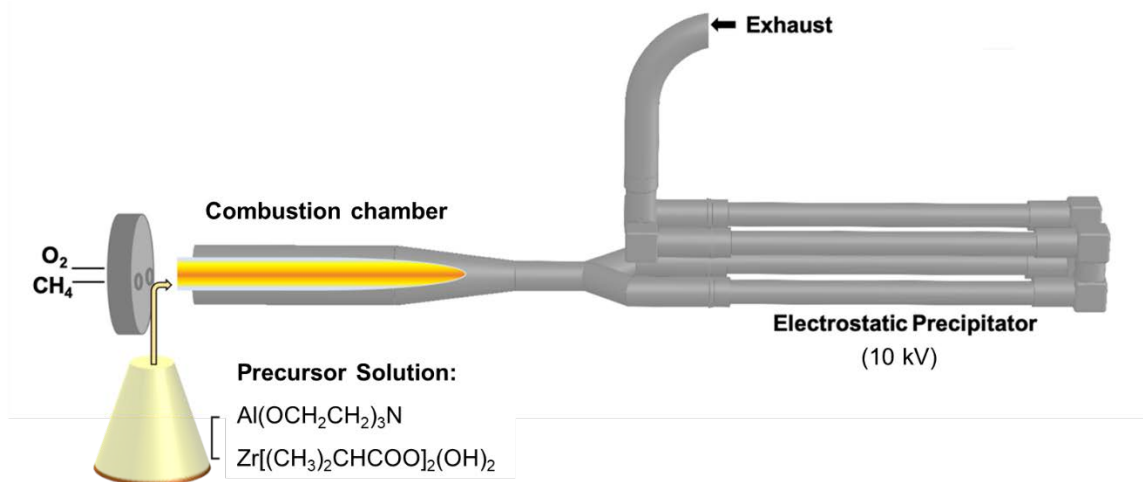
Alumatrane [Al(OCH₂CH₂)₃N] was synthesized by reacting triethanolamine [N(CH₂CH₂OH)₃, 99+ %, Acros Organics, Morris Plains, NJ] with aluminum sec-butoxide {Al[OCH(CH₃)CH₂CH₃]₃, 97 %, Alfa Aesar, Ward Hill, MA} in a 1 L round bottom flask equipped with a still head at room temperature in N₂ atmosphere. Residue was filtered off and alumatrane was obtained as a solution (ceramic yield or CY = 7.5 wt.% by TGA).

Zirconium isobutyrate {Zr[(CH₃)₂CHCOO]₂(OH)₂} was synthesized by reacting zirconium carbonate [2ZrO₂(CO₂) \cdot x(H₂O), 99 %, Alfa Aesar] with excess isobutyric acid [(CH₃)₂CHCOOH, 99+ %, Acros organics] in a 1 L round bottom flask equipped with a still head and an addition

funnel. The solution was heated to 120 °C/2 h under N₂ with magnetic stirring to distill off by-product water and excess propionic acid. The CY of the resulting precursor is 38 wt.%.

Liquid-Feed Flame Spray Pyrolysis (LF-FSP)

Metalloorganic precursors at selected compositions were dissolved in alcohol, usually ethanol, at 1-10 wt.% solids loading. The solution is fed (30-80 mL/min) into an atomizing nozzle (BETE XA-PR, Greenfield, MA) and aerosolized with oxygen (80 psi, 40 mL/min) into a quartz chamber where it is ignited with methane/oxygen (40 mL/min /30 mL/min) pilot torches on the spray head. Oxygen shield gas (150 mL/min) provides an oxygen-rich environment to minimize carbon residues. Initial combustion takes place producing temperatures of ≥ 1500 °C followed by a quenching step that drops the temperature to 300-500 °C over 1.5 m, equivalent to a 1000 °C quench in <100 ms, to produce NPs. Powders are collected downstream in rod-in-tube electrostatic precipitators (ESP) operating at 10 kV. Scheme **D.1** illustrates the LF-FSP apparatus for NP production.



Scheme D.1. Liquid feed flame spray pyrolysis (LF-FSP) for nanopowder production.

As-produced NPs were then dispersed in ethanol (200 proof, Decon Labs, King of Prussia, PA) using an ultrasonic horn (Vibra cell VC-505, Sonics & Materials Inc. Newtown, CT) at 100 W/10

min. The suspension was allowed to settle for 5 h to remove larger particles. The supernatant was decanted and allowed to oven dry (60 °C/12 h) providing the starting ZrO₂ doped δ -Al₂O₃ NPs.

Film processing

Generally, LF-FSP synthesized NPs were mixed with polymeric additives such as binder, plasticizer, curing agent, and dispersant, in a selected solvent system by ball-milling (Rotary Tumbler Model B, Tru-Square Metal Products) using spherical Al₂O₃ ($\Phi = 3.0$ mm) as the milling media. One fifth of the container (20 mL) was filled with the milling media (≈ 6 g). An example suspension of ZrO₂ doped Al₂O₃ is given in Table **D.2**.

Table D.2. Starting materials of *t*-ZrO₂ (0-50 mol.%) doped δ -Al₂O₃ suspension.

Components	Roles	Mass (g)	Wt.%	Vol.%
<i>t</i> -ZrO ₂ doped δ -Al ₂ O ₃	NP	1.00	25.8	6.4
Polyvinyl butyral	Binder	0.135	3.5	3.2
Benzyl butyl phthalate	Plasticizer	0.135	3.5	3.2
Ethanol	Solvent	1.3	33.6	43.4
Acetone	Solvent	1.3	33.6	43.7

The suspensions were cast on Mylar film using a wire-wound rod coater (Automatic Film Applicator-1137, Sheen Instrument, Ltd. Santa Fe Springs, CA). The cast thickness was adjusted to 100-255 μm to control the thickness of the final ceramic film. A glass cover was used to control the solvent drying rate to avoid mud cracking.

After solvents evaporated, dried green films were uniaxially pressed between stainless steel dies at 100 °C at 10 ksi/5-30 min using a heated benchtop laboratory manual press (Model 3851-0, Carver, Inc., Wabash, IN) to improve packing density.^{10,34-36} One/two layers for thin films (20-80 μm thick) and 8-10 layers for thick films (≈ 200 μm thick) were pressed together.

Film sintering

Green films (typically 5×5 mm²) were placed between two Al₂O₃ substrates ($\Phi = 42$ mm) and sintered to selected temperatures, times and ramp rates, using a vacuum tube furnace (GSL-1600X,

Richmond, CA). The substrates were used to prevent warping of the ceramic films.

Films were subject to binder burnout process prior to sintering by heating them to 800 °C/1 h in extra dry grade O₂ (60 mL/min). Subsequently, they were sintered at various conditions: 1120-1500 °C at 1-10 °C/min under a constant gas (O₂ or 95%N₂/5%H₂) flow of 60 mL/min. For convenience, 95%N₂/5%H₂ is referred to as N₂/H₂ in the following sections.

Figure D.1 shows typical sintering schedules in O₂ and N₂/H₂. For both cases, the films were first subject to binder burnout at 800 °C/1 h/O₂. The sintering temperature and ramp rate may vary according to the ceramic systems.

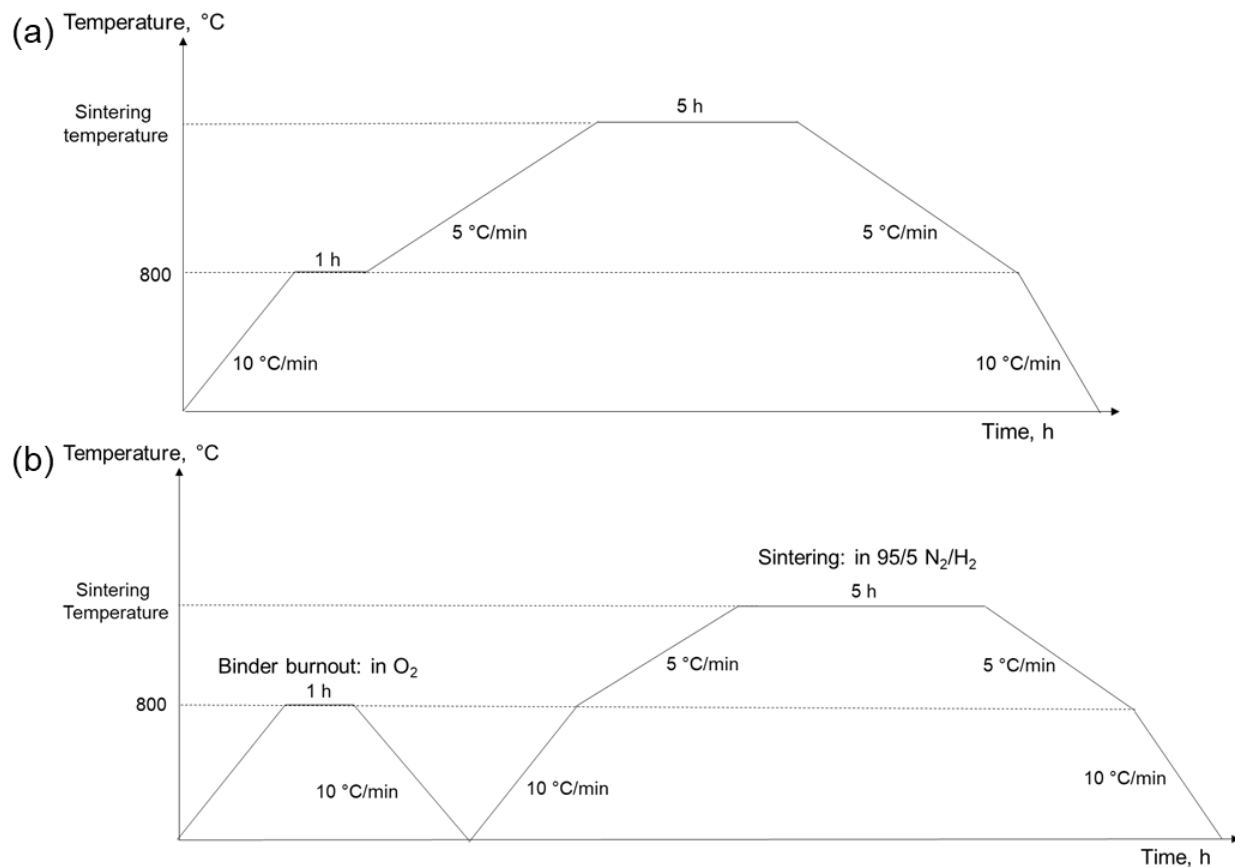


Figure D.1. Typical sintering schedules, **a.** in O₂, **b.** in N₂/H₂.

Coating Si₃N₄ substrates

Suspensions of 10 mol.% ZrO₂ doped δ -Al₂O₃ for coating Si₃N₄ substrates (Rogers Corp.) were

prepared per Table **D.3**. The ceramic nanopowder (NP) is a mixture of 30 mol.% ZrO₂ doped Al₂O₃ (0.33 g), 2 wt.% MgO doped Al₂O₃ (0.66 g) and 1 wt.% TiO₂ NP (0.01 g).

Si₃N₄ films were coated one side at a time. The suspension was first cast on one side of Si₃N₄ samples with 25 μm spacers using the coating setup shown in Figure **D.2**; then the films were thermally pressed at 100 °C bottom, 60 °C top, 4 ksi. They were sintered in two steps: binder burnout at 800 °C/1 h/O₂; and sintering at 1500 °C/5 h/N₂/H₂ (Figure **D.1b**) The other side of the films was then coated and sintered following the same procedure.

Table D.3. Suspension of coating material: 10 % ZrO₂ doped δ-Al₂O₃.

Components	Roles	Mass (g)
10 mol.% ZrO ₂ doped δ-Al ₂ O ₃ with 1 wt.% TiO ₂ and 1 wt.% MgO NPs	NP	1.0
Polyvinyl butyral	Binder	0.135
Benzyl butyl phthalate	Plasticizer	0.135
Ethanol	Solvent	1.5
Acetone	Solvent	1.5

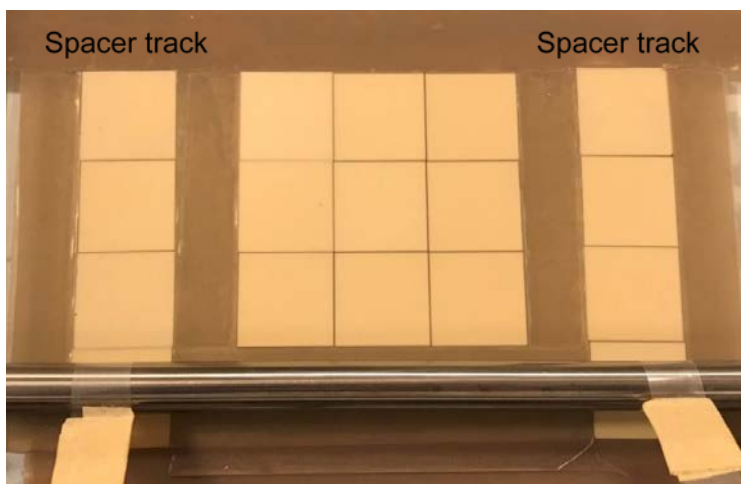


Figure D.2. Coating setup of Si₃N₄ films.

Specific surface areas (SSAs) analysis by Brunauer, Emmett and Teller (BET) theory

SSAs of (ZrO₂)_x(Al₂O₃)_{1-x} (x = 0, 15, 30, 50 mol.%) NPs were measured by a Micromeritics ASAP 2020 sorption analyzer. Samples (≈300 mg) were degassed at 400 °C/5 h; analyses were

run at 77 K with liquid N₂. The SSAs were determined by the BET multipoint method using ten data points at relative pressures of 0.05-0.3. Average particle sizes (APSs) of NPs were calculated using the equation $APS (\Phi) = 6/(SSA \times \rho)$, where ρ is the density of the NP.

X-ray diffraction (XRD) analysis

Measurements were carried out using a Rigaku Rotating Anode Goniometer (Rigaku Denki., LTD., Tokyo, Japan) at 40 kV and 100 mA with Cu K α radiation (1.541 Å). Scan range was between 10 and 80° 2 θ , using a scan rate of 5 °/min with 0.02° intervals. The Jade program 2010 (Version 1.1.5 from Materials Data, Inc.) and Rigaku PDXL II (version 2.8.4.0) were used to determine the crystallographic phases, crystallite domain sizes from line broadening and weight fractions with the aid of Rietveld refinement. Peak positions and intensities were evaluated by comparison with ICDD files.

Scanning electron microscopy (SEM) and energy-dispersive X-ray spectroscopy (EDS)

Particle and grain morphologies and sizes were characterized by a JSM-IT300 SEM (JEOL Ltd., Akishima, Tokyo, Japan). Since the samples lacked electrical conductivity, they were sputter coated prior to SEM analyses with a gold/palladium film using a Technics Hummer VI sputtering system (Anatech Ltd., Alexandria, VA, United States) to avoid charging and to improve resolution.

Using SEM fracture surface images, average grain sizes (AGSs) of sintered films are measured by ImageJ, at least 50 grains for each film are measured and averaged.

Archimedes density measurement

Density Determination Kit (OHAUS Corp., Columbus, OH) was used to measure film densities based on the Archimedes method. The film weights in ambient atmosphere (*A*) and in ethanol bath (*B*) were measured by a Voyager Pro scale (OHAUS Corp.), each sample weight was measured three times for accuracy. The density was calculated per equation (D.1).

$$\rho = \frac{A}{A - B} \times \rho_e \quad (D.1)$$

Where ρ is the film density, $\rho_e (= 0.78522 \text{ g/cm}^3)$ is the density of ethanol.

Lateral shrinkage measurement

Lateral lengths of rectangular films before and after sintering were measured, the lateral shrinkage of each side was calculated per equation (D.2), and the average of four sides was obtained for each film. Each lateral shrinkage value given in this work was averaged over at least three films.

$$S_L = \frac{L_2 - L_1}{L_1} \times 100 \% \quad (D.2)$$

Where S_L is the lateral shrinkage, L_1 and L_2 are the lateral lengths before and after sintering, respectively.

Single-Edged Precracked Beam (SEPB) test

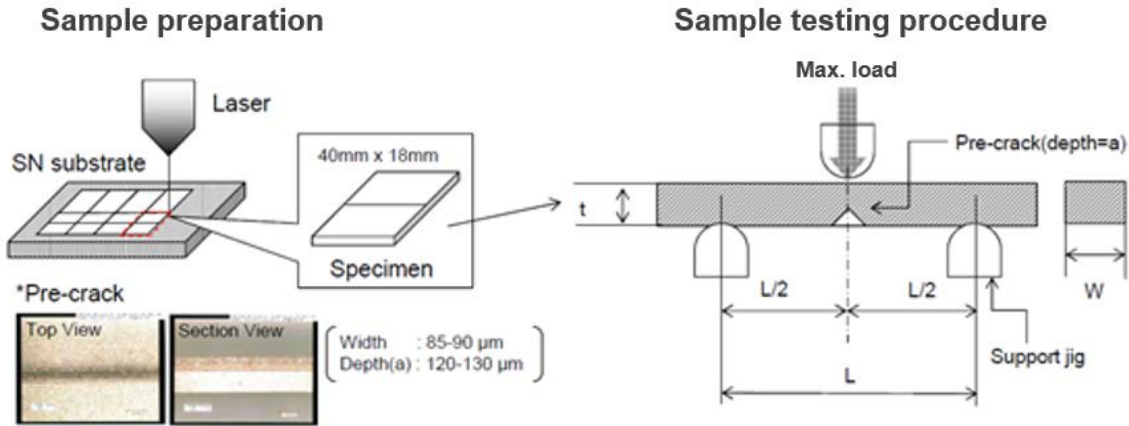
The fracture toughness (K_{1C}) of sintered ZTA films was determined by SEPB test,⁶³ performed by Rogers Germany GmbH. As illustrated in Scheme **D.2**, pre-crack at the surface center of the specimen was introduced by laser. Thickness (t) and width (w) of the specimen and distance between two supporting jigs (L) were measured, the pre-cracked side was faced on the side of support jig, and the pre-cracked area was placed directly under the load (P). The maximum load when the specimen breaks was recorded, the pre-crack length (a) was measured, and K_{1C} value was calculated per equation (D.3).

$$K_{1C} = Y \frac{3PL}{2Wt^2} \sqrt{a} \quad (3 - \text{point method}) \quad (D.3)$$

Where

$$\begin{aligned} Y &= A_0 + A_1 \frac{a}{t} + A_2 \left(\frac{a}{t}\right)^2 + A_3 \left(\frac{a}{t}\right)^3 + A_4 \left(\frac{a}{t}\right)^4 \\ &= 1.964 - 2.837 \frac{a}{t} + 13.711 \left(\frac{a}{t}\right)^2 - 23.250 \left(\frac{a}{t}\right)^3 + 24.129 \left(\frac{a}{t}\right)^4 \end{aligned}$$

$$(0 \leq \frac{a}{t} \leq 0.6).$$



Scheme D.2. Schematics of sample preparation and testing procedure of SEPB test.

D.3 Results and discussion

In the following sections, we first characterize microstructures, sinterability and phase compositions of ZTA thin films ($\approx 40 \mu\text{m}$) derived from $(\text{ZrO}_2)_x(\text{Al}_2\text{O}_3)_{1-x}$ ($x = 0-50 \text{ mol.}\%$) NPs sintered under select conditions. Film thicknesses were then increased to $\sim 200 \mu\text{m}$ to explore their potential utility as substrates for power electronics. The effects of different sintering conditions were explored to minimize cracking while optimizing microstructures and densities. Finally, ZTA coatings on Si_3N_4 substrates were processed and optimized as characterized by a dye penetration test, an oxygen damage test, XRD and SEM.

D.3.1 ZTA $\sim 40 \mu\text{m}$ thin films

To identify the mix of phases required to optimize the properties of the final sintered products, $(\text{ZrO}_2)_x(\text{Al}_2\text{O}_3)_{1-x}$ ($x = 0, 15, 30, 50 \text{ mol.}\%$) NPs were produced by LF-FSP. APSs and SSAs were calculated using BET data per Table D.4. All NPs show similar SSAs of $40-50 \text{ m}^2/\text{g}$ and APSs of $\sim 30 \text{ nm}$; $(\text{ZrO}_2)_{0.3}(\text{Al}_2\text{O}_3)_{0.7}$ shows the lowest APS of 25 nm . Figure D.3 shows SEMs of as-produced Al_2O_3 and $(\text{ZrO}_2)_{0.5}(\text{Al}_2\text{O}_3)_{0.5}$ NPs, both exhibit a broad size distribution with APSs $< 50 \text{ nm}$,

and a few particles >100 nm that are likely agglomerated in overall agreement with Table D.4 APSs. Nanosized powders with log normal particle size distributions are advantageous for processing in that they reduce sintering temperatures due to high surface energies and provide high packing densities.

Table D.4. Selected properties of $(\text{ZrO}_2)_x(\text{Al}_2\text{O}_3)_{1-x}$ ($x = 0, 15, 30, 50$ mol.%) NPs.

ZrO ₂ content, mol.%	ZrO ₂ content, wt.%	Density, g/cm ³	SSA, m ² /g	APS, nm
0	0	3.95	49 ± 0.5	31 ± 0.3
15	17.6	4.25	50 ± 0.5	28 ± 0.3
30	34.1	4.54	53 ± 0.5	25 ± 0.2
50	54.7	4.90	40 ± 0.3	30 ± 0.3

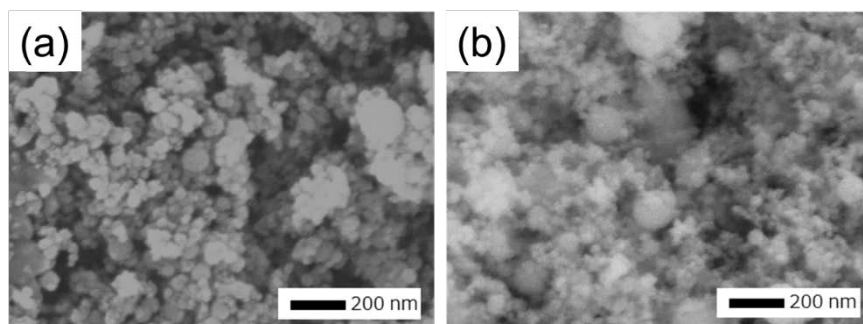


Figure D.3. SEMs of **a.** as-produced LF-FSP Al₂O₃ and **b.** 50 mol.% ZrO₂ doped Al₂O₃ nanoparticles.

Figure D.4 compares XRDs of as-produced $(\text{ZrO}_2)_x(\text{Al}_2\text{O}_3)_{1-x}$ NPs. As produced LF-FSP Al₂O₃ is a mixture of δ -Al₂O₃ phases, as expected from previous work.^{10,27,59} For ZrO₂ ($x > 0$ mol.%) doped Al₂O₃, a mixture of δ -Al₂O₃ and t -ZrO₂ is observed, as previously reported for $(t\text{-ZrO}_2)_x(\delta\text{-Al}_2\text{O}_3)_{1-x}$ ($x = 0.02\text{-}0.8$) core-shell NPs.²⁷⁻²⁹

Figure D.5 compares SEMs of $(\text{ZrO}_2)_x(\text{Al}_2\text{O}_3)_{1-x}$ thin films (40-60 μm thick) sintered under different conditions in O₂ (see Figure D.1a schedule). All films show uniform grain sizes (100-500 nm, Figure D.6), AGSs and densities increase with the sintering temperature, but pores are not fully eliminated even at 1500 °C.

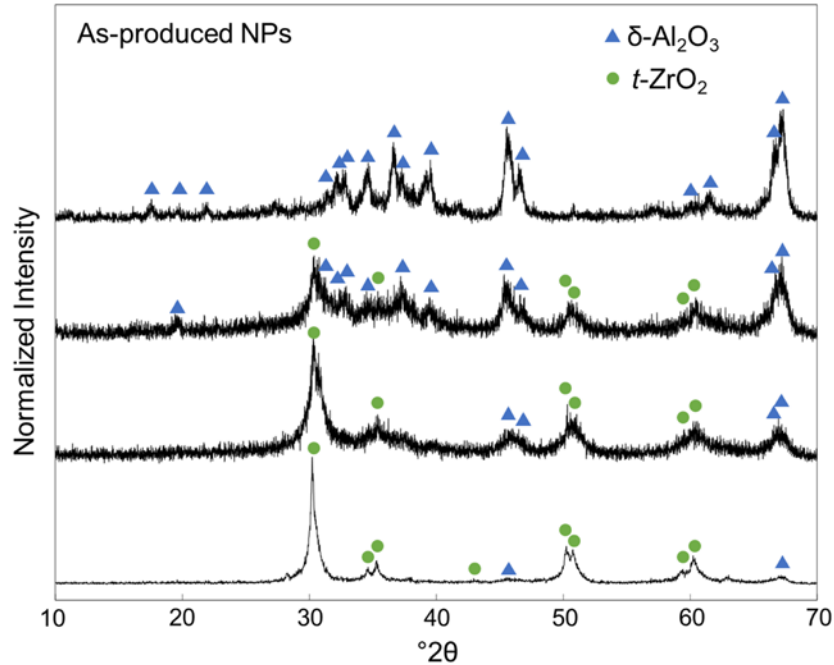


Figure D.4. XRDs of $(\text{ZrO}_2)_x(\text{Al}_2\text{O}_3)_{1-x}$ ($x = 0, 15, 30, 50$ mol.%) NPs.

Figure **D.6a** suggests that grain sizes decrease slightly with increasing ZrO₂ content, although the difference for higher contents is not significant. As seen in Figure **D.6b**, film thicknesses decrease with increasing sintering temperature. Overall, the 30 mol.% ZrO₂ film shows the smallest final AGSs and the greatest decrease in thickness at higher temperatures.

Previous reports indicate that sintering α -Al₂O₃ in a hydrogen atmosphere improves densification and reduces porosity.^{10,64} These results prompted efforts here to sinter thin $(\text{ZrO}_2)_x(\text{Al}_2\text{O}_3)_{1-x}$ ($x = 15, 30, 50$ mol.%) films in N₂/H₂ following a two-step procedure per Figure **D.1b**: binder burnout at 800 °C/1 h/O₂ and sintering at 1400 °C/5 h/N₂/H₂. As shown in Figure **D.7**, compared to films sintered in O₂ (Figure **D.5**), an N₂/H₂ atmosphere improves densification slightly, and AGSs appear to be smaller. However, the films are porous suggesting incomplete densification.

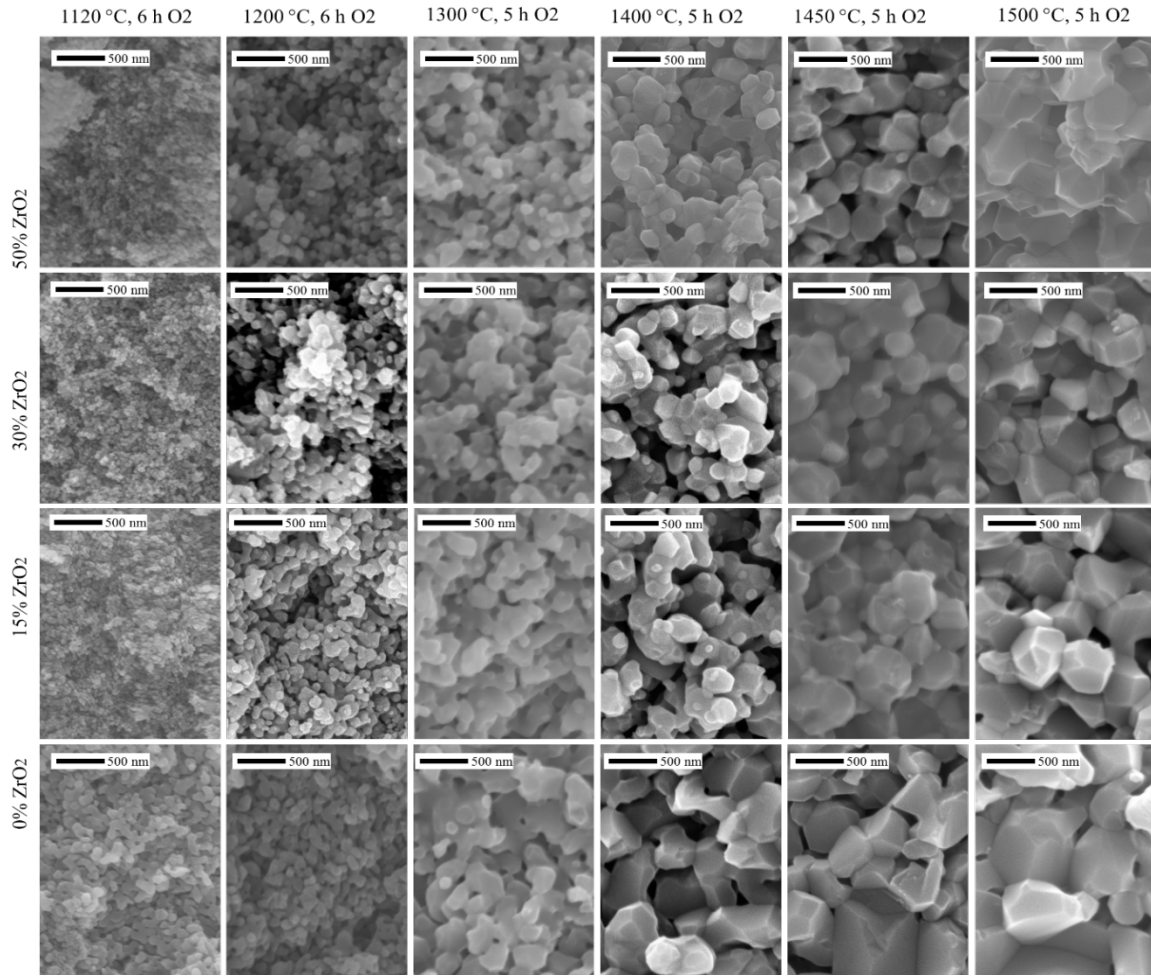


Figure D.5. SEM fracture surfaces of sintered $(\text{ZrO}_2)_x(\text{Al}_2\text{O}_3)_{1-x}$ ($x = 0, 15, 30, 50$ mol.%) thin films.

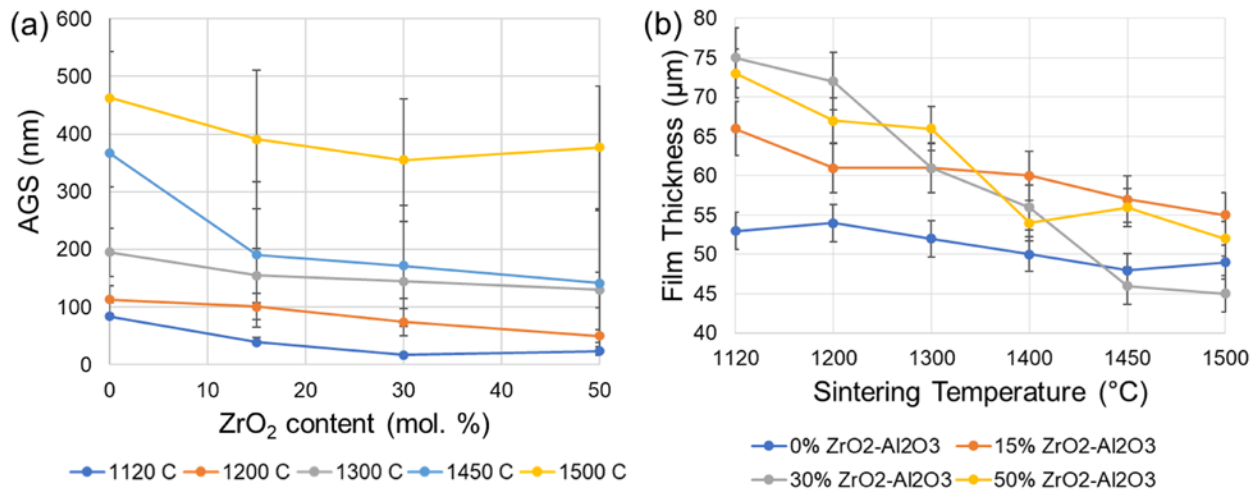


Figure D.6. AGSs vs ZrO₂ content **b.** sintered film thicknesses for $(\text{ZrO}_2)_x(\text{Al}_2\text{O}_3)_{1-x}$ ($x = 0, 15, 30, 50$ mol.%).

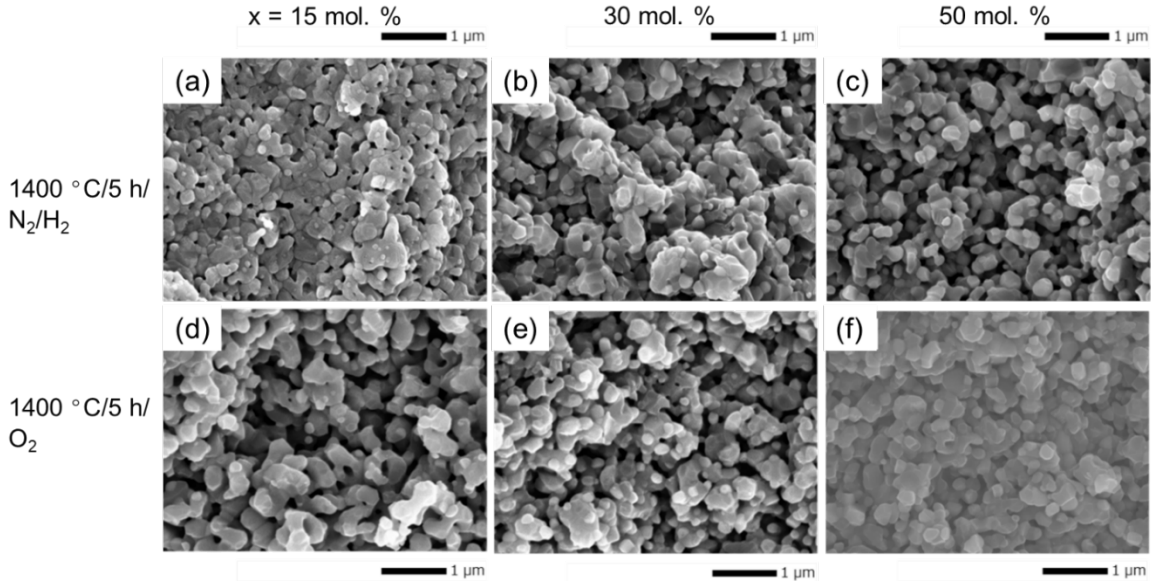


Figure D.7. SEM fractures surfaces of $(\text{ZrO}_2)_x(\text{Al}_2\text{O}_3)_{1-x}$ films sintered at $1400\text{ }^\circ\text{C}/5\text{ h}/\text{N}_2/\text{H}_2$ (a, b, c) and O_2 (d, e, f), where $x = 15$ (a, d), 30 (b, e), and 50 mol.% ZrO_2 (c, f).

As demonstrated in Figures D.5 and D.6, 30 mol.% ZrO_2 doped Al_2O_3 films show limited grain growth and the most significant decrease in thickness on sintering at $1400\text{--}1500\text{ }^\circ\text{C}$ compared to other compositions. As discussed in the introduction, TiO_2 doping improves Al_2O_3 densification but increases grain sizes,^{7,8,37–40} while MgO limits grain growth.^{10,40–51} Therefore, to further improve sinterability, the effects of TiO_2 and MgO additives (1 wt.% each) to 30 mol.% ZrO_2 doped Al_2O_3 were investigated.

As seen in Table D.5, we studied sintering effects of two different TiO_2 powders (1 wt.% doping): TiO_2 commercial powder (CP, claimed APS ≈ 20 nm), and TiO_2 NP by LF-FSP (APS = 20–30 nm). For composition D, MgO doping was introduced by mixing LF-FSP produced 30 mol.% ZrO_2 doped Al_2O_3 and 2 wt.% MgO doped Al_2O_3 NPs, the resulting mixture has a 10 mol.% ZrO_2 and ~ 1 wt.% MgO content. MgO (2 wt.%) doped Al_2O_3 NP was chosen based on work by Takeuchi *et al.*¹⁰ that generated dense and flexible sintered thin films ($<10\text{ }\mu\text{m}$). The ZrO_2 content was reduced because typical power electronic ZTA substrates contain <30 mol.% ZrO_2 .^{13–15}

Table D.5. Compositions of ZTA films.

Composition	ZrO ₂ content	Dopants, wt.%
A	30 mol.%	-
B	30 mol.%	1 wt.% TiO ₂ CP ^a
C	30 mol.%	1 wt.% TiO ₂ NP ^b
D ^c	10 mol.%	1 wt.% TiO ₂ NP, 1 wt.% MgO

^aCP: commercial powder from Evonik Industries AG, Germany. APS \approx 20 nm but may be agglomerated. ^bNP: nanopowder by LF-FSP, APS = 20-30 nm. ^cA mixture of LF-FSP produced 30 mol.% ZrO₂ doped Al₂O₃, 2 wt.% MgO doped Al₂O₃,¹⁰ and 1 wt.% TiO₂ NP.

Figure **D.8** compares the SEM fracture surfaces of films **A-D** (Table **D.5**) sintered at 1300-1500 °C/5 h/O₂ (Figure **D.1a**). At 1300 °C, all films are not dense, but the grains of 30 mol.% ZrO₂ doped Al₂O₃ supplemented with TiO₂ (**B** and **C**) show significant grain growth compared to films without TiO₂ (**A**) as expected.^{7,8,37-40} In contrast, the Al₂O₃ film doped with 10 mol.% ZrO₂, 1 wt.% TiO₂ NP and MgO (**D**) shows small AGSs which are comparable to film **A**, a result of MgO doping that prevents excessive grain growth.^{10,40-51}

At 1400 °C, films 30 mol.% ZrO₂ doped Al₂O₃ supplemented with TiO₂ (**B** and **C**) are already dense with intergranular fracture surfaces. The Al₂O₃ film with 10 mol.% ZrO₂ (**D**) starts to densify. At 1450 °C, films **B** and **C** show abnormal grain growth; the 30 mol.% doped Al₂O₃ without TiO₂ (**A**) starts to densify with uniform grain sizes.

These films show significant differences in AGSs when sintered at 1500 °C per Figure **D.8** bottom. Film **A** shows a rather small AGSs of \sim 200 nm with visible pores. Excess grain growth is exhibited in film **B** (AGSs = 1-2 μ m). Films **C** and **D** show similar AGSs of \sim 500 nm. Film **D** exhibits some transgranular (intra-) fracture behavior (marked with red arrow) suggesting improved mechanical properties at grain boundaries.

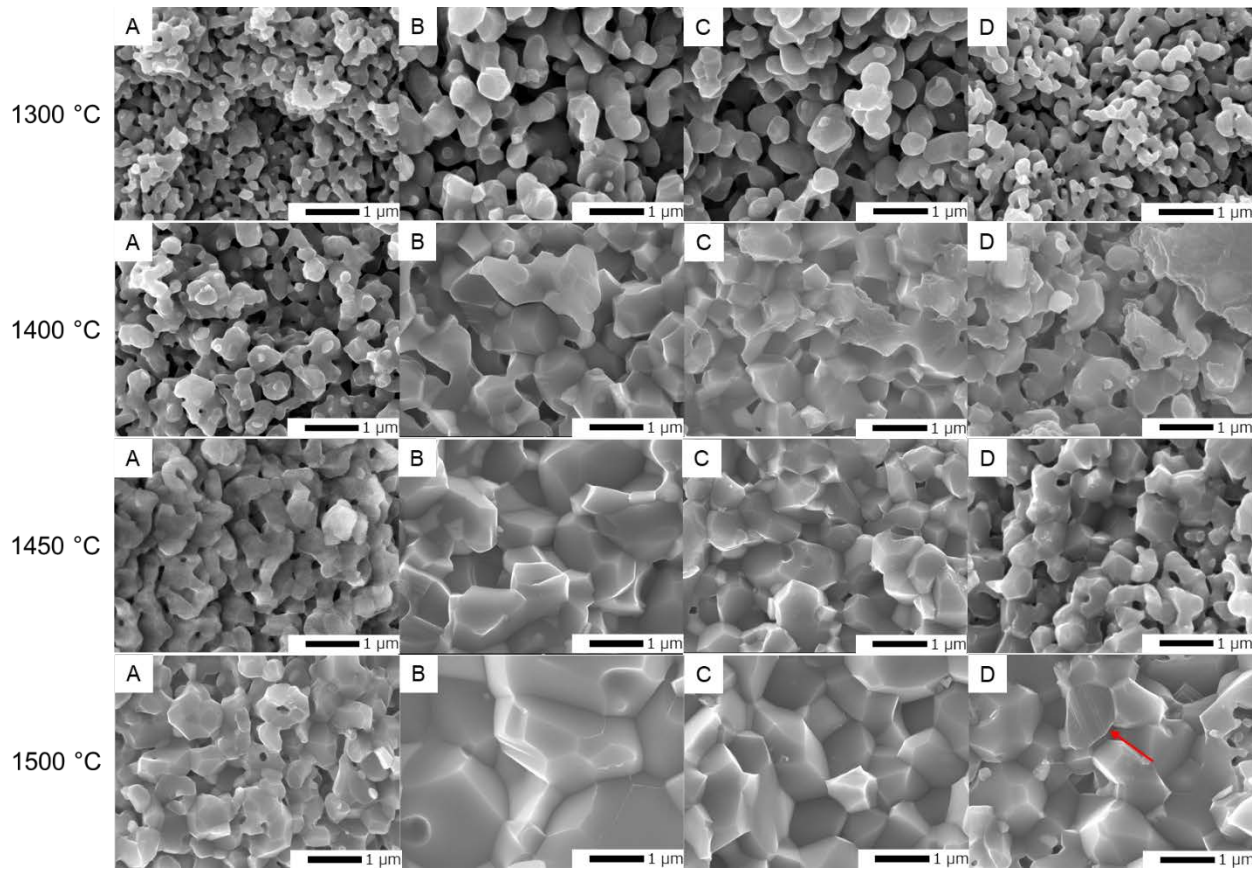


Figure D.8. SEM fracture surfaces of ZTA films (A-D per Table D.5) sintered at 1300-1500 °C/5 h/O₂. The red arrow suggests transgranular fracture.

Figure D.9 presents the XRDs of the films sintered at 1300-1500 °C/5 h/O₂. The films consist mainly of α -Al₂O₃ (corundum, hexagonal, space group 167, PDF-98-001-1217) and *t*-ZrO₂ (tetragonal, space group 137, PDF-04-013-6616); some films show small peaks at 36, 40, 48 and 49° 2 θ (not marked in Figure D.9) corresponding to a calcite phase (hexagonal, space group 167), which is likely a result of residual carbon from insufficient O₂ during LF-FSP. Overall, no *m*-ZrO₂ is observed; similar phases are exhibited for films with different compositions and sintering conditions.

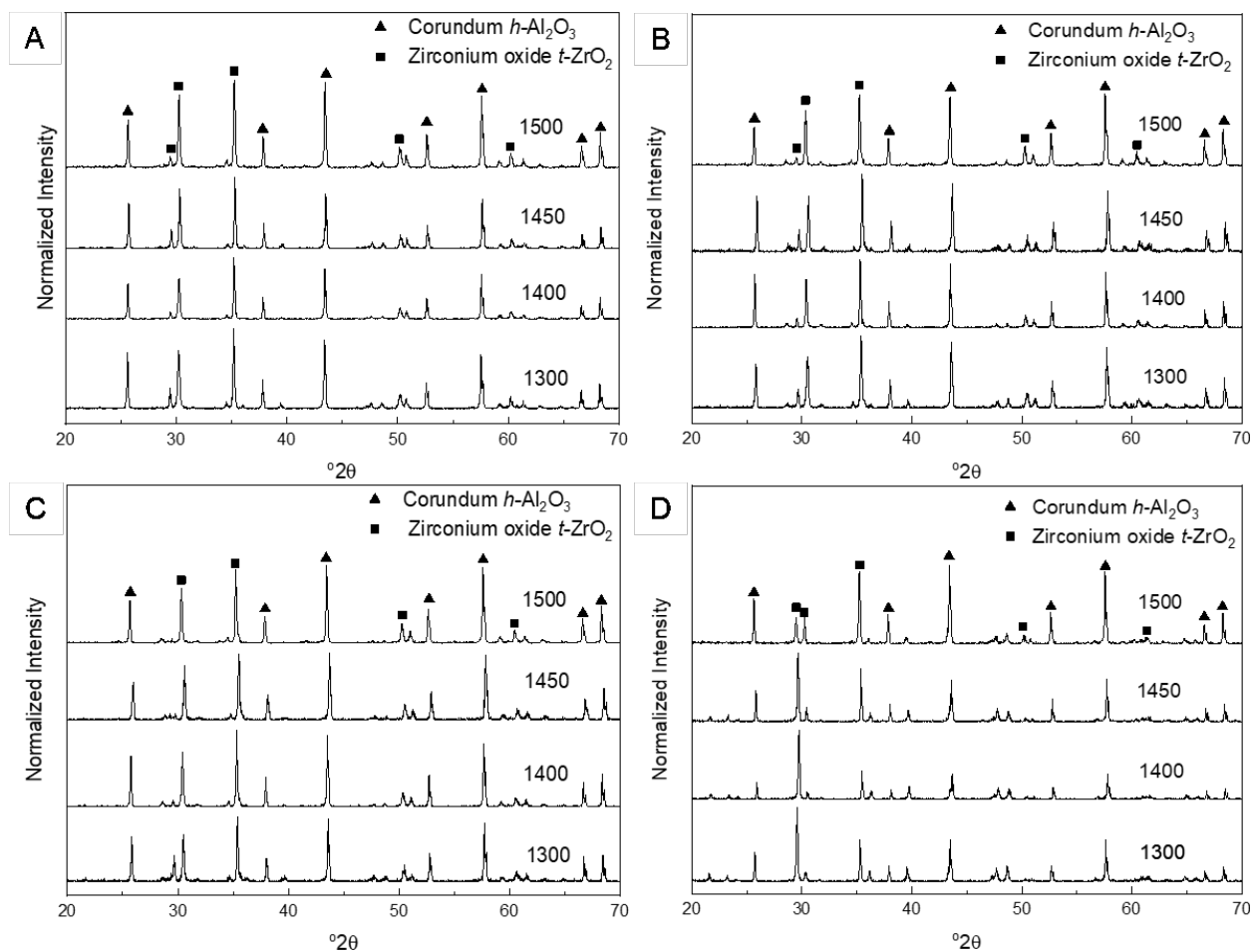


Figure D.9. XRDs of ZTA films (**A-D** per Table **D.5**) sintered at 1300-1500 °C/5 h/O₂.

A similar sintering study on the films **A-D** was repeated in N₂/H₂ (see Figure **D.1b** schedule). Since the films barely sinter at 1300 °C/5 h/O₂ (Figure **D.8**), a similar outcome in N₂/H₂ is expected and therefore only sintering at 1400-1500 °C/5 h/N₂/H₂ was explored.

Figure **D.10** compares SEM fracture surfaces of films **A-D** sintered at 1400-1500 °C/5 h/N₂/H₂. Similar densification behaviors are observed as in O₂. Films **B** and **C** start to densify at 1400 °C, obvious grain growth can be seen at 1500 °C, especially for film **B**. Films **A** and **D** show similar sintering behavior, they densify at 1500 °C, and exhibit finer grain sizes (0.5-1 μm) than **B** and **C** (≥1 μm). As discussed, TiO₂ promotes grain growth and densification,^{7,8,37-40} while MgO tends to diffuse to the grain boundaries and limits grain growth.^{10,40-51}

After sintering at 1500 °C, all films show some transgranular fracture behavior (marked with red arrows) suggesting improved mechanical properties.

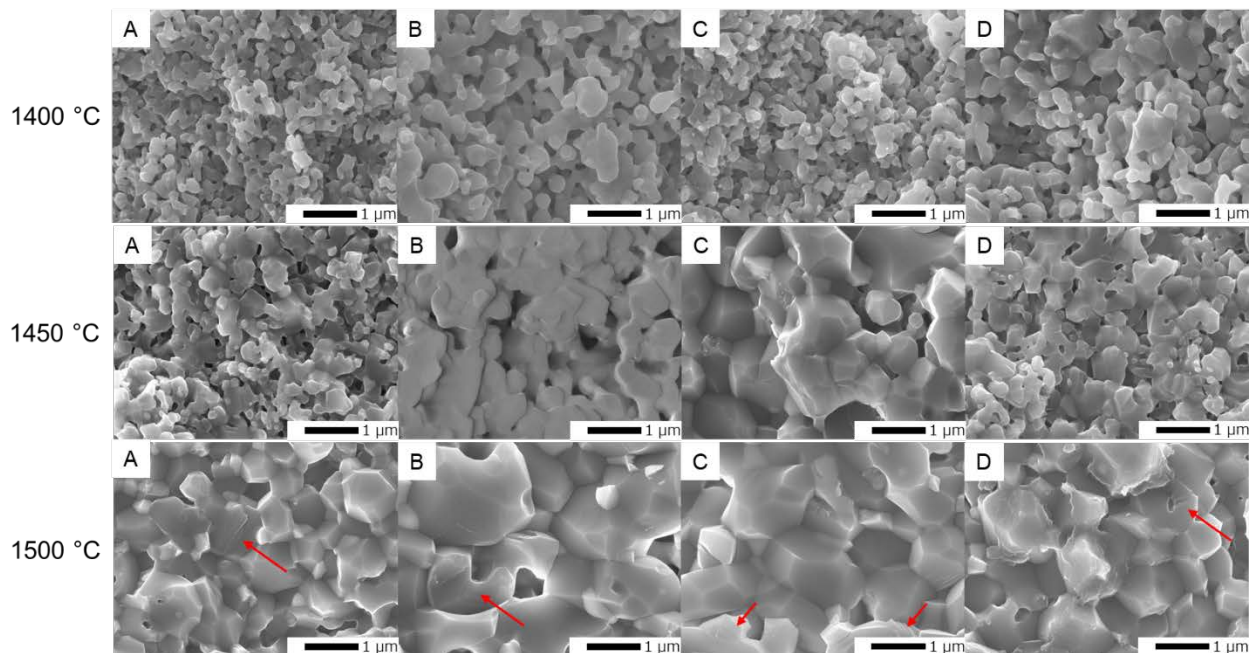


Figure D.10. SEM fracture surfaces of ZTA films (A-D per Table D.5) sintered at 1400-1500 °C/5 h/N₂/H₂. Red arrows suggest transgranular fracture.

Film lateral shrinkage was measured before and after sintering per Table D.6. Overall, shrinkage increases with sintering temperature. At 1500 °C in both O₂ and N₂/H₂, films with different compositions show similar lateral shrinkages of ~20%. Films with composition **B** have the highest lateral shrinkage, recall that they have much larger AGSs (1-2 µm at 1500 °C/O₂ and N₂/H₂), as seen in Figures D.8 and D.10. This suggests, as expected, that TiO₂ CP promotes densification and grain growth, resulting in higher shrinkages and larger AGSs. TiO₂ LF-FSP NPs also promote densification (Figures D.8 and D.10), film **C** starts to densify at 1400 °C, but smaller AGSs result compared to film **B**, likely a result of the smaller APSs of TiO₂ LF-FSP NPs compared to TiO₂ CP. Film **D** with both TiO₂ and MgO doping generally shows both smaller and more uniform AGSs compared to film **C** under different sintering conditions (Figures D.8 and D.10).

Table D.6. Lateral shrinkage of ZTA films (A-D per Table D.5) sintered at 1400-1500 °C/5 h/N₂/H₂.

Sintering condition	Lateral shrinkage, %			
	A	B	C	D
1400 °C/5 h/N ₂ /H ₂	14	10	14	12
1450 °C/5 h/N ₂ /H ₂	16	19	22	18
1500 °C/5 h/N ₂ /H ₂	24	25	24	22
1500 °C/5 h/O ₂	19	25	22	22

Figure D.11 shows XRDs of the films sintered at 1400-1500 °C/5 h/N₂/H₂. Similar to films sintered in O₂, they mainly contain α -Al₂O₃ and *t*-ZrO₂; the impurity calcite phase (36, 40, 48 and 49° 2 θ) is also observed in some films. Phase compositions of the different films are also very similar, and no *m*-ZrO₂ is observed. The composition does not change with different sintering conditions.

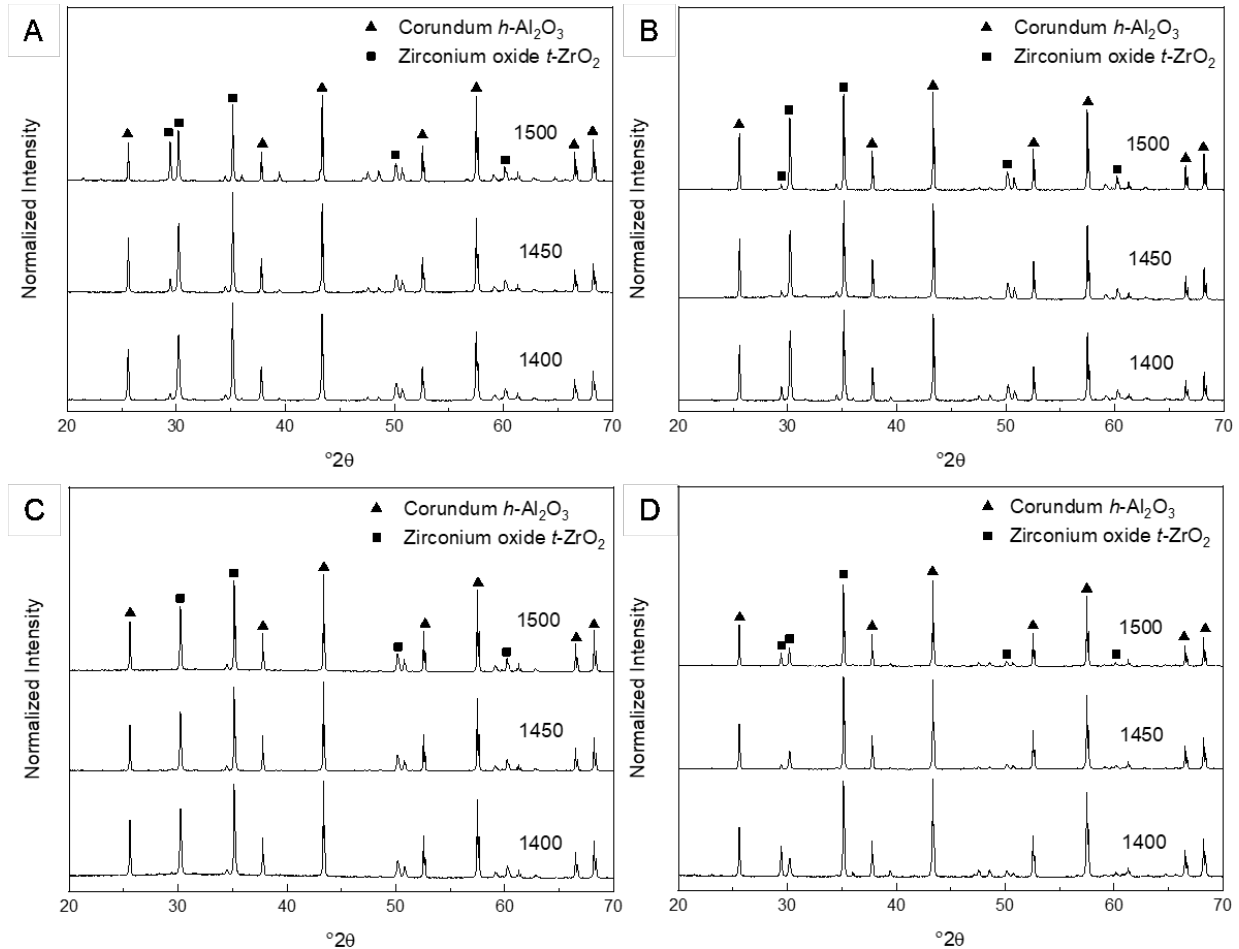


Figure D.11. XRDs of ZTA films (A-D per Table D.5) sintered at 1400-1500 °C/5 h/N₂/H₂.

The conclusions from the thin film work are that films with composition **D** per Table **D.5** show small and uniform grain sizes (0.5-1 μm), and low porosity. They are almost fully dense when sintered at 1500 $^{\circ}\text{C}/5$ h, in either O_2 or N_2/H_2 per SEM observations (Figures **D.8** and **D.10**). These results were then extended to processing ~ 200 μm thick ZTA films with the same composition.

D.3.2 ZTA ~ 200 μm thick films

In this section, the sinterability, microstructures and fractural toughness of ZTA films up to ~ 200 μm thick and $\sim 2 \times 2$ cm^2 were investigated for possible application as power electronic substrates¹¹⁻¹⁴ using composition **D** from the above studies.

We first started by targeting ~ 200 μm thick ZTA films with small sizes ($\sim 1 \times 1$ cm^2) sintered at 1500 $^{\circ}\text{C}/5$ h in O_2 or N_2/H_2 to compare sintering behavior in different atmospheres. Figure **D.12** compares SEM fracture surfaces of ZTA films (composition **D**) sintered at 1500 $^{\circ}\text{C}/5$ h in O_2 and N_2/H_2 . Films sintered in different atmospheres show similar morphologies with AGSs of 0.5-1 μm . Films sintered in N_2/H_2 shows slightly smaller AGSs, greater shrinkage in both lateral and vertical dimensions (Figure **D.12** and Table **D.7**), and lower porosity (Figure **D.12d** vs. **D.12c**), suggesting that N_2/H_2 provides higher densities, in agreement with previous work on MgO (0-5 wt.%) doped Al_2O_3 thin films.¹⁰

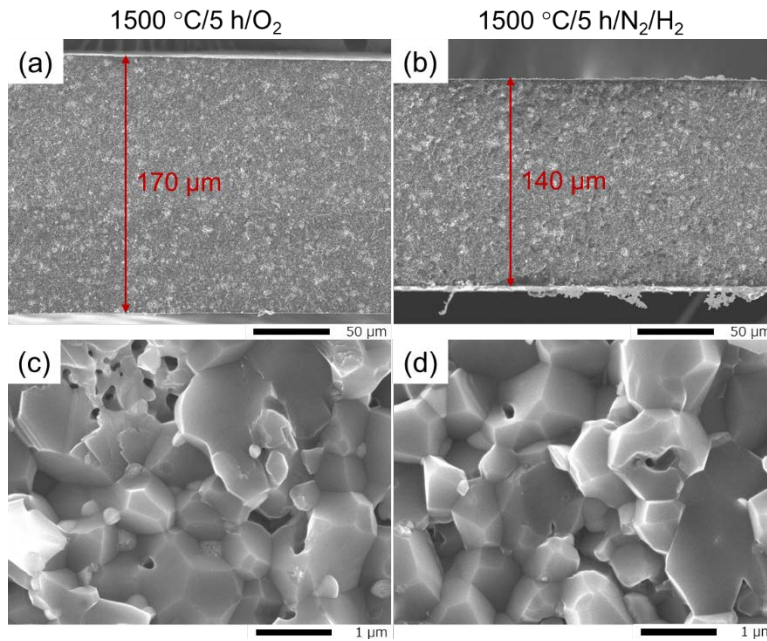


Figure D.12. SEM fracture surfaces of ZTA films (composition **D**, size $\approx 1 \times 1 \text{ cm}^2 \times 200 \text{ }\mu\text{m}$) sintered at $1500 \text{ }^\circ\text{C}/5 \text{ h}/\text{O}_2$ (a, c) and $1500 \text{ }^\circ\text{C}/5 \text{ h}/\text{N}_2/\text{H}_2$ (b, d). Initial thickness $\approx 200 \text{ }\mu\text{m}$ before sintering.

Table D.7. AGSs and shrinkages of ZTA films (composition **D**, size $\approx 1 \times 1 \text{ cm}^2 \times 200 \text{ }\mu\text{m}$).

Sintering condition	AGS, μm	Lateral shrinkage, %	Vertical shrinkage, %
$1500 \text{ }^\circ\text{C}/5 \text{ h}/\text{O}_2$	0.9 ± 0.2	19	17
$1500 \text{ }^\circ\text{C}/5 \text{ h}/\text{N}_2/\text{H}_2$	0.8 ± 0.2	22	24

Figure **D.13** shows XRDs of ZTA films (composition **D**) sintered in O_2 and N_2/H_2 , respectively. Similar to thin films above, both films exhibit two main phases: $\alpha\text{-Al}_2\text{O}_3$ (hexagonal) and $t\text{-ZrO}_2$, but the impurity phase (calcite) disappears. No obvious difference in phase compositions is observed for films sintered in different atmospheres.

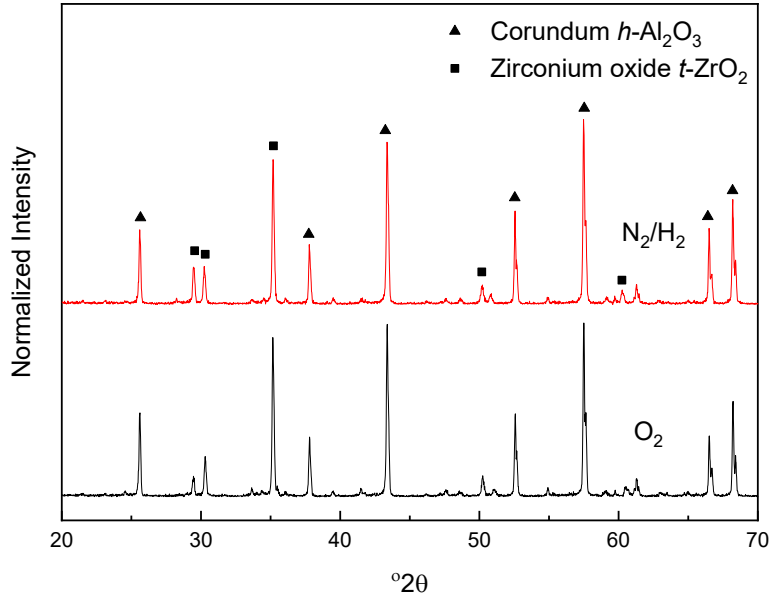


Figure D.13. XRDs of ZTA films (composition **D**, size $\approx 1 \times 1 \text{ cm}^2 \times 200 \text{ }\mu\text{m}$) sintered at $1500 \text{ }^\circ\text{C}/5 \text{ h}/O_2$ (bottom) and $1500 \text{ }^\circ\text{C}/5 \text{ h}/N_2/H_2$ (top).

Studies on smaller ($\sim 1 \times 1 \text{ cm}^2$), $\sim 200 \text{ }\mu\text{m}$ ZTA films suggested that N_2/H_2 sintering provides higher densities. Therefore, we continued studies on larger films ($\sim 2 \times 2 \text{ cm}^2$) sintered in N_2/H_2 . Initially, the same sintering schedule with a ramp rate of $5 \text{ }^\circ\text{C}/\text{min}$ was used (Figure **D.1b**). However, as seen in Figure **D.14**, the larger films cracked while smaller films remained intact after sintering.

It's likely that the fast ramp rate leads to fast shrinkage and cracking. Therefore, the ramp rate was reduced to 2.5 and then $1 \text{ }^\circ\text{C}/\text{min}$ while following the same schedule per Figure **D.1b**, but the larger films still cracked (Figure **D.14**). Only one large film out of three sintered at $1 \text{ }^\circ\text{C}/\text{min}$ was crack-free. This suggests that a slow ramp rate will prevent cracking, but it is a very inefficient method (long sintering time: $>24 \text{ h}$) that provides small improvements.

In addition, these films bonded to the Al_2O_3 substrates after sintering, a likely source of stress that results in cracking. Therefore, an insulating boron nitride (BN) powder layer was introduced as it is stable to $\sim 2000 \text{ }^\circ\text{C}$, see below.

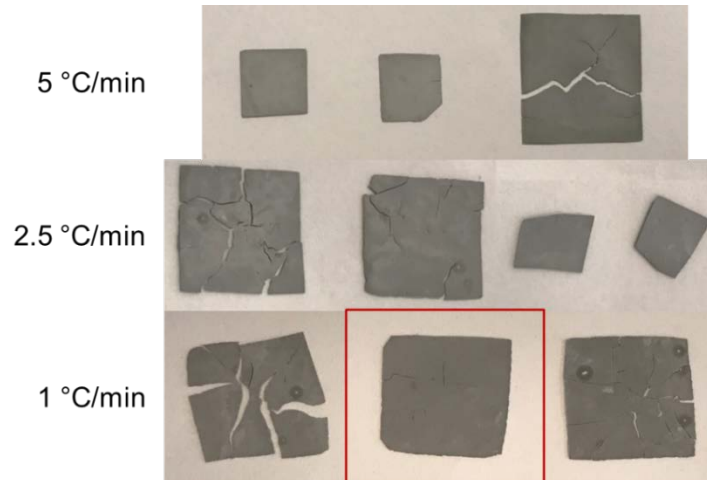


Figure D.14. Optical images of $\sim 200 \mu\text{m}$ ZTA films (composition **D**) sintered at $1500 \text{ }^\circ\text{C}/5 \text{ h}/\text{N}_2/\text{H}_2$ with different sintering ramp rates.

SEMs of $\sim 200 \mu\text{m}$ ZTA films sintered at different ramp rates show small differences (Figure **D.15**). All films were dense with similar AGSs of $1\text{-}2 \mu\text{m}$. However, films sintered at lower ramp rates (2.5 and $1 \text{ }^\circ\text{C}/\text{min}$) show slightly larger grains (Figure **D.15** and Table **D.8**), likely due to the longer sintering times. The sintered thicknesses varied between $175\text{-}210 \mu\text{m}$. Table **D.8** summarizes AGSs, shrinkage and density changes on sintering.

Generally, slower ramp rates caused greater shrinkages and higher densities, but overall densities ($\sim 90 \%$) are low while AGSs increased compared to small films per Figure **D.12** and Table **D.7**, likely due to undesired adherence of the ZTA films to the Al_2O_3 substrates inhibiting shrinkage and therefore densification, while coincidentally generating larger AGSs.

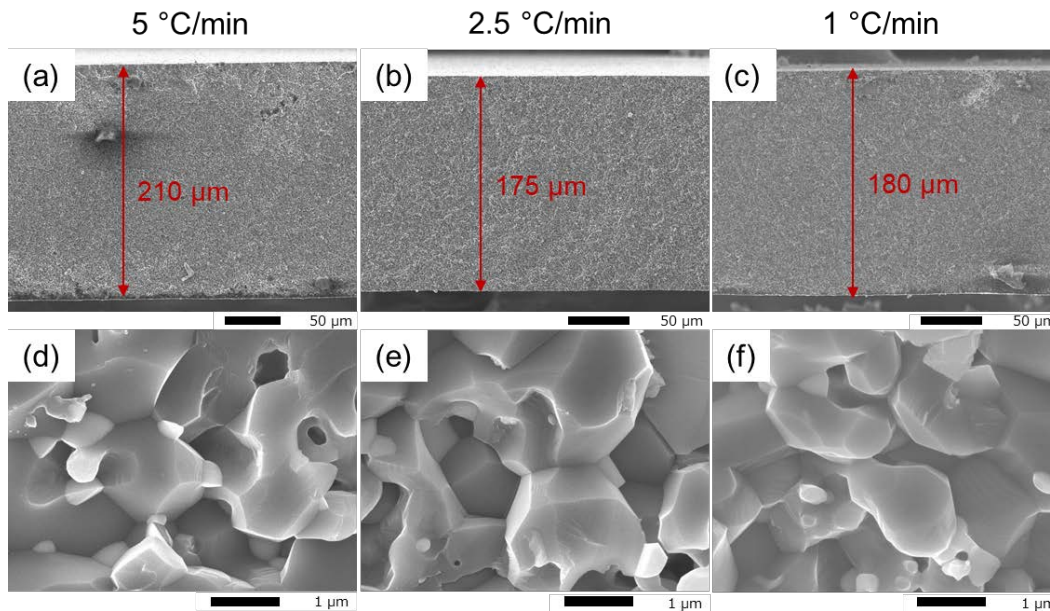


Figure D.15. SEM fracture surfaces of $\sim 200 \mu\text{m}$ ZTA films (composition **D**) sintered ($1500 \text{ }^\circ\text{C}/5 \text{ h}/\text{N}_2/\text{H}_2$) at $5 \text{ }^\circ\text{C}/\text{min}$ (a, d), $2.5 \text{ }^\circ\text{C}/\text{min}$ (b, e) and $1 \text{ }^\circ\text{C}/\text{min}$ (c, f). Green film thicknesses were $220\text{-}250 \mu\text{m}$ before sintering.

Table D.8. Selected properties of $\sim 200 \mu\text{m}$ ZTA films (composition **D**) sintered at $1500 \text{ }^\circ\text{C}/5 \text{ h}/\text{N}_2/\text{H}_2$ with different sintering ramp rates.

Ramp rate, $^\circ\text{C}/\text{min}$	AGS, μm	Lateral shrinkage, %	Vertical shrinkage, %	Measured density*, g/cm^3	Theoretical density*, g/cm^3	Relative density, %
5	1.3 ± 0.3	20	16	3.62	4.04	89.7
2.5	1.5 ± 0.3	22	24	3.66	4.03	90.7
1	1.6 ± 0.4	23	23	3.68	4.04	91.2

*Film densities are measured by the Archimedes method; theoretical densities are calculated from phase compositions analyzed by XRD refinement.

Figure **D.16** compares XRDs of $\sim 200 \mu\text{m}$ ZTA films sintered at different ramp rates. No obvious differences can be seen; all the films show two main phases without impurities: $\alpha\text{-Al}_2\text{O}_3$ and $t\text{-ZrO}_2$.

To eliminate cracking, an insulating BN layer (powder from Sigma-Aldrich) was introduced to prevent bonding with the Al_2O_3 substrates. Additionally, sintering following different binder burnout temperatures of 600° , 800° and $1100 \text{ }^\circ\text{C}$ was investigated. The binder burnout atmosphere

was changed from O₂ to air reducing the rate of oxidative decomposition. The sintering schedule is provided in Figure D.17.

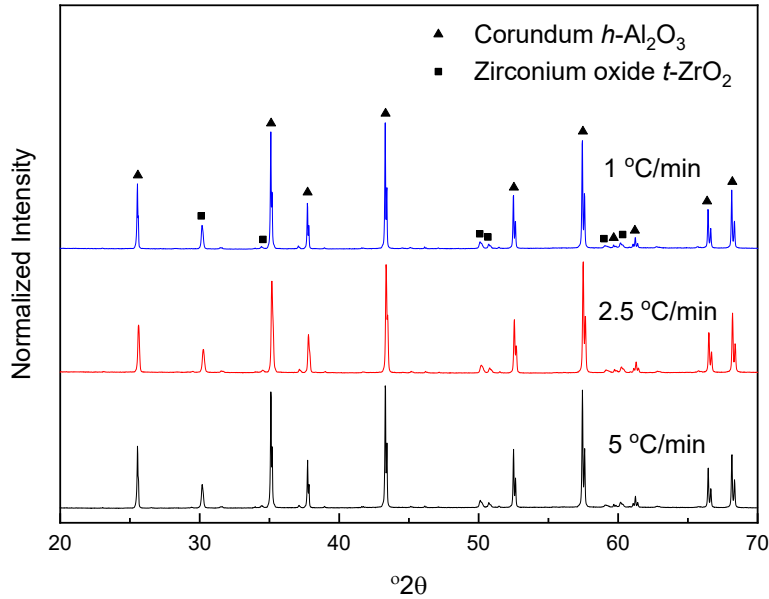


Figure D.16. XRDs of ~200 μm ZTA films (composition **D**) sintered at 1500 °C/5 h/N₂/H₂ with different sintering ramp rates.

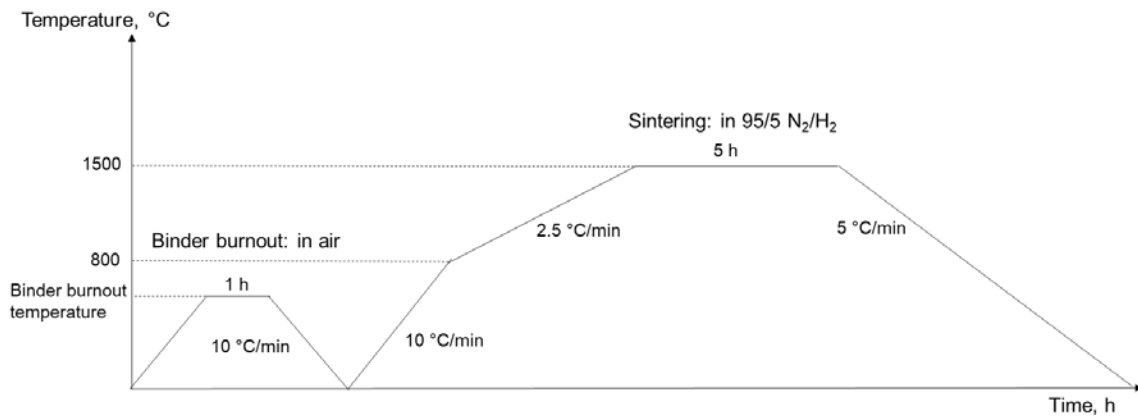


Figure D.17. Sintering schedule of ~200 μm ZTA films (composition **D**) with different binder burnout temperatures of 600, 800 and 1100 °C in air, with BN insulation.

Figure D.18 compares films sintered at different binder burnout temperatures with BN interfaces. Films debinded at 800 °C/1 h/air stayed mostly intact after sintering. However, films debinded at 600 °C/1 h/air formed large cracks, and films debinded at 1100 °C/1 h/air cracked

into pieces. Such differences in film quality suggest that cracking is primarily related to binder burnout.



Figure D.18. Optical images of $\sim 200\ \mu\text{m}$ ZTA films (composition **D**) sintered at $1500\ \text{°C}/5\ \text{h}/\text{N}_2/\text{H}_2$, $2.5\ \text{°C}/\text{min}$ with different binder burnout temperatures and BN insulation.

Figure **D.19** compares SEMs of $\sim 200\ \mu\text{m}$ ZTA films with different binder burnout temperatures with BN insulation. Films debinded at $600\ \text{°C}/1\ \text{h}/\text{air}$ show the lowest porosities and smallest AGSs of $0.7\ \mu\text{m}$ among the three (see Table **D.9** below). All films show similar vertical shrinkages of $\sim 20\ \%$ (Table **D.9**). Figure **D.20** compares XRDs of $200\ \mu\text{m}$ ZTA films with different binder burnout temperatures. As with the above XRD studies, no obvious differences are observed; all films show two main phases of $\alpha\text{-Al}_2\text{O}_3$ and $t\text{-ZrO}_2$ without impurity.

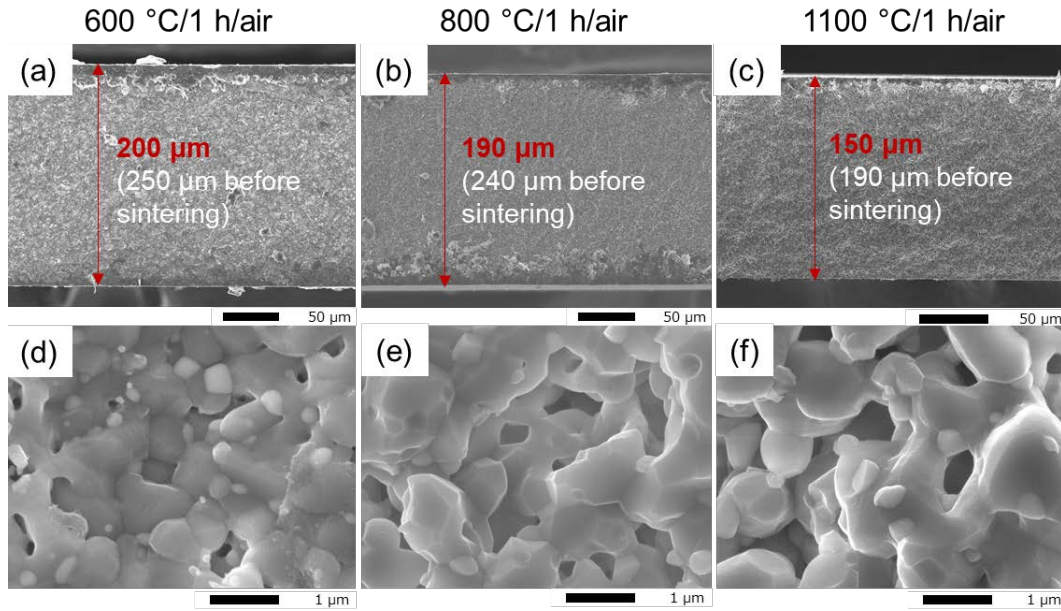


Figure D.19. SEM fracture surfaces of $\sim 200 \mu\text{m}$ ZTA films (composition **D**, sintered at $1500^\circ\text{C}/5 \text{ h}/\text{N}_2/\text{H}_2$, $2.5^\circ\text{C}/\text{min}$) debinded at $600^\circ\text{C}/1 \text{ h}/\text{air}$ (a, d), $800^\circ\text{C}/1 \text{ h}/\text{air}$ (b, e), and $1100^\circ\text{C}/1 \text{ h}/\text{air}$ (c, f) with BN insulation.

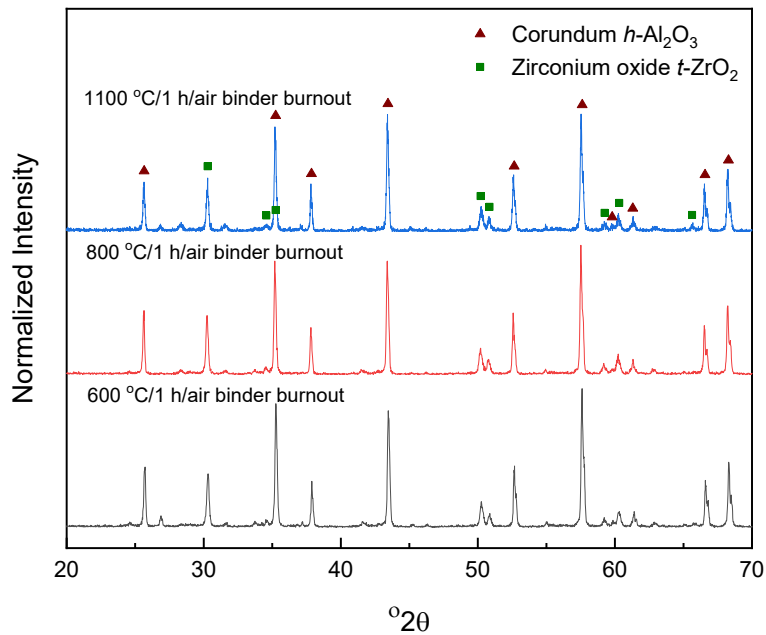


Figure D.20. XRDs of $\sim 200 \mu\text{m}$ ZTA films (composition **D**) sintered at $1500^\circ\text{C}/5 \text{ h}/\text{N}_2/\text{H}_2$, $2.5^\circ\text{C}/\text{min}$ with different binder burnout temperatures and BN insulation.

To further investigate the binder burnout mechanism, a TGA-DTA was run on the 10 mol.% ZrO₂ doped Al₂O₃ green films (composition **D**, Figure **D.21**). A decomposition exotherm for the organics appears between ~180-500 °C. Accordingly, the sintering schedule was modified per Figure **D.22** with a three-step binder burnout procedure: first holding at 200 °C/1 h and slowly (1 °C/min) ramping up to 500 °C, then ramping up (2.5 °C/min) to 800 °C/1 h.

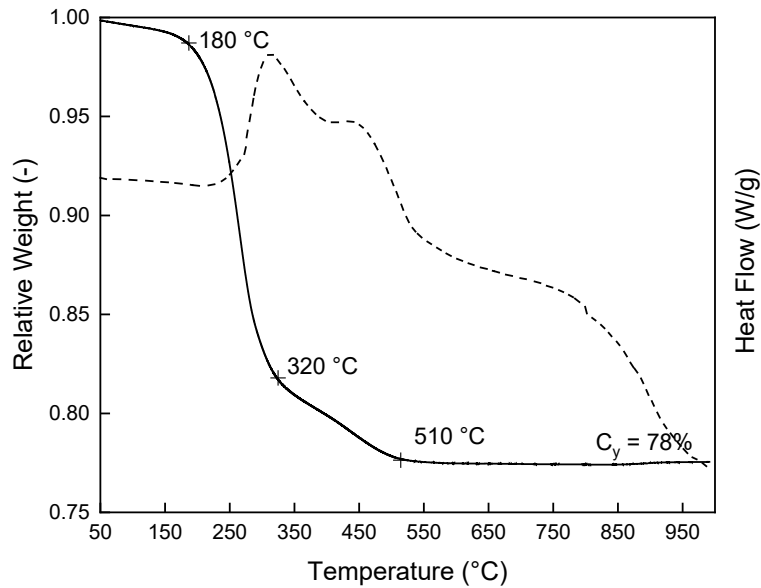


Figure D.21. TGA (1000 °C/air) of 10 mol.% ZrO₂ doped Al₂O₃ (composition **D**) green films.

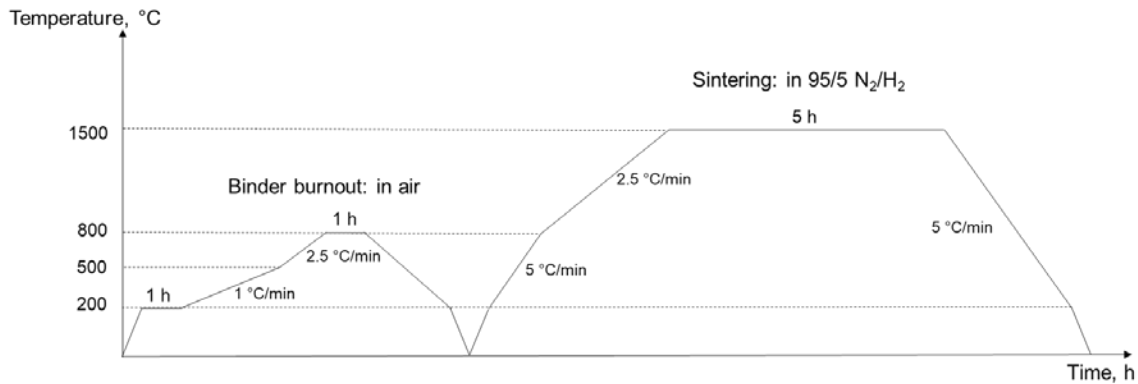


Figure D.22. Sintering schedule of 200 μm ZTA films with slow binder burnout ramp rates and BN insulation.

Figure **D.23** shows optical images of ~ 200 μm ZTA films before and after sintering. After binder burnout, all films only show minimal size changes. Shrinkage and coincident densification occur primarily during sintering. Films with thicknesses ≤ 200 μm after sintering are crack-free, while films with thicknesses >220 μm exhibit small cracks. All films remain mostly intact with better quality compared to the above films (Figures **D.14** and **D.18**).

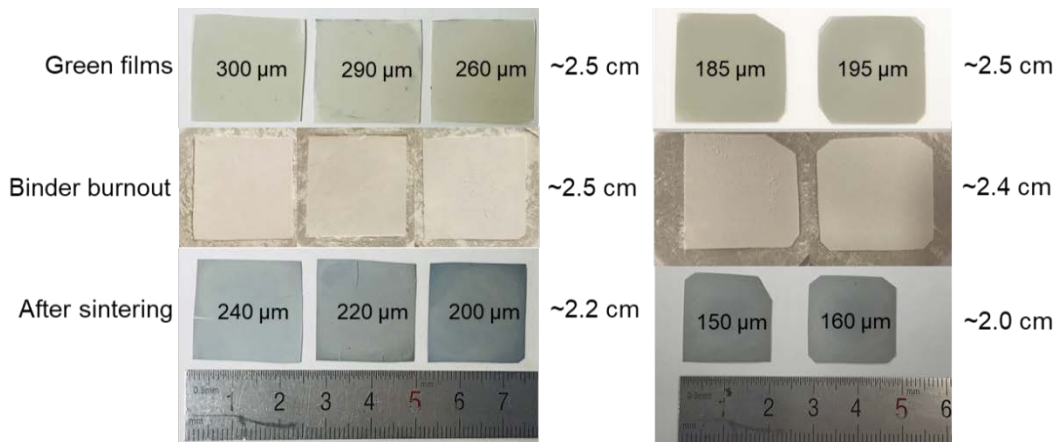


Figure D.23. Optical images of ~ 200 μm ZTA films (composition **D**) before and after binder burnout and sintering. Thicknesses and lateral lengths are given on the films and on the right, respectively.

As shown in Figure **D.24**, films sintered using the 3-step binder burnout procedure show low porosities and small AGSs of 0.7 μm after sintering. Table **D.9** compares AGSs, shrinkages and densities of ZTA films sintered using different binder burnout conditions with BN insulation. All films have densities of 97-99 % determined by Archimedes method, which improve significantly from films sintered without BN insulation (~ 90 % dense, Table **D.8**). In addition, the AGSs of films sintered with BN decreased (≤ 1 μm) compared to films without (1.3 - 1.6 μm , Table **D.8**). The use of BN powder between ZTA films and Al_2O_3 improves film densities and reduces AGSs, as the substrate effects are eliminated.

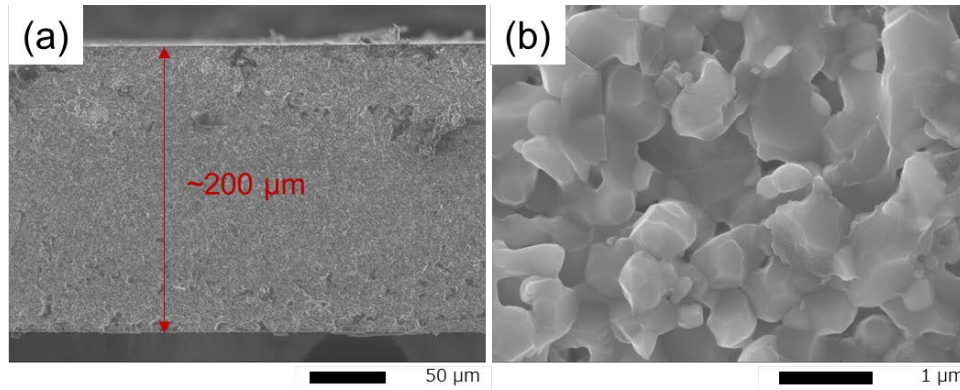


Figure D.24. SEM fracture surfaces of ~200 μm ZTA film (composition **D**) sintered with 3-step binder burnout procedure per Figure **D.22**.

Table D.9. Selected properties of ~200 μm ZTA films (composition **D**) sintered at different binder burnout conditions with BN insulation.

Binder burn-out condition	AGS, μm	Lateral shrinkage, %	Vertical shrinkage, %	Measured density, g/cm^3	Theoretical density, g/cm^3	Relative density, %
600 °C/1h/air	0.7 \pm 0.1	20	20	4.05	4.10	98.8
800 °C/1h/air	0.8 \pm 0.1	21	21	4.07	4.12	98.8
1100 °C/1h/air	1.1 \pm 0.1	N/A*	21	4.00	4.12	97.1
3-step burnout	0.7 \pm 0.1	17	19	4.02	4.10	98.1

*Films debindered at 1100 °C/1h/air cracked into pieces and failed to give accurate lateral lengths after sintering.

Fracture toughness (K_{1C}) measurements were undertaken using a single-edge precracked beam test (SEPB) on the ~200 μm ZTA films (composition **D**) sintered with a 3-step binder burnout procedure (Figure **D.22**) as they show optimum qualities compared to other films. As given in Figure **D.25**, ~200 μm 10 mol.% ZrO_2 doped Al_2O_3 films show K_{1C} values in a range of 15-38 $\text{MPa m}^{1/2}$ (three samples) with an average of 24 $\text{MPa m}^{1/2}$, which is 2-4 times higher than reported values. Such a high K_{1C} value may be attributed to the fine and uniform ceramic microstructures sintered from NPs by LF-FSP, retained *t*- ZrO_2 phase after sintering, TiO_2 and MgO doping, and improved film qualities through sintering refinement.

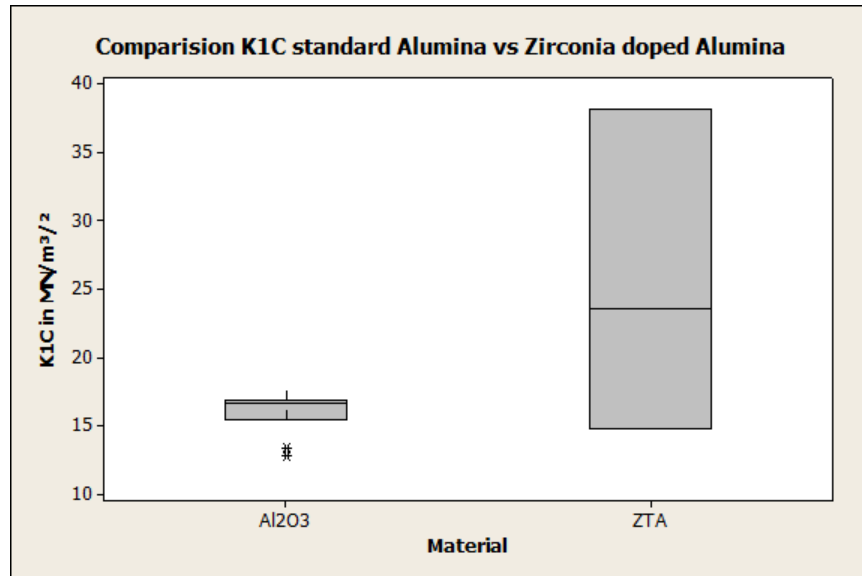


Figure D.25. Fracture toughness (K_{1C}) of standard Al_2O_3 films and $\sim 200 \mu m$ ZTA films (composition **D**) sintered with 3-step binder burnout procedure per Figure **D.22**, experiment performed by Rogers Germany GmbH.

D.3.3 Coating Si_3N_4 substrates with ZTA thin films

In this section, above results provide the basis for formulating and processing thin ZTA films (composition **D** per Table **D.5**) on $\sim 300 \mu m$ Si_3N_4 films as a bonded physical layer to minimize oxidation for high-temperature substrates and power electronic applications. As discussed in the previous section, ZTA films with composition **D** show a high K_{1C} and density, therefore we continued coating studies with the same composition.

Figure **D.26a** shows surfaces of coated Si_3N_4 films sintered at $1500 \text{ }^\circ\text{C}/5 \text{ h}/N_2/H_2$. Compared to uncoated films in Figure **D.2**, the coating appears to be light grey and uniform. As shown in Figure **D.26b**, a coated Si_3N_4 film was marked with red dye and then rinsed with ethanol. After rinsing, the red mark disappears completely, which suggests that the dye does not penetrate through unseen cracks and that the coating is stable, smooth and crack free.

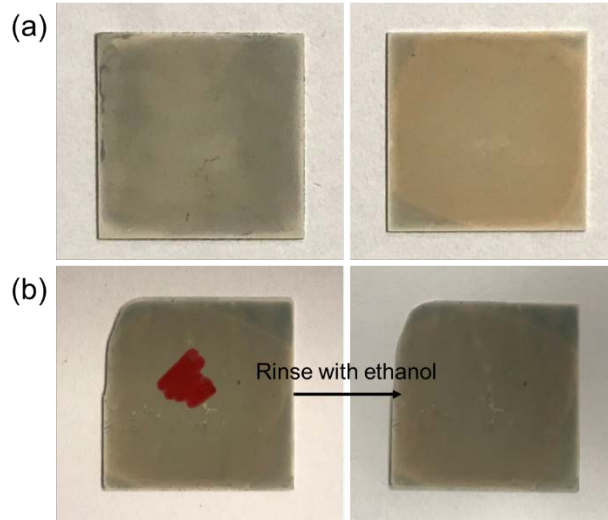


Figure D.26. Representative examples (a) and dye test (b) of Si_3N_4 films coated with ZTA (composition **D**) after sintering at $1500\text{ }^\circ\text{C}/5\text{ h}/\text{N}_2/\text{H}_2$.

Figures **D.27** and **D.28** show SEMs and EDSs of coated Si_3N_4 films. For coated films, the rod-like Si_3N_4 structure at the surface (Figure **D.27c**) is replaced by a dense, homogeneous Al-rich coating with finer grains (Figures **D.27b** and **D.28**). The fracture surface suggests the coating is $2\text{--}3\text{ }\mu\text{m}$ thick (Figure **D.27a**). However, there are small cracks propagating along the surface (Figure **D.27b**), which may be introduced by thermal pressing or the sample breaking during SEM preparation, which requires small sample sizes ($\leq 0.5 \times 0.5\text{ cm}^2$).

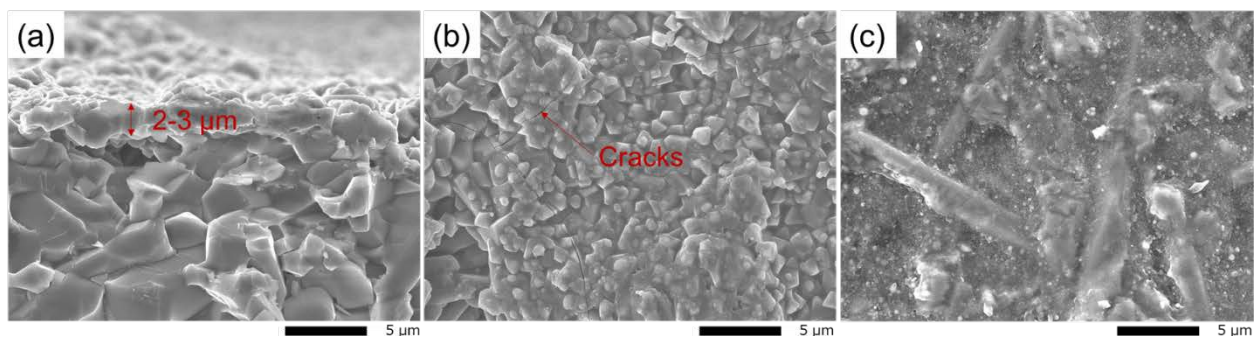


Figure D.27. SEM fracture surface (a) and surface (b) of Si_3N_4 films coated with ZTA (composition **D**) sintered at $1500\text{ }^\circ\text{C}/5\text{ h}/\text{N}_2/\text{H}_2$. **c.** SEM surface of an uncoated Si_3N_4 film.

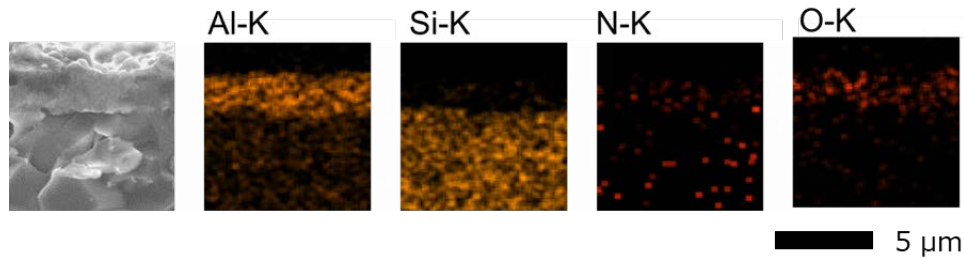


Figure D.28. EDSs of a Si_3Ni_4 film coated with ZTA (composition **D**) sintered at $1500\text{ }^\circ\text{C}/5\text{ h}/\text{N}_2/\text{H}_2$.

As shown in the Figure **D.29** XRDs, coated Si_3N_4 films present hexagonal $\beta\text{-Si}_3\text{N}_4$, as found in the original Si_3N_4 film. A cubic $\gamma\text{-Al}_{2.66}\text{O}_4$ phase appears with a trace of cubic ZrO_2 , indicating that the 10 mol.% ZrO_2 doped Al_2O_3 likely reacts or partially reacts with the Si_3N_4 substrate resulting in a structural distortion again suggesting good bonding.

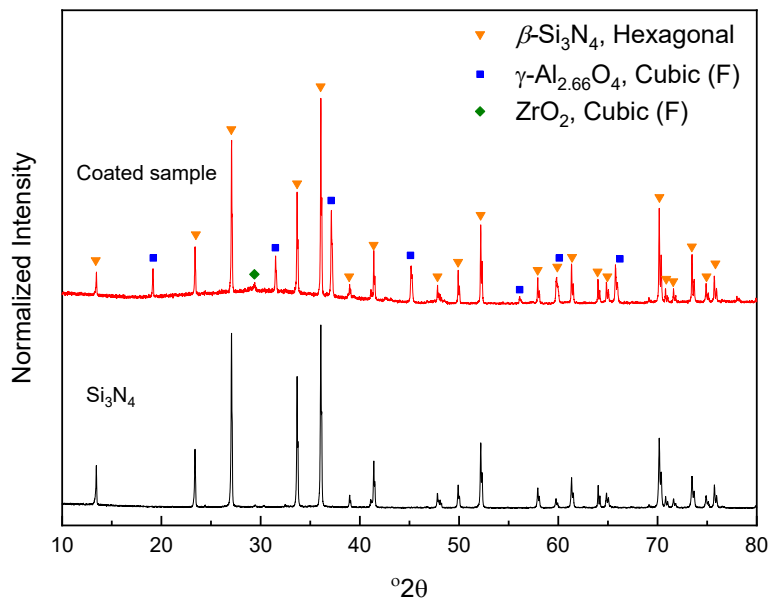


Figure D.29. XRDs of Si_3N_4 films coated with ZTA (composition **D**) sintered at $1500\text{ }^\circ\text{C}/5\text{ h}/\text{N}_2/\text{H}_2$.

Uncoated and coated Si_3N_4 films were heated to $1500\text{ }^\circ\text{C}/1\text{ h}/\text{O}_2$ to assess resistance to oxidation. As shown in Figure **D.30**, the uncoated Si_3N_4 film suffers more damage than the coated sample. The edges of both films show more visible damage than the centers. During heating, films were sandwiched between Al_2O_3 substrates; the edges were more exposed to O_2 than the center. SEM surface images of the uncoated Si_3N_4 film reveal large cavities from obvious oxidation, while the coated film exhibits a smoother microstructure (Figure **D.30c** and **d**). Overall, it is evident that the coating protects Si_3N_4 films against oxidization, even under extreme conditions.

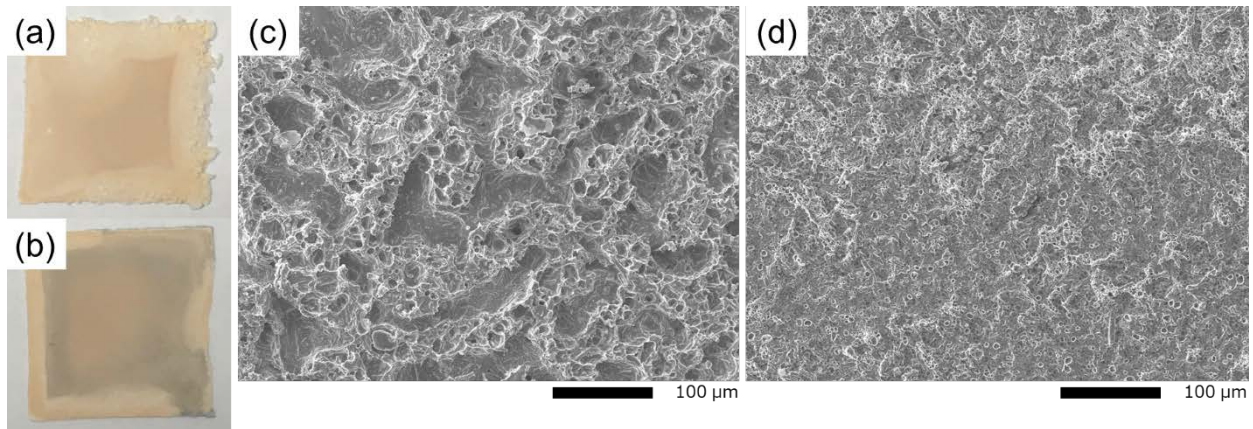


Figure D.30. Optical images of **a.** uncoated and **b.** coated Si_3N_4 films and SEM surfaces of **c.** uncoated and **d.** coated Si_3N_4 films with ZTA (composition **D**) after heating at $1500\text{ }^\circ\text{C}/1\text{ h}/\text{O}_2$.

D.4 Conclusions

In summary, we investigated the sinterability, microstructures and phase compositions of ZTA thin films ($\sim 40\text{ }\mu\text{m}$) with varying compositions and sintering conditions starting from $(\text{ZrO}_2)_x(\text{Al}_2\text{O}_3)_{1-x}$ ($x = 0\text{-}50\text{ mol.}\%$) NPs by LF-FSP. Studies suggest that 1 wt.% MgO and TiO_2 additives improve the sintering behavior, resulting in dense films (composition **D**: 10 mol.% ZrO_2 doped Al_2O_3 with 1 wt.% TiO_2 and MgO) with final AGSs of $0.5\text{-}1\text{ }\mu\text{m}$ at $1500\text{ }^\circ\text{C}$. Comparison

of films sintered in O₂ and N₂/H₂ suggests that the N₂/H₂ atmosphere improves film quality coincident with higher shrinkages and densities, and smaller reductions in AGSs.

For potential applications as power electronic substrates, ZTA film thicknesses were increased to 150-250 μm. Sintered films exhibit hexagonal α -Al₂O₃ and *t*-ZrO₂ phases, which in principle provide good mechanical properties, and was proved by SEPB test that a high K_{1C} value of ~24 MPa m^{1/2} is obtained. By investigating the effects of different sintering conditions, we were able to sinter crack-free 150-250 μm thick 10 mol.% ZrO₂ doped Al₂O₃ films with AGSs of 0.7 μm by using BN insulation between films and Al₂O₃ substrates with a three-step binder burnout procedure.

Finally, ZTA thin films (composition **D**) form homogenous coatings on Si₃N₄ substrates with thicknesses <5 μm that offer protection under extreme oxidative conditions (1500 °C/1 h/O₂), suggesting an alternate application of ZTA films for high-temperature ceramics and power electronic substrates.

References

1. Dorre, E.; Hubner, H. *Alumina: Processing, Properties and Applications*; 1984.
2. Rao, P. K.; Jana, P.; Ahmad, M. I.; Roy, P. K. Synthesis and Characterization of Zirconia Toughened Alumina Ceramics Prepared by Co-Precipitation Method. *Ceram. Int.* **2019**, *45* (13), 16054–16061.
3. Isfahani, T.; Javadpour, J.; Khavandi, A. Formation Mechanism and Phase Transformations in Mechanochemically Prepared Al₂O₃-40wt% ZrO₂ Nanocomposite Powder. *Compos. Interfaces* **2019**, *26* (10), 887–904.
4. Sarkar, D.; Mohapatra, D.; Ray, S.; Bhattacharyya, S.; Adak, S.; Mitra, N. Synthesis and Characterization of Sol-Gel Derived ZrO₂ Doped Al₂O₃ Nanopowder. *Ceram. Int.* **2007**, *33* (7), 1275–1282.
5. Sarkar, D.; Adak, S.; Mitra, N. K. Preparation and Characterization of an Al₂O₃-ZrO₂ Nanocomposite, Part I: Powder Synthesis and Transformation Behavior during Fracture. *Compos. Part Appl. Sci. Manuf.* **2007**, *38* (1), 124–131.
6. Ganesh, I.; Olhero, S. M.; Torres, P. M. C.; Alves, F. J.; Ferreira, J. M. F. Hydrolysis-Induced Aqueous Gelcasting for near-Net Shape Forming of ZTA Ceramic Composites. *J. Eur. Ceram. Soc.* **2009**, *29* (8), 1393–1401.
7. Zu, Y.; Chen, G.; Fu, X.; Luo, K.; Wang, C.; Song, S.; Zhou, W. Effects of Liquid Phases on Densification of TiO₂-Doped Al₂O₃-ZrO₂ Composite Ceramics. *Ceram. Int.* **2014**, *40* (3), 3989–3993.
8. Chen, G.; Zu, Y.; Luo, J.; Fu, X.; Zhou, W. Microstructure and Superplastic Behavior of TiO₂-Doped Al₂O₃-ZrO₂ (3Y) Composite Ceramics. *Mater. Sci. Eng. A* **2012**, *554*, 6–11.
9. Yu, W.; Zheng, Y.; Yu, Y.; Su, X. Microstructural Evolution of Supra-Nanostructure Al₂O₃/ZrO₂ Eutectic Powders by Combustion Synthesis-Spray Cooling. *J. Am. Ceram. Soc.* **2019**, *102* (12), 7689–7698.
10. Takeuchi, M.; Niedermaier, M.; Jansohn, M.; Umehara, N.; Laine, R. M. Processing Thin (<10μm), Dense, Flexible α-Al₂O₃ Films from Nanopowders. *J. Ceram. Soc. Jpn.* **2019**, *127* (2), 81–89.
11. Gundel, P.; Persons, R.; Bawohl, M.; Challingsworth, M.; Czwickla, C.; Garcia, V.; Modes, C.; Nikolaidis, I.; Reitz, J.; Shahbazi, C.; Nowak, T. Highly Reliable and Cost Effective Thick Film Substrates for Power LEDs. In *2016 IEEE Applied Power Electronics Conference and Exposition (APEC)*; IEEE: Long Beach, CA, 2016; pp 3069–3074.
12. Maeder, T.; Jacq, C.; Ryser, P. Long-Term Mechanical Reliability of Ceramic Thick-Film Circuits and Mechanical Sensors under Static Load. *Sens. Actuators Phys.* **2012**, *186*, 210–218.
13. Srikanth, C.; Madhu, G. M. Effect of ZTA Concentration on Structural, Thermal, Mechanical and Dielectric Behavior of Novel ZTA–PVA Nanocomposite Films. *SN Appl. Sci.* **2020**, *2* (3), 422.
14. Mussavi Rizi, S. H.; Ghatee, M. A Study of Mechanical Properties of Alumina–Zirconia Composite Films Prepared by a Combination of Tape Casting and Solution Impregnation Method. *J. Aust. Ceram. Soc.* **2020**, *56* (1), 167–174.
15. Miric, A.; Dietrich, P. *Inorganic Substrates for Power Electronics Applications*. 2013.
16. Chen, I.-W.; Xue, L. A. Development of Superplastic Structural Ceramics. *J. Am. Ceram. Soc.* **1990**, *73* (9), 2585–2609.

17. Wang, X.; Padture, N. P.; Tanaka, H. Contact-Damage-Resistant Ceramic/Single-Wall Carbon Nanotubes and Ceramic/Graphite Composites. *Nat. Mater.* **2004**, 3 (8), 539–544.
18. Chen, P.; Chen, J.; Guo, B.; Liu, H. Measurement of the Dynamic Fracture Toughness of Alumina Ceramic. In *Dynamic Behavior of Materials, Volume 1*; Song, B., Lamberson, L., Casem, D., Kimberley, J., Eds.; Conference Proceedings of the Society for Experimental Mechanics Series; Springer International Publishing: Cham, 2016; pp 33–38.
19. Casellas, D.; Nagl, M. M.; Llanes, L.; Anglada, M. Fracture Toughness of Alumina and ZTA Ceramics: Microstructural Coarsening Effects. *J. Mater. Process. Technol.* **2003**, 143–144, 148–152.
20. GREEN, D. J. Critical Microstructures for Microcracking in Al₂O₃-ZrO₂ Composites. *J. Am. Ceram. Soc.* **1982**, 65 (12), 610–614.
21. Tuan, W. H.; Chen, R. Z.; Wang, T. C.; Cheng, C. H.; Kuo, P. S. Mechanical Properties of Al₂O₃/ZrO₂ Composites. *J. Eur. Ceram. Soc.* **2002**, 22 (16), 2827–2833.
22. Dresvyannikov, A. F.; Petrova, E. V.; Khairullina, A. I. Electrochemical Synthesis and Physicochemical Properties of Nanostructured Al₂O₃-ZrO₂-MgO Oxide Systems. *Prot. Met. Phys. Chem. Surf.* **2020**, 56 (1), 89–93.
23. Abi, C. B.; Emrullahoğlu, O. F.; Said, G. Microstructure and Mechanical Properties of MgO-Stabilized ZrO₂-Al₂O₃ Dental Composites. *J. Mech. Behav. Biomed. Mater.* **2013**, 18, 123–131.
24. Gao, L.; Liu, Q.; Hong, J. S.; Miyamoto, H.; De La Torre, S. D.; Kakitsuji, A.; Liddell, K.; Thompson, D. P. Phase Transformation in the Al₂O₃-ZrO₂ System. *J. Mater. Sci.* **1998**, 33 (6), 1399–1403.
25. Wakai, F.; Iga, T.; Nagano, T. Effect of Dispersion of ZrO₂ Particles on Creep of Fine-Grained Al₂O₃. *J. Ceram. Soc. Jpn.* **1988**, 12, 1206–1209.
26. Yoshida, H.; Okada, K.; Ikuhara, Y.; Sakuma, T. Improvement of High-Temperature Creep Resistance in Fine-Grained Al₂O₃ by Zr⁴⁺ Segregation in Grain Boundaries. *Philos. Mag. Lett.* **1997**, 76 (1), 9–14.
27. Kim, M.; Laine, R. M. Liquid-Feed Flame Spray Pyrolysis (LF-FSP) for Combinatorial Processing of Nanooxide Powders along the (ZrO₂)_{1-x}(Al₂O₃)_x Tie-Line. Phase Segregation and the Formation of Core-Shell Nanoparticles. *J. Ceram. Process. Res.* **2007**, 8 (2), 129–136.
28. Kim, M.; Laine, R. M. Pressureless Sintering T-Zirconia@ δ -Al₂O₃ (54 Mol%) Core-Shell Nanopowders at 1120 °C Provides Dense t-Zirconia-Toughened α -Al₂O₃ Nanocomposites. *J. Am. Ceram. Soc.* **2010**, 93 (3), 709–715.
29. Kim, M. Mixed-Metal Oxide Nanopowders By Liquid-Feed Flame Spray Pyrolysis (LF-FSP): Synthesis and Processing of Core-Shell Nanoparticles, 2008.
30. Zhao, Z.; Zhang, L.; Song, Y.; Wang, W.; Wu, J. Microstructures and Properties of Rapidly Solidified Y₂O₃ Doped Al₂O₃/ZrO₂ Composites Prepared by Combustion Synthesis. *Scr. Mater.* **2006**, 55 (9), 819–822.
31. Pena, J. I.; Merino, R. I.; Harlan, N. R.; Larrea, A.; De la Fuente, G. F.; Orera, V. M. Microstructure of Y₂O₃ Doped Al₂O₃-ZrO₂ Eutectics Grown by the Laser Floating Zone Method. *J. Eur. Ceram. Soc.* **2002**, 22 (14–15), 2595–2602.
32. Lee, J. H.; Yoshikawa, A.; Kaiden, H.; Lebbou, K.; Fukuda, T.; Yoon, D. H.; Waku, Y. Microstructure of Y₂O₃ Doped Al₂O₃/ZrO₂ Eutectic Fibers Grown by the Micro-Pulling-down Method. *J. Cryst. Growth* **2001**, 231 (1–2), 179–185.

33. Yoshida, H.; Kuwabara, A.; Yamamoto, T.; Ikuhara, Y.; Sakuma, T. High Temperature Plastic Flow and Grain Boundary Chemistry in Oxide Ceramics. *J. Mater. Sci.* **2005**, *40* (12), 3129–3135.
34. Yi, E.; Wang, W.; Mohanty, S.; Kieffer, J.; Tamaki, R.; Laine, R. M. Materials That Can Replace Liquid Electrolytes in Li Batteries: Superionic Conductivities in $\text{Li}_{1.7}\text{Al}_{0.3}\text{Ti}_{1.7}\text{Si}_{0.4}\text{P}_{2.6}\text{O}_{12}$. Processing Combustion Synthesized Nanopowders to Free Standing Thin Films. *J. Power Sources* **2014**, *269* (10), 577–588.
35. Yi, E.; Wang, W.; Kieffer, J.; Laine, R. M. Flame Made Nanoparticles Permit Processing of Dense, Flexible, Li^+ Conducting Ceramic Electrolyte Thin Films of Cubic- $\text{Li}_7\text{La}_3\text{Zr}_2\text{O}_{12}$ (c-LLZO). *J. Mater. Chem. A* **2016**, *4* (33), 12947–12954.
36. Yi, E.; Temeche, E.; Laine, R. M. Superionically Conducting $\text{B}''\text{-Al}_2\text{O}_3$ Thin Films Processed Using Flame Synthesized Nanopowders. *J. Mater. Chem. A* **2018**, *6*, 12411–12419.
37. Wang, C. J.; Huang, C. Y. Effect of TiO_2 Addition on the Sintering Behavior, Hardness and Fracture Toughness of an Ultrafine Alumina. *Mater. Sci. Eng. A* **2008**, *492* (1–2), 306–310.
38. BAGLEY, R. D.; CUTLER, I. B.; JOHNSON, D. L. Effect of TiO_2 on Initial Sintering of Al_2O_3 . *J. Am. Ceram. Soc.* **1970**, *53* (3), 136–141.
39. Brook, R. J. Effect of TiO_2 on Initial Sintering of Al_2O_3 . *J. Am. Ceram. Soc.* **1972**, *55* (2), 114–114.
40. ROY, S. K.; COBLE, R. L. Solubilities of Magnesia, Titania, and Magnesium Titanate in Aluminum Oxide. *J. Am. Ceram. Soc.* **1968**, *51* (1), 1–6.
41. Kosmac, T.; Wallace, J. S.; Claussen, N. Influence of MgO Additions on the Microstructure and Mechanical Properties of $\text{Al}_2\text{O}_3\text{-ZrO}_2$ Composites. *J. Am. Ceram. Soc.* **1982**, *65* (5), c66–67.
42. Coble, R. L. Sintering Crystalline Solids. II. Experimental Test of Diffusion Models in Powder Compacts. *J. Appl. Phys.* **1961**, *32* (5), 793–799.
43. Bennison, S. J.; Harmer, M. P. Grain-Growth Kinetics for Alumina in the Absence of a Liquid Phase. *J. Am. Ceram. Soc.* **1985**, *68* (1), C22–C24.
44. BERRY, K. A.; HARMER, M. P. Effect of MgO Solute on Microstructure Development in Al_2O_3 . *J. Am. Ceram. Soc.* **1986**, *69* (2), 143–149.
45. SHAW, N. J.; BROOK, R. J. Structure and Grain Coarsening During the Sintering of Alumina. *J. Am. Ceram. Soc.* **1986**, *69* (2), 107–110.
46. Greskovich, C.; Brewer, J. A. Solubility of Magnesia in Polycrystalline Alumina at High Temperatures. *J. Am. Ceram. Soc.* **2001**, *84* (2), 420–425.
47. Bennison, S. J.; Harmer, M. P. Effect of Magnesia Solute on Surface Diffusion in Sapphire and the Role of Magnesia in the Sintering of Alumina. *J. Am. Ceram. Soc.* **1990**, *73* (4), 833–837.
48. Rhamdhani, M. A.; Soepriyanto, S.; Ramelan, A.; Barliansyah, A. Determination of Mechanism and Grain Growth Kinetics of MgO Doped Al_2O_3 . *J. Trop. Med.* **2005**, *12* (3), 148–158.
49. Lin, F. J. T.; De Jonghe, L. C. Initial Coarsening and Microstructural Evolution of Fast-Fired and MgO -Doped Al_2O_3 . *J. Am. Ceram. Soc.* **1997**, *80* (11), 2891–2896.
50. Kottada, R. S.; Chokshi, A. H. The High Temperature Tensile and Compressive Deformation Characteristics of Magnesia Doped Alumina. *Acta Mater.* **2000**, *48* (15), 3905–3915.
51. Yoshizawa, Y.; Sakuma, T. Improvement of Tensile Ductility in High-Purity Alumina Due To Magnesia Addition. *Scanning* **1992**, *40* (11), 2943–2950.

52. Backhaus-Ricoult, M.; Guerin, V.; Huntz, A.-M.; Urbanovich, V. S. High-Temperature Oxidation Behavior of High-Purity α -, β -, and Mixed Silicon Nitride Ceramics. *J. Am. Ceram. Soc.* **2002**, *85* (2), 385–392.
53. Raider, S. I.; Flitsch, R.; Aboaf, J. A.; Pliskin, W. A. Surface Oxidation of Silicon Nitride Films. *J. Electrochem. Soc.* **1976**, *123* (4), 560–565.
54. Narushima, T.; Goto, T.; Hirai, T.; Iguchi, Y. High-Temperature Oxidation of Silicon Carbide and Silicon Nitride. *Materials Transactions, JIM*. 1997, pp 821–835.
55. Andrews, P.; Riley, F. L. The Microstructure and Composition of Oxide Films Formed during High Temperature Oxidation of a Sintered Silicon Nitride. *J. Eur. Ceram. Soc.* **1989**, *5* (4), 245–256.
56. Zhou, Y.; Hyuga, H.; Kusano, D.; Yoshizawa, Y.; Hirao, K. A Tough Silicon Nitride Ceramic with High Thermal Conductivity. *Adv. Mater.* **2011**, *23* (39), 4563–4567.
57. Fukuda, S.; Shimada, K.; Izu, N.; Miyazaki, H.; Iwakiri, S.; Hirao, K. Crack Generation in Electroless Nickel Plating Layers on Copper-Metallized Silicon Nitride Substrates during Thermal Cycling. *J. Mater. Sci. Mater. Electron.* **2017**, *28* (11), 8278–8285.
58. Hirao, K.; Fukuda, S.; Miyazaki, H.; Zhou, Y.; Hyuga, H.; Iwakiri, S. Evaluation of Residual Thermal Stress in Cu Metalized Silicon Nitride Substrates by Raman Spectroscopy. In *2018 International Conference on Electronics Packaging and iMAPS All Asia Conference (ICEP-IAAC)*; 2018; pp 194–196.
59. Kim, S.; Gislason, J. J.; Morton, R. W.; Pan, X. Q.; Sun, H. P.; Laine, R. M. Liquid-Feed Flame Spray Pyrolysis of Nanopowders in the Alumina-Titania System. *Chem. Mater.* **2004**, *16* (12), 2336–2343.
60. Kim, M.; Laine, R. M. One-Step Synthesis of Core-Shell $(\text{Ce}_{0.7}\text{Zr}_{0.3}\text{O}_2)_x(\text{Al}_2\text{O}_3)_{1-x}$ [$(\text{Ce}_{0.7}\text{Zr}_{0.3}\text{O}_2)@\text{Al}_2\text{O}_3$] Nanopowders via Liquid-Feed Flame Spray Pyrolysis (LF-FSP). *J. Am. Chem. Soc.* **2009**, *131* (26), 9220–9229.
61. Kim, M.; Hinklin, T. R.; Laine, R. M. Core-Shell Nanostructured Nanopowders along $(\text{CeO}_x)_x(\text{Al}_2\text{O}_3)_{1-x}$ Tie-Line by Liquid-Feed Flame Spray Pyrolysis (LF-FSP). *Chem. Mater.* **2008**, *20* (16), 5154–5162.
62. Laine, R. M.; Marchal, J.; Sun, H.; Pan, X. Q. A New $\text{Y}_3\text{Al}_5\text{O}_{12}$ Phase Produced by Liquid-Feed Flame Spray Pyrolysis (LF-FSP). *Adv. Mater.* **2005**, *17* (7), 830–833.
63. Japanese Industrial Standards. *Testing Methods for Fracture Toughness of High Performance Ceramics*; JIS R-1607, 1990.
64. Wei, G. C.; Rhodes, W. H. Sintering of Translucent Alumina in a Nitrogen–Hydrogen Gas Atmosphere. *J. Am. Ceram. Soc.* **2000**, *83* (7), 1641–1648.